Fall 2014

Measurements of entropy-layer instabilities over cone-ogive-cylinders at Mach 6

Roger T Greenwood
Purdue University

Graduate School Form 30
(Revised 08/14)

PURDUE UNIVERSITY
GRADUATE SCHOOL
Thesis/Dissertation Acceptance

This is to certify that the thesis/dissertation prepared

By Roger Greenwood

Entitled
Measurements of Entropy-Layer Instabilities over Cone-Ogive-Cylinders at Mach 6

For the degree of Doctor of Philosophy

Is approved by the final examining committee:

Steven P. Schneider

Steven H. Collicott

Sally Bane

Charles Campbell

To the best of my knowledge and as understood by the student in the Thesis/Dissertation Agreement, Publication Delay, and Certification/Disclaimer (Graduate School Form 32), this thesis/dissertation adheres to the provisions of Purdue University's "Policy on Integrity in Research" and the use of copyrighted material.

Steven P. Schneider

Approved by Major Professor(s): _____

_____

Approved by: Wayne Chen 10/27/2014

Head of the Department Graduate Program Date

MEASUREMENTS OF ENTROPY-LAYER INSTABILITIES OVER CONE-OGIVE-CYLINDERS AT MACH 6

A Dissertation

Submitted to the Faculty

of

Purdue University

by

Roger T. Greenwood

In Partial Fulfillment of the

Requirements for the Degree

of

Doctor of Philosophy

December 2014

Purdue University

West Lafayette, Indiana

This thesis is dedicated to my wonderful wife and children, in recognition of their love, support, and belief that you're never too old to go to school.

ACKNOWLEDGMENTS

The author would like to thank the United States Air Force, particularly Col Neal Barlow and Dr. Russ Cummings at the USAF Academy, for my assignment as a PhD student, providing me the opportunity to spend the past three years at Purdue to immerse myself in this research. Funding for this research was provided by the Air Force Office of Scientific Research under grant number FA9550-12-1-0167.

I would like to thank my advisor, Dr. Steven Schneider for allowing me to join his research group and work with the Boeing/AFOSR Mach-6 Quiet Tunnel. His support, inspired guidance, and direction the past three years has been extremely valuable. Thanks also to the members of my thesis committee, Dr. Steven Collicott, Dr. Sally Bane, and Dr. Chuck Campbell. They each provided excellent direction and insight that was instrumental in making this research a success.

Thanks to"Team Schneider" for their indispensable help and advice throughout my time at Purdue. The ASL machine shop–Jerry Hahn, Robin Snodgrass, and Jim Younts provided excellent design advice and help, fixed hot wires in a timely fashion, and expertly fabricated hardware that was essential to accomplish this work.

I would like to thank Heath Johnson at the University of Minnesota for installing STABL on our Purdue computer. Thanks goes to Lindsay Kirk at NASA Johnson Space Center for her much appreciated help in the design optimization process. I would also like to thank Pedro Paredes and Helen Reed for performing stability analyses on several of the Purdue designs.

Finally, thanks goes to my God who has given me so much, and the most important people in my life– my lovely wife and our wonderful children, who have provided an endless supply of love, support, and encouragement.

TABLE OF CONTENTS

Page

Page

Page

Page

LIST OF TABLES

LIST OF FIGURES

Figure Page

SYMBOLS

ρ	density
ρ_0	stagnation density
M	Mach number
P_0	total pressure
P'	pressure fluctuations
P_{mean}	average pressure
T_0	total temperature
T_w	wall temperature
V	voltage
V'	voltage fluctuations
V_{mean}	average voltage
x	axial distance from model leading edge
y^+	dimensionless wall spacing parameter

ABBREVIATIONS

AAE	Purdue School of Aeronautics and Astronautics
AFOSR	Air Force Office of Scientific Research
AoA	Angle of Attack
BAM6QT	Boeing/AFOSR Mach-6 Quiet Tunnel
CTA	constant-temperature anemometer
CNC	computer numerical control
DPLR	Data-Parallel Line Relaxation
LED	light-emitting diode
LST	linear stability theory
MOC	method of characteristics
PSD	power spectral density
PSE	parabolized stability equations
SSJ	supersonic jet
STABL	Stability and Transition Analysis for hypersonic Boundary Layers
TSP	temperature-sensitive paint

ABSTRACT

Greenwood, Roger T. Ph.D., Purdue University, December 2014. Measurements of Entropy-Layer Instabilities over Cone-Ogive-Cylinders at Mach 6. Major Professor: Steven Schneider.

Predicting the onset of boundary layer transition is critical in hypersonic flight. To improve transition prediction methods, it is necessary to understand the underlying instability mechanisms that cause transition. Entropy-layer instabilities are of particular interest in the design of blunt reentry vehicles and other blunt supersonic and hypersonic vehicles. Entropy-layer instabilities from outside the boundary layer may enter the boundary layer and have a significant effect on transition. There is little experimental data for entropy-layer instabilities.

Experimental measurements of what appear to be entropy-layer instabilities have been made in the Boeing/AFOSR Mach-6 Quiet Tunnel (BAM6QT) using surface pressure transducers and hot-wire anemometry. A long cone-ogive-cylinder model with interchangeable cone-ogive noses was used to generate the shock curvature that resulted in an entropy layer conducive to instability growth. The nosetip angles of the cone-ogive range from 25 to 40 degrees, with a majority of the measurements taken with the sharp 30 to 35-degree nosetips.

Surface measurements of the entropy-layer instabilities using the 30 to 35-degree configurations show disturbances between 15 and 50 kHz. As the nosetip angle increases, the frequency of the instability decreases slightly. Results also show that the instability magnitude as measured on the model surface increases with downstream distance, then decreases, before starting to increase again. The decrease is likely due to stabilization that occurs during the entropy-layer swallowing process.

Off-surface measurements using hot wires have also been made for each of the cone-ogive-cylinder configurations. These measurements show the location, frequency, and relative magnitude of the entropy-layer instability. As the instability progresses downstream, it grows inside the entropy layer, then at a certain distance downstream, the instability approaches the model surface and enters the boundary layer. Results show a smooth variation of the location of this instability descent with nosetip angle. As the angle increases, the instability approaches the model further upstream.

Cross-correlations between the surface transducer and hot-wire anemometry measurements confirm that the same instability is being measured at both locations. Cross-correlations between axially-displaced surface sensors were used to calculate an instability convection velocity that is approximately equal to the numerically-calculated flow velocity. And cross-correlations between azimuthally-displaced sensors show that the instability is primarily axisymmetric. The model angle of attack for all measurements was nominally zero. However, the actual angle of attack may vary by up to 0.1 degrees. The experimental results were also compared with mean-flow computations for several of the model configurations.

1. INTRODUCTION

Boundary-layer transition is particularly important in hypersonic flight. Heat transfer increases by three to eight times requiring more thermal protection. Vehicle forces and moments also change significantly after transition, affecting control authority. However, hypersonic transition is extremely complex with additional instabilities and parametric influences that are not a factor at subsonic speeds [1].

The current understanding of transition and the physics behind it is too limited in most flow conditions to be used for predictive purposes [2]. Therefore, for current designs, questionable correlations and/or conservative estimates are routinely made that require significant overcompensation in areas such as heat shielding and control authority. This results in heavier and less cost-effective designs.

Accurate methods for estimating transition over a range of conditions must be based on an understanding of the underlying physical transition mechanisms, to improve these designs [1, 3–5]. Mack suggests that one of the best ways to apply theory to experiments is to measure disturbances as they are growing, before they lead to transition [6]. Experimental measurements of instabilities are an essential step to developing a better understanding of these instabilities in order to produce more accurate computational models.

For much of the hypersonic regime, transition can be traced to fast-growing second-mode instabilities. A method for measuring second-mode instabilities with surface transducers has been successful in various conventional and quiet hypersonic tunnels [7, 8]. However, blunt vehicles are also susceptible to first-mode and entropy-layer instabilities. First-mode instabilities become important when the edge Mach number is lowered sufficiently due to the strong leading-edge shock. Entropy-layer instabilities can grow inside the flow-normal layer of high gradients outside the boundary layer. This entropy layer is formed by the shock curvature as a result of the blunt

leading edge. The entropy-layer instabilities can then enter the boundary layer and affect transition characteristics [9–11].

Hypersonic vehicle configurations that are sensitive to first-mode and entropy-layer instabilities are of interest to the user community. Experimental measurements are required to understand which mechanisms induce transition under different conditions. A better understanding of the physics behind these instabilities will help develop mechanism-based prediction methods.

This work began with a computational analysis to determine an axisymmetric geometry that is predisposed to the growth of first-mode instabilities under Boeing/AFOSR Mach-6 Quiet Tunnel (BAM6QT) conditions. Initial experimental measurements on the surface of this geometric model showed an instability in the predicted first-mode frequency range. However, variations in flow conditions did not result in the predicted frequency shifts.

A series of experimental methods were then used to more precisely determine the location and characteristics of the measured instabilities. This experimental inquiry culminated in hot-wire measurements that show what appear to be entropy-layer instabilities at several axial locations outside of the predicted boundary layer. These measurements show the instability grow and approach the model with downstream distance. Surface and off-surface measurements made with various nosetip configurations are used to evaluate the effect of a change in the shock curvature. The results show the effect of model geometry on the strength and location of the instability.

2. REVIEW OF LITERATURE

2.1 Boundary Layer Instabilities

Instabilities in a laminar boundary layer leading to transition have been studied for many years. In the early 20th century, Prandtl conducted an experiment in which he believed he saw amplifying instability waves in a flow that was at the time considered stable. He used these results to present a physical argument that all laminar profiles will eventually become unstable [12]. Later, Tollmien and Schlichting presented analytically-derived boundary layer instability theories, but these theories were disputed by many experimentalists because instability waves had never been measured [13]. Then in 1947, Schubauer and Skramstad presented the results of previously classified experiments in a low-noise wind tunnel in which they discovered velocity fluctuations in a flat plate boundary layer. These sinusoidal fluctuations, referred to as "laminar boundary-layer oscillations", were measured by a hot-wire anemometer as part of the first experiments to confirm the boundary-layer instability theories previously presented by Tollmien and Schlichting [14]. This experimental confirmation resulted in wider acceptance of stability theory, which theory provides the basis for analytically predicting the parametric effects of various flow parameters, such as Mach number and pressure/temperature gradients, on boundary layer stability [13].

In incompressible flow, a typical boundary layer starts out laminar. As it proceeds down the surface, unstable two-dimensional Tollmien-Schlichting waves start to appear. As the Reynolds number increases, the instability waves grow, eventually breaking the boundary layer down into turbulence. Even in incompressible flow this is a complex process with multiple possible paths to turbulence which makes transition prediction very difficult [15]. In the compressible subsonic regime, this process

becomes significantly more complex due to the addition of density and temperature fluctuations, but three-dimensional waves can still typically be ignored. However, at supersonic speeds, that is no longer possible [13]. So while subsonic boundary layer instability is important and provides a framework for understanding supersonic and hypersonic boundary layers, in many cases the subsonic transition concepts cannot simply be extended to hypersonic flight regimes [15].

Mack states that in favorable pressure gradients, subsonic boundary layers are stable to inviscid disturbances and viscous forces create the instabilities. However, as the Mach number increases for supersonic and hypersonic boundary layers, the inviscid instability increases and the viscous instability mechanism weakens. Eventually, at about a freestream Mach number of 3, viscosity has only a stabilizing influence in the boundary layer. Mack then discusses what he considered the most significant difference between the supersonic boundary layer instability and its subsonic counterpart: the multiple instability modes. Mack identifies the source of these modes in the second-order inviscid stability equation for the pressure-fluctuation amplitude function. These higher modes are acoustic instability waves that reflect between the surface and the sonic line and are most amplified when two-dimensional. Each of these higher modes is theoretically unstable, with the second mode being the most unstable [12, 16].

Another unique feature of hypersonic boundary layers is that the Tollmien-Schlichtling waves, which dominate in subsonic boundary layers as two-dimensional disturbances, are more unstable in hypersonic boundary layers as three-dimensional oblique first-mode waves [17]. Several other types of linear instabilities, such as the Görtler, cross-flow, and attachment-line instabilities, also exist and can lead to transition under specific circumstances [18]. Linear boundary-layer instabilities can also be bypassed by large initial disturbances to nonlinear levels leading directly to turbulent flow [19].

As the study of boundary layer transition has progressed, it has become apparent that in order to understand and eventually be able to predict the location of transition, we must understand the physical mechanisms that lead to transition [20]. Therefore,

an understanding of transition can best be gained by studying the growth of disturbances upstream of transition, rather than recording the direct effect of parameters on transition location [21].

Many experimental measurements of instabilities have been conducted over a variety of conditions and using a variety of sensors. Laufer and Vrebalovich performed some of the earliest measurements of fluctuations in supersonic boundary layers over flat plates using hot wires. They spent considerable effort to reduce the noise level in the Jet Propulsion Laboratory supersonic wind tunnels and then measured the instability fluctuations in the boundary layer both from naturally-occuring and artificially-generated disturbances [22].

Fujii conducted an experimental investigation on the effects of roughness on transition. He used a 5-degree half-angle sharp cone at Mach 7.1 and tested over a range of conditions. In doing so, Fujii was able to measure second-mode instabilities using high-frequency piezoelectric pressure transducers. This was significant because of the robust and inexpensive nature of these pressure sensors [23]. This new instrumentation setup provided a significant advance in the measurement of instabilities [24].

In hypersonic flow, two of the critical transition mechanisms that must be measured and studied, particularly in light of their importance to boundary layer transition location on blunt hypersonic vehicles, are the first-mode and entropy-layer instabilities.

2.2 First-Mode Instabilities

At hypersonic Mach numbers, the viscous cause for first-mode instabilities decreases and they become relatively low-frequency vorticity disturbances. In many hypersonic designs, these first-mode instabilities tend to be overshadowed by the more unstable, two-dimensional second-mode disturbances that can be an order of magnitude greater than disturbances found in subsonic and supersonic boundary layers [17]. For this reason, a majority of past research has focused on slender vehicles

because of the preconception that slender vehicles are affected more by transition. However, under certain conditions in supersonic and hypersonic flow, blunt vehicles and other geometries are also affected by boundary layer transition and first-mode instabilities may be a critical factor in that transition process [25].

Schneider summarized the current understanding of transition effects on blunt vehicles such as reentry capsules and planetary probes as obtained through computations, ground and flight test experiments, as well as program flight data. Transition was shown to be a significant issue for heating on the blunt face, particularly on the lee side at an angle of attack. Earlier transition requires more heat shielding and thus greater weight requirements. Weight is a critical parameter and a reasonable estimate of transition location is important to reduce vehicle weight. The second main effect of transition that Schneider discussed was the localized heating and aerodynamic moment issues on the afterbody due to the shear layer. Transition affects the flow separation from the rim of the heat shield and the subsequent flow reattachment. The reattachment of the shear level creates high levels of heating that significantly affect the design. A sufficient understanding of transition-inducing instabilities early in the design process will allow better design decisions that reduce or mitigate some of the negative effects of transition [25].

One recent example of a first-mode-dominant design is that of the entry vehicle for the Mars Science Laboratory (Curiosity). Due to the larger size and weight of Curiosity, turbulent surface heating was a much greater concern than for previous entry vehicles. Computations of the vehicle design showed the dominance of first-mode instabilities and correlated them to the transition seen in ground tests, but actual experimental measurements of the first-mode instabilities were not made [26].

Because there is no established method for measuring first-mode instabilities in hypersonic tunnels, there is a significant risk that the current, incomplete understanding of this flow mechanism could result in unexpected transition behavior [1]. This could also include the occurrence of bypass transition due to nonlinear transient growth [27].

Experimental measurements of first-mode instabilities are limited. Demetriades performed experimental measurements on a 5-degree sharp cone at Mach 8. Second-mode instabilities were clearly dominant, but Demetriades refers to a range of amplified lower frequencies in the figures as first-mode instabilities and indicates that these are "apparently observed in the data". There is no further discussion of the first-mode instabilities in the paper [28].

Later, Demetriades conducted experiments on a flat plate at Mach 3. He measured a range of low frequency disturbances that began amplifying at about the same time. These frequencies all amplified until the boundary layer transitioned. Inside that range of amplified frequencies, Demetriades identified a frequency that compared well with linear stability theory, as a first-mode instability. However, he called that measurement "almost incidental" due to the wide range of amplified frequencies. He declared that linear stability theory could not explain the large amplification of disturbances that he measured [29].

Stetson conducted Mach-8 water-cooled stability experiments on a hollow cylinder and a cone. In agreement with previous stability experiments, he showed that planar second-mode disturbances have smaller growth rates than conical second-mode waves. However, data from this and other transition experiments had shown earlier planar transition than conical transition. Stetson's experiments showed that the transition mechanism for the cone was the second mode. The transition mechanism for the planar boundary layer was a band of low-frequency disturbances. These disturbances were not predicted by linear stability theory, which had calculated the boundary layer to be stable for first-mode instabilities [30].

In 1974 Kendall presented data from wind tunnel experiments on a 4-degree half-angle cone. He measured laminar boundary layer fluctuations for several Mach numbers between 1.6 and 8.5 and compared his results to Mack's theoretical results. Kendall's amplification rate results at Mach 4.5 showed the best agreement with Mack's data. They showed a maximum amplification rate at around 4 kHz and indicated that under these conditions, the lower frequencies may be more critical to

transition than the second mode. The experimental measurements of low frequency disturbances in the first mode range were limited in frequency due to the rolloff of the energy spectrum. However, the available experimental data, which is under 6 kHz, matches well with the theory. Kendall also attempted to gain an understanding of the wave obliqueness by cross-correlating the signal from a boundary layer probe with the delayed signal of a probe at the plate leading-edge and found indications of wave obliqueness [21].

Wendt et al. performed hot-wire and pressure-fluctuation boundary-layer measurements in a Mach-5 Ludwieg Tube. Previous conical measurements by Stetson had shown the existence of the second-mode instability as predicted by linear stability theory. However, flat plate measurements by Kendall had not shown the expected second-mode instability, but had instead shown a growth of low-frequency disturbances. Wendt et al. were also not able to find the expected second-mode instabilities on the flat plate, nor did they show up on the cone. This may have been due to probe-traversing inaccuracies. However, on both the flat plate and the sharp cone, they measured broad disturbance bands in lower frequency ranges. These measured amplifications are in good agreement with the theoretical results for first-mode instabilities [31].

Bountin et al. performed experimental wind tunnel measurements on a sharp, adiabatic, half meter long, 7-degree half-angle cone at Mach 5.92. They used hot-wire anemometry to measure instability frequencies up to 612 kHz. They clearly measured the fast-growing second-mode waves, but they also determined that the main energy of the free-stream disturbances was concentrated in the lower frequencies. They then hypothesized that the slow-growing first-mode disturbances play the main role in laminar-turbulent transition [32].

Dougherty and Fisher found evidence of first-mode instabilities in a flight experiment with a 10-degree half-angle sharp cone. They conducted flight-test measurements at an edge Mach number of about 1.35 and measured amplified frequencies in the laminar boundary layer between 10 and 20 kHz. They also present evidence

of these instability waves from two of their wind tunnel experiments using the same model with edge Mach numbers of 1.6 and 2.0. However they go on to say that their measurements were not detailed enough to "define precise mechanisms responsible" for transition [33, 34].

In 1983, Stetson et al. presented their stability experiments on a sharp 7-degree half-angle cone at Mach 8 and also compared their results to Mack. As predicted, at this high Mach number, the dominant instability was the second mode and its first harmonic. However, they also highlight a portion of amplified lower frequency fluctuations that merges with the second-mode instabilities and identify these fluctuations as first-mode instabilities. They also indicate that these instabilities do not show "special selectivity in [the] frequency of the disturbances which are amplified". This is the last paragraph in which the first-mode instabilities are discussed in the paper body [35]. Much of this data is included again in the 1992 report by Stetson and Kimmel and first-mode instabilities are identified in the figures, but not discussed in the paper [17].

Recent measurements by Munoz et al. in the Braunschweig Mach-6 tunnel were originally believed to show first-mode instabilities. They used arrays of surface pressure transducers to measure the second mode and what they believed were first-mode instabilities. They also used infrared images to identify crossflow instabilities on the surface of a 7-degree half-angle cone. The instabilities that they believed to be the first mode are shown in the power spectra between 20 and 50 kHz. They appeared at earlier axial locations than the measured second-mode instabilities. Munoz et al. also measured the instability wave angles by moving the array of sensors circumferentially and these wave angles corresponded to the angles expected for first-mode waves. Although these measurements were very promising, Munoz et al. recommended that future comparisons should be made with stability analysis to confirm the findings [36]. Follow-on computations were performed by Perez et al. These computations indicated that the measured instabilities were probably traveling crossflow waves, not first-mode waves as originally believed [37].

At present, no experimental data is available demonstrating that oblique instabilities can lead directly to transition. Since this may be of importance in supersonic flight in low-disturbance environments or on blunt vehicles, Mayer et al. conducted a direct numerical simulation of Mach 3 flow over a flat plate while introducing disturbances. They concluded that it is numerically possible for oblique waves to lead to a fully-developed turbulent boundary layer [38]. Malik praised Mayer's work and used it as evidence of the increasing role DNS plays in investigating the mechanisms of transition. Malik suggests that as computational power is increased, a DNS analysis of the complete transition regime, starting from a lower magnitude disturbance more typical of freestream, would help provide a better transition prediction. However, modeling the actual freestream environment is a long way off [39].

Another interesting direct numerical simulation and linear stability analysis that predicted first-mode dominance in certain cases with conditions similar to those in the BAM6QT was conducted by Cai-hong and Heng. This simulation was of Mach 6 flow over a 5-degree cone with small bluntness (nose radius of 0.5mm). They used the e^N method with an N factor of 10 to predict transition location and concluded that in the case of an isothermal wall with $\frac{T_w}{T_\infty} = 3.7$, second-mode instabilities lead to transition. It appears that in the isothermal case, heat was transferred from the wall to the flow, which destabilizes the second mode and stabilizes the first mode. However, in the case of an adiabatic wall where no heat is transferred to or from the wall, first-mode instabilities lead to transition, even though they have a much lower maximum amplification rate. The unstable frequency range for first mode is much wider than that of the second mode on an adiabatic wall [40].

In the search for a model design with maximum first-mode instabilities in the BAM6QT, Kirk and Candler performed a numerical study of the effect of geometric changes on the amplification of first-mode instabilities. They calculated computational mean flow solutions for multiple axisymmetric configurations under conditions similar to those in the BAM6QT. They then performed stability analyses and compared the boundary-layer instability amplification rates of each configuration. The

results most applicable to this research are those showing the effect of nose radius, cone half-angle, and body curvature (convex and concave curvature on a cone). They concluded that a smaller nose radius and half cone angles of around 10-20 degrees resulted in higher first-mode N factors downstream. They analyzed the effect of concave and convex curvature on a 10-degree half-angle cone and found that convex curvature has similar results to a larger nose radius, decreasing the maximum first-mode N factors. However, increased concave curvature (flare) maintained a constant boundary layer thickness which allowed the instabilities to amplify quickly. Kirk and Candler then used an optimization package to come up with a composite geometry with high first-mode N factors. The design they came up with was a slender cone with a slight flare that had high first-mode N factors, but even higher second-mode N factors [41].

2.3 Entropy-Layer Instabilities

Another source of instability is the entropy layer. In supersonic flow, the variation of shock strength along its length creates entropy gradients normal to the streamlines. These entropy layers are characterized by large temperature and velocity gradients that affect the downstream flow characteristics close to the body [42, 43]. Entropy layers travel along the flow streamlines and are eventually "swallowed" by the growth of the boundary layer. The entropy layer can increase heat transfer significantly and therefore is particularly important for blunt objects that have large strength variations along the shock [44, 45].

The effect that the entropy layer has upon boundary-layer stability is not very well understood. In 1973, Sullivan and Koziak noted discrepencies between experimental and theoretical density profiles inside a boundary layer and contended that the isentropic assumption typically made outside the boundary layer is invalid in many cases [46]. The idea that entropy-layer effects need to be included to accurately model hypersonic boundary layers has been generally accepted for several decades [47, 48].

Ongoing research has continued to show that the entropy layer may have a significant effect on boundary-layer stability. Numerical and experimental studies have shown the existence of instabilities within the entropy layer [11, 49]. They are an inviscid phenomenon and the most amplified waves are not necessarily oblique [9]. Many studies have concluded that these instabilities within the entropy layer may partially explain the phenomenon of transition reversal [9–11, 50].

Since entropy layers exist because of the variation in the angle of the bow shock, nosetip bluntness is one of the easiest ways to change the entropy layer strength. Several reports have published findings on the effect of nosetip bluntness on transition location. In one of the earliest reports, Rotta compiled data for cones with various degrees of nose bluntness and defined relationships between the bluntness and the transition Reynolds number [48]. Stetson and Rushton did a Mach 5.5 shock tunnel investigation on this subject and found that a small amount of bluntness increased the distance to the transition location. They also found that as the nose bluntness was increased further, there came a point where the transition location started to move forward on the frustum. They hypothesized that this transition reversal is an effect of the interaction between the entropy and boundary layers [51]. These results showing increased stability with a small amount of bluntness and then a transition reversal with a further increase in bluntness were consistent with shock tunnel experiments at hypersonic velocities ranging from Mach 10 to 15 conducted by Softley et al. on a 5-degree half-angle cone [52, 53].

Stetson also conducted a comparison of bluntness effects on transition location in multiple tunnels and at various Mach numbers and compared the results. He determined that transition reversal with increasing nosetip bluntness was not unique to a specific facility. He also determined that transition reversal occurs at different Mach numbers. At higher freestream Mach numbers, a significantly higher rearward displacement occurs [54]. Stetson also showed that when the transition Reynolds numbers were reached just before the entropy layer was swallowed, the transition Reynolds numbers were the largest [49].

In 1946, Lees and Lin concluded that among the necessary conditions for a supersonic instability is a generalized inflection point, or local maximum in the angular momentum [19, 55]. Dietz performed a numerical analysis of a flat plate and compared the numerical results with Schlieren and hot-wire measurements under Mach 2.5 flow. His results showed an entropy-layer instability that was connected with a generalized inflection point in the entropy layer. He also cited preliminary calculations that indicate that there may be interactions that transport disturbance energy from the entropy layer into the boundary layer [9].

Lysenko made measurements of boundary and entropy-layer instabilities above a flat plate while varying the degree of bluntness at the leading edge. He varied the bluntness of the flat plate in a similar manner to Stetson's variation of the cone nosetip bluntness and showed a transition reversal analogous to that shown by Stetson [51]. Using hot wires, Lysenko measured the existence of inviscid, entropy-layer instabilities at Mach 4 and 6. The entropy-layer instabilities measured at Mach 4 were smaller in magnitude than the measured boundary-layer instabilities. However, as the Mach number increased, the magnitude of the entropy-layer instabilities surpassed that of the boundary-layer instabilities. This led to the conclusion that the role of entropy-layer instabilities increases with increasing Mach number. Lysenko also showed that increasing the degree of bluntness destabilizes the perturbations in the entropy layer. In this same study, Lysenko also tried to measure the pressure fluctuations using surface pressure transducers but was unsuccessful due to the low signal levels [11].

Stetson et al. made hot-wire measurements of low-frequency instabilities off the surface of a blunt, 7-degree cone in Mach-8 flow. Stetson et al. followed the instability by measuring the location of peak energy using hot wires. They made measurements of the instability at each axial location from its beginning outside of the boundary layer until it was swallowed up in the boundary layer. They discovered that the entropy-layer disturbances grew slowly outside the boundary layer, diminished slightly as they entered the boundary layer, and then proceeded to grow rapidly inside the boundary layer. They presented the instability growth rates and fluctuation ampli-

tudes with respect to axial location for the frequencies of 30, 48, and 75 kHz. The maximum amplitude of these disturbances was found to coincide with the inflection in the profile of $\frac{\delta M}{\delta y}$ [49].

The discovery of these instabilities by Stetson et al. was unexpected, but later they learned of a recently-completed computational stability analysis by Reshotko and Khan that was consistent with their experimental results. Reshotko and Khan had conducted a numerical analysis of the stability of a laminar boundary layer on a blunt flat plate that took into account the effect of the entropy layer. They combined the inviscid rotational outer flow, that includes the entropy layer, with the viscous inner flow of the boundary layer using the method of matched-asymptotic expansions and showed that both layers can be separately unstable. Their composite mean flow and stability analyses showed that as the entropy-layer streamline swallowing progresses, stabilization occurs due to the swallowing of the more unstable inner streamlines. Once the entropy layer has been completely swallowed by the boundary layer, the outer flow instability becomes irrelevant and flow instability characteristics are nearly the same as for a sharp leading edge. They also showed that the calculated pressure distribution for the entropy layer is similar to that of the first mode calculated for a supersonic boundary layer [56].

Fedorov built upon this numerical work, corrected a boundary condition from the Reshotko and Khan analysis, and used linear theory to analyze self oscillations in the entropy layer. He showed that the boundary layer had a stabilizing influence on the unstable entropy-layer modes, particularly if the wall was cold. He also showed that further downstream as the boundary layer thickens, the instabilities inside the boundary layer become closer in scale to the instabilities inside the entropy layer. He concludes by stating his expectation of rapid growth of instabilities inside the boundary layer once it is penetrated by entropy-layer instabilities [10]. Fedorov cites the experimental measurements of Stetson as evidence for this rapid growth [49].

In 1997, Kufner used linear stability theory to analyze the Stetson blunt cone experiments [49] and was also unable to show the transition reversal numerically [57].

However, in 2007 Hein presented results where he used mean flow data provided by Kufner as the first step to another numerical stability analysis of Stetson's blunt cone experiment. Hein confirmed Stetson's experimental results when he calculated weakly amplified disturbances inside the entropy layer at the same frequency as the disturbances measured by Stetson. Hein found that this disturbance was most amplified at a wave angle of zero. Hein's calculations show entropy-layer modes that are dominated by fluctuations in density and temperature. Also, as was shown by Stetson, the location of the disturbance maxima is correlated with the generalized inflection point in the entropy layer [50, 58].

Lei and Zhong performed a linear stability analysis of transition reversal and compared their results to the experimental results of Stetson and Rushton's Mach 5.5 experiments [51]. They analyzed cones with three different nosetip radii and were unable to replicate the experimentally-found transition reversal as the bluntness increased. Their linear stability results showed that when only the second-mode instabilities are considered, transition continues to move downstream as the nose radius increases, with no reversal evident. They speculate that the transition reversal found in the experiments may be a function of some tunnel noise that has a large enough amplitude to bypass the linear region and force early transition. Also of note is that they found no first-mode instabilities to be present for any of the three cases. They attributed this to the wall cooling effect of the constant room temperature boundary condition that they set. Wall cooling tends to stabilize first-mode waves [59].

Fedorov and Tumin investigated linear and nonlinear dynamics of entropy layer disturbances on a flat plate with a blunt leading edge. They performed a linear stability analysis as well as a direct numerical solution using the space-time conservation element and solution element (CE/SE) method developed by Chang [60]. Although the entropy layer is an inviscid phenomenon, they hypothesized that the entropy layer's interaction with the viscous boundary layer may cause transition reversal by changing the overall stability characteristics and the resultant transition locus. This

numerical investigation was an initial step in determining the role the entropy layer may have on transition reversal [61] [62].

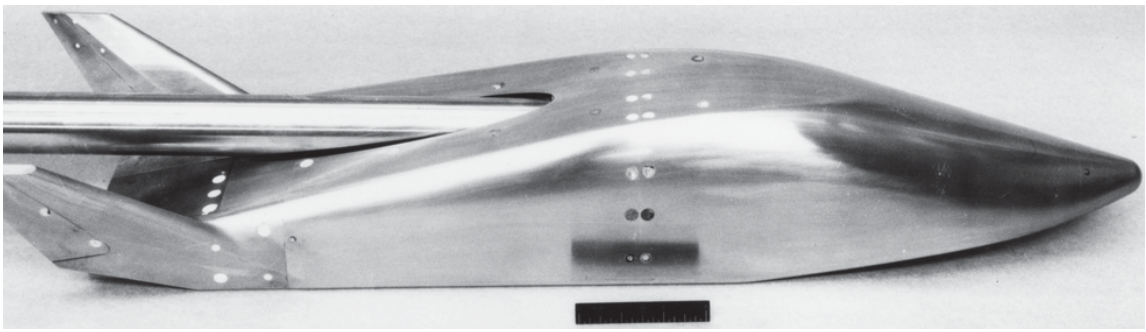

Fig. 2.1. Picture of the Lifting Entry Vehicle model used by Young, Reda, and Roberge.

There is little understanding of how entropy-layer instabilities enter the boundary layer to cause transition. However, under certain conditions, the entropy layer has been shown to have an immediate effect on transition. In 1972, Young et al. conducted Mach-10 transition measurements on the lifting body shown in Figure 2.1. They used a wide array of thermocouples and pressure taps to measure the location of transition on the model. Shadowgraphs taken during these experiments show the entropy layer as a white line that approaches the lower surface of the model. The shadowgraph taken with the model at 20° angle of attack is shown in Figure 2.2. Young et al. found that for angles of attack between $10 - 30°$, transition immediately followed the interaction of the entropy layer with the boundary layer. This interaction was thus presented as a possible mechanism for the transition behavior exhibited by this model [63].

Malik et al. tried to numerically calculate the variable entropy effects for increasing nose bluntness on a 7-degree half-angle cone. They performed a computational analysis of Mach-8 flow using the conditions of the blunt cone experiments of Stetson et al. [49]. Their predicted transition locations, using the e^N method, were in qualitative agreement with Stetson's experiments, with the most amplified frequency being predicted well, but with predicted growth rates being larger than the experimental

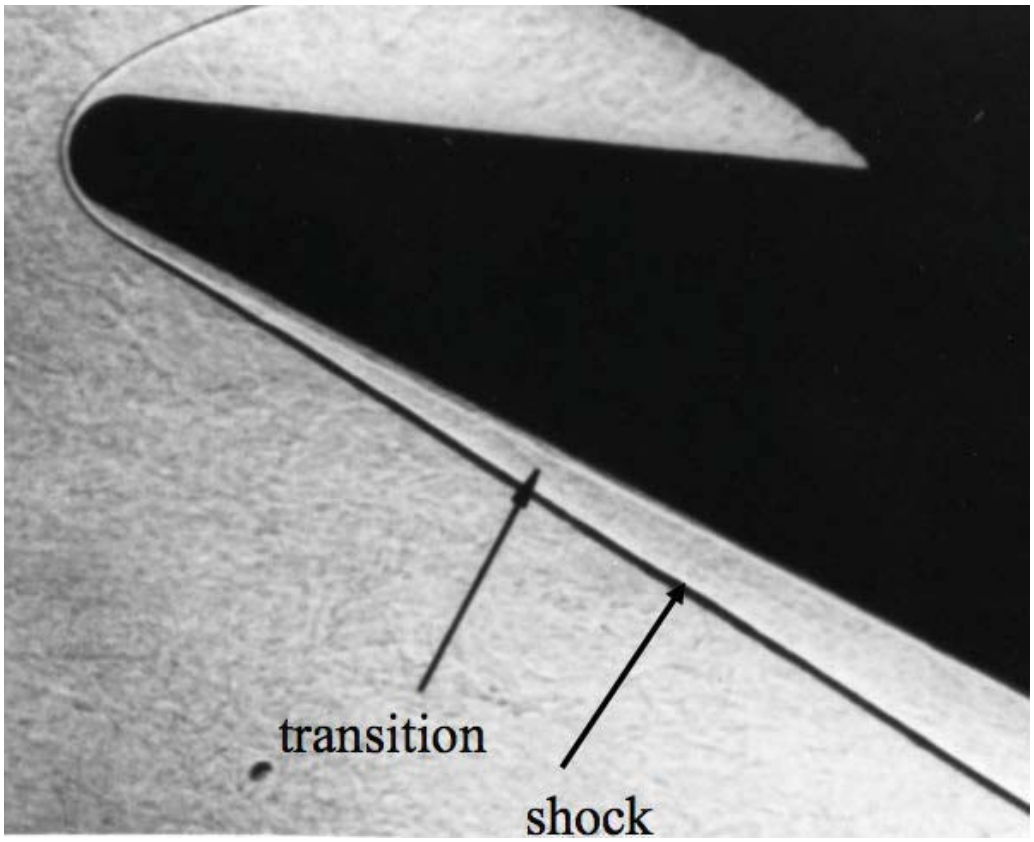

Fig. 2.2. Shadowgraph taken by Young et al. showing the shock (black line) with the vehicle at 20° AoA and the entropy layer (white line) interacting with the boundary layer on the lower surface of the model.

results. Malik et al. showed that the bluntness stabilized the initial high frequency instabilities that exist in flow over a sharp cone, but also increased the strength and bandwidth of the unstable frequencies once instability sets in. They also investigated the entropy-layer instability observed by Stetson and observed a low-frequency instability between the boundary layer and shock that was very sensitive to the farfield boundary conditions [64].

Dietz showed in his numerical calculations that the conditions at the edge of the boundary layer affect the stability characteristics within the boundary layer. In his analysis of a blunt plate, he determined that increasing the bluntness of the flat plate had a stabilizing effect on the boundary layer. He determined that this stabilization was a result of the the reduction in the boundary-layer edge Reynolds number, as well as the increased vorticity induced by the entropy-layer [65].

The effect of the entropy layer on boundary-layer stability is not completely understood. Hein contends that the small amplification rate of entropy-layer instabilities suggests that they cannot be held directly responsible for transition reversal. He discusses receptivity changes, nosetip roughness, and transient growth as among the possible mechanisms that may trigger transition reversal, but concludes that a systematic analysis may be necessary to conclusively identify the mechanism responsible for this phenomenon [50]. However, while the entropy-layer has not been shown as the primary mechanism leading to transition reversal, many suggest that it may play an important part [9–11, 50].

2.4 Effect of Tunnel Noise on Instabilities

The measurement of boundary layer instabilities in hypersonic tunnels has, in many cases, been impeded by the effect of tunnel noise [66]. So, although much has been published, much research remains to be done. More stability experiments, particularly hypersonic quiet tunnel stability experiments, are needed to understand and clarify theoretical and experimental discrepancies [17]. Nearly 40 years ago, aero-

dynamicists such as Reshotko and Beckwith discussed the need for a high Reynolds number quiet tunnel in order to study the development of boundary layers without the noise radiation that comes from turbulent nozzle wall boundary layers [67, 68]. That was the motivation behind the original design of the Boeing-AFOSR Mach-6 Quiet Tunnel (BAM6QT) located at Purdue University, to study hypersonic boundary layer instabilities in a "quiet" environment [69]. So while no single tunnel can duplicate flight conditions, Schneider contended that studying controlled disturbances in a controlled quiet environment can produce data suitable for reliable development of theory [2].

The capability of "quiet" flow in the BAM6QT to provide noise conditions more similar to flight may be of particular importance to this project because of the low frequency waves that are being measured. Chen and Malik conducted experiments in a Mach-3.5 quiet tunnel that compared quiet and noisy flow results in an effort to resolve discrepancies between linear stability theory results and conventional supersonic tunnel transition results. They showed that tunnel noise reduces the transition Reynolds number on cones and flat plates. They hypothesized that this reduction was greater on flat plates than cones because the most amplified modes on flat plates are closer in frequency to the waves emanating from the turbulent boundary layers on the walls [70]. However, Demetriades conducted a portion of his Mach-3 flat-plate instability measurements in a nozzle with a laminar side-wall boundary layer and found that hypothesis "unlikely" [29]. Stetson discusses Demetriades' experiments and states that "experiments in quiet tunnels would be helpful" in determining the identity of these low frequency disturbances [30].

Chen and Malik's experiments were a follow-on to the work by Pate that showed that transition location is dependent upon the freestream disturbances of the specific tunnel. Pate conducted experiments in different tunnels of various sizes and saw a direct correlation between the size of the tunnel and the transition location. This is because the thickness of the turbulent boundary layer impacts the amount of "noise"

emanating from it and the boundary layer thickness is a result of the size of the tunnel [71–74].

Dougherty and Fisher also discussed the effect of tunnel noise on transition location. They performed well-controlled experiments on a sharp, 10-degree half-angle cone over a period of eight years. They made correlative measurements in 23 different wind tunnels and in a free flight test in order to understand the effect of wind tunnel disturbances. While many of these measurements were at subsonic and low supersonic speeds with an emphasis on the transonic regime, measurements were made up to Mach 5.5. In these experiments Dougherty and Fisher showed that in the noisier wind tunnels, the transition Reynold's number was as much as a factor of two lower than in flight [33, 34].

King performed both quiet and noisy Mach 3.5 transition experiments on a sharp, 5-degree half-angle cone. He measured the transition location of this cone at various angles of attack and concluded that the first-mode instability is significantly more receptive to noise radiated from the tunnel walls than the crossflow instability [75].

In 2001, Schneider reviewed the known effects of tunnel noise on transition. He highlighted the need for the experimental database to validate the advancing numerical results and improve the modern theory with an improved understanding of the mechanisms involved in transition. Because tunnel noise can change or bypass the transition mechanisms in low-noise environments, quiet tunnels will play an essential role in providing the controlled conditions needed to obtain detailed instability measurements in an environment more representative of flight [76].

2.5 Predicting Boundary Layer Instabilities and Transition

Linear stability theory (LST) and the parabolized stability equations (PSE) have significantly increased the ability to predict boundary layer instabilities and transition. Correctly-used LST and PSE computations have led to focused experiments

with better measurements. In turn, these experimental results have and will be used to calibrate the computational simulations, resulting in more accurate predictions [1].

Mack was one of the pioneers in compressible linear stability theory. In 2000, he gave a historical review of this theory, detailing how fundamental physical results were found using a computer and the governing equations. He referred to several physical results that were discovered computationally before they were confirmed experimentally. These computational discoveries include the fact that multiple unstable modes exist and that it is the three-dimensional (not two-dimensional) disturbances that are most important for first-mode instabilities [77]. The linear stability theory results from Mack are still being used today to compare to experimental and other computational data.

In 1991, Reshotko reviewed the efficacy of the e^N transition prediction and argued that linear methods such as the e^N method have been the most successful. The strength of the e^N method is the ability to evaluate trade-offs for multiple designs and compare their transition behavior without knowing the exact environmental disturbances present. Reshotko concludes by stressing that an understanding of the physics involved is essential in order to be able to predict transition computationally [4].

Parabolized stability equation codes include high temperature effects found in high speed boundary layers. They provide a low cost capability to perform boundary layer stability computations that can greatly increase experimental effectiveness. DNS codes are available to complement the PSE codes, but they have a much higher computational cost and are really only feasible for small problems [78].

Malik performed mean flow and PSE calculations on a sharp, 5-degree half-angle cone at Mach 6 and compared those results to results from other computational packages. He also performed calculations for the Reentry F and Sherman-Nakamura cones and compared them with the flight test data. He showed that the transition location in each case occurred at an N factor of about 10 (range of 9.5 - 11.2) using the e^N method. This result compares well with earlier supersonic flight experiments

and quiet tunnels. This study provided credence to extending the e^N method to hypersonic, chemically reacting flows [79].

Johnson and Candler also did stability and transition computations for Reentry F using the computational package STABL (Stability and Transition Analysis for Hypersonic Boundary Layers) and its associated PSE (Parabolized Stability Equations) stability solver and compared their results to those of Malik. Their results compared well. For example, Johnson calculated an N factor of 8.7 at the experimentally-measured transition location where Malik calculated an N factor of 9.5 [80].

Alba et al. used STABL and PSE to calculate first and second-mode two-dimensional and oblique disturbances in the boundary layers of a flat plate and of cylinders in a supersonic flow. In the latter case, the boundary-layer was calculated on the outer surface of the cylinder with the flow parallel to the center axis. They compared their results with identical cases published earlier by Malik and Mack. Their results showed very good agreement to all the published cases and they took this as validation that STABL could accurately compute the characteristics of first-mode oblique waves. Alba et al. then extended their analysis to a blunt wedge in Mach-4.7 flow at various angles of attack. The growth rate of first-mode oblique waves is relatively small compared to the two-dimensional second-mode waves. However, at all positive angles of attack, they were the most amplified waves for the first 2.5 meters on the wedge. The first-mode oblique waves were at an average angle of about 60° [81].

Computational work has advanced quickly, and in some ways it is ahead of the experimental database to which it can be compared [1]. With the continued advance in computing power, DNS has now become feasible for small, well-defined problems. While DNS has a role to play, and that role will increase as computing power continues to increase, there is still a great need for theoretical models to set up experiments and DNS simulations. These will assist in interpreting experimental and numerical results and aid in transition control decisions. As such, theoretical models play an important role in the overall transition research process [15].

3. COMPUTATIONAL METHODS

3.1 Geometry Design and Constraints

The BAM6QT was designed to provide conditions for dominant second-mode instabilities on a cone at zero angle of attack. A Mach number of 6 was specifically selected as high enough to preclude the dominance of first-mode instabilities [82]. Therefore, in an effort to get measurable first-mode instabilities, significant effort went into the design of the model geometry. The idea was to use computations to find the simplest axisymmetric geometry that maximized the first-mode instability waves under BAM6QT conditions. In order to obtain measurable first-mode instabilities, care was taken to ensure that other predicted instabilities were significantly smaller in amplitude than the predicted first-mode instability. An axisymmetric design was necessary to simplify both the computational analysis and the machining of the physical model.

The original idea was to run a sharp axisymmetric cone at a high enough vertex angle to reduce the edge Mach number to a point where first-mode waves would dominate. However, as the vertex angle is increased, the length of the model must be decreased to keep the base diameter small enough for the model to start. In the BAM6QT, this maximum base diameter is approximately 4 inches. Preliminary calculations by Meelan Choudhari [83] indicated that under these constraints the large vertex angle required for a simple cone geometry would result in an axial length too short to obtain large N factors.

The next design consideration was to use a more complex shape. It would begin with a sharp cone nosetip to lower the edge Mach number sufficiently for first-mode instabilities to dominate. At a certain diameter, this cone would merge into an ogive,

then into a cylinder of a constant diameter that would allow adequate length for the first-mode instabilities to grow large enough to induce transition on the model.

If this design proved to be insufficient to induce transition within a reasonable length, a slight flare could be added to the cylinder that would maintain the boundary layer at a fairly constant thickness. This would allow the same frequency instability waves to amplify over a longer distance and increase the possibility of transition within a reasonable distance downstream. This same concept has been used successfully to induce very large second-mode waves in the BAM6QT [84] on a sharp, flared cone.

3.2 Computational Design Process

The design process included several steps of increasing complexity and fidelity. An external-flow Method of Characteristics (MOC) code [85] was used initially to determine a feasible geometry with an edge Mach number ≤ 5 where first-mode instabilities tend to dominate. Once a general design space was determined, further analysis was conducted using the Stability and Transition Analysis for Hypersonic Boundary Layers (STABL) software suite. STABL is a two-dimensional/axisymmetric hypersonic flow and stability analysis code developed at the University of Minnesota. It was remotely installed by Heath Johnson on an eight processor computer at Purdue. STABL can solve the full laminar Navier-Stokes mean flow using implicit Data-Parallel Line Relaxation (DPLR). Its associated stability solver, PSE-Chem, can solve the parabolized stability equations [80].

STABL and PSE-Chem were used to calculate the mean flow and boundary-layer stability characteristics of a series of geometric configurations in an effort to find the design that would provide the best opportunity to measure first-mode instability waves in the BAM6QT. The process of design brought to light many characteristics of first and second-mode instability wave growth and resulted in a cone-ogive-cylinder design that has been used for experimental measurements in the BAM6QT [86].

Purdue does not currently have the computational capability to perform stability calculations outside of the boundary layer. So when measurements using the cone-ogive-cylinder showed what appeared to be an entropy-layer instability, these results were shared with other institutions that are set up to do entropy-layer instability calculations. Stability calculation comparisons will provide significant insight into the flow characteristics of entropy-layer instabilities.

While computations were being performed at Purdue in an effort to come up with a design that would be dominated by first-mode instabilities, other computations were being made at NASA-Johnson Space Center by Lindsay Kirk. She used an optimization tool based upon the STABL software suite to optimize first-mode waves on a model under the BAM6QT conditions. During this numerical design process several characteristics of first-mode instabilities came to light [41]. The optimization produced a flared-cone model that was built by the Purdue machine shop. Measurements were also made in the BAM6QT using this model.

3.2.1 Method of Characteristics Calculations

A Fortran-based MOC code developed by Zucrow and Hoffman and printed in volume 2 of their Gas Dynamics book [85] was used in the initial design stages. This external flow code is based on a cone-ogive-cylinder design where the user inputs the leading-edge cone half-angle (θ), the model length (x_e), and the cylinder radius (y_e). The slopes are matched at the intersection of the ogive with the cone and the cylinder and the ogive dimensions are calculated using Equation 3.1. The coefficents are calculated using Equations 3.2, 3.3, and 3.4.

$$\mathbf{y} = a + b * \mathbf{x} + c * \mathbf{x^2} \tag{3.1}$$

$$a = \zeta * y_e \tag{3.2}$$

$$b = tan(\theta) - 2 * c * x_a \tag{3.3}$$

$$c = -\frac{tan(\theta^2)}{4 * y_e * (1 - \zeta)} \tag{3.4}$$

The Method of Characteristics code was used to make quick calculations of the Mach number along the edge of the cone-ogive-cylinder boundary layer. The edge Mach number for each configuration is mostly dependent upon the half-angle of the cone. Calculated edge Mach numbers ranged from nearly 5.5 with a cone half-angle of 20 degrees, to Mach 3.9 with a 45-degree half-angle cone.

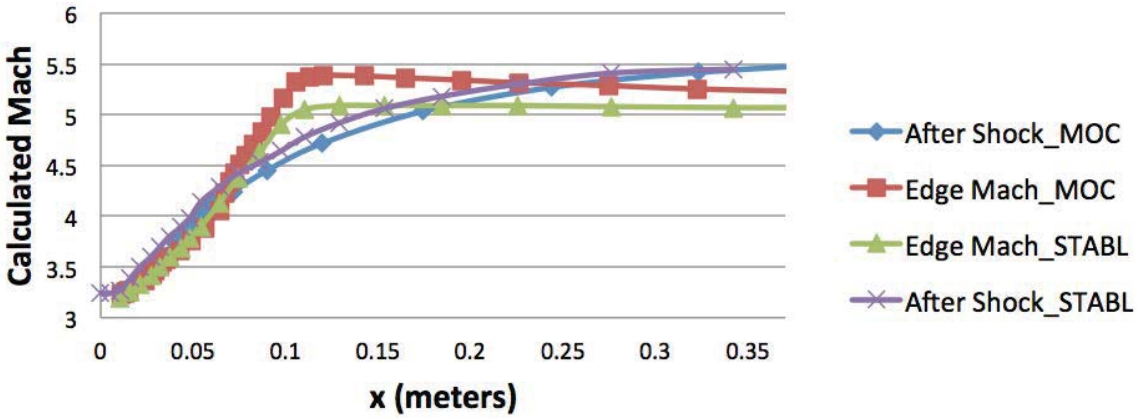

Fig. 3.1. Comparison of STABL and MOC edge-Mach calculations for flow over a 25-degree cone-ogive-cylinder.

Several validation runs were made, comparing the Method of Characteristics code output to that of STABL. They compared quite well, confirming that the MOC results were sufficiently accurate for the first stage of the design process. One example of these comparisons is shown in Figure 3.1 that compares the edge Mach number as well as the Mach number calculated after the shock for each code. Figure 3.2 compares the predicted surface and shock pressure ratios for one of the compared designs. The pressure measurement profiles also compare favorably with Mach 4.04 experimental and computational results for an ogive-cylinder body, conducted by Lord and Ulmann [87].

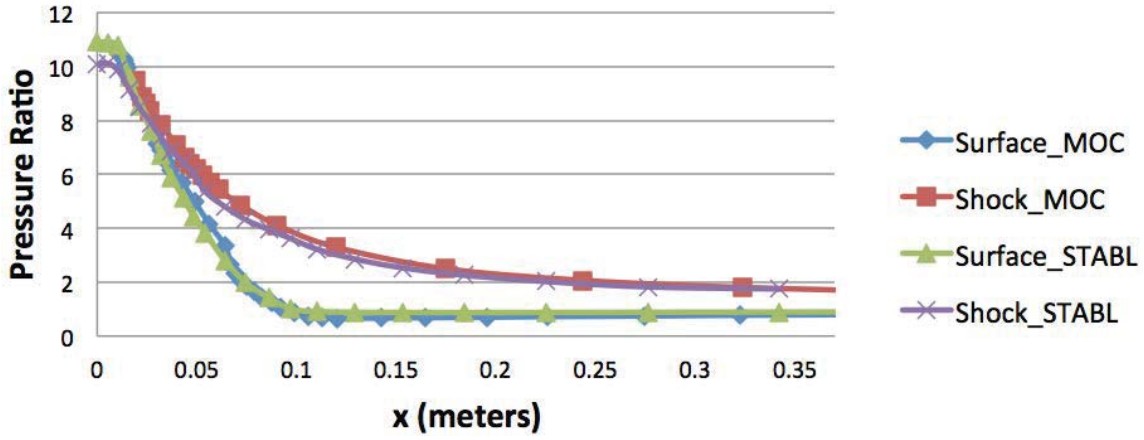

Fig. 3.2. Comparison of STABL and MOC surface pressure ratios.

The MOC code provided a design that was easily modified for different nosetip angles. This is the basic design for each of the cone-ogive-cylinders used. It also provided a tool to rapidly calculate the edge Mach for several nosetip angles. These results provided a starting point from which more involved calculations were made.

3.2.2 STABL Mean Flow and Stability Calculations

The next step used mean flow and stability calculations to further refine the design. The flow around multiple cone-ogive-cylinder geometries created using Equations 3.1 through 3.4 was computed. Each grid was created by importing a data file with discretized profile coordinates into STABL and using the grid generation module. Approximately 450 grid points were used along the model surface with 425 grid points extending into the flow. The grid format used in the STABL grid generation tool was "Lower Shape Power-Law Upper". Successful grid creation was very sensitive to the grid shape parameters and stretching factors, so these are included in Table 3.1. These parameters were successfully used to create the grid for each cone-ogive-cylinder configuration.

In order to get better resolution downstream, close to the model, grid tailoring was performed after an initial mean-flow solution was obtained. The shock location

Table 3.1
STABL settings for the outer surface and interior parameters used for creating cone-ogive-cylinder grids.

npj	nbc	nslf	nsrt	y0	oga	ogn	ora	orb	oxf
425	0	0.1	0.05	0.0	30-35	1	0.12	0.12	0.0

was used to perform the tailoring with exponential grid spacing off the body surface up through the shock and an additional 15 grid points outside of the shock. After grid tailoring, a new solution was computed for mean-flow analysis and stability computations. The y^+ parameter is often used to determine if the grid near the wall is sufficiently dense to resolve the boundary layer. It is a non-dimensional distance from the wall and values of less than unity are recommended to obtain a well-resolved solution. After tailoring, the grids had maximum y^+ values of about 0.3.

During the initial mean-flow and stability calculations, two design parameters were used to describe the geometry while all the other parameters were held constant. The independent parameters chosen were the leading-edge cone half-angle and the diameter of the cylinder. An example of one of these geometries with a 25-degree nosetip is shown in Figure 3.3.

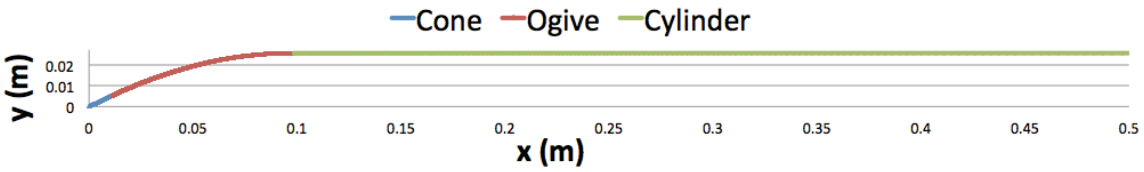

Fig. 3.3. Cone-ogive-cylinder geometry with 25-degree leading-edge half-angle and 5cm diameter.

Upon selecting an optimal design with these two parameters, their optimized values were set constant and a flare was added to the model downstream of the ogive. This was done in an attempt to maintain a more constant boundary-layer thickness and get greater instability growth. An analysis of the results of these calculations

was used to settle upon an design that was considered the most likely to produce measurable first-mode instabilities when used in the BAM6QT.

During the design phase, each case was run under conditions that simulate the BAM6QT at a stagnation pressure of 160 psia. Calculations assumed Mach-6 flow with a total temperature of 433 K, a static temperature of 53 K, and a wall temperature of 300 K. Stability calculations were made using these mean-flow results. In later calculations the flow conditions were varied in order to predict the effect of Reynolds number on the boundary-layer stability characteristics and to compare with experimental data. Table 3.2 lists several sets of tunnel conditions that were used for a majority of the computations. The temperature inputs are the same as for the 160-psia conditions. The STABL input file for a 35-degree cone-ogive-cylinder under 120-psia conditions is included in Appendix D.

Table 3.2
BAM6QT test-section flow conditions used for mean-flow computations.

Total Pressure (psia)	Static Pressure (Pa, [psia])	Density ($\frac{kg}{m^3}$, [$\frac{slug}{ft^3}$])
80	350, [.051]	$2.301 * 10^{-2}$, $[4.476 * 10^{-5}]$
120	520, [.076]	$3.446 * 10^{-2}$, $[6.714 * 10^{-5}]$
160	690, [.101]	$4.533 * 10^{-2}$, $[8.833 * 10^{-5}]$

After STABL has computed the mean flow for a geometry, PSE-Chem can estimate the frequency of the first and second-mode instabilities. This estimate is used to create a test matrix that shows the location and frequency of the stability calculations that will be performed. An example of first and second-mode stability estimates and a stability calculation matrix is shown in Figure 3.4. This matrix was created using the build-in test matrix wizard in STABL.

The stability calculations were done in several steps. The first step was to calculate the two-dimensional N factors for each frequency and location given in a test matrix

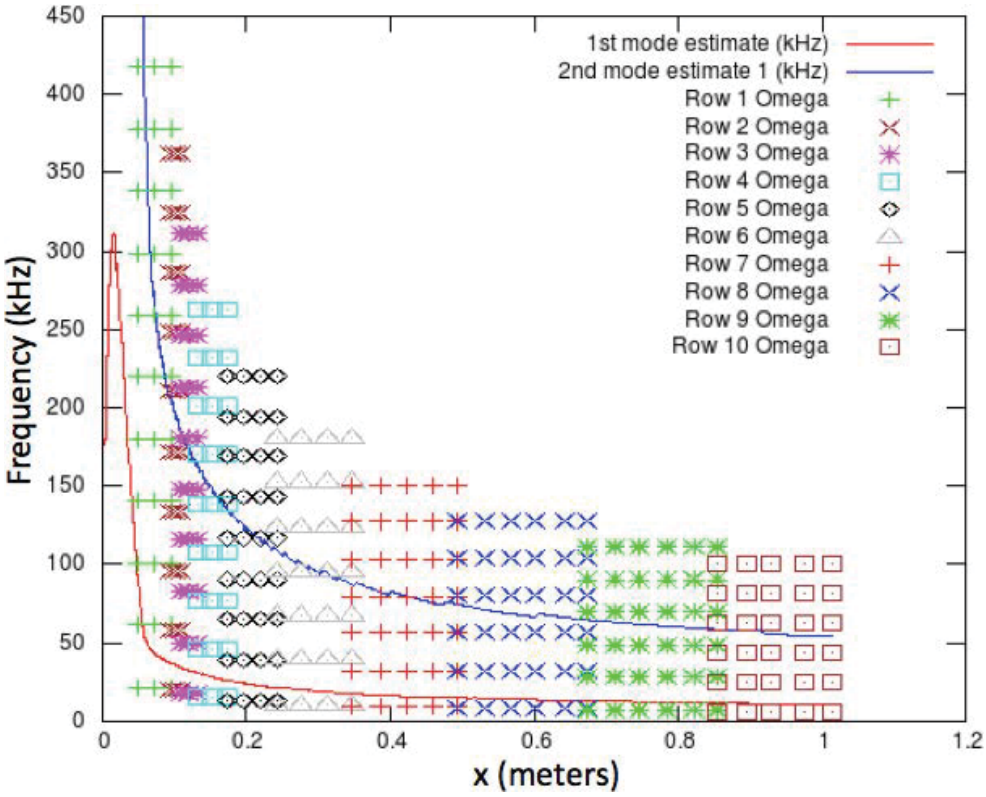

Fig. 3.4. Example PSE-Chem stability matrix showing the frequency and location of stability calculations. Also shown are the estimated frequencies for the first and second-mode instabilities.

like that shown in Figure 3.4. Then the calculations were repeated with a test matrix built using just the first-mode estimate. The first-mode stability calculations were also made over a range of wave angles in order to calculated oblique instabilities.

Mean-flow computations were also conducted for each of the cone-ogive-cylinder configurations in order to compare the flow properties with the experimental entropy-layer instability measurements. Flow profile analyses, inside and outside of the boundary layer, were conducted. Since a majority of the experimental hot-wire measurements were made starting at a total pressure of just over 120 psi ($Re/m = 7.5 * 10^6$), computations were also made under these flow conditions.

4. EXPERIMENTAL METHODS AND SETUP

4.1 Boeing/AFOSR Mach-6 Quiet Tunnel

A majority of the experimental work was conducted in the Boeing/AFOSR Mach-6 Quiet Tunnel (BAM6QT) shown in Figure 4.1. It is a Ludweig tube design with a long, pressurized tube leading to a converging-diverging nozzle through which the flow is accelerated. The last 0.77 meters of the nozzle have a slowly-varying diameter and serve as the BAM6QT test section. Flow goes through the test section and diffuser and past the open ball valve into the large vacuum tank.

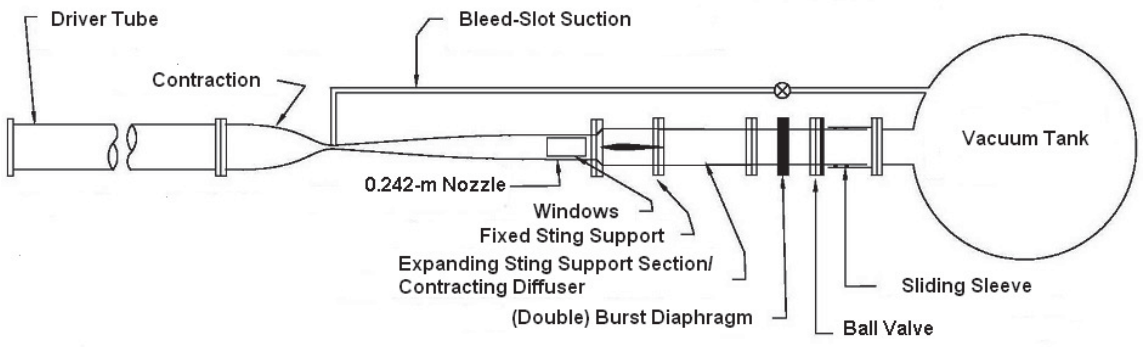

Fig. 4.1. Schematic of Boeing/AFOSR Mach-6 Quiet Tunnel.

Before each run, the vacuum and pressurized sections are typically separated by two diaphragms maintaining an average of the upstream and downstream pressures between them. Alternatively, the 12-inch diameter ball valve can also be used to separate the high-pressure air from the vacuum tank, but tunnel start time is increased due to the time required for the ball valve to fully open. To start the flow with the diaphragms, the air between them is evacuated, putting all the pressure on one diaphragm and causing them to burst in quick succession. Flow initiation starts an

expansion wave traveling upstream which continues reflecting back and forth between the upstream end of the driver tube and the contraction. The reflection cycle repeats approximately 5 times a second for the duration of the run, each time changing the flow conditions slightly by lowering the total pressure and temperature.

Hypersonic tunnels are considered quiet if they are able to maintain a laminar boundary layer on the tunnel walls through the test section [4]. This eliminates the acoustic radiation that would come from a turbulent boundary layer. Maintaining this laminar boundary layer on the tunnel walls is key to creating a successful low-disturbance environment [88] and requires significant modifications from a conventional hypersonic tunnel. In the BAM6QT, these modifications include a sub-micron particle filter, bleed slots in the throat to remove the contraction boundary layer, a highly-polished nozzle, and a large settling chamber [89]. For comparison, the BAM6QT is also able to run noisy at nearly the same operating condition as its quiet runs by closing the valve between the throat bleed slots and the vacuum tank [90].

The BAM6QT is one of three operating quiet hypersonic tunnels in the world. A quiet hypersonic tunnel was recently put into operation at Peking University in China [91]. The other operational hypersonic quiet tunnel was built at NASA Langley but then removed and reinstalled at Texas A & M where it is currently operational. The BAM6QT was developed to provide high Reynolds number quiet flow of approximately twice that of the Langley Mach-6 nozzle [69] for studying transition [89]. With typical quiet flow run times of 3-5 seconds, the BAM6QT continues to achieve quiet-flow unit Reynolds numbers near 11.5×10^6 per meter (3.5×10^6 per foot) [90] with low noise levels of less than 0.05%, which is similar to flight conditions and an order of magnitude lower than conventional tunnels [92, 93].

4.2 Experimental Model Designs

The models were constructed on the CNC lathe in the Purdue AAE department machine shop. They were built with a hollow centerline and holes were drilled at

each desired sensor location. In this manner the surface sensors could be installed flush with the surface and the wires fed through the center and out the back of the model. Larger holes were also drilled at various locations, typically on the opposite side from the sensor holes, to provide access to the model centerline and allow for sensor mounting. All of the models and most of the nosetips were made using 6061-T6 aluminum, with a few of the nosetips made out of stainless steel.

4.2.1 Cone-Ogive-Cylinder Design

Fig. 4.2. Picture of the original cone-ogive-cylinder tested in the BAM6QT.

The majority of the measurements were made using cone-ogive-cylinder models with a 5-centimeter diameter. The first model built is 1-meter long with a 30-degree half-angle nosetip. Pressure transducer ports were machined at 5 axial locations of 0.58, 0.61, 0.71, 0.81, and 0.91 meters. One additional port was machined on each side of the 0.61-meter location. Each was displaced azimuthally from the original port at 0.61 meters by 6 degrees, resulting in a distance between port centers of 2.5 millimeters. This model is shown in Figure 4.2 with the 30-degree nosetip installed.

4.2.2 Early Modifications to the Cone-Ogive-Cylinder

Initial experiments with the cone-ogive-cylinder showed indications of an entropy-layer instability. Entropy-layer instabilities in an axisymetric flow field are due to the radial variation of shock strength. Two additional nosetips, with 28 and 33 degree cone half-angles, were built to see it they would alter the shock shape sufficiently

Fig. 4.3. Photo of 28, 30, and 33-degree nosetips for the cone-ogive-cylinder

to change the measured instability. A change in instability with different nosetips would be an indication that the measured instability is in the entropy-layer. These nosetips are shown in Figure 4.3. Kulite pressure transducers were used on the model surface and in pitot mode with each of the nosetips installed. The results showed little change in the measured instability, and the attempt to see distinguishable differences in the entropy-layer instability by altering the shock shape with the 28 and 33-degree nosetips was considered unsuccessful.

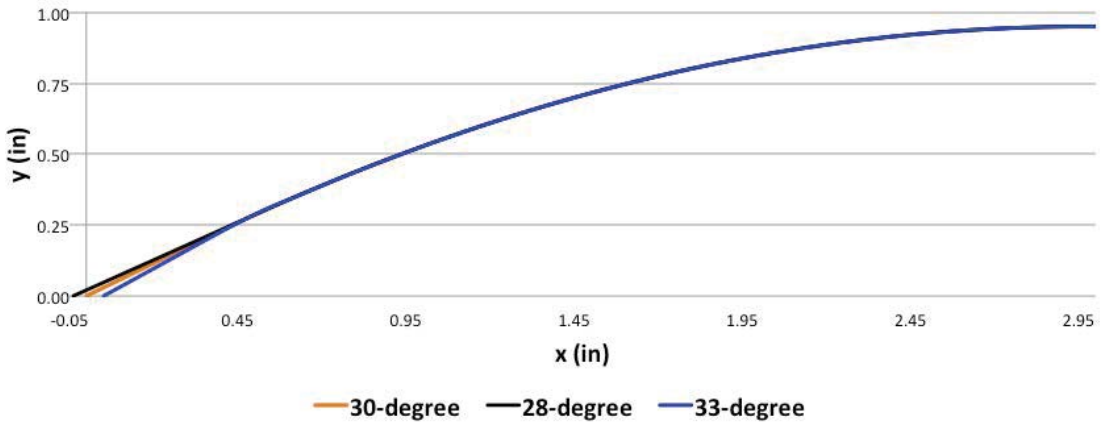

Fig. 4.4. Profiles of the 28, 30, and 33-degree nosetips for the original cone-ogive-cylinder

Hot-wire measurements were never made above the 28 or 33-degree configurations. It is possible that more precise measurements with hot wires would show differences in the instability frequency and location. However, as shown by the profiles in Figure 4.4, the nosetip angle is only a small part of the overall cone-ogive shape. It is likely that any measured instability differences between these three configurations would be quite small.

4.2.3 Cone-Ogive-Cylinder Model with Interchangeable Cone-Ogive Portions

The shock shape in front of the cone-ogive-cylinder is affected by the entire cone-ogive forebody shape. In order to change this shape more significantly, a new model was designed that allowed the entire cone-ogive portion to be changed. The new model consists of a 0.86 meter-long (34 in) cylinder with the same 5-cm diameter as the original model but with detachable cone-ogive nosetips.

Fig. 4.5. Photo of cone-ogive-cylinder with interchangeable cone-ogive sections

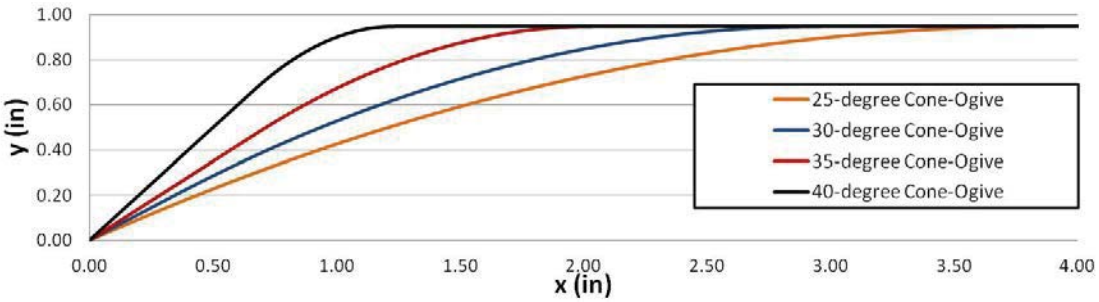

Fig. 4.6. Profiles of four cone-ogive-cylinder leading-edge configurations.

For initial experiments with this model, four different cone-ogive forebody configurations were built. The leading-edge half-angles of these cone-ogive portions vary from 25 to 40 degrees in 5-degree increments. A picture of the second cone-ogive-cylinder model with its interchangeable cone-ogive sections is shown in Figure 4.5 and the profiles of these four nosetips are shown in Figure 4.6. When the new model has the 30-degree nosetip installed, it has the same dimensions as the original 30-degree cone-ogive-cylinder.

Measurements with the 30 and 35-degree cone-ogive forebodies provided the best data for what appears to be an entropy-layer instability. Hot-wire measurements using the 25-degree model showed no evidence of an instability. The 40-degree model were suspect because it was difficult to start in the BAM6QT. This difficulty in starting the 40-degree model is possibly due to its increased bluntness in comparison with the other models. Peter Gilbert discusses the difficulties in starting blunt models in his thesis [94].

Fig. 4.7. Picture of all eight interchangeable cone-ogive portions of the cone-ogive-cylinder model.

In order to better understand the effect of shock curvature on the measured instability, four additional cone-ogive portions were built with 31, 32, 33, and 34-degree leading-edge half angles. A picture of all eight interchangeable nosetips is shown in Figure 4.7 and their profiles are shown in Figure 4.8.

Figure 4.9 shows the locations of the pressure transducer ports. Kulite pressure transducers were installed in these ports to measure surface pressure fluctuations. The ports were machined in the cone-ogive-cylinder at 9 axial locations ranging from

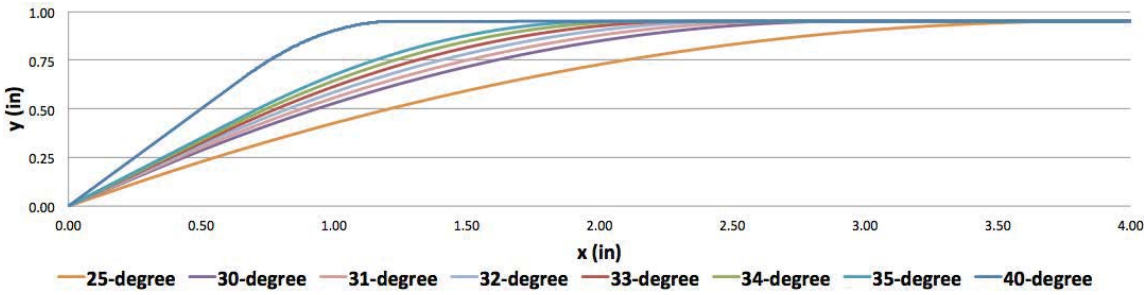

Fig. 4.8. Profiles of all eight cone-ogive-cylinder leading-edge configurations.

0.52 to 0.86 meters. (The original model had surface pressure transducers installed from 0.58 to 0.91 meters).

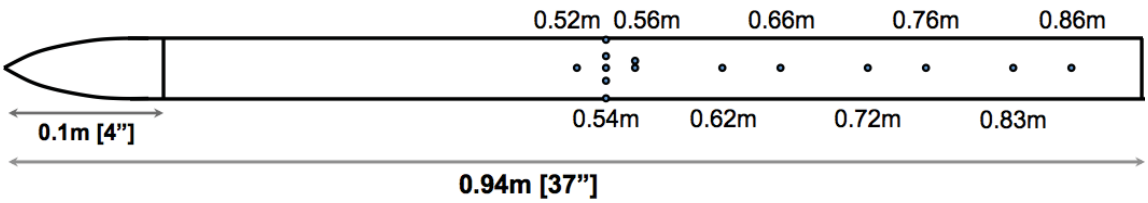

Fig. 4.9. Sketch of the new cone-ogive-cylinder model with surface sensor locations labeled.

One additional port was machined at the 0.56-meter location, azimuthally-separated from the other port by 6 degrees. The five surface sensor ports at 0.54 meters were added for later measurements. One of these ports was inserted along the same line as the other ports and the other four were drilled at -90, -15, 25 and 90 degrees from the center hole. Figure 4.10 shows a picture of the three ports closest to the centerline with sensors installed. Also shown in this picture is a sensor installed at x = 0.52 meters and the two sensor ports at x = 0.56 meters.

4.2.4 Flared-Cone Design

Measurements were also made using a flared cone. The flared-cone design was optimized by Lindsay Kirk for maximum first-mode instability N-factors under BAM6QT

Fig. 4.10. Picture of Kulite pressure transducers at x=52 and 54 cm as well as two open sensor ports at x=56 cm.

conditions [41]. The result was a very slender cone with a slight flare down the length, reaching a diameter of 0.08 meters at 1 meter downstream. A curve fit was made to match the optimized design coordinates in order create the computational and experimental flared-cone models. The curve fit is shown in Equation 4.1 and the design profile is plotted up to 0.75 meters in Fig 4.11.

$$y = 0.375x + 0.000115x^2 - 0.000001x^3 \tag{4.1}$$

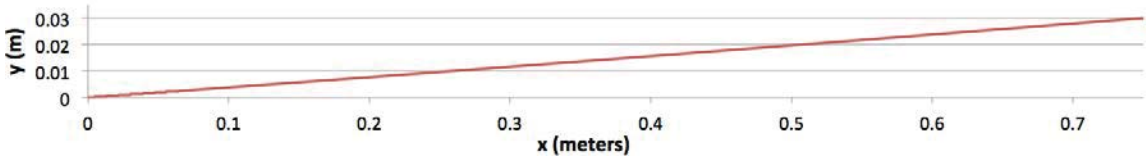

Fig. 4.11. Profile of flared cone designed to optimize first-mode instabilities.

The mean flow was calculated for the flared-cone design under tunnel conditions for the BAM6QT as shown in Table 3.2. Then, using these mean-flow results, a

stability analysis was performed for each of these computations. These computations were used to determine the predicted first and second-mode N factors.

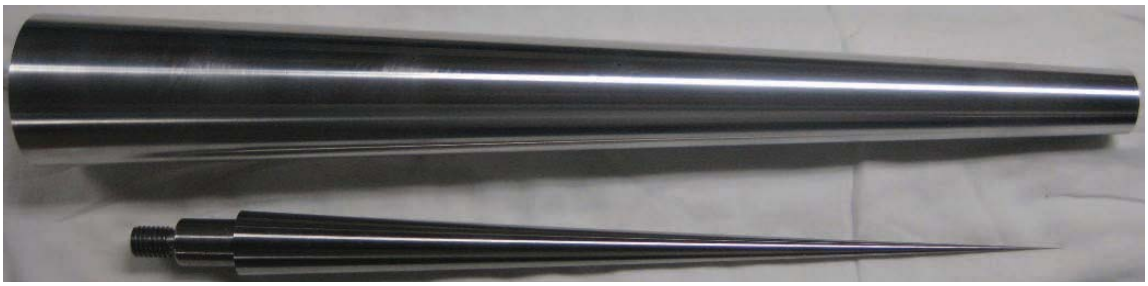

Fig. 4.12. Picture of the flared cone tested in the BAM6QT.

A picture of the flared cone with the nosetip detached from the rest of the body is shown in Figure 4.12. The model is 0.76 meters long. It has a base diameter of 6 centimeters and comes to a nearly-sharp point at the leading edge. The tip broke off during machining and has a diameter of about 0.1 millimeters. Kulite pressure transducer ports were machined along a single ray of this model at axial locations of 0.5, 0.53, 0.55, 0.58, 0.6, 0.63, 0.66, and 0.68 meters. A schematic of the flared cone and the port locations is shown in Figure 4.13.

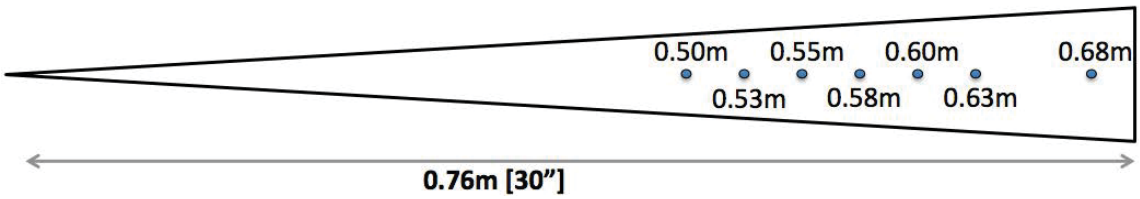

Fig. 4.13. Sketch of the flared cone with surface sensor locations labeled.

4.2.5 Angle of Attack Measurements

The model installation for each measurement was at an angle of attack of nominally zero. Each time, the model was fastened to the zero-degree adaptor which was in turn fastened tightly to the sting. The sting was inserted into the fixed sting

mount inside the BAM6QT and tightened into place using six small set screws. For a majority of the runs, no angle of attack measurements were made on the installed model. They were always assumed to be at a zero-degree angle of attack.

Post-data measurements using a Mitutoyo Pro 3600 digital inclinometer identified a small angle of attack on the installed cone-ogive-cylinder model. The inclinometer has an accuracy of $\pm 0.05^\circ$ for measurements up to ten degrees. The sting has a small amount of movement when inserted into the sting mount and the angle of attack can be changed slightly by adjusting the set screws. To determine the extent that the attack angle can vary, measurements were made with the model mounted with the maximum positive and negative angles of attack. The measurements indicated that the model can have a positive angle of attack of up to 0.1 degrees. The model could not be adjusted to a negative angle of attack. No yaw measurements were made on the model. The slight positive angle of attack may account for some of the differences between experiments and computations.

4.3 Temperature Sensitive Paint

Temperature sensitive paint (TSP) has been used successfully in the BAM6QT to measure global temperature distributions on the surface of models and identify important flow features such as transition, vortices, and shocks [95–98].

TSP is made up of a polymer coating that is infused with a chemical that luminesces when subjected to light. This compound is sprayed on the model surface over the top of an insulating layer. During the run, a blue LED light source excites the luminescent molecules and a high-speed camera is used to capture the light emitted from the painted model. The intensity of emitted light changes as the temperature changes.

In order to postprocess the recorded images, it was necessary to take a dark photo with all of the lights in the room off. Another photo was taken with the LED light on after the tunnel was pressurized just prior to each run. These images were used

to account for any background light and to calculate the temperature change of the model during the run. The images were aligned and postprocessing was completed using Matlab code originally provided by Dr. John Sullivan and modified by Chris Ward. The Matlab code is shown in Appendix E. Additional details regarding the use of TSP in the BAM6QT can be found in the MS theses of Ward and Dussling (References [98] and [99]).

After postprocessing of the recorded images, the surface temperature gradients are visible, showing clearly which portions of the model are at higher temperatures due to some physical phenomenon (shocks, transition, etc.). In this research, TSP was used as a method of flow visualization in an attempt to identify reflected shocks on the model. It was also used to measure the vertical displacement of the model that occurs during tunnel startup. Figure 4.14 shows a picture of the aft end of the 30-degree cone-ogive-cylinder with the rear two-thirds of the model painted with TSP. It is also possible to measure heat transfer on the model to compare with the TSP images, however these measurements did not include heat transfer.

Fig. 4.14. Picture of the aft end of the cone-ogive-cylinder after being painted with TSP.

4.4 Instrumentation

4.4.1 Surface Pressure Sensors

Kulite XCQ-062-15A pressure transducers were installed flush with the model surface. Each of these pressure sensors has a silicon diaphragm with a four-arm

Wheatstone bridge that is used to measure pressure fluctuations at a high frequency. The resonant frequency varies slightly between sensors, but is between 250 and 300 kHz. Because the test section of the BAM6QT is pressurized during the tunnel filling process, the transducers are stopped above 103 kPa (15 psi) to prevent breakage at high pressures.

Fig. 4.15. Picture of a Kulite XCQ-062-15A pressure transducer.

The Kulite pressure transducers have a 1.6 millimeter diameter with a screen to protect the sensor. The transducers that were installed flush with the model were fitted with an A-screen which has a large central hole of 0.81 mm^2. The A-screen offers limited protection, but provides flatter frequency response than more protective screens. Installing the sensors flush with the surface also provides a better frequency response than would be found with recessed sensors [100]. Figure 4.15 is a close-up picture of one of the uninstalled Kulite pressure transducers.

The transducers were installed by inserting the sensors through the back of the model and through the ports. With the sensors pushed fully through the ports, the outsides of the sensors were coated with fingernail polish. The excess fingernail polish was carefully removed as the sensors were pushed down into the model. The sensors were made flush by tapping them down until a finger could slide smoothly over the surface. A picture of several transducers installed flush with the model is shown in Figure 4.10.

4.4.2 Pitot Probe Pressure Sensors

Kulite XCQ-062-15A transducers were also used in a pitot configuration to measure instabilities away from the model surface. Because of the increased exposure to the flow, the pressure sensors used in the pitot configuration have a more protective B-screen. The B-screen is a solid screen with eight small holes around the outside edges. The transducers were installed in a pitot probe as shown in Figure 4.16. A similar pitot configuration has been used previously in the BAM6QT for doing boundary-layer instability measurements close to the nozzle wall [101].

Fig. 4.16. Pitot probe with installed B-screen Kulite pressure transducer.

This probe was attached to a traversing apparatus that is inserted through a slot in the tunnel wall in the vertical center plane. The traversing system can be moved axially by a manual screw drive between runs. It also has a stepping motor that can move the probe vertically during runs. The traversing system is shown in Figure 4.17. It was used to place the pitot Kulite sensor, and in later experiments the hot-wire probes, at various axial and circumferential locations with respect to the models.

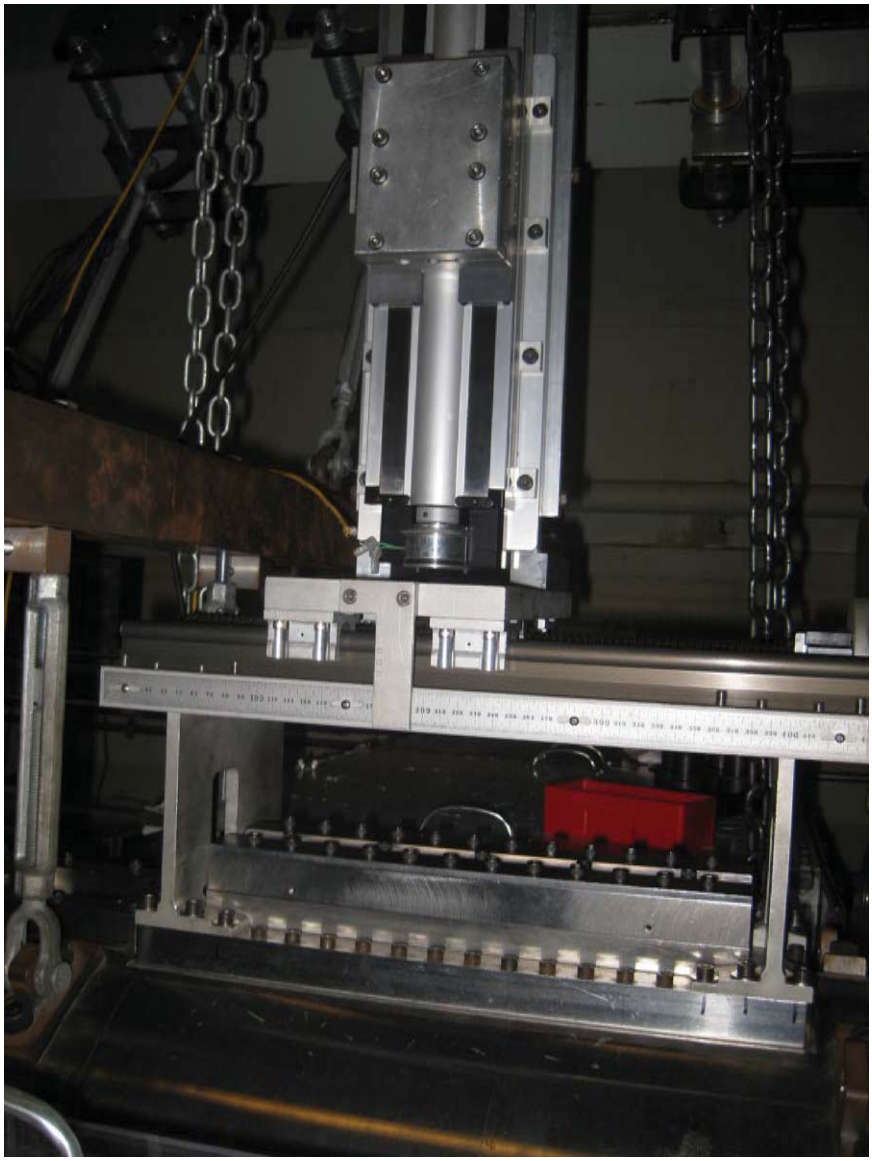

Fig. 4.17. Traverse assembly on top of the BAM6QT test section used for in-flow placement of the pitot Kulite and hot-wire probes.

4.4.3 Hot-Wire Anemometry

Hot-wire anemometry has been used successfully in many hypersonic tunnels, including the BAM6QT, because it provides the high frequency response necessary to measure the instabilities in hypersonic boundary layers. Hot wires also provide

excellent spatial resolution. This spatial resolution was important in the entropy-layer measurements due to the small radial span of the measured instability.

The hot wires were used with an IFA-100 constant-temperature anemometer (CTA). It was manufactured by TSI, Inc. and has been modified to work with higher resistance probes [102]. The CTA keeps the hot wire at a constant temperature by changing the voltage applied across the wire. An overheat ratio was set by attaching a balance resistor to the anemometer. The ratio of the balance resistance to that of the hot-wire probe was typically set in the range of 1.7 to 1.9. This corresponds to an overheat ratio of around 1. These recommended resistance ratios, as well as additional details regarding the setup and use of the hot-wire probes, can be found in the PhD thesis of Shann Rufer [102].

Fig. 4.18. Hot-wire probe with 1.9cm (3/4") vertical strut.

Hot-wire probes were placed at a specific axial location for each run, then traversed in small radial increments during the run to measure disturbances above the surface of the model. The hot-wire probes used in this research were built by Jim Younts at

Purdue University. A picture of one of these hot-wire probes is shown in Figure 4.18. The hot-wire filament is welded to the end of the two barely-distinguishable prongs protruding from the probe at the bottom right-hand corner of the picture. Figure 4.19 shows the hot-wire probe installed near the surface of the cone-ogive-cylinder inside the BAM6T. Platinum-Rhodium Wollaston wires with a diameter of 0.0002 inches were used for a majority of the measurements. This diameter was chosen because it is more robust than the 0.00015-inch diameter wire while still providing sufficiently high frequency response. The wire length varies slightly between probes but is approximately 0.026 inches [0.65 millimeters] for an aspect ratio of 130.

Fig. 4.19. Picture of the hot-wire probe installed inside the BAM6QT and held directly over the surface of the cone-ogive-cylinder.

Proper tuning of the hot wire before measurements is critical to obtaining usable and clear power-spectra estimates. Each hot wire was tuned while installed in the tunnel at atmospheric conditions. Tuning was conducted by using a square-wave generator that is built into the anemometer and adjusting the gain and cable compensation to reduce the oscillations. Figure 4.20 shows time traces of the CTA voltage

output in response to the generated square wave from two different tunings. The frequency response is calculated by measuring the period between the point where the voltage first rises and the trough of the voltage dip that follows the peak. The red line is with the hot wire tuned to a frequency response of about 180 kHz. The black line shows a frequency response of about 80 kHz. The 0.0002-inch diameter wires used in these measurements were typically tuned to a frequency response of about 90 kHz. A lower frequency response than the maximum obtainable (approximately 180 kHz) was sufficient and often preferred because it resulted in cleaner spectra. An example of what is meant by cleaner spectra is shown in Section 9.4.1.

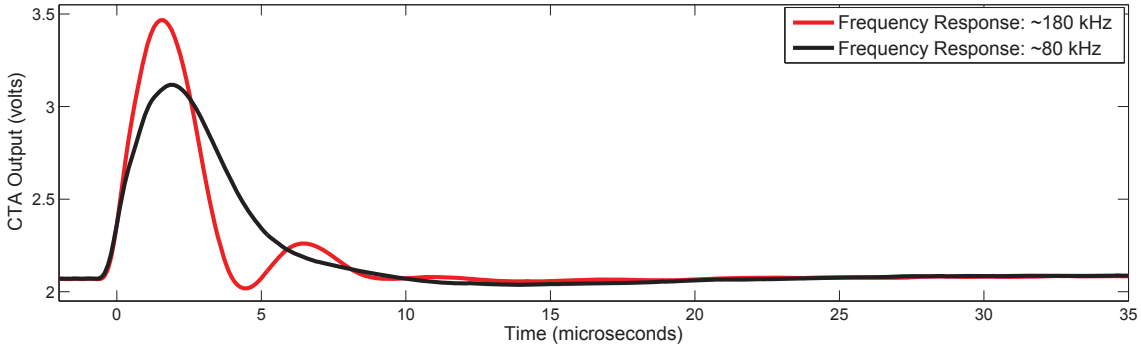

Fig. 4.20. Time traces of hot wire responses to a square wave input with different tunings. Hot wires were tuned while in the tunnel with no flow.

4.4.4 Hot-Wire Survivability

Due to the fragile nature of hot wires and the hostile nature of the hypersonic environment, these filaments broke frequently during usage. Several steps were taken in order to maximize the number of measurements made by each hot wire. The first was to limit the unit Reynolds number for each run to about $7.5 * 10^6$/meter. This corresponds to a starting total pressure of about 123 psia. A few measurements were successfully made at higher Re, but none of the hot wires lasted more than a couple runs at the higher pressures. Some measurements were also made at lower pressures.

However, a decrease in pressure resulted in a significant decrease in the amplitude of the measured instabilities. Therefore, a majority of measurements were made with a starting total pressure of just above 120 psia.

After starting the flow through the BAM6QT nozzle, flow continues until the ball valve is closed. On a typical run when sensor survivability is not an issue, the ball valve is closed when the pressure in the driver tube is as close as possible to atmospheric. This allows the user to open the tunnel immediately after shutdown. However, it soon became apparent that a majority of the hot wires broke during the shutdown process. This led to the practice of shutting the ball valve immediately after the hot wire and other data were taken by the oscilloscopes. This practice reduces the severity of the shutdown process and significantly decreases the chance that the hot wire will break. The downside of this practice is that the tunnel is still pressurized after the run is complete. Shutting the ball valve 4 to 5 seconds after tunnel start for a run at 120 psia typically left the BAM6QT with a driver tube pressure of about 60 psia.

Several depressurization methods were used, but the most effective method was to wait for several minutes for the vacuum tank to get to a fairly low pressure again ($<$50 torr). Then the ball valve was opened again until the pressure in the driver tube was reduced to approximately atmospheric pressure. This depressurization from 60 psia seldom caused wires to break. Ideally the hot wire would be positioned close to the model during this process to further mitigate the risk of breakage.

The hot wires were placed as close as possible to the model during tunnel startup and shutdown. This was done upon the suggestion of Dr. Corke of the University of Notre Dame. The close placement decreases the magnitude of the flow fluctuations to which the hot wire is exposed and appeared to significantly reduce the breakage rate. An Infinity Model K2 long-distance microscope with a reticle was used to measure the distance between the hot wire and the installed model. This allowed the hot wire to be placed close to the model. Figure 4.21 shows this microscope mounted outside the

BAM6QT in preparation to make the measurements through the porthole windows. Measurements with the microscope had an accuracy of approximately ±0.05mm.

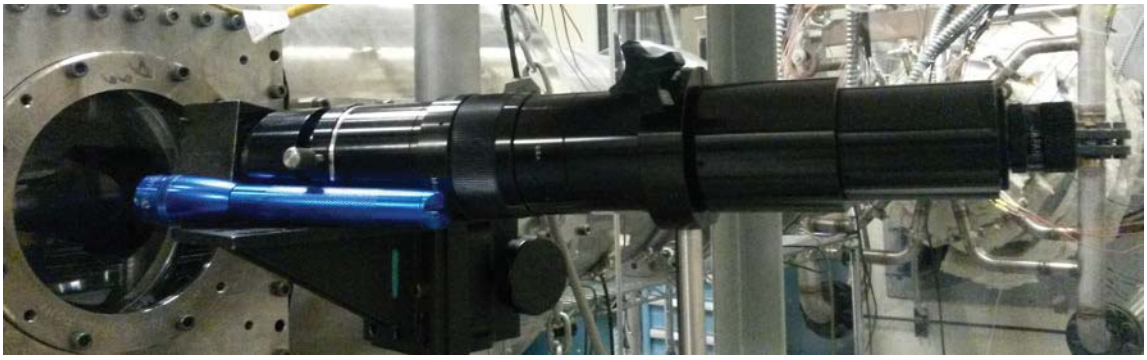

Fig. 4.21. Picture of the long-distance microscope used to measure the distance between the hot-wire probe and the surface of the cone-ogive-cylinder.

Placed on the stand next to the microscope is a blue flashlight. The flashlight was used to provide the necessary light inside the tunnel. A picture taken through the microscope is shown in Figure 4.22. This picture shows the view of the hot-wire probe and the model surface. Light from the flashlight reflects off the probe and the microscope is focused on that surface. The light also reflects off the cylinder surface, but because of the model curvature, the microscope is unable to focus on all the features of the model and the hot wire. However, the dark area between the two reflective surfaces was used to provide a reasonably accurate estimate of the distance between the probe and the surface.

Tunnel startup and shutdown results in vibrations throughout the tunnel. The extent of the model movement during tunnel operation was determined by postprocessing TSP data. For each photo, a Matlab function was used to determine the number of pixels the model had moved from its original location. The vertical displacement of the 30-degree cone-ogive-cylinder during the first four seconds of several runs is shown in Figure 4.23. The blue trace shows the vertical vibrations with a run starting at 30 psia and the green trace is for a 150-psia run. These traces show

Fig. 4.22. Picture of the view through the microscope. The dull grey on the bottom third of the photo is the model. The shiny silver above it is the lower portion of the hot-wire probe with the prongs holding the hot wire extending forward. The dark space dividing them was measured with the reticle to determine the distance between the hot wire and the surface of the cone-ogive-cylinder.

that the displacement magnitude in either direction during these vibrations reached a maximum of less than 0.1 millimeter.

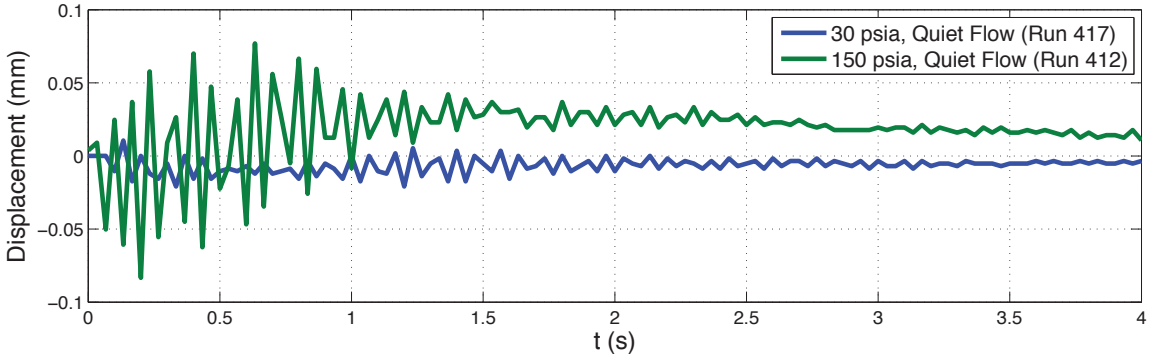

Fig. 4.23. Vertical displacement of the 30-degree cone-ogive cylinder measured by TSP during the first four seconds of two different runs.

These measurements were used to show an approximate safe distance at which the hot-wire probe can be placed off the surface of the cone-ogive-cylinder during startup

and shutdown. Most runs started and ended with the hot wire about 0.3 millimeters off the model surface.

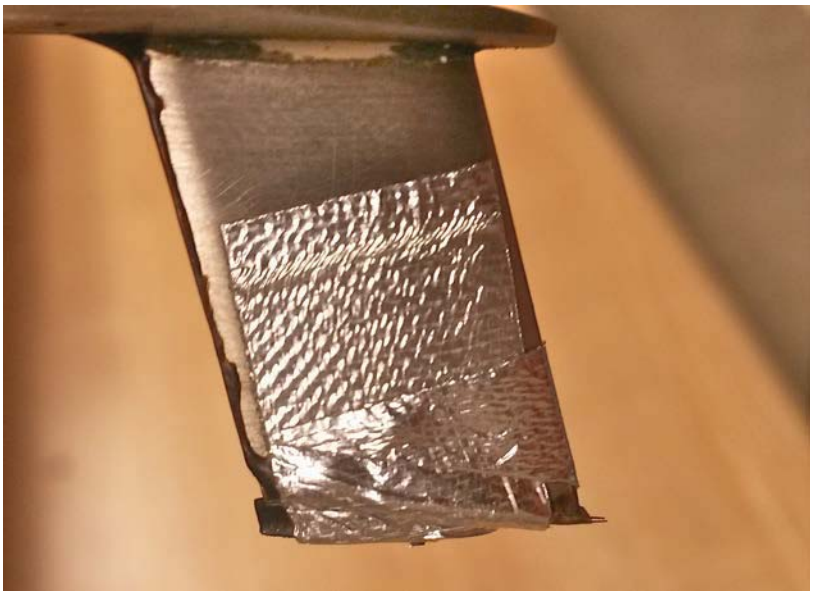

Fig. 4.24. Picture of a rubber "boot" taped to the bottom of the hot-wire probe to protect the wire from accidentally touching the model surface.

To further reduce the chance of the hot wire touching the model surface, either due to tunnel vibrations or accidental traverse movement, a rubber wedge was taped to the foot of the hot wire with heat resistant tape. The back of this rubber "boot" is shown extending out the left of the silver tape at the bottom of the probe in Figure 4.24. The rubber piece was taped to extend below the hot wire in order to rest on the model while keeping the hot wire a short distance off the model. This allowed for much greater confidence in placing the hot wire as close to the model as possible because it reduced the chance that model vibrations or accidental traverse movements would cause the hot wire to touch the surface.

Other procedures that were suggested by previous hot-wire users were also used. One of these procedures was to keep the external control resistor and the wire bundle isolated so they would not get bumped. Another was to keep the constant temperature anemometer in "standby" mode except when tuning the hot wire and during the

measurement portion of the run. This required turning the anemometer to "run" just before starting the tunnel and then turning it back to "standby" as soon as the measurement portion of the run was completed (Reference [101]). Since one user cannot turn the anemometer to "standby" and close the ball valve at the same time, the user must choose which do do first and complete them in succession. Experience suggests that closing the ball valve immediately after the measurement portion of the run is more important than turning the anemometer to "standby" immediately after the run and should be done first.

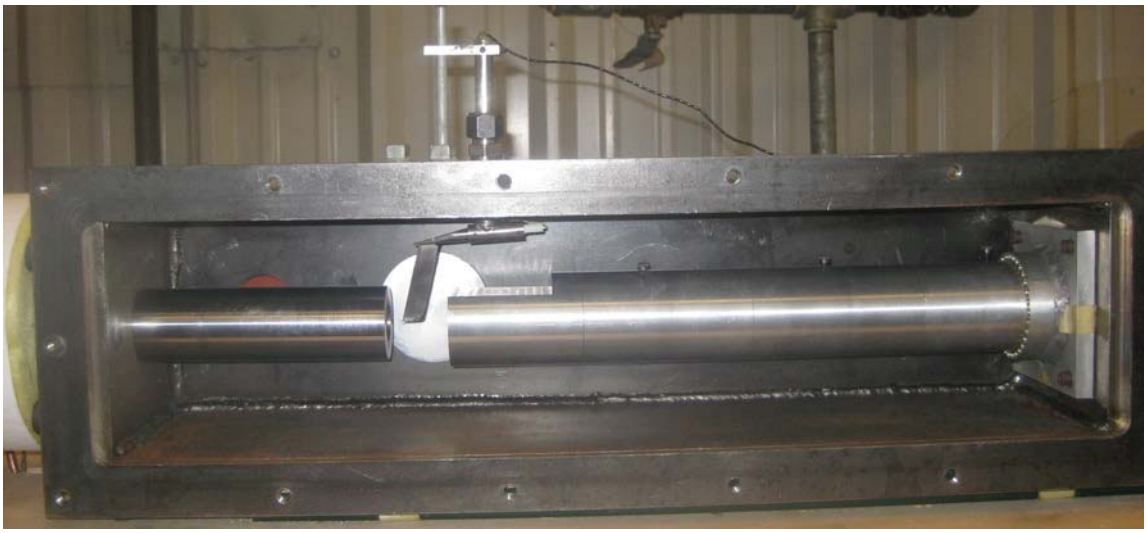

Fig. 4.25. Picture of the Purdue supersonic jet with the front panel removed and a 2-inch-long hot-wire probe inserted into the flow path between the nozzle and the diffuser.

Rufer suggests that the strain hardening of the hot wire which occurs during the cold and hot-wire calibration may also increase the life of the hot wires in the BAM6QT [102, 103]. The first step in this process was to heat the hot wires to a temperature of 180° Celsius. This was done using a Thermo Scientific Lindberg Blue M electric oven.

The heat-treated hot wires were then strain hardened in Purdue's Mach-4 supersonic jet (SSJ). A picture of the SSJ with the front panel removed to show the plenum and a hot-wire probe is shown in Figure 4.25. It operates by sending heated,

compressed air through a 2.5-centimeter nozzle. The nozzle exhausts into a plenum where the hot wires are placed between the nozzle exit and the diffuser inlet. The pressurized air flows past the hot wire, through the diffuser, and into the vacuum tank. The hot wires were strain hardened by keeping them in the flow path as the SSJ was operated over a range of total pressures.

This strain-hardening procedure was pursued rigorously for a couple months on a total of 17 hot wires. 6 hot wires stopped working after being heat treated. 9 more broke during strain harding in the SSJ. Only two hot wires survived the entire process. Both of the hardened hot wires performed well, providing measurements for 11 and 16 runs respectively. However, after December of 2013, this procedure was no longer followed due to the extremely low survival rate of the hot wires and the amount of work required to get only a few functioning hot wires.

Due to the high number of hot wires broken in the initial tunnel entries, larger-diameter wires with a 0.0003-inch diameter were used for several measurements. The larger wires are slightly more robust than the smaller wires, but their frequency response was typically around 40 kHz, which is lower than is preferred to measure the entropy-layer instabilities.

Appendix G provides a summary of all the hot wires used to make measurements in the BAM6QT. It also includes the hot wires that broke during the oven heat-treating and supersonic jet strain-hardening processes. One item of interest that could be significant is that the same hot-wire probes seem to be repeat survivors. For example, only four hot wires survived over 10 runs. Of these four, hot-wires W and Y both survived over 10 runs two different times. This may be coincidence due to the small data set, but it appears that the wires survive better when attached to certain hot-wire probes than when attached to other probes. The PhD thesis of Rufer contains a similar table. It also shows specific hot wires repeatedly surviving over 10 runs [102].

4.4.5 Hot-Wire Calibration

Both calibrated and uncalibrated data are reported. Hot-wire calibration in the BAM6QT is an extensive undertaking and each hot wire has a limited life. Furthermore, since the use of uncalibrated hot-wire data is not uncommon in supersonic conditions [104] the calibration process was not repeated for each hot wire used.

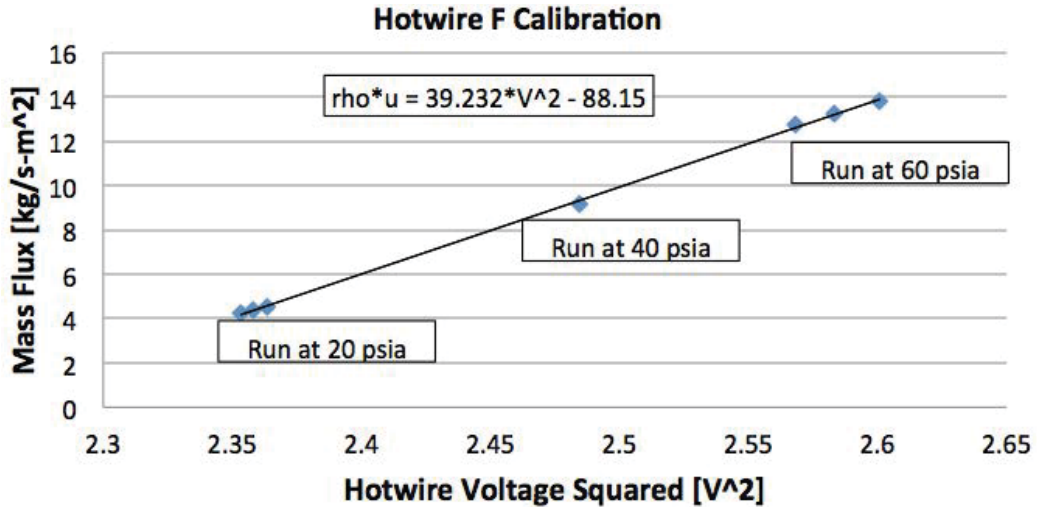

Fig. 4.26. Hot-wire mass-flux calibration curve for one of the hot wires used.

However, a majority of the measurements were made with two of the calibrated hot wires that lasted 6 and 53 runs respectively. One of these calibrations is shown in Figure 4.26. The calibration runs were made in the BAM6QT with the model removed. The model length did not allow for freestream measurements without interference from the shock. This made calibration a more difficult procedure than would be the case for shorter models that allow for the model to be pulled back far enough to remove this interference.

$$\rho u = P_0 M \sqrt{\frac{\gamma}{RT_0}\left[1 + \frac{(\gamma - 1}{2} M^2\right]^{\frac{-\gamma-1}{\gamma-1}}} \tag{4.2}$$

Mass-flux calibrations were performed by performing several runs at various initial stagnation pressures and recording the anemometer voltage and the stagnation

pressure. The mass flux was then calculated using those values, the freestream Mach number, and assumptions of a perfect gas and an isentropic change in stagnation pressure during the run. The equation used to make this calculation is shown in Equation 4.2 [102, 105].

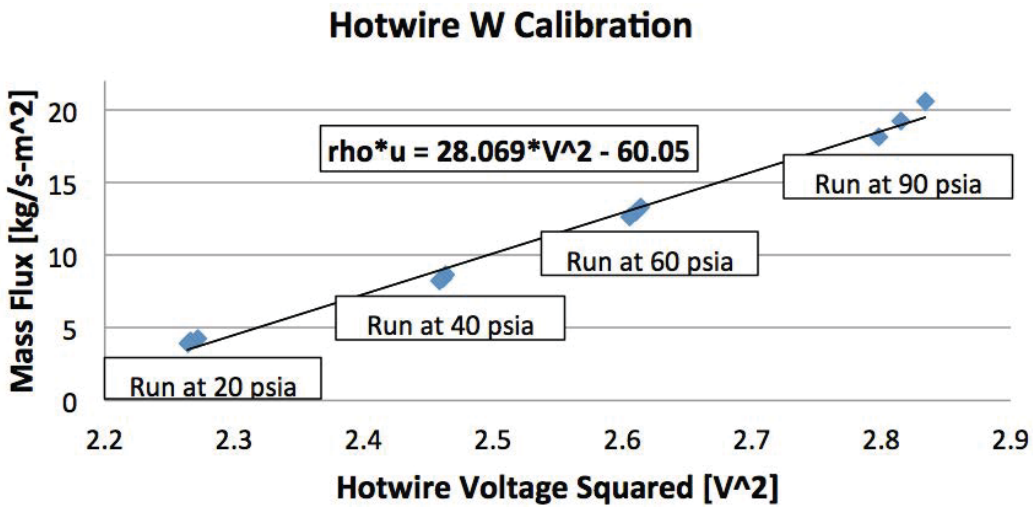

Fig. 4.27. Hot-wire mass-flux calibration curve for the hot-wire used for a majority of the measurements made in January and March 2014.

Another mass-flux calibration curve is shown in Figure 4.27. This calibration curve was made by taking freestream measurements during runs starting at four different stagnation pressures ranging from 20 to 90 psia. The hot wire from which this curve was taken provided a majority of the measurements taken during the last two hot-wire tunnel entries in January and March 2014. It survived for 53 runs, a majority of which were at 120 psia. That is longer than any of the other hot wires used.

Figure 4.28 shows the measured hot-wire voltages from several runs plotted against the mass flux determined from the linear calibration curve from Figure 4.27. These measurements were made with the model installed in the BAM6QT. The measurements tend to be at either the higher or lower end of the calibration curve. Those measurements inside the boundary layer have lower mass-flux values and fall on the lower end of the curve. Those measurements made with the hot wire further from the model have greater mass-flux values.

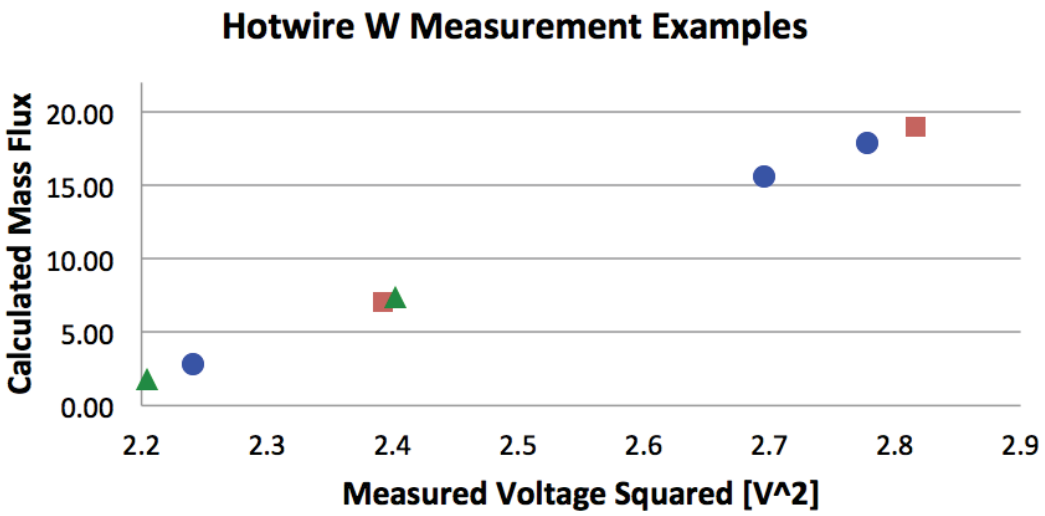

Fig. 4.28. Hot-wire measured voltage (squared) plotted against the calculated mass flux.

4.4.6 Data Acquisition and Processing

The hot-wire and Kulite pressure transducer measurements were recorded using Tektronix Digital Phosphor Oscilloscopes. The oscilloscope models used were TDS7104, DPO7104, and DPO7054. Each oscilloscope has four available channels and up to three oscilloscopes were used at any given time. The oscilloscopes were operated in "Hi-Res" mode. In this mode the oscilloscopes sample at the maximum sampling rate and average the data to provide higher signal resolution.

All of the hot-wire, and a majority of the pressure transducer measurements, were acquired at 1 MHz. Five seconds of data were recorded from each run. The data were processed using sample lengths of 0.5 seconds for the Kulites and 0.16 seconds for hot-wire measurements. Turbulent bursts in the tunnel occasionally required deviations in the sample length. In those cases the sample was typically taken immediately before or after the turbulent burst, resulting in a shorter sample length. Power spectral densities were calculated from the samples using the Matlab's spectrum.welch function with an FFT length of 32768 (2^{15}). Blackman windows containing 800 points were used with a 50% overlap. This corresponds to 625 windows for the

transducer measurements and 200 windows for the hot-wire measurements. The large number of windows used to calculate the power spectra from hot-wire and transducer measurements resulted in reduced variance, but also rather smooth spectral traces.

Cross-correlations were also made between many of the measured signals using the "xcorr" function in Matlab. Cross-correlations apply a time difference between two signals and determine how closely the two signals match. It is used as a measure of similarity between two signals. A perfect match between signals would result in a correlation equal to 1.0. This is done quickly over a range of time differences in Matlab. The magnitude squared coherence estimate function in Matlab, "mscohere", was also used. It is used to compare how the power spectral densities between two signals compare. An FFT length of 2048 was used with a Hanning window and a 50-percent overlap.

4.5 Glow Perturber

When initial surface measurements did not show clear first-mode instabilities, an attempt was made to excite the first-mode instability using a variable-frequency glow perturber. The glow perturber was inserted into the 30-degree cone-ogive-cylinder as shown in Figure 4.29 and was used to introduce perturbations into the boundary layer at a similar frequency as the predicted first-mode instability. This was done in an attempt to use these artificial perturbations to excite the first-mode instability and stimulating them to grow with downstream distance to a measurable magnitude.

The optimal location for the glow perturber is at the neutral point of the boundary-layer instability that is being excited. This allows for the instability to get excited at the earliest possible location and then continue to grow with downstream distance. Computations predict that the neutral point of first-mode instabilities for the 30-degree cone-ogive-cylinder is at an axial location of about 0.15 meters. To ensure that the glow perturber was inserted after the neutral point, it was inserted onto the model at 0.25 meters.

Fig. 4.29. Close up picture of glow perturber inserted in the cone-ogive-cylinder model for testing in the BAM6QT.

Operation of the glow perturber in the BAM6QT requires a significant amount of electronic equipment. The setup is shown in Figure 4.30 and includes a pulse generator, a two function generators, an oscilloscope, a power supply, and a custom circuit built by Ladoon [106]. A more complete description of the process by which the variable-frequency glow perturber is operated is included in Ladoon's PhD thesis [106] and Dupuy's final internship report [107] .

The glow-perturber design and setup was initially developed by Ladoon for the Purdue Mach-4 tunnel [106]. Casper then redesigned the glow perturber for use in the BAM6QT on both a 7-degree cone and an insert for the tunnel wall [108]. The glow perturber works by providing a plasma disturbance on the model surface. It consists of two electrodes with a cylindrical Macor insulator separating them by a distance of 1.32 millimeters. The center electrode is a copper pin and the outer electrode is a thick-walled tube made of brass. This distance between the two electrodes was calculated using Paschen's Law which plots the minimum voltage required to create

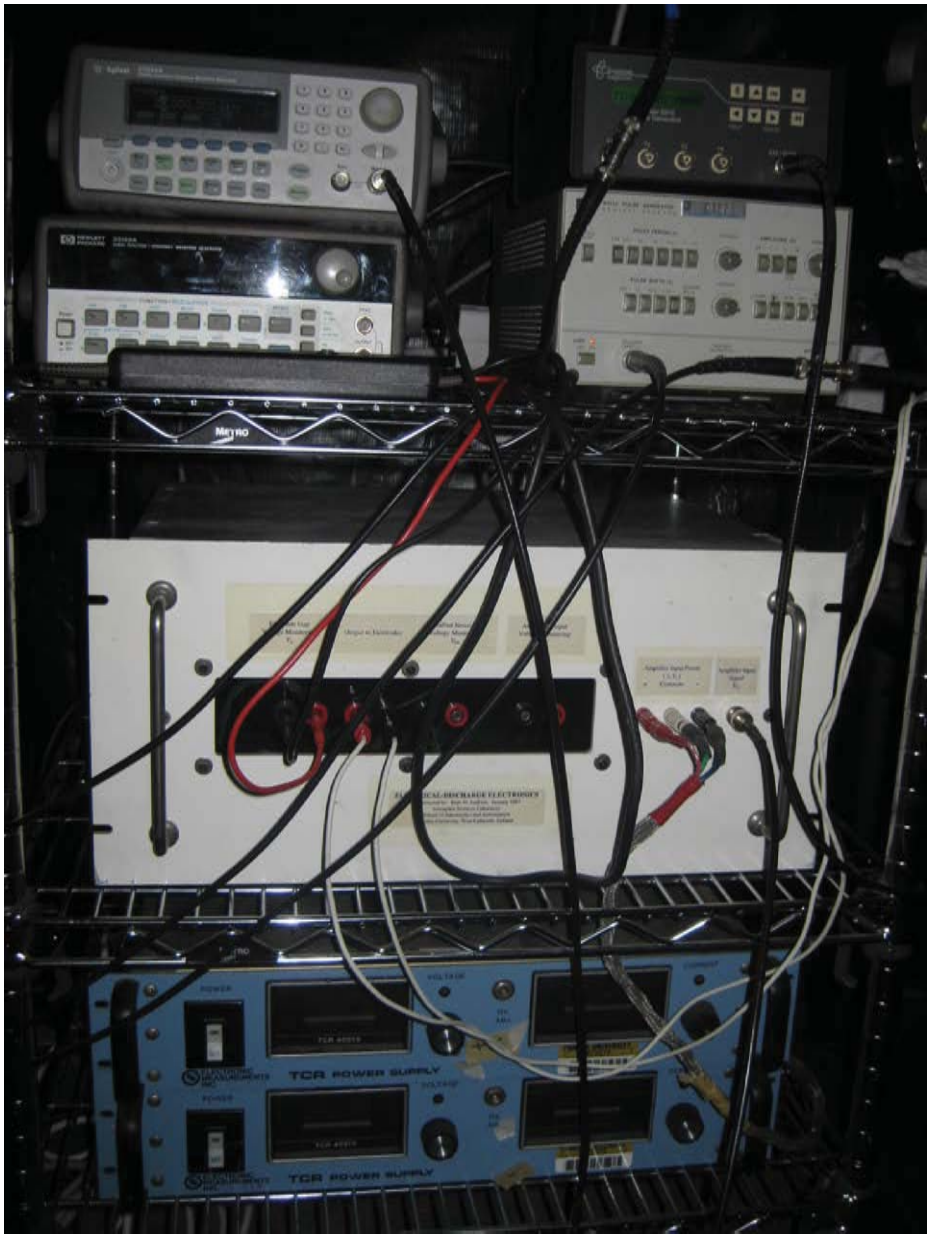

Fig. 4.30. Picture of the setup required to run the variable-frequency glow perturber in the BAM6QT.

an arc ("breakdown voltage") against the product of the ambient pressure and the distance between electrodes. Since the glow perturber is required to operate under tunnel conditions, the distance was optimized using the BAM6QT static pressure that experiments were planned for. This pressure varied from about 0.05 to 0.1 psia. A

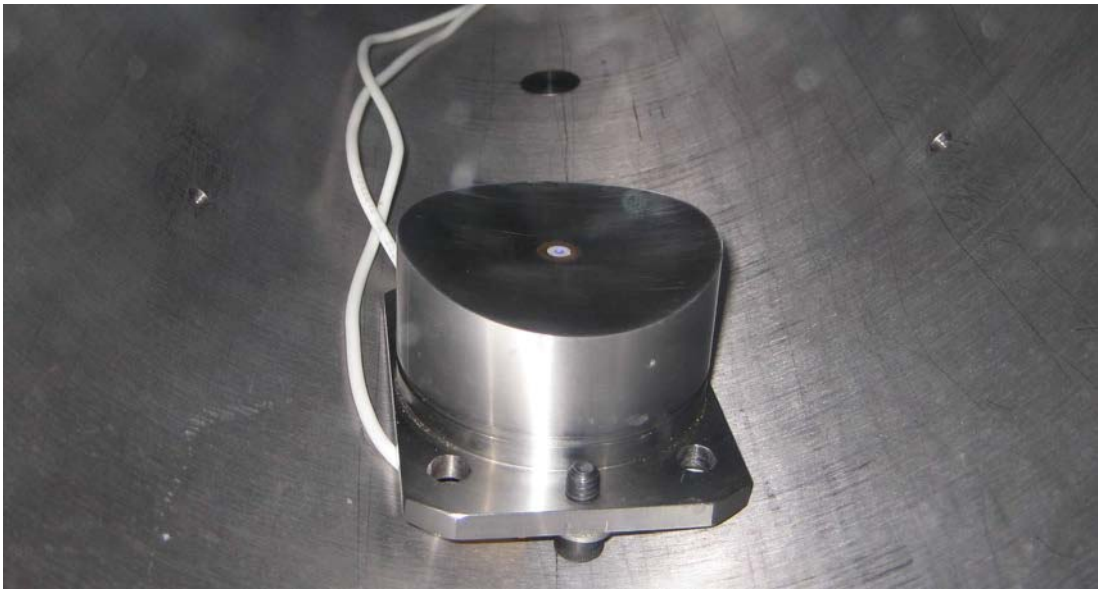

Fig. 4.31. Picture of the tunnel-insert glow perturber operating inside the Purdue vacuum test cell.

diagram of the glow perturber design inserted into the 30-degree cone-ogive-cylinder is shown in detail in Appendix F.

Fig. 4.32. Picture of the glow emitting from the glow perturber operating inside the Purdue vacuum test cell.

Although the design used in the cone-ogive-cylinder is different, the distance between the electrodes is the same as the tunnel-insert glow perturber design used by Casper [108]. Because of this, and the fact that the cone-ogive-cylinder model is too long to fit in the test cell, the tunnel-insert perturber was used in preliminary experiments made in the test cell. It was successfully operated in the test cell at frequencies between 0.1 and 75 kHz with the most intense glow at around 50 kHz. For these experiments to simulate the BAM6QT conditions, it was necessary to match the density of the air within the test cell to the density of the BAM6QT at the operating static pressures. Pictures of the tunnel-insert glow perturber operating in the test cell with and without external lighting are shown in Figures 4.31 and 4.32.

5. COMPUTATIONAL AND EXPERIMENTAL RESULTS FOR THE FLARED CONE

5.1 Stability Analysis for the Flared Cone

The original design intent for the cone-ogive-cylinder and the flared cone described in Section 4.2.4 was to produce measurable first-mode instabilities. Yet the two designs are significantly different. The main reason for this difference is that the optimization that produced the flared cone did not stipulate that second-mode instabilities had to be smaller than the first mode.

STABL was used to do a stability analysis of the flared cone. The maximum first and second-mode N factors at 160 psia are shown in Figure 5.1. These computations assumed a total temperature of 433 K and a wall temperature of 300 K. The dash-dot-dot grey and black lines show the predicted first-mode instability N factors and the colored lines show the second-mode instability N factors. The flare on the cone maintains the boundary layer at a more constant thickness. For this reason, the instabilities are able to grow over a longer distance and reach greater N factors than for a straight cone.

At a total pressure of 160 psia, the flared cone was predicted to have a first-mode N factor of about 5 at 0.5 meters from the leading-edge. At this same axial location, the flared-cone analysis predicted a second-mode N factor of about 8.5, significantly larger than the first-mode.

Figure 5.2 shows the predicted first and second-mode N factors for the flared cone at 80 psia. The N-factor charts look very similar for the two different flow conditions, with the second-mode N factors significantly greater than those of the first mode. However, the lower-pressure flow conditions result in lower first and

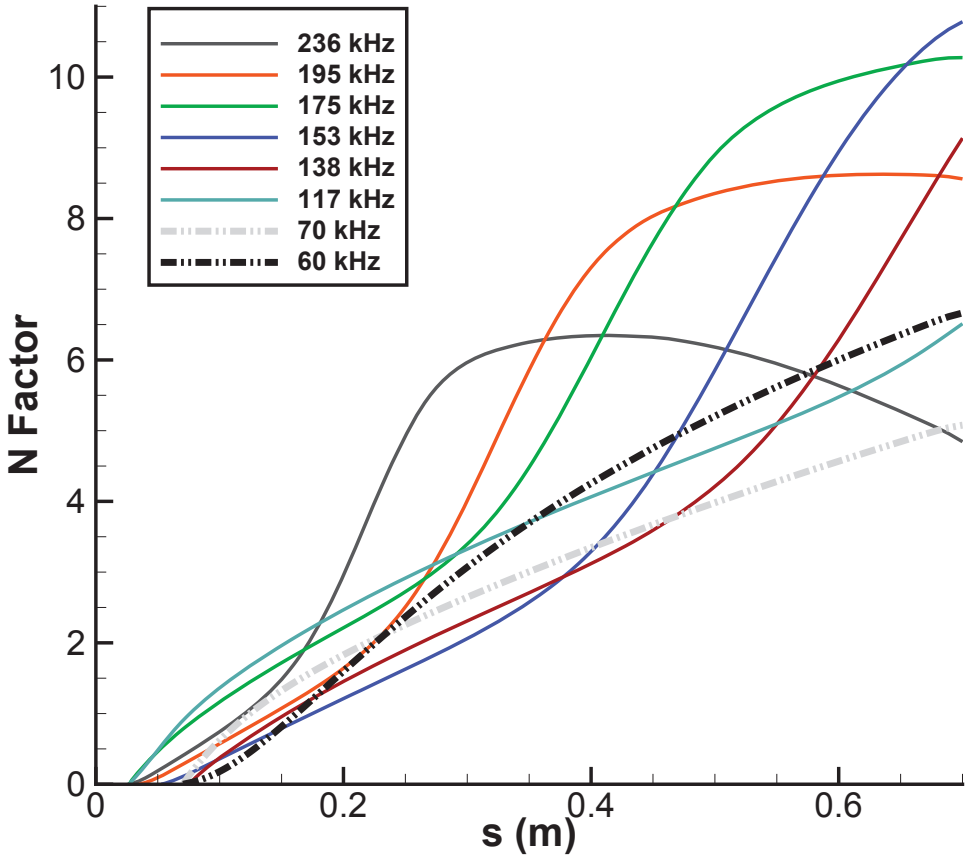

Fig. 5.1. Computed first and second-mode N factors for the flared-cone design under BAM6QT conditions (P_0=160psia).

second-mode N factors. The frequencies of the instabilities also decrease as the total pressure decreases.

One unique feature of the stability chart for the flared cone at 80 psi is the difference between the two frequencies with the highest first-mode N factors. The 81-kHz line (grey dash-dot-dot) starts early on the cone with a high growth rate that decreases with increased axial location. The 35-kHz line (black dash-dot-dot) starts later on the model with a low growth rate that increases with axial location. The decrease in growth rate of the 81-kHz instability and simultaneous increase for the 35-kHz instability are a result of the slowly-increasing boundary-layer thickness. This is because the instability frequency decreases as the boundary-layer thickness increases.

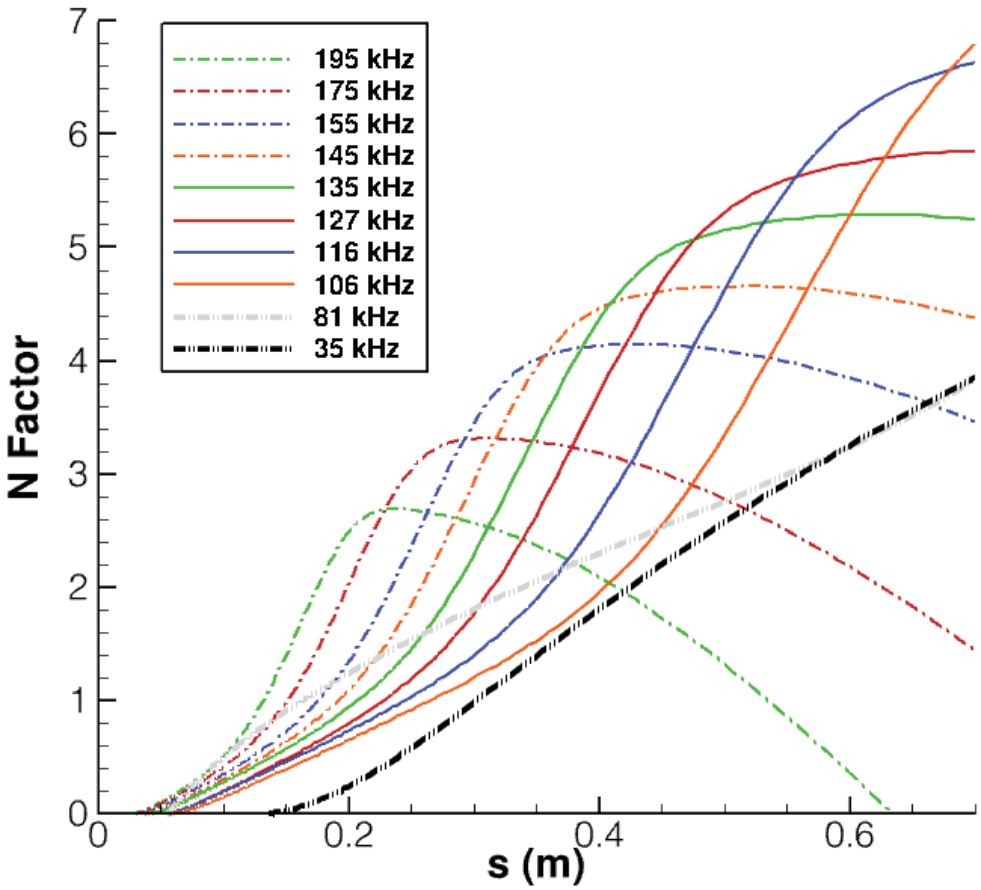

Fig. 5.2. Computed first and second-mode N factors for the flared-cone design under BAM6QT conditions (P_0=80psia).

5.2 Experimental Results for the Flared Cone

Surface measurements were made on the flared cone with Kulite pressure sensors installed flush with the surface. The power spectra from surface measurements at 0.5, 0.58, and 0.68 meters are shown in Figure 5.3. The blue and black lines are from measurements made above a unit Reynolds number of $10.0 * 10^6$ per meter and show large peaks in the spectra. At 0.5 meters, the instability peak is around 190 kHz. The frequency of the instability decreases as it progresses downstream and at 0.58 meters the peak frequency is about 170 kHz. The frequency has decreased to just above 150 kHz by 0.68 meters and the magnitude has increased significantly.

Power spectra from measurements at 0.68 meters also show a lower-frequency peak at about 25 kHz. The peak magnitude of this peak is affected by the change in Reynolds number, but the frequency of peak does not change. The source of the spectral peak is unknown, but it is believed to be something other than a boundary-layer instability since its frequency does not change with Reynolds number.

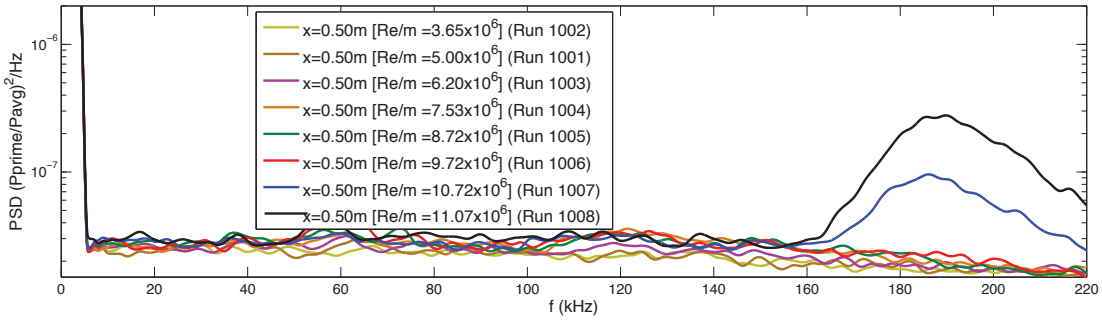

(a) PSD on the flared cone at 0.50m.

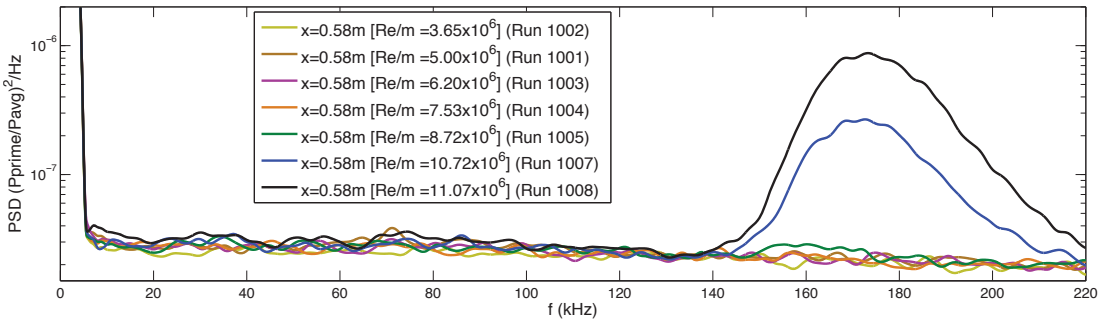

(b) PSD on the flared cone at 0.58m.

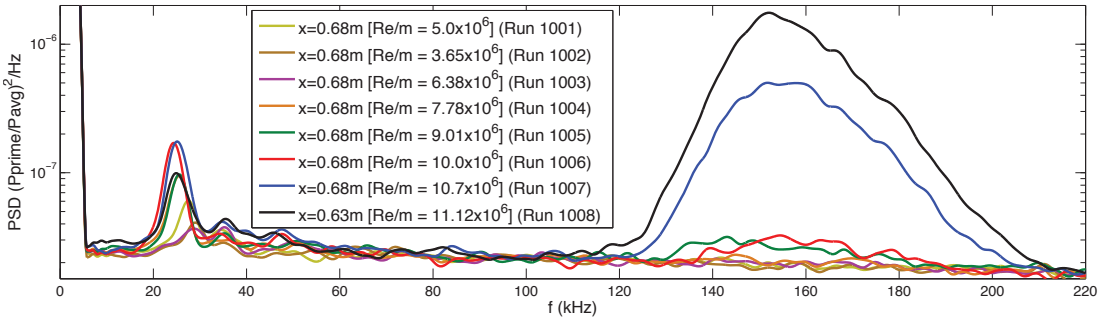

(c) PSD on the flared cone at 0.68m.

Fig. 5.3. Power spectra at several locations on the flared cone over a range of tunnel conditions.

5.3 Comparison of Experimental and Computational Results

The computational stability analysis performed at 160 psia corresponds to an experimental $Re/m = 10.9*10^6$ under the conditions outlined in Table 3.2. Figure 5.4 compares the experimental measurements with the computations. The orange, green, and blue lines in Figure 5.4(a) show spectra from measurements at 0.5, 0.58, and 0.68 meters at a unit Reynolds number of $10.9*10^6$. The peaks increase in magnitude and decrease in frequency with downstream distance.

The computed second-mode instability N factors with the frequencies that match closest to the frequencies of the measured peaks are shown in Figure 5.4(b). Annotations have been added to the figure. They show the location of measurements, predicted second-mode instability frequencies at those locations, and the N factors at those frequencies. The measured and predicted frequencies are compared in Table 5.1.

The root mean square (RMS) amplitude was calculated to compare with the predicted N factors. The signal power was found by integrating the square of the power spectral density over the frequency band. The spectra were integrated over the frequency range between 120 and 240 kHz. The RMS amplitude was then calculated by taking the square root of the integrated signal power and dividing it by the average pressure for normalization. These RMS values are included in Table 5.1.

Table 5.1
Comparison of the predicted second-mode instabilities with experimental measurements (flared cone, Run 1007)

	Frequency (kHz)		Magnitude	
x (m)	Predicted	Measured	Predicted N factor	Measured RMS
0.5m	195	190	8.4	0.064
0.58m	175	170	9.8	0.082
0.68m	153	153	10.6	0.109

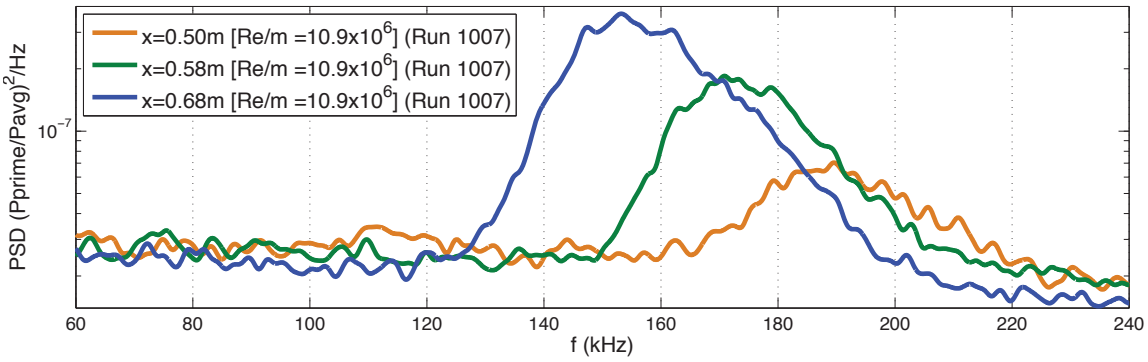

(a) Power spectra on the flared cone at 0.5, 0.58, and 0.68 meters.

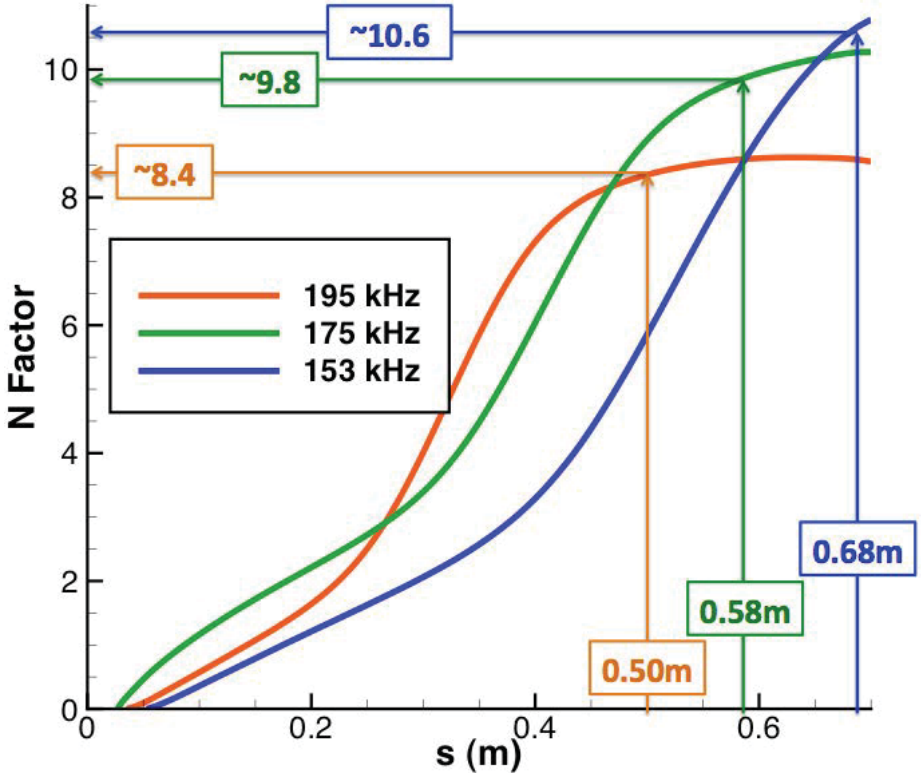

(b) Computed N factors for the flared-cone design with annotations for experimental comparison.

Fig. 5.4. Comparison of experimental and computational flared-cone results at $Re/m = 10.9 * 10^6$ (P_0=160psia).

The measurements and computations at 0.68 meters are shown by the blue lines in Figure 5.4. They both show a 153 kHz instability. The green and orange lines compare the measured 170 and 190-kHz peaks with the computed second-mode N factors at 175 and 195 kHz respectively. The measured and computed frequencies are comparable at each location. Additionally, the predicted N factor and the RMS both increase with downstream distance showing an increase in instability magnitude. The increase in the predicted N factor between 0.5 and 0.68 meters is greater than the measured RMS increase. This is possibly due to nonlinear saturation in the experiments. Notwithstanding, the high correlation of the measured peaks with the predicted second-mode instabilities suggests that they are second-mode instabilities. Measurements with a different sensor type could be made to provide more conclusive evidence.

Second-mode instabilities have been measured in many different tunnels using several different sensor types [109]. However, the author is not aware of another instance where second-mode instabilities have been measured using Kulite pressure transducers.

Attempts to measure first-mode instabilities were unsuccessful. Low-frequency peaks show up in the power spectra at 0.68 meters (Figure 5.3(c)). However, the frequency of those peaks do not change with Reynolds number as would be expected of a boundary-layer instability. The measured frequency is also lower than the predicted first-mode instability frequencies on the flared cone. Calculations predict the most-amplified first-mode frequency to be between 35 and 81 kHz when calculated under BAM6QT conditions at 80 and 160 psia.

6. COMPUTATIONAL AND EXPERIMENTAL RESULTS FOR THE CONE-OGIVE-CYLINDER

6.1 Stability Effects of Geometric Changes

The design process identified the effects of cone angle, cylinder diameter, and flare on the predicted boundary-layer instabilities. A summary of these computational results are included to provide a basic understanding of some features that are important when designing a first-mode dominant geometry.

6.1.1 Leading-Edge Cone Angle

The leading-edge cone angle had the greatest effect on the edge Mach number which dictated whether the first or second-mode instability was dominant. Figure 6.1 shows the edge Mach calculated by the MOC code for several cone-ogive-cylinder models with varying leading-edge half-cone angles.

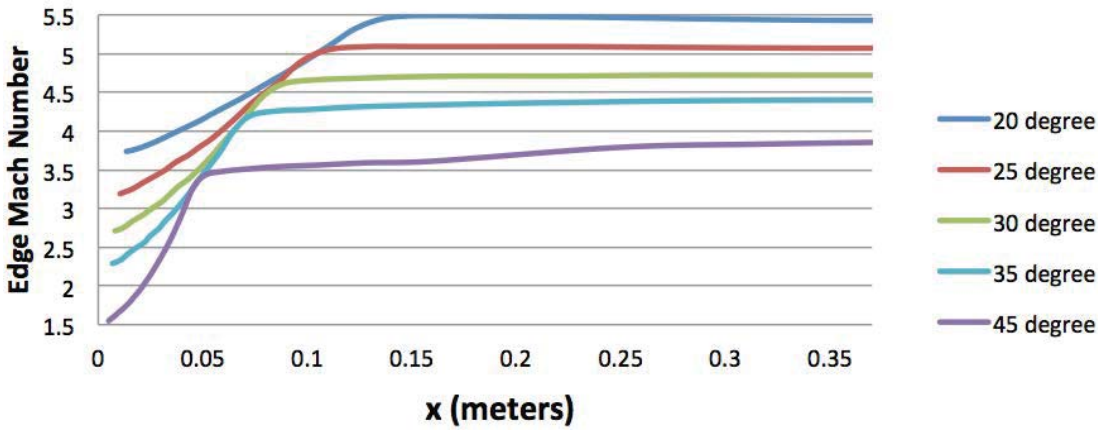

Fig. 6.1. Edge Mach numbers calculated with the MOC code for cone-ogive-cylinder geometries with varying leading-edge angles.

These MOC calculations show that an nosetip angle of greater than 25 degrees is necessary to decrease the edge Mach below 5. They were used as an initial estimate of when first-mode instabilities would become dominant.

Stability calculations using PSE-Chem were made for several different nosetip angles to determine the first and second-mode N factors. The conditions for these calculations are outlined in Section 3.2.2.

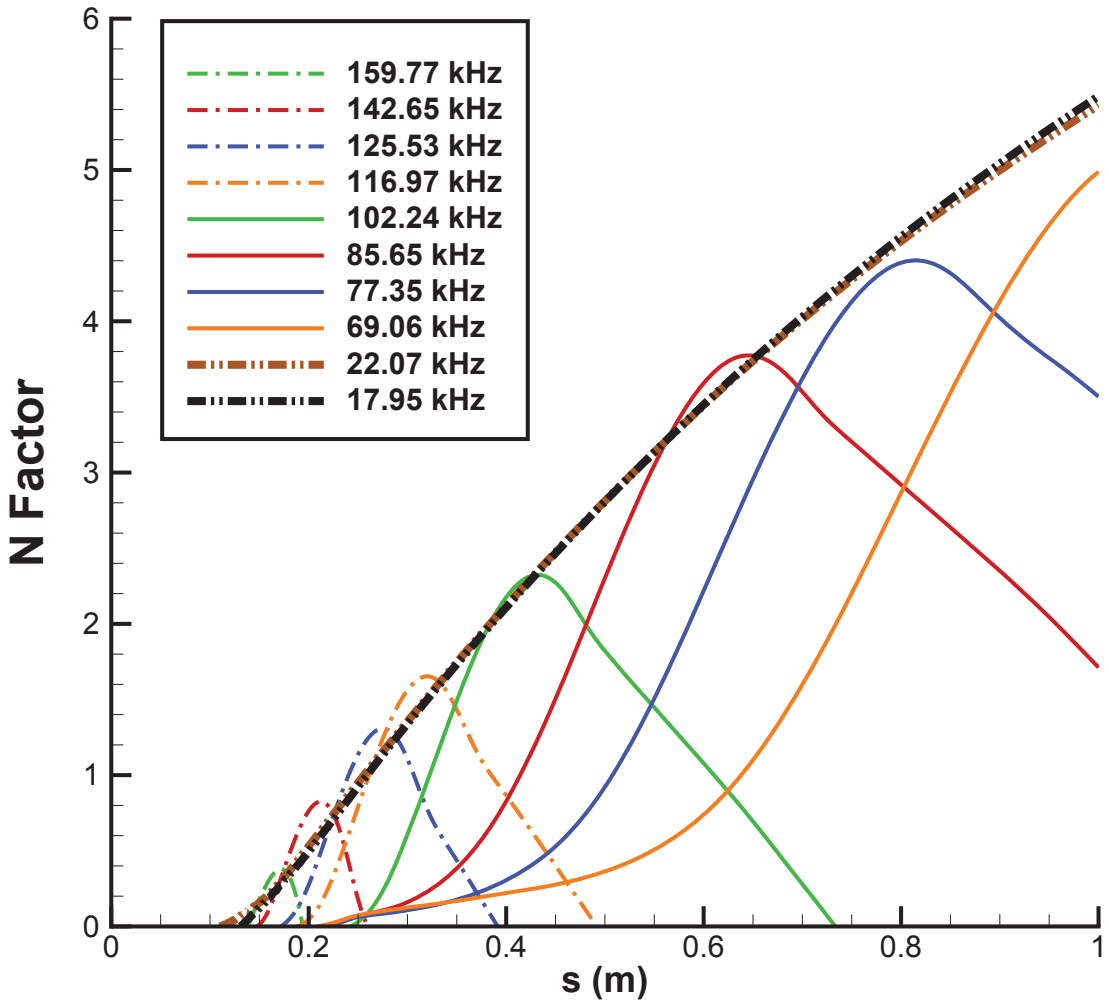

Fig. 6.2. Computed first and second-mode N factors for the 25-degree cone-ogive-cylinder under BAM6QT conditions (P_0=160psia).

The stability diagram for the 25-degree model is shown in Figure 6.2. The dash-dot-dot lines that correspond to the 17.95 and 22.07-kHz frequencies show the maxi-

mum calculated N factors for the first-mode instability. The solid and dash-dot lines corresponding to the 69.06 thru 159.77-kHz frequencies show the maximum N factors for the second-mode instabilities. At a stagnation pressure of 160 psia, computations show first and second-mode N factors that are nearly equal. They predict an N factor of nearly 5 at the latest measurement location of 0.86 meters.

Table 6.1 shows the calculated first and second-mode N factors at 0.38 meters for cone-ogive-cylinders with nosetip angles ranging from 20 to 45 degrees. It shows that the second-mode instability is dominant at cone half-angles less than 25 degrees. At angles greater than 25 degrees, the first-mode N factors are slightly larger than the second-mode N factors. As the cone angle increases to 35 and 45 degrees, the calculations show a significant decrease in both first and second-mode instabilities.

Table 6.1
Computed N factors at 0.38m for first and second-mode instabilities for various leading-edge cone angles.

Leading-Edge Cone Half-Angle (degrees)	1st Mode N Factor	2nd Mode N Factor
20	0.05	3
25	2.0	2.1
30	1.9	1.3
35	1.6	0.7
45	0.7	0.3

6.1.2 Cylinder Diameter

Cylinder diameter had very little effect on the instabilities computed in STABL. Computations showed that as the cylinder diameter was increased from 2 to 3 inches, the magnitude of the dominant N factors remained fairly constant. However, the frequency of the instabilities decreased slightly as the diameter increased.

6.1.3 Flare

The purpose of adding flare to the cylinder was to maintain an approximately-constant boundary-layer thickness in order for the same frequency waves to be amplified over a longer distance and thus reach larger N factors on the model. A comparison of the flared and non-flared geometries is shown in Figure 6.3.

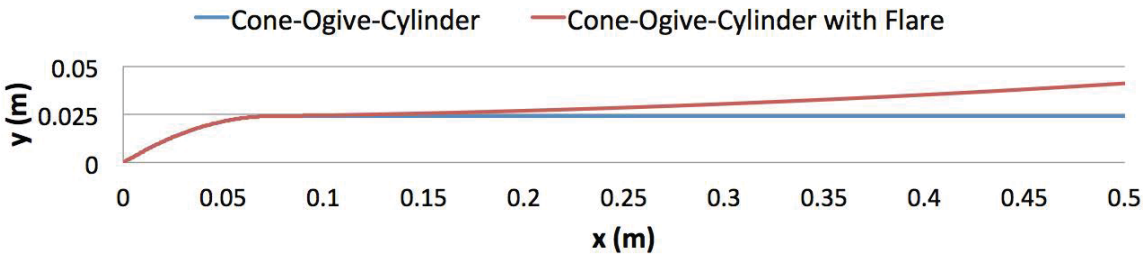

Fig. 6.3. Comparison of cone-ogive-cylinder geometries with and without flare.

The addition of flare was effective in increasing the magnitude of the first-mode instability and is the main concept behind the optimized design developed by Lindsay Kirk. However, one unanticipated result is that the flare caused the second-mode N factors to increase at a much greater rate than the first-mode waves. Because of this, the flared design had higher second-mode N factors at the trailing edge than the first mode, even though in the original (non-flared) design the first-mode N factors were much larger.

This is shown in Figure 6.4. It shows the effect of the flare on the N factors of the cone-ogive-cylinder with the 30-degree leading-edge half-angle. Figure 6.4(a) shows the most amplified first-mode instability on the cone-ogive-cylinder with and without flare. The solid green line shows the maximum first-mode N factor for the cone-ogive-cylinder. The blue dash-dot line shows the N factors with the addition of flare. It shows that the frequency of the most amplified instability increases with the addition of flare. It also shows a slight increase in the maximum N factor of the first-mode instability.

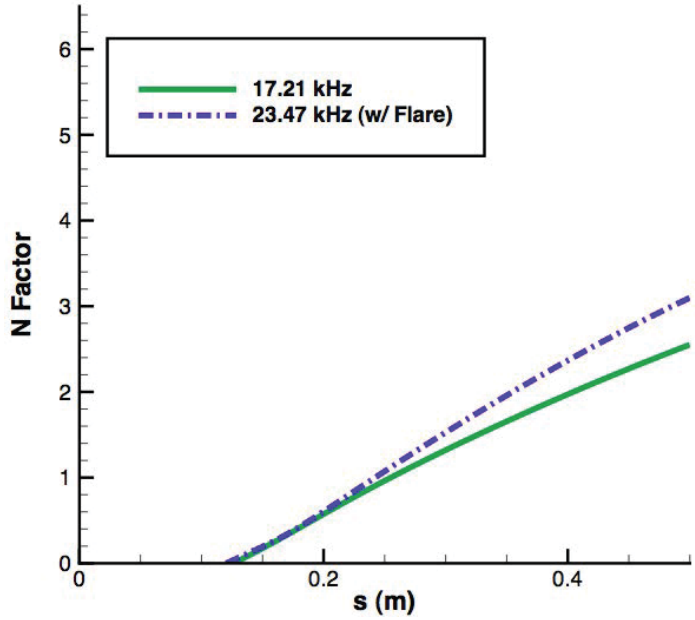

(a) Maximum first-mode N factors on a cone-ogive-cylinder with and without flare.

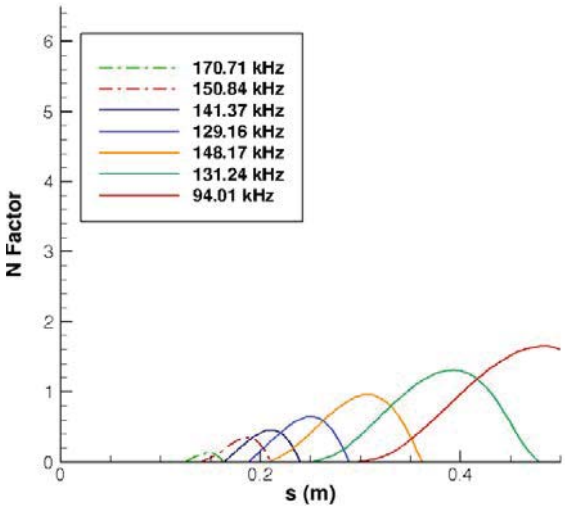

(b) Maximum second-mode N factors on a cone-ogive-cylinder.

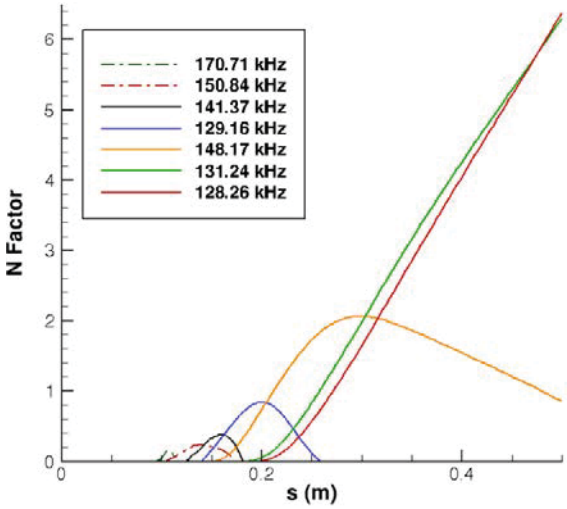

(c) Maximum second-mode N factors on a cone-ogive-cylinder with flare.

Fig. 6.4. Plots showing the effect of flare on first and second-mode instabilities.

Figure 6.4(b) shows the maximum N factors on the cone-ogive-cylinder and Figure 6.4(c) shows the maximum N factors with the addition of flare to the design. Together, these figures clearly show the large effect that flare has on the second-mode instabilities. As in the case with the first-mode instability, the boundary layer stays at a thinner, near-constant thickness that increases the frequency of the most amplified instabilities. However, this near-constant thickness has a much more profound effect on the second-mode instabilities as it allows these fast-growing waves to grow over a greater distance. This results in significantly higher second-mode N factors at the trailing edge of the flared geometry.

The reason the flare has a much greater effect on the second-mode than the first-mode is not completely understood. However, one explanation is that the second-mode instabilities have a larger growth rate than the first mode, but a more narrow band of frequencies over which they are amplified. That being the case, the constant boundary-layer thickness of the flared design would allow the amplified second-mode instability to grow over a greater distance and achieve higher N factors. However, if the first-mode instability has a wider band of amplified frequencies, it would grow more slowly than the second mode but over a greater distance on the non-flared design, resulting in greater N factors at the trailing edge.

In 1993, Masad reached a similar conclusion in his research using the e^N method to compare first and second-mode instabilities. Although the maximum growth rate for the second-mode was much larger than that of the first-mode, the streamwise unstable range for the first-mode instability waves was much longer for the first mode. Therefore, the N factor for the first-mode waves reached predicted transition levels earlier than the second-mode waves. His calculations were done for adiabatic flow over a flat plate at a freestream Mach number of 5 [110].

6.2 Cone-Ogive-Cylinder Design

Because of the significant increase in the N factors of second-mode instabilities when the flare is added, flare was not used in the Purdue design. The first geometry built was an axisymmetric cone-ogive-cylinder with a 30-degree leading-edge half-angle with a 1.9-inch diameter. Then, to allow the first-mode instabilities to grow as long as possible, the model was extended to a length of 1 meter [40 in]. Later, an additional cone-ogive-cylinder model was built with interchangeable nosetips as described in Section 4.2.3.

6.2.1 Boundary-Layer Thickness and Edge Mach Calculations

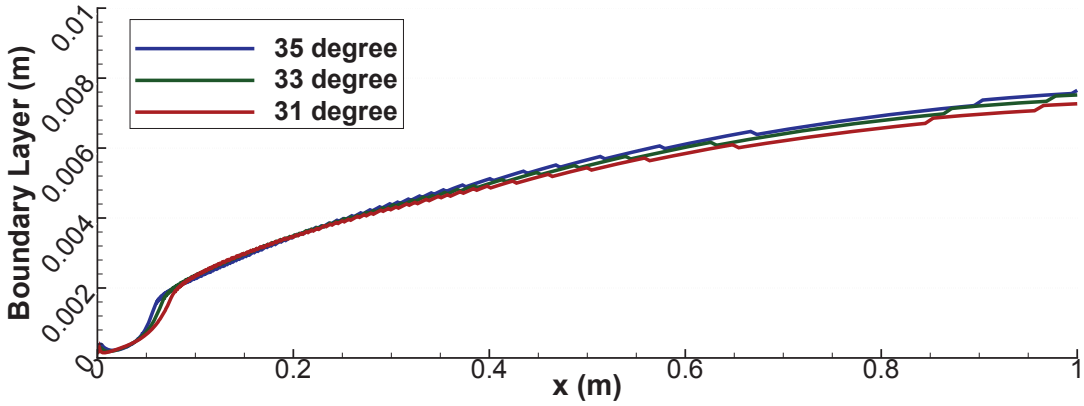

Fig. 6.5. Calculated boundary-layer thickness ($\delta_{99.5}$) values for the 31, 33, and 35-degree models (P_0=120psia).

Mean-flow calculations for each cone-ogive-cylinder configuration show that the boundary-layer thickness on the cone-ogive-cylinder increases slightly as the nosetip angle increases. Figure 6.5 shows the computed $\delta_{99.5}$ thickness for three of the configurations at a stagnation pressure of 120 psia. Unless otherwise noted, the edge of the boundary layer is considered to be the height where the local velocity is 99.5% of the freestream velocity ($\delta_{99.5}$). This estimate of the edge of the boundary layer,

combined with the instability location obtained by hot-wire measurements, identifies the approximate location where the measured instability enters the boundary layer.

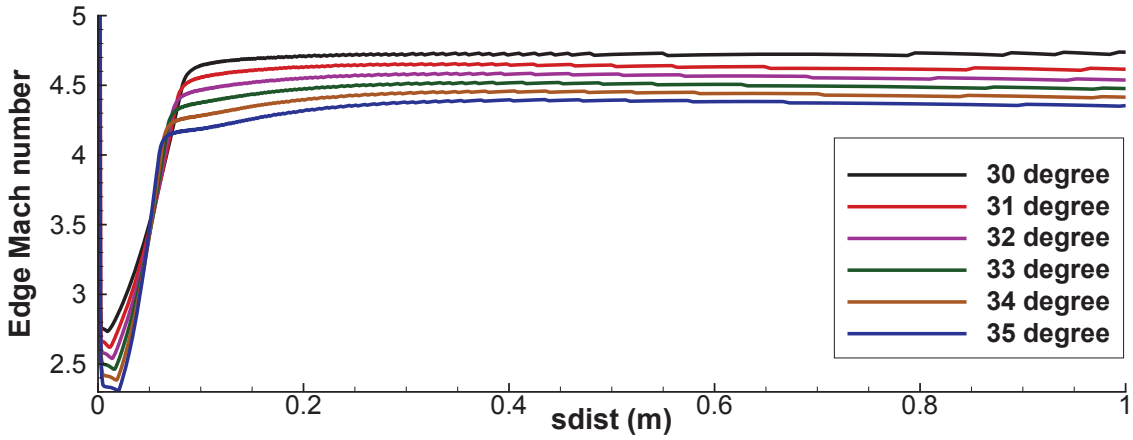

Fig. 6.6. Calculated edge Mach number for the cone-ogive-cylinder models (P_0=120psia).

The Mach number was also calculated using the STABL mean-flow solution for each cone-ogive-cylinder configuration. The Mach numbers at the edge of the boundary layer for each nosetip angle are shown in Figure 6.6. The edge Mach number decreases as expected with increasing nosetip angle.

6.2.2 Calculated Velocity and Mass Flux Profiles

Figures 6.7 and 6.8 show the velocity profiles at 0.43 and 0.62 meters for each of the cone-ogive-cylinder configurations. Figure 6.7 shows a rapid velocity increase inside the boundary layer. The knee in the curve shows the edge of the boundary layer which is between about 5 and 6 millimeters off the surface. At the edge of the boundary layer, the velocity is between 830 and 850 meters per second for each configuration.

Figure 6.8 also shows the velocity profiles, but the horizontal axis range is reduced to show the velocity outside of the boundary layer. As the nosetip angle increases, the boundary-layer edge velocity decreases. In addition, the velocity profiles for the

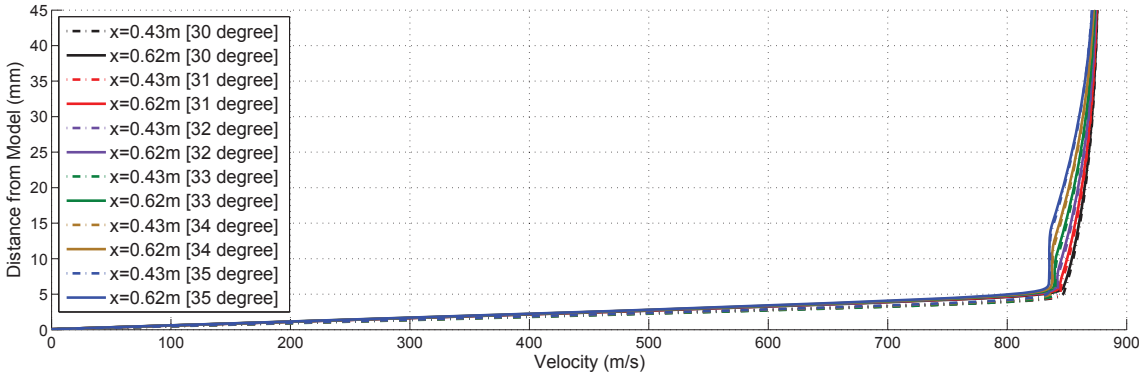

Fig. 6.7. Calculated velocity profiles above the cone-ogive-cylinder configurations.

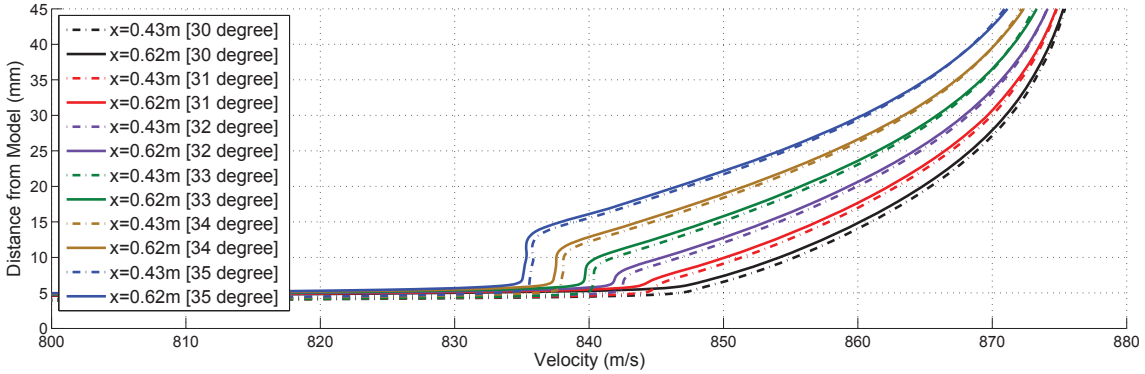

Fig. 6.8. Calculated velocity profiles outside of boundary layer.

35-degree model (blue lines) show a near-constant velocity for about 7 millimeters just above the edge of the boundary layer. This distance decreases with decreased nosetip angle and is no longer visible on the 30-degree model.

Figure 6.9 shows the mass flux profiles at two axial locations above the 31, 33, and 35-degree cone-ogive-cylinder models. The blue dot-dash line shows the calculated mass flux above the 35-degree model at 0.43 meters and the solid blue is for 0.62 meters. At both locations above the 35-degree model, the mass flux is nearly constant for several millimeters outside of the boundary layer. This is corresponds to the several millimeters of constant velocity seen outside of the boundary layer in the velocity profiles.

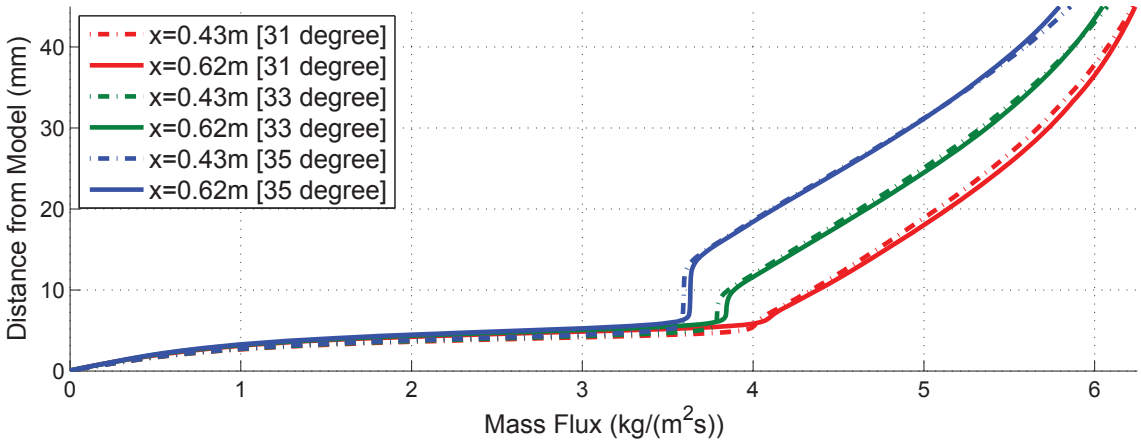

Fig. 6.9. Calculated mass flux profiles above the 31, 33, and 35-degree cone-ogive-cylinder configurations.

The green lines show the calculated mass flux above the 33-degree model and the red lines are for the 31-degree model. As was seen in the velocity profiles, the distance the nearly-constant mass flux extends above the boundary layer decreases as the nosetip angle increases.

6.2.3 Stability Analysis for the 30-degree Cone-Ogive-Cylinder

The calculated N factors for the 30-degree cone-ogive-cylinder at the BAM6QT 160-psia conditions outlined in Section 3.2.2 are shown in Figure 6.10. The colored lines show the N factors of calculated second-mode instabilities at various frequencies that at some axial location had the highest second-mode N factor. As the boundary-layer thickness increases, the frequency of the amplified instability decreases. Figure 6.10 shows how the calculated second-mode instability frequency near the front of the mode is around 170 kHz. This instability frequency decreases to about 69 kHz by the end of the cylinder. Since the most-amplified second-mode instabilities are tyically two-dimensional, stability calculations for oblique second-mode waves were not conducted.

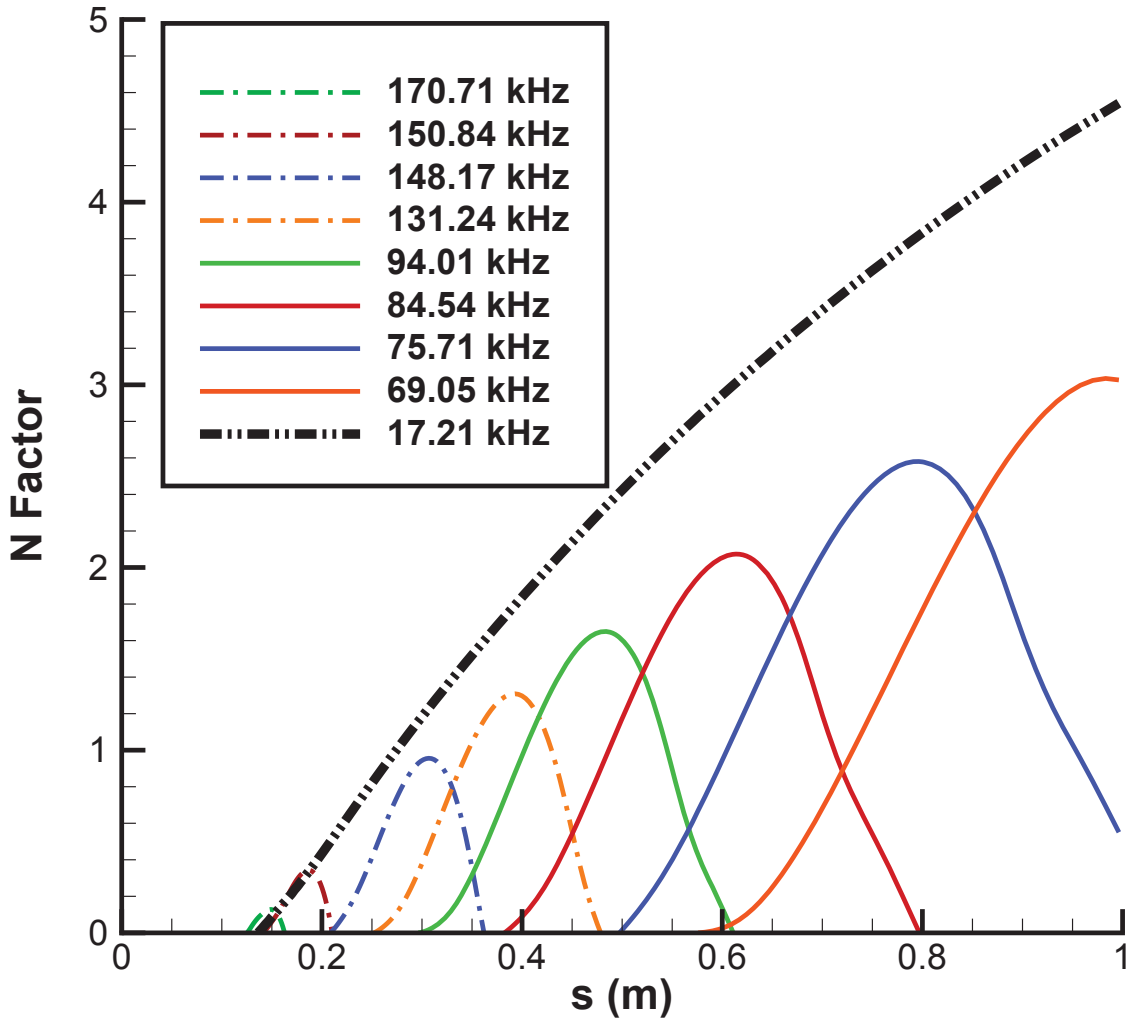

Fig. 6.10. Computed first and second-mode N factors for the 30-degree cone-ogive-cylinder under BAM6QT conditions (P_0=160psia).

The black dash-dot-dot line shows the maximum computed first-mode N factor as it increases along the length of the model. The most amplified first-mode instability waves are three-dimensional so stability calculations were made over a range of frequencies and wave angles. From these PSE-Chem calculations, a 17-kHz instability was calculated to have the highest first-mode N factor all along the model. The wave angle of the calculated 17 kHz instability lies between 63 and 68 degrees and is shown

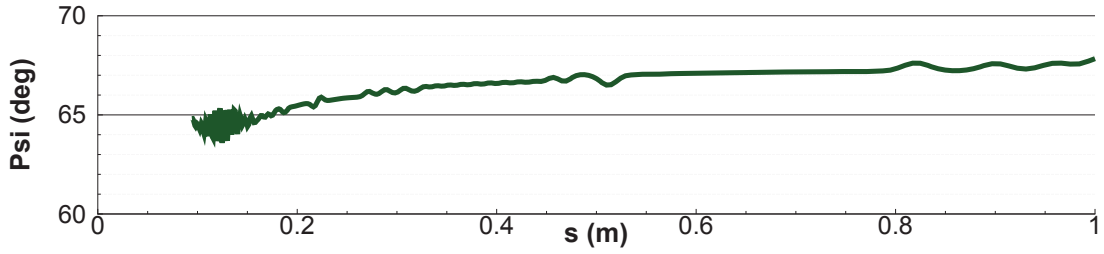

Fig. 6.11. Wave angle of the predicted first-mode instability along the length of the 30-degree cone-ogive-cylinder.

in Figure 6.11. Calculated wave angles between 60 and 70 degrees were typical for the first-mode instabilities above the cone-ogive-cylinder models.

As the Reynolds number decreases, the magnitude of the predicted first and second-mode instabilities also decrease. Figure 6.12 shows the calculated N factors for the 30-degree cone-ogive-cylinder at a stagnation pressure of 80 psia. At this lower pressure, the maximum computed first-mode N factor at an axial location of 1 meter is only about 3. For comparison, the first-mode N factor under 160-psia tunnel conditions is predicted to be above 4.5.

The frequencies for both first and second-mode instabilities also decrease with decreasing Reynolds number (also shown in Figure 6.12). On the 30-degree cone-ogive-cylinder, the most amplified first-mode instability decreases from 17 kHz to about 10 kHz as the stagnation pressure decreases from 160 to 80 psia. This decrease in instability frequency is due to the increase in boundary-layer thickness at the lower Reynolds numbers and was expected.

6.2.4 Stability Analysis for the 35-degree Cone-Ogive-Cylinder

The N factors of the first and second-mode instabilities decrease as the nosetip angle increases on the cone-ogive-cylinder. The maximum predicted N factors on the 35-degree model at 160 psia are shown in Figure 6.13. As the nosetip angle increases from 25 (Figure 6.2) to 35 degrees, the maximum first-mode N factor at 0.5 meters

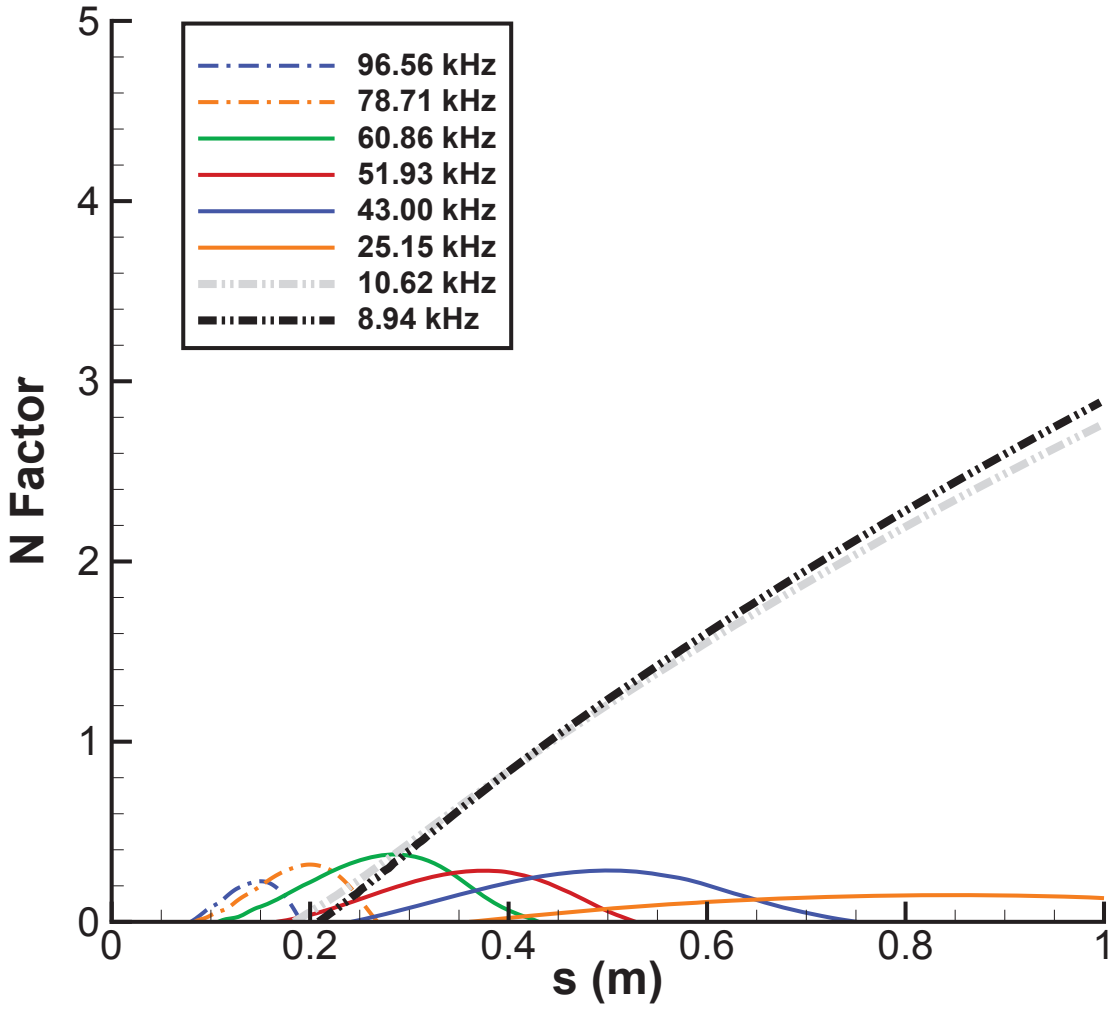

Fig. 6.12. Computed first and second-mode N factors for the 30-degree cone-ogive-cylinder under BAM6QT conditions (P_0=80psia).

decreases from about 3 to 1.3. At the same axial location, the second-mode N factor decreases from about 3 to 0.4.

6.2.5 Surface Measurements on the 30-degree Cone-Ogive-Cylinder

The original 30-degree cone-ogive-cylinder was used in the attempt to measure first-mode instabilities. It was selected because the computations predicted higher

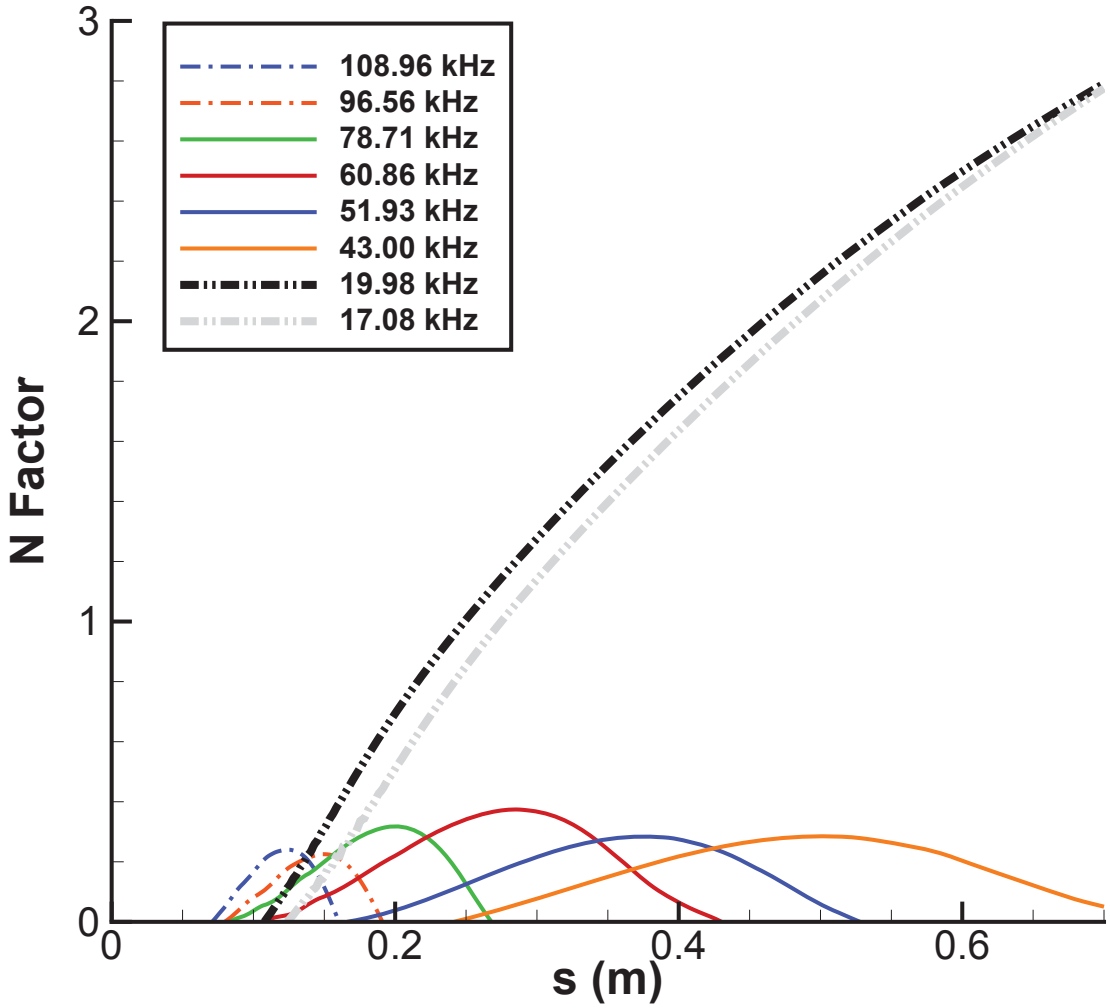

Fig. 6.13. Computed first and second-mode N factors for the 35-degree cone-ogive-cylinder under BAM6QT conditions (P_0=160psia).

first-mode N factors than second-mode N factors. The coordinates of this design are included in Appendix A.1.

The power spectra from surface measurements at 0.58 and 0.61 meters are shown in Figure 6.14. The yellow line shows the power spectra at a $Re/m = 4.8 * 10^6$. That corresponds to a stagnation pressure of about 70 psia. There is little indication of a disturbance under those conditions.

The green, blue and black lines show the power spectra at increasingly higher Reynolds numbers. As the Reynolds number increases, several disturbance peaks

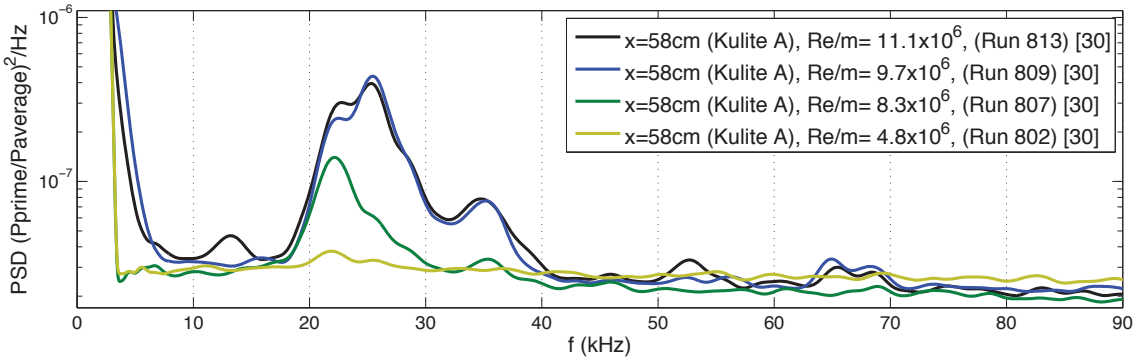

(a)

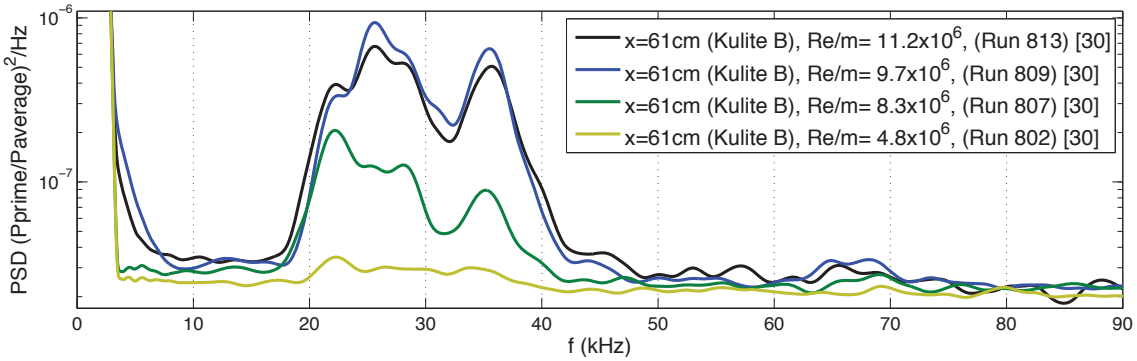

(b)

Fig. 6.14. Power spectra showing low-frequency disturbances on the 30-degree cone-ogive-cylinder at 0.58, and 0.61 meters.

appear between 20 and 40 kHz. For the green line ($Re/m = 8.3 * 10^6$), the most distinct peaks are at about 22 and 35 kHz. A further increase in Reynolds number results in power spectra shown by the blue and black lines. They show the most defined peaks at frequencies of about 25 and 35 kHz. The reason the disturbance peak magnitudes did not increase as Re/m increased from $9.7 * 10^6$ to $11.1 * 10^6$ is unknown.

Between $Re/m = 4.8 * 10^6$ and $9.7 * 10^6$, the peak magnitudes increase as the Reynolds number increases. However, the disturbance frequency range does not change. Table 6.2 compares the frequencies of the predicted first and second-mode instabilities with the measured disturbance frequencies. In contrast to the measured disturbance, the predicted first and second-mode boundary-layer instabilities change frequency as the Reynolds number changes. This suggests that the measured disturbance is not a first or second-mode boundary-layer instability.

Table 6.2
Comparison of the predicted boundary-layer instability frequencies with the measured disturbance peaks at 0.61 meters using the 30-degree cone-ogive-cylinder.

P_0 (psia)	First-Mode (kHz)	Second-Mode (kHz)	Disturbance Range (kHz)
160	17	85	20-40
80	10	43	20-40

6.2.6 Surface Measurements on the 25-degree Cone-Ogive-Cylinder

Surface measurements were also made on the cone-ogive-cylinder with the 25-degree nosetip. Measurements were made on the 25-degree model because the STABL computations predicted slightly higher N factors on it than the 30-degree model. The power spectra for the measurements made at 0.56 meters are shown in Figure 6.15. The measurements at lower Reynolds numbers do not show much of a disturbance.

However, as the Reynolds number increases, the disturbance peaks appear between 30 and 40 kHz.

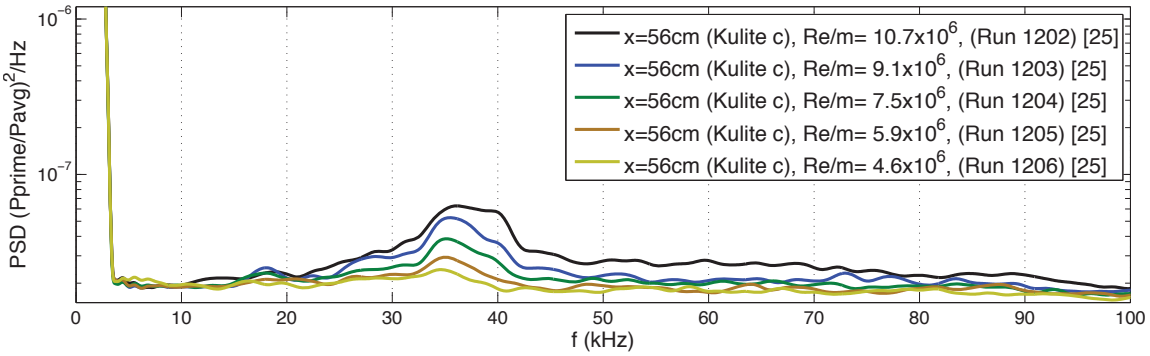

Fig. 6.15. Power spectra showing disturbances measured on the 25-degree cone-ogive-cylinder at 0.56 meters.

As with the surface measurements on the 30-degree cone-ogive-cylinder, the magnitude of the instability increases with Reynolds number, but the frequency does not change. This indicates that the measured disturbance on the 25-degree model is also not a first or second-mode boundary-layer instability.

6.2.7 Glow Perturber Measurements

A variable-frequency glow perturber was used in another attempt to produce measureable first-mode instabilities on the original 30-degree cone-ogive-cylinder. Figure 6.16 shows the glow perturber electrodes installed flush with the model surface at 0.25 meters from the nosetip. The perturber was operated at 17 kHz, the predicted frequency of the most-amplified first-mode instabilities under BAM6QT conditions at 160 psia. It was also operated at 10, 15, 22, and 35 kHz. These frequencies were chosen because they appeared as peaks in initial experimental measurements.

However, the electrical noise produced by the operating glow perturber reduced the ability to make clean instability measurements on the model surface. It was known beforehand that the perturber would create significant electronic noise. Several steps

Fig. 6.16. Picture of the glow perturber electrodes installed flush on the surface of the cone-ogive-cylinder.

were taken to minimize the effect of this noise, but they proved inadequate. The perturber and pressure transducer leads go down the center of the cone-ogive-cylinder model and exit out the back of the model. This close proximity of the perturber and transducer leads over the second half of the meter-long model results in significant electronic interference in the measurements.

One step taken to reduce interference was to use electromagnetic shielding over the glow perturber leads. Figure 6.17 shows the leads for the perturber and the pressure tranducers running out the back of the model. Another step was to run the perturber only during a small portion of the run. It was set to turn on 0.5 seconds into the run, remain on for 0.5 seconds, and then turn off for the remainder of the run. Measurements were made with the transducers before, during, and after the time when the perturber was operational.

Power spectra from the measurements when the perturber was running were too inundated by the electronic perturber noise to measure any first-mode instabilities that may have been in the boundary layer. Before and after the perturber operation,

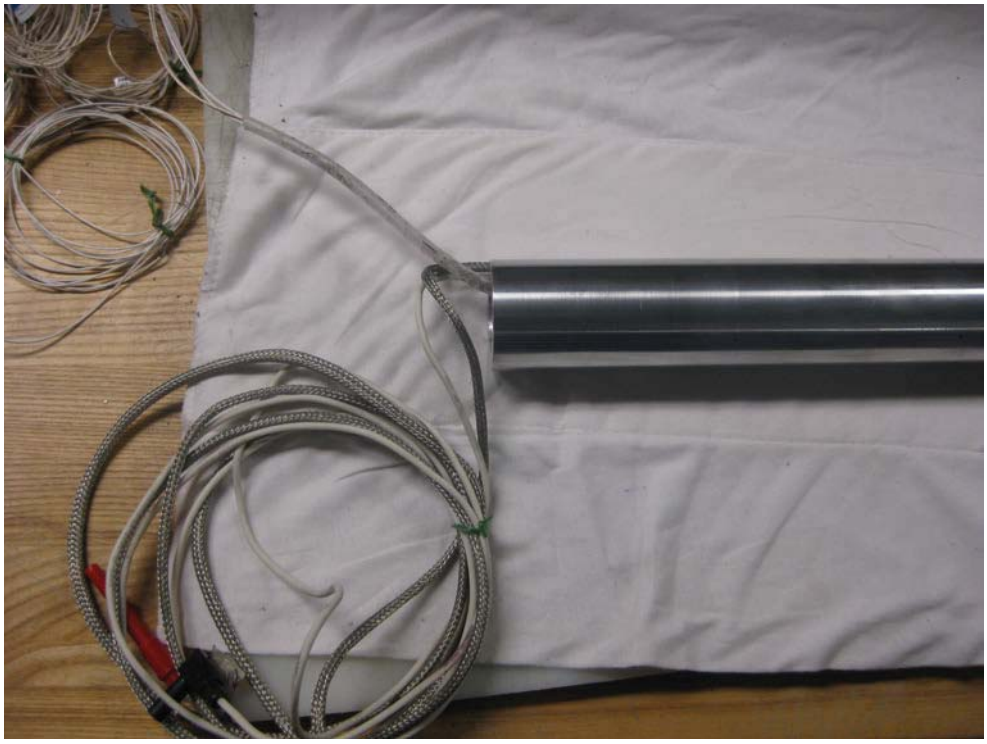

Fig. 6.17. Picture of the leads to the glow perturber and the Kulite pressure transducers coming out the back of the 30-degree cone-ogive-cylinder model.

measurements made by the surface sensors matched very well with previous and subsequent surface measurements on the 30-degree cone-ogive-cylinder.

Calculations of the power spectra were focused on measurements made immediately after the glow perturber was turned off. It was hoped that this would allow for the disturbance initiated by the glow perturber to convect downstream and be measured at the sensor without electronic interference. However, the spectra from these measurements also showed no signs of a first-mode instability.

7. EXPERIMENTAL DETECTION OF AN OFF-SURFACE INSTABILITY

7.1 Background

The search for experimental evidence of entropy-layer instabilities began after attempts to measure first-mode instabilities provided evidence of a different type of instability. These initial surface measurements on the 30-degree cone-ogive-cylinder were made in 2012 and are discussed in Section 6.2.5. Spectra from these and subsequent surface measurements showed a disturbance that did not change in frequency with increasing Reynolds number as would be expected for a boundary-layer instability. This initiated a search for experimental evidence to confirm whether this was a real instability or an artificial result of the experiments.

This investigation resulted in a set of experimental evidence from surface and hot-wire measurements. They show what appears to be a real instability that originates above the boundary layer, most likely in the entropy layer. In order to better understand the properties of the apparent instability, several additional sets of measurements were performed. These measurements show the instability grow outside of the boundary layer, then enter the boundary layer as it proceeds downstream. As the nosetip angle of the cone-ogive-cylinder is increased in 1-degree increments from 30 to 35 degrees, the properties of the measured instability change in a smoothly-varying manner.

A majority of the surface measurements made in the initial stages of this investigation were at a stagnation pressure of 160 psia. This pressure was ideal because it provided large peaks in the surface measurement spectra. However, the investigation soon led to off-surface measurements using hot wires and measurements at 160 psia were no longer practical. Measurements at a lower stagnation pressure were necessary

in order to increase the hot-wire survivability. A stagnation pressure near 120 psia was found to be ideal. As a result, most of the hot-wire measurements were made at the lower pressure. This decrease in stagnation pressure from 160 to 120 psia changes the predicted boundary-layer thickness (99.5%) on the 30-degree model from 5.1 to 5.8 millimeters.

While there is significant evidence that an entropy-layer instability has been measured, there are unanswered questions and the evidence is not unequivocal. Additional measurements and stability calculations are necessary to strengthen this premise and further define the instability.

7.2 Experimental Investigation of Measured Disturbance

7.2.1 Instability is not Measured by Surface Sensor that is Isolated from the Flow

The original 30-degree cone-ogive-cylinder has three surface sensors at 0.61 meters. The two outside sensors are azimuthally-displaced from the center sensor by 6 degrees. When all of the sensors are fully exposed to the flow, measurements from each sensor have a similar power spectra. The spectra from one of these measurements is shown in Figure 7.1. The spectra come from 0.5-second sample of Kulite pressure measurements make a 1 MHz and averaged using Blackman windows as discussed in Section 4.4.6. Each sensor measures a clear disturbance with multiple peaks between 20 and 40 kHz. The peaks in the spectra of each sensor are at the same frequencies.

Cross-correlations between the azimuthally-displaced sensors also show that all three sensors are measuring the same instability. The coherence between these sensors are shown in Figure 7.2. It shows coherence values greater than 0.5 for all frequencies between 20 and 40 kHz, with several peaks over 0.9.

To verify that the measured disturbance was not due to model vibrations or electronic interference, individual sensors were isolated during measurements. To do this, one of the three sensors at 0.61 meters was isolated from the flow by covering it with

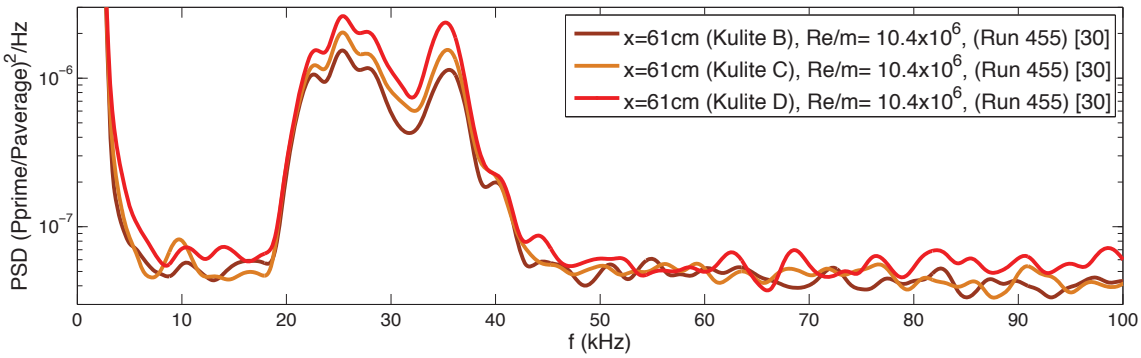

Fig. 7.1. Power spectra showing disturbances measured on each of the sensors at x=0.61 meters.

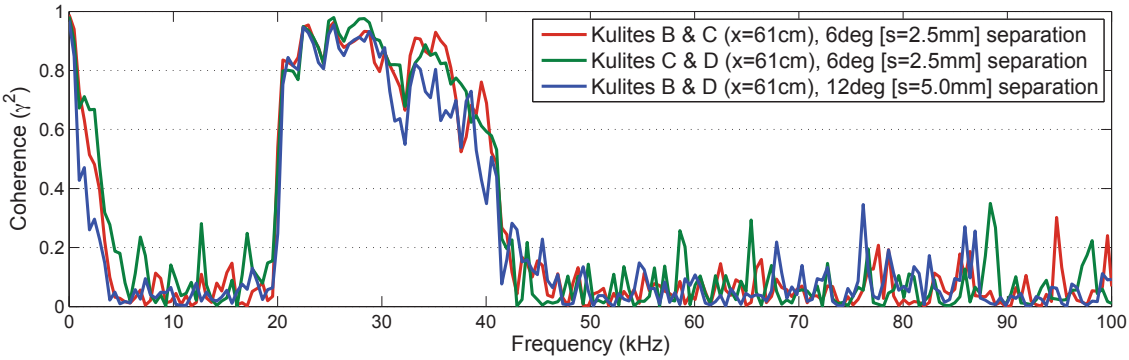

Fig. 7.2. Coherence between azimuthally-displaced surface Kulites at x=61cm (original 30-degree cone-ogive-cylinder, Run 455).

tape. The tape covering one sensor, as well as three of the sensors not covered, are shown in Figure 7.3.

Spectra for each of the sensors, with one sensor isolated from the flow, are shown in Figure 7.4. The spectra for the covered sensor is shown by the dashed red line and does not show the disturbance. At the same time, spectra for the two uncovered sensors clearly show the disturbance with distinct peaks between 20 and 40 kHz. To ensure that this difference in power spectra could not be attributed to the measurements of a specific sensor, the experiment was repeated with a different sensor covered. The repeat measurements yielded similar results, indicating that the measured disturbance is not due to model vibrations or electrical noise.

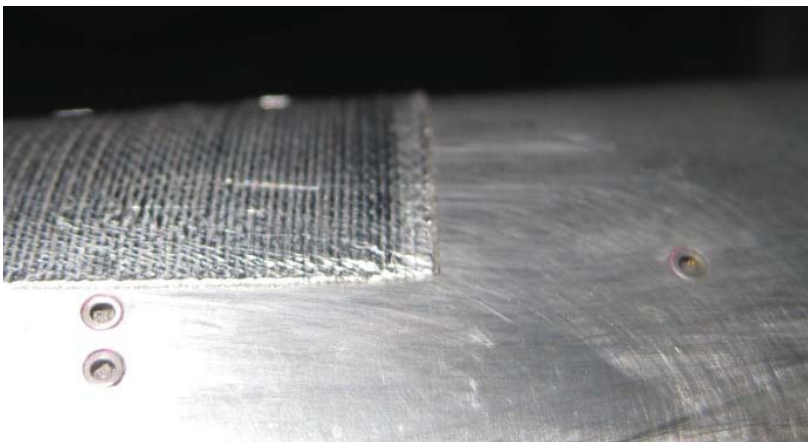

Fig. 7.3. Tape covering one of the sensors on the cone-ogive-cylinder (flow is right to left).

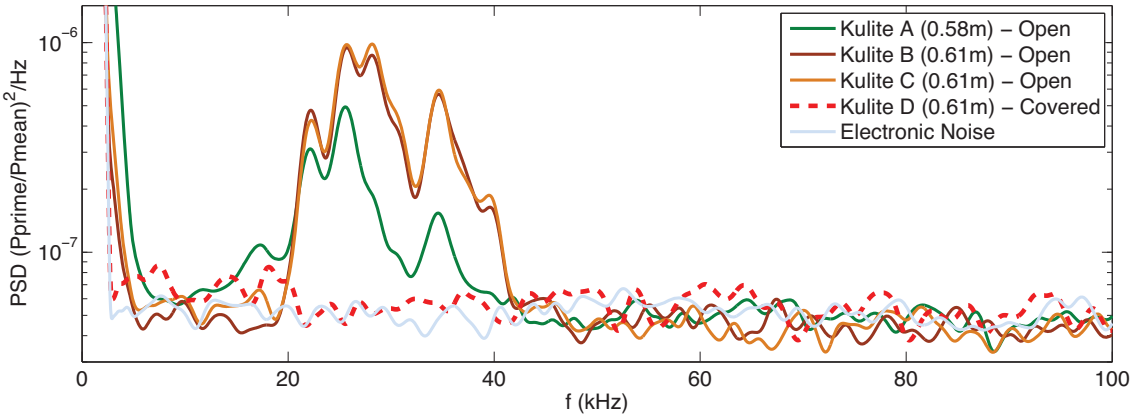

Fig. 7.4. Power spectra showing disturbances with one sensor (Kulite D) isolated from the flow (Run 459).

7.2.2 Boundary-Layer Disruptions do not change Measured Instability

The next set of experiments were designed to determine if the measured disturbance was inside of the boundary layer. An instability inside the boundary layer would be expected to change as a result of disruptions of the boundary layer. On the other hand, if boundary-layer disruptions have little or no effect on the measured disturbance, it can be assumed that the source of the disturbance is outside

the boundary layer. Surface sensor measurements were made with different sizes of disruptions placed just before the array of 3 pressure sensors at 0.61 meters. Figure 7.5 shows pictures of the disruptions with heights of 1 and 4 millimeters. These disruption heights are approximately 20 and 80% of the predicted boundary-layer thickness.

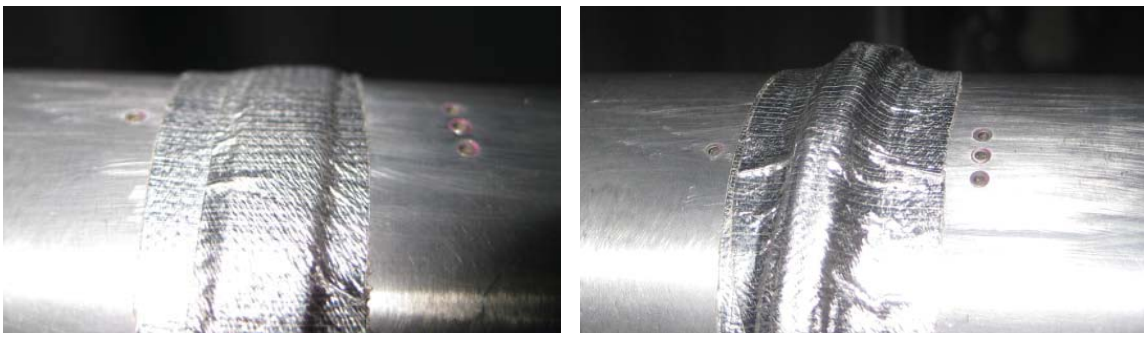

(a) Disruption with height of 1 millimeter. (b) Disruption with height of 4 millimeters.

Fig. 7.5. Two boundary-layer disruptions on the cone-ogive-cylinder at 0.6 meters.

The power spectra from measurements taken when the 4-mm disruption was in place are shown in Figure 7.6. The solid lines show spectra from measurements at 0.58 and 0.61 meters with the disruption. The dash-dot lines show spectra from measurements at the same locations with no disruption. There is no significant change in the measured disturbance due to the 4-millimeter disruption.

There was also no change in the spectra when smaller disruptions were placed on the model. The measured disturbance was insensitive to blockages of up to 80% of the boundary-layer thickness. This was taken as an indication that the disturbance was not inside the boundary layer at the measured location.

7.2.3 Frequency of Measured Instability does not change with Reynolds Number

Another indication that the measured disturbance does not originate in the boundary layer was discussed in Section 6.2.5. It presented power spectra from surface

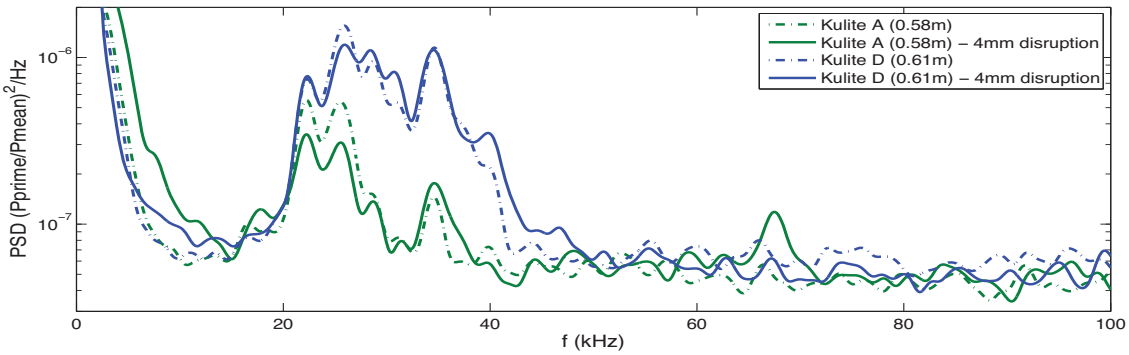

Fig. 7.6. Power spectra from measurements at 0.58 and 0.61 meters with and without the 4 mm disruption at 0.6 meters.

measurements at 0.58 and 0.61 meters over a range of stagnation pressures. The spectra showed the magnitude of the disturbance increase with increasing Reynolds number, but the frequencies of the peaks remain constant. This is not characteristic of boundary-layer instabilities whose frequencies are highly dependent on the Reynolds number. This dependence is because the Reynolds number directly affects the thickness of the boundary layer.

In order to determine if the peaks in the measured disturbance change frequency as they progress downstream, surface measurements were made at axial locations ranging from 0.58 to 0.91 meters on the original 30-degree cone-ogive-cylinder. The power spectra from these measurements over a range of stagnation pressures are shown in Figure 7.7. Labels are included to show the measurement location for each power spectra shown. At each measured location, there are distinct spectral peaks at about 26 and 35 kHz. Two vertical grey lines are superimposed on the spectra to show those two peaks at each axial location. The frequency is the same at each location even though the magnitudes of the individual peaks change. This insensitivity to Reynolds number was taken as another indication that the measured disturbance was not a boundary-layer instability.

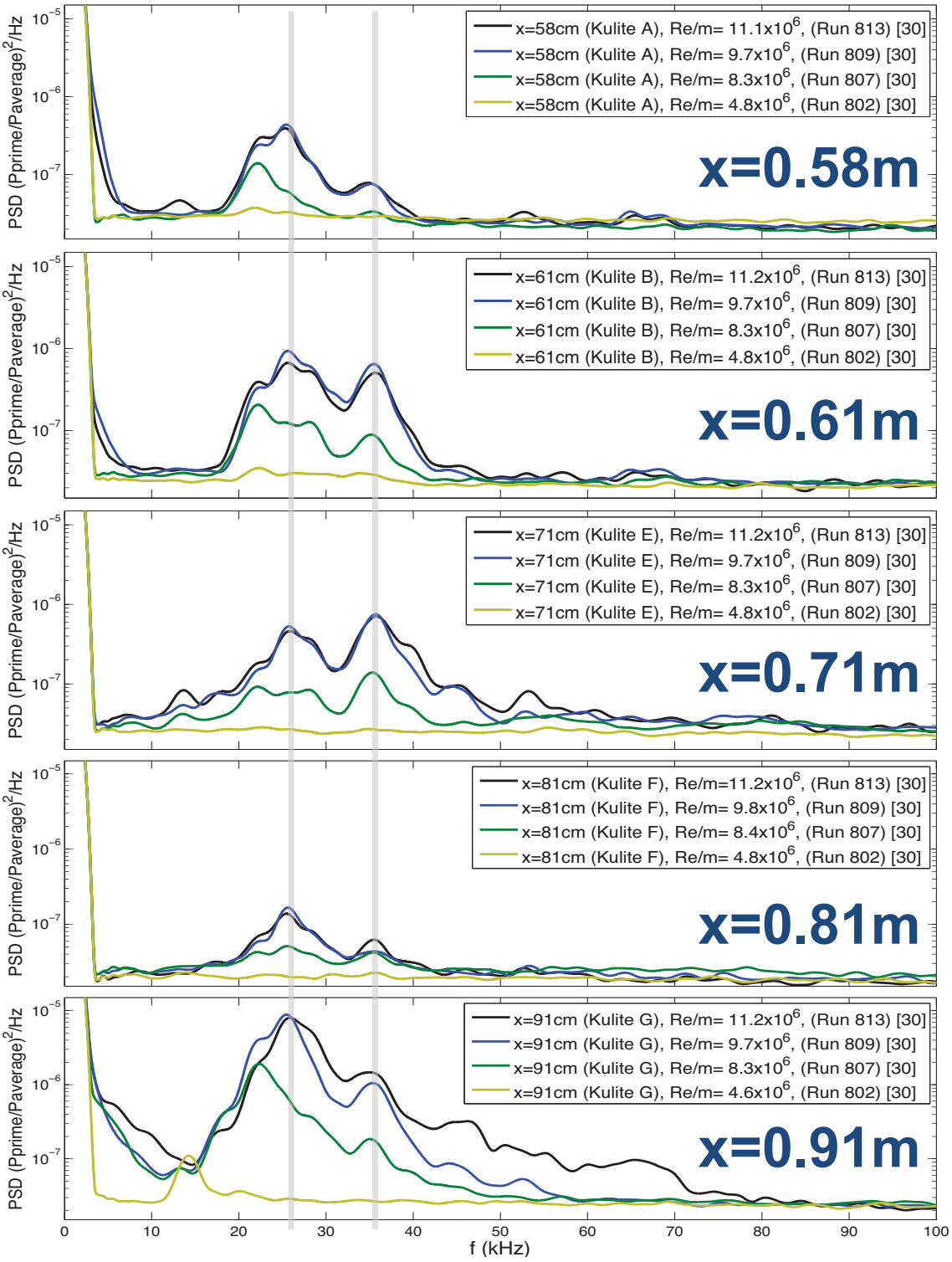

Fig. 7.7. Power spectra from measurements at several axial locations on the 30-degree cone-ogive-cylinder. The grey lines highlight two of the frequencies that have distinct peaks at each of the locations.

7.2.4 Decrease in Instability Magnitude may be a Result of the Entropy-Layer Swallowing Process

A qualitative analysis of Figure 7.7 also shows a decrease in the magnitude of the spectral peaks after an initial period of growth. This decrease is indicative of a disturbance stabilization and is inconsistent with the boundary-layer stability calculations. Between the first two measurement locations (58 and 61 cm), the disturbance magnitude increases. The next two locations (71 and 81 cm) show the magnitude level out and then decrease significantly. The disturbance then grows substantially before being measured at the last sensor at 91 cm.

The longitudinal growth and decay of the fluctuations can also be shown by comparing the RMS at each axial location. The RMS amplitudes were calculated by integrating the spectra over the frequency range between 10 and 50 kHz. Figure 7.8 shows the calculated RMS amplitudes for measurements made on the surface of the 30-degree geometry during four different entries. The stagnation pressure at the start of each of the runs was between 145 and 150 psia. Entries 4 and 8 used the original 30-degree cone-ogive-cylinder model that had a total length of 1 meter. In Entries 12 and 17, the new model cone-ogive-cylinder model was used with the same 30-degree nosetip. The RMS calculated during each of these entries show a similar magnitude for each downstream position.

The highest-magnitude RMS value is at 0.91 meters and and was only measured during Entry 8. There was no sensor at that location during Entry 4 and the new model configuration only has sensor ports up to 0.86 meters. To increase confidence that it is not an outlier, the RMS was calculated at similar Reynolds numbers during four different runs in Entry 8. Table 7.1 compares the calculated RMS amplitudes with Reynolds number. It shows that the RMS amplitude increases rapidly as the Reynolds number increases above $9 * 10^6$. So although the data point at 0.91 meters appears to be an outlier, the data is repeatable.

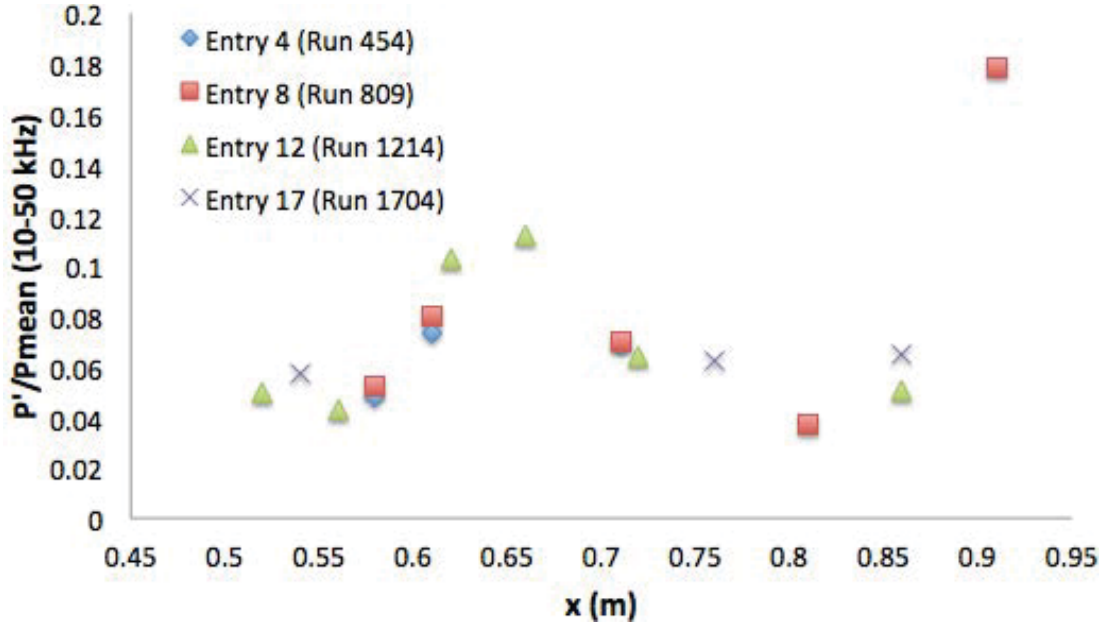

Fig. 7.8. Calculated RMS amplitude vs axial location on the 30-degree cone-ogive-cylinder [data taken from runs 454, 809, 1214, and 1704 with Re/m= $9.3 * 10^6, 9.2 * 10^6, 9.1 * 10^6$, and $8.4 * 10^6$ respectively].

Table 7.1
Variation in RMS during Entry 8 on the original cone-ogive-cylinder at 0.91 meters.

Reynolds Number ($\frac{1}{m}$)	RMS ($\frac{P'}{P_{mean}}$)	Run
$8.7 * 10^6$	0.093	822
$8.8 * 10^6$	0.114	822
$9.0 * 10^6$	0.109	810
$9.1 * 10^6$	0.161	809
$9.3 * 10^6$	0.155	810
$9.5 * 10^6$	0.238	809
$10.2 * 10^6$	0.204	823

It is possible that this trend of an initial growth, followed by a magnitude decrease, and finally rapid growth is an entropy-layer swallowing effect. The stabilizing effect

of the entropy-layer being swallowed by the boundary layer is described by Stetson in Reference [49] as well as Reshotko and Khan in Reference [56].

7.2.5 Surface Measurements are Repeatable

Measurements of the disturbance using surface sensors are very repeatable. One example of this repeatability is shown in Figure 7.9. The black line shows the power spectra from measurements at 0.56 meters on the 30-degree cone-ogive-cylinder that were made in October of 2013. The blue and orange lines show spectra from two different measurements in May of 2014. They all show peaks between 15 and 40 kHz and for each measurement the highest peaks were at about 22 and 25 kHz. The relative magnitude of these peaks change only slightly between runs.

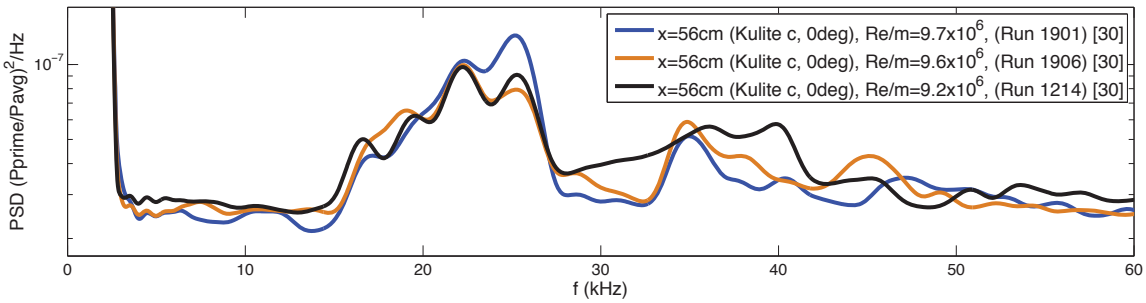

Fig. 7.9. Comparison of spectra from surface measurements on the 30-degree cone-ogive-cylinder at x=56cm.

Another example of the repeatability of the surface measurements is shown in Figure 7.10. The black line shows the power spectra from measurements at an axial location of 0.58 meters on the original cone-ogive-cylinder in November 2012. The blue line shows power spectra from measurements in May 2013. These measurements were also made at 0.58 meters using the original cone-ogive-cylinder model. The green line shows the power spectra from measurements made on the other 30-degree cone-ogive-cylinder. These measurements were made in October 2013 and at an axial

location of 0.56 meters. The power spectra from each of these measurements show peaks between 15 and 40 kHz with slight variability between the different runs.

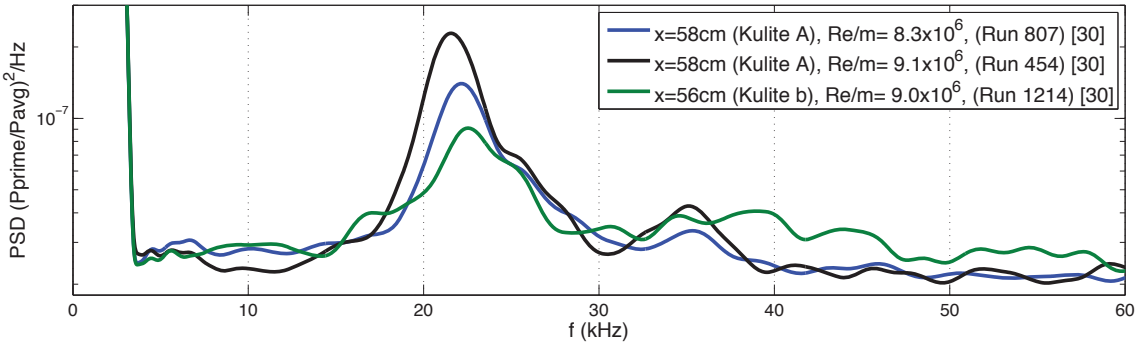

Fig. 7.10. Comparison of spectra from surface measurements on both 30-degree cone-ogive-cylinder models at similar axial locations.

7.2.6 TSP Measurements for the 30-degree Cone-Ogive-Cylinder

Due to the length of the cone-ogive-cylinder, it was expected that the oblique shock from the leading edge of the model would reflect off the test section walls and could impinge upon the model at some point. Letterman had performed measurements on a similar ogive cylinder and was able to measure the location of the reflected shock on her model using temperature-sensitive paint (TSP) in noisy flow [95]. Because of the uncertainty of the location of this reflected shock on the long cone-ogive-cylinder, and the effect it may have on the instabilities, the 30-degree model was painted with temperature-sensitive paint and tested in the BAM6QT under a wide range of both noisy and quiet flow conditions to determine the location of the reflected shock.

The reflected shock showed up very clearly in the noisy-flow TSP results. It impinged upon the 30-degree model between about 0.66 and 0.68 meters from the leading-edge. The TSP results for the noisy flow shock are shown in Figure 7.11.

Under quiet flow conditions, a reflected shock location is not evident. An abrupt temperature rise does not appear at any point on the model. There is a temperature increase at a distance of about 0.85 meters from the leading-edge that is shown in

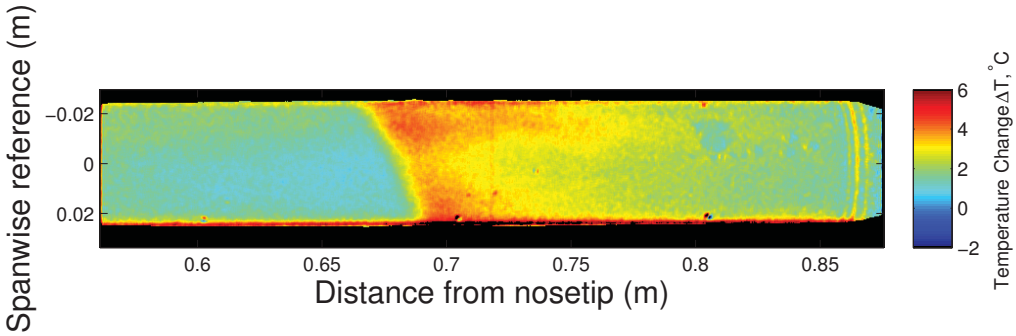

Fig. 7.11. TSP clearly showing the location of the reflected shock under noisy flow (30-degree cone-ogive-cylinder, Run 418).

Figure 7.12. However, there is no clearly-defined line as would be expected from a shock and the temperature increase is much less than that which was measured under noisy flow.

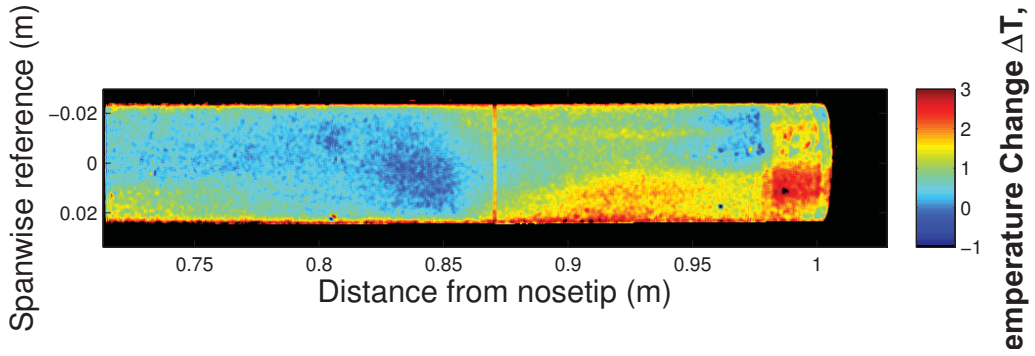

Fig. 7.12. TSP on the 30-degree cone-ogive-cylinder under quiet flow (Run 412).

If the reflected shock impinges on the model in quiet flow, it does not appear to happen before the temperature rise at 0.86 meters. If that temperature rise is a result of the reflected shock, that is another possible explanation for the sudden rise in RMS from the sensor measurements at 0.91 meters. However, it does not account for the decrease in the disturbance magnitude measured at the earlier locations.

7.2.7 Higher-Angle Nosetips also show a Decrease in Instability Magnitude

The decrease in disturbance magnitude discussed in Section 7.2.4 is not unique to the 30-degree model. RMS calculations from measurements on each of the configurations show the measured disturbances increase, decrease, then increase again. Figure 7.13 plots the RMS amplitude against the axial location for the 30 to 35-degree configurations.

At the first and last measured locations (0.52 and 0.86 meters) the RMS value correlates fairly well with the nosetip angle. The 35-degree nosetip has the highest RMS values at those locations. Between those two sensors, the RMS values do

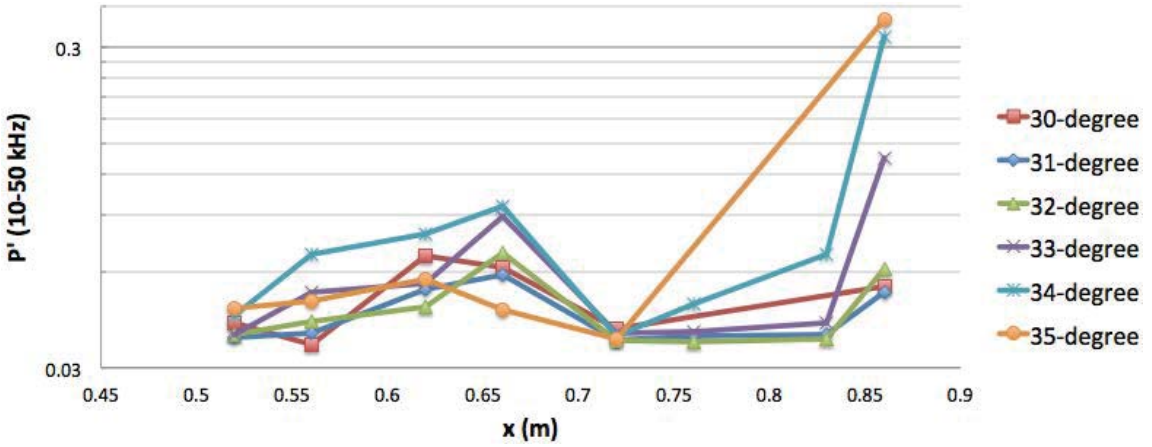

Fig. 7.13. Comparison of the calculated RMS amplitude vs axial location for each of the cone-ogive-cylinder configurations [data taken from runs 1213, 1522, 1516, 1510, 1503 and 1219 with Re/m= $7.4 * 10^6, 7.8 * 10^6, 7.7 * 10^6, 7.6 * 10^6, 7.7 * 10^6$, and $6.8 * 10^6$ respectively].

not correlate well with the nosetip angle. However, Figure 7.13 does show that the measured disturbance on each of the cone-ogive-cylinder configurations decreases in amplitude at some location after x=0.6 meters. One possible explanation for this decrease is the stabilization that occurs when the entropy layer is swallowed. Since each nosetip creates a different entropy layer, each swallowing location would be different. This would result in stabilization at different axial locations for each of the configurations. The current data set is too small to verify this theory. Additional surface sensors would be required to better see the axial location at which stabilization and the subsequent growth occurs for each nosetip configuration.

7.2.8 Measured Instability is Affected by Nosetip Angle

Different nosetip geometries were used to induce a change in the entropy layer. If the measured disturbance is an entropy-layer instability, a change in the entropy layer should also affect the disturbance properties. Measurements were made over a range of pressures using the 30 to 35-degree nosetips. The power spectra from measurements taken at 0.52 meters are shown in Figure 7.14 with labels added showing the nosetip

angle for each set of spectra. For each nosetip, the spectra show at least two distinct peaks. Lines have been added to the figure in an attempt to show how the frequency of these peaks change with nosetip angle.

A solid grey line connects the higher-frequency peak for each nosetip. There appears to be a nearly-linear relationship between the frequency and the nosetip angle. On the 30-degree model, the higher-frequency peak has a frequency around 43 kHz, but this frequency decreases to about 34 kHz for the 35-degree model. The lower-frequency peaks for each nosetip are connected by a red dashed line. From 30 to 32-degrees, there again appears to be a linear decrease in frequency with increasing nosetip angle. However, as the nosetip angle increases to 35 degrees, the frequency remains approximately the same at around 16 kHz.

There are other peaks in the spectra for each of the nosetips. One of the characteristics of the measured disturbance is to have several peaks within a band of frequencies. This can make it difficult to compare spectra from different nosetips. For example, the 34-degree nosetip has peaks between 20 and 30 kHz that are greater in magnitude than the peaks used for comparison with the other nosetips. It is also difficult to see a pattern in the disturbance magnitude as the nosetip angle changes. However, the comparison does show that the measured disturbance is highly sensitive to a change in nosetip angle. This supports the idea that the surface sensors could be measuring an entropy-layer instability.

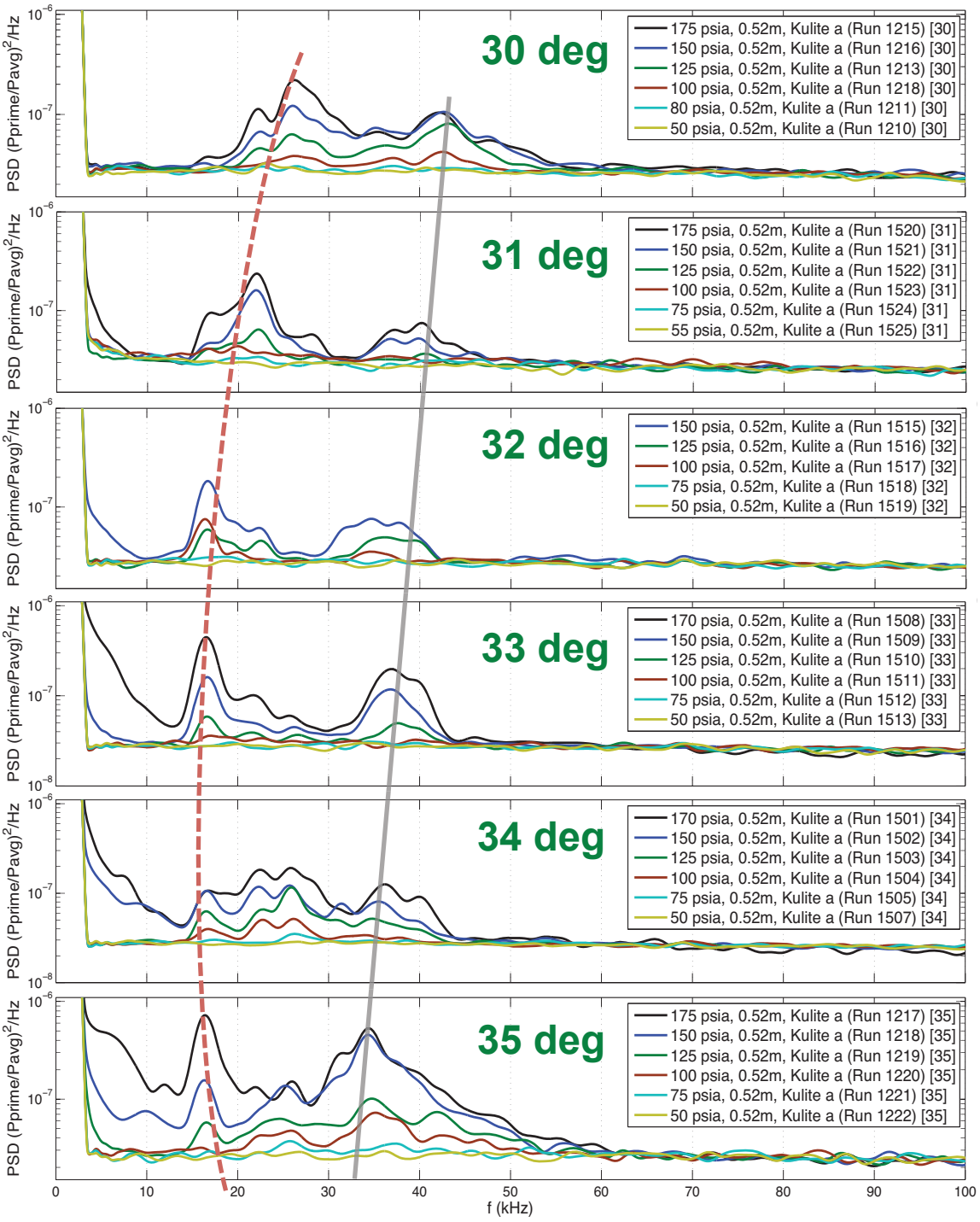

Fig. 7.14. Power spectra of surface measurements at 0.52 meters for the 30 to 35-degree cone-ogive-cylinder configurations.

7.2.9 Off-Surface Measurements show that the Measured Instability Originates Outside of the Boundary Layer

Off-surface measurements were required in order to determine if the disturbance measured with surface sensors originated outside of the boundary layer. The first off-surface measurements were made using a pitot Kulite probe. The power spectra from these measurements are shown in Section 9.3. They showed what appeared to be a disturbance outside the boundary layer. Hot-wire anemometry was then used in order to get more definitive measurements than the bulky pitot probe could provide. Clear measurements of the disturbance were important to determine its characteristics in order to compare with future calculations.

Figure 7.15 shows an image of the digital oscilloscope screen after a typical hot-wire measurement. The blue line in the figure shows the distance of the hot wire from the model surface. In most runs, including the one shown here, the hot wire started the run about 0.3 millimeters from the model surface. This close proximity reduced the risk of breakage during tunnel startup and shutdown. The traverse system was triggered with the startup of the tunnel, at which point the traverse commenced moving the hot wire in set increments from the model surface.

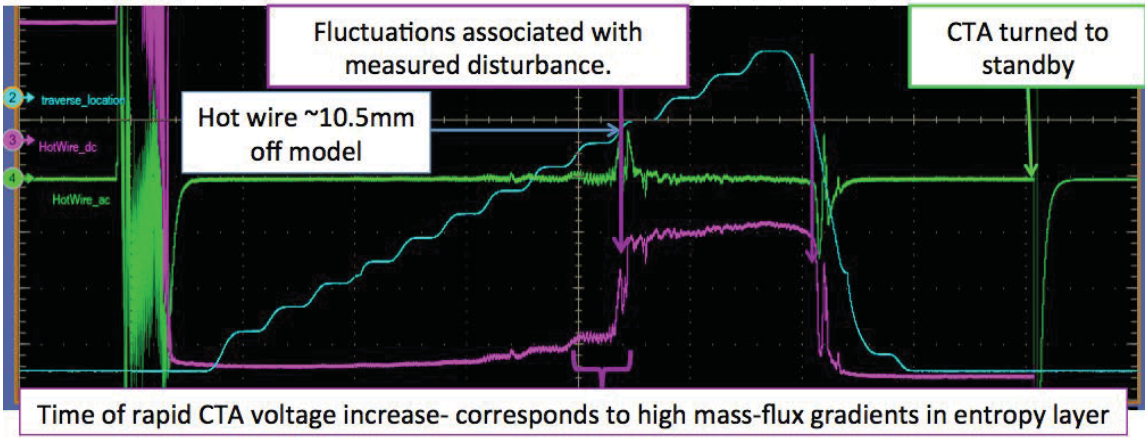

Fig. 7.15. Image of hot-wire voltage traces on the digital oscilloscope screen after measurements over the 30-degree cone-ogive-cylinder at x=0.52 meters (Run 1435, P_0=120psia).

The green and purple lines in Figure 7.15 are the hot-wire ac and dc voltage traces respectively. The dc trace (purple line) in this image provides a visual understanding of the increase in mass flux as the hot wire crosses the entropy layer. Near the center of the screen, as the hot-wire probe is about 10 millimeters off the model surface, there is an rapid increase in the voltage measured by the CTA. This increase corresponds to high mass-flux gradients in what appears to be the entropy layer. It is also at this location, just past the center of the screen, that the hot wire measures the fluctuations that show the measured disturbance. About a second later the hot wire probe is moved back towards the model surface and the decrease in mass flux and instability fluctuations are momentarily visible as the probe passes this same vertical location.

The hot wire signal drops off the screen after the hot wire is back near the model surface and tunnel shutdown is about to start. The signal drops off because the CTA was physically switched to standby mode after the measurements were taken. This was done to increase the likelihood of the hot wire surviving the tunnel shutdown process.

The hot wire was above the 30-degree cone-ogive-cylinder at an axial location of 0.52 meters during the run from which these oscilloscope traces were collected. The power spectra obtained from the hot-wire measurements at several vertical locations are shown in Figure 7.16. The spectra from hot-wire measurements has a different shape at the lower frequencies than was the case for the Kulite measurements. The dotted black line in Figure 7.16 shows the power spectra from hot-wire measurements made just prior to starting the tunnel to capture any electronic noise that may be present. It shows the general shape of the hot-wire spectra. Between the frequencies of about 5 and 15 kHz, it has a very low noise floor. This floor then increases gradually until about 50 kHz after which frequency it remains fairly constant. Spectra from measurements during tunnel operation are shown by the solid colored lines. They also show a dip at the lower frequencies. They then rise and become fairly constant after 30 kHz. The dashed green line is the power spectra obtained from surface

measurements at the same axial location. It has been offset to allow comparison with the hot-wire spectra.

Each of the solid colored lines in Figure 7.16 shows the power spectra from measurements at a different vertical location. The first four spectra from measurements ranging from 4 to 10 millimeters off the model surface have a similar shape. Spectra from the measurement made at 10.5 millimeters are shown by the red line. It has several small peaks between 20 and 35 kHz. The spectra at 11 millimeters are shown by the light blue line and also show some smaller peaks. Spectra from measurements above 11 millimeters no longer show these peaks. For the measurement at 14 millimeters, shown by the grey line, the noise floor between 15 and 30 kHz gets a little closer to that shown by the electronic noise measurement.

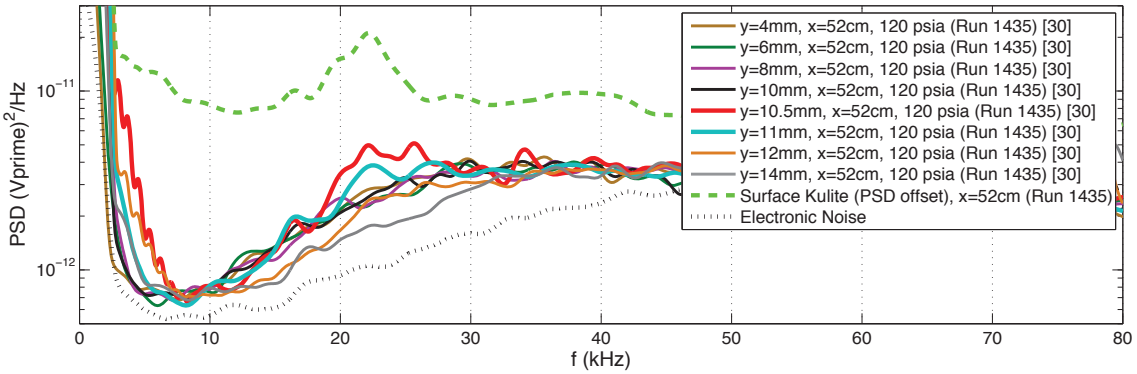

Fig. 7.16. Power spectra from hot-wire measurements above the 30-degree model at x=0.52m, P_0=120psia.

It should be noted that in this run, the hot wire was never stopped at a distance of 10.5 millimeters above the surface. The power spectra shown are from measurements taken while the hot wire was moving vertically from 10 to 11 millimeters. These initial hot-wire measurements showed the small vertical extent of the measured disturbance and most later measurements were made at 0.5 millimeter increments.

Although the surface and hot-wire spectral peaks in Figure 7.16 do not line up exactly, they are both in approximately the same frequency range. The peaks are

also very small, but there seems to be a distinctly-measured disturbance at a specific distance from the model that is well outside the boundary layer.

7.2.10 Measured Instability Grows and Approaches Model Downstream

The power spectra from hot-wire measurements over the 30-degree model at 0.52 meters show only small spectral peaks for the measurements made 10.5 millimeters above the model surface (Figure 7.16). Hot-wire measurements were also made at several downstream axial locations above the 30-degree model. At each location, the hot wire was moved vertically during the run to make measurements at various distances from the model. These measurements are shown in Figure 7.17. The black dotted lines in each of the spectral plots show the power spectra from measurements just before tunnel operation.

The power spectra from measurements at 0.54 meters is shown in Figure 7.17(a). The orange line shows spectra from measurements made 11 millimeters above the model surface. The peaks are much more pronounced than those seen at 0.52 meters. The spectra also show the small vertical extent of the disturbance. The red and blue spectral traces are from 10 and 12 millimeters off the model surface. Neither of those traces show significant peaks. However, when the hot wire is 11 millimeters off the surface, the spectral peaks become very clear.

Further downstream the hot-wire measurements show the disturbance get closer to the model surface. At 0.59 meters, spectra from measurements 8 and 8.5 millimeters off the model surface are shown by the purple and blue lines in Figure 7.17(b). They both show large peaks in the spectra between 15 and 40 kHz. Measurements made at a height of 7.5 and 9 millimeters have much smaller peaks in their spectra. None of the other measurements have any distinguisable peaks.

The power spectra from hot-wire measurements made at 62 cm are shown in Figure 7.17(c). The measured disturbance shows up in peaks in the spectra between 15 and 40 kHz starting at a height of 5.5 millimeters as shown by the brown line. At

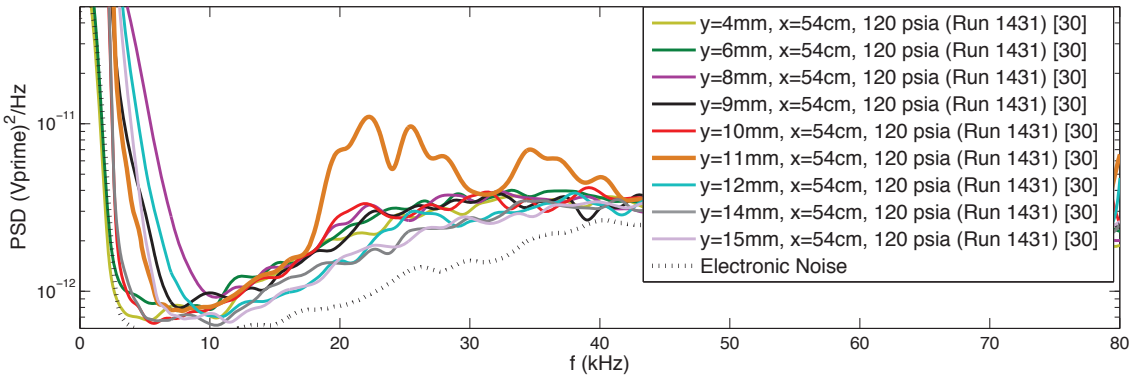

(a) Hot-wire PSD above the 30-degree model at x=0.54m, P_0=120psia.

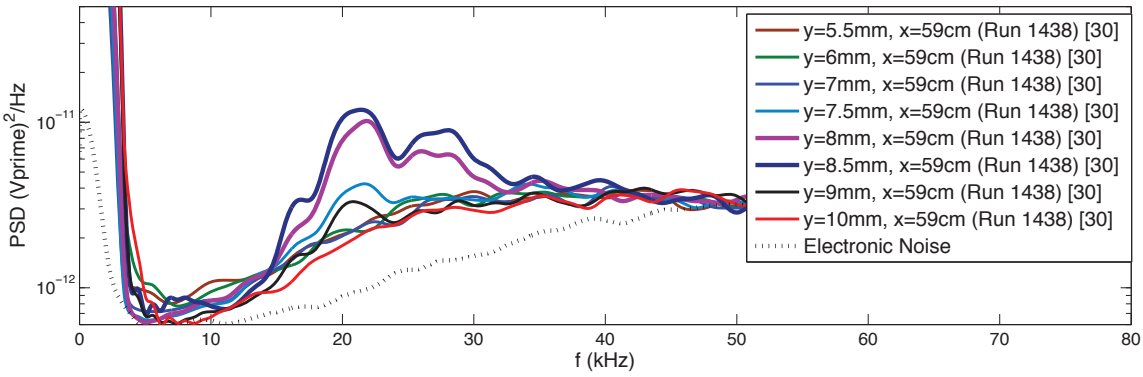

(b) Hot-wire PSD above the 30-degree model at x=0.59m, P_0=120psia.

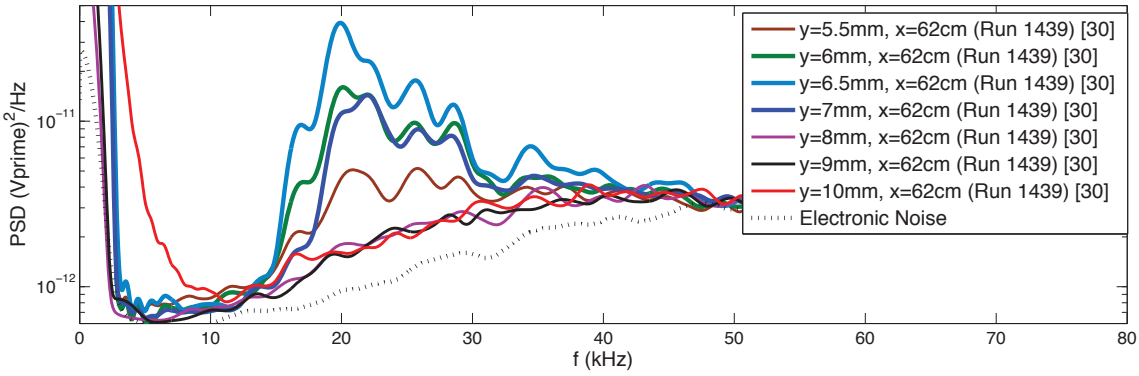

(c) Hot-wire PSD above the 30-degree model at x=0.62m, P_0=120psia.

Fig. 7.17. Power spectra from hot-wire measurements above the 30-degree cone-ogive-cylinder at several axial locations showing the instability approach the model as it proceeds downstream.

6 millimeters, the magnitude of the measured disturbance has increased significantly. The spectrum from the 6-mm measurement is shown by the green line. The light blue line shows the spectrum at 6.5 millimeters. That appears to be the locus of the measured disturbance since the spectral peaks are the highest at this location. At 7 millimeters (blue line) there are still large peaks in the spectra. However, at 8 millimeters above the model surface, there spectrum shows no indication of a disturbance.

With a locus at 6.5 millimeters off the 30-degree model at 0.62 meters, the disturbance measured is very close to the edge of the boundary-layer. At a stagnation pressure of 120 psia the predicted boundary-layer thickness is about 5.8 mm at this location. The measured disturbance is also much larger and closer to the surface than was measured at 0.52 meters. While there are still a lot of unknowns about the disturbance, the hot-wire measurements clearly show it increasing in magnitude and approaching the model as it proceeds downstream.

7.2.11 Instability Location is Affected by the Nosetip Angle

Section 7.2.8 showed how the angle of the nosetip affects the spectra of the surface measurements. The next two sections use spectra from hot-wire measurements made over other nosetip configurations to show the effect that the nosetip angle has on the location of the disturbance with respect to the model.

Spectra from the hot-wire measurements made over the 33-degree model at various axial locations are shown in Figures 7.18 and 7.19. The power spectra of the measurements at 0.49 meters are shown in Figure 7.18(a). None of the spectra show indications of a disturbance except for when the hot wire was 11.5 millimeters off the model surface. That is shown by the small peaks between 15 and 40 kHz on the green line.

As with the 30-degree model, the disturbance grows in magnitude and approaches the model as it progresses downstream. At 0.54 meters, the greatest disturbance

magnitude is measured 7 millimeters off the model surface. The spectrum for that measurement is shown by the black line in Figure 7.18(b). There are also smaller peaks in the spectra at 6.5 and 8 millimeters as shown by the purple and red lines. The individual peaks measured at 0.54 meters are easier to identify than the 0.49 meter measurements. They are at approximately 16, 25, and 35 kHz.

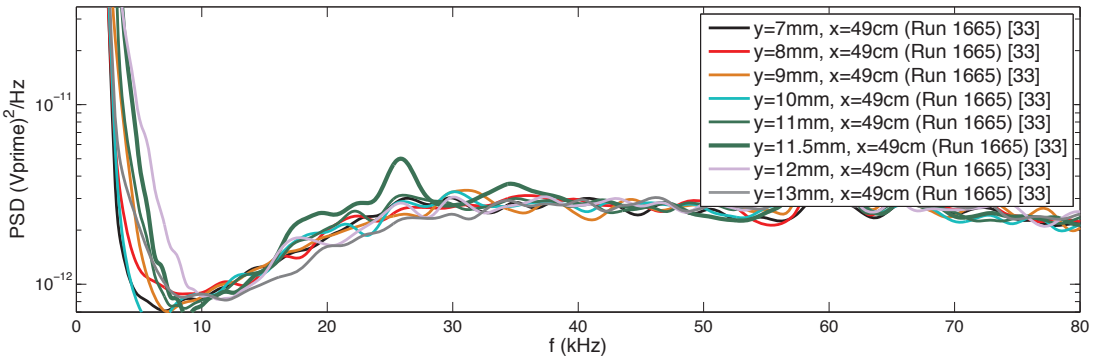

(a) Hot-wire PSD above the 33-degree model at x=0.49m, P_0=120psia.

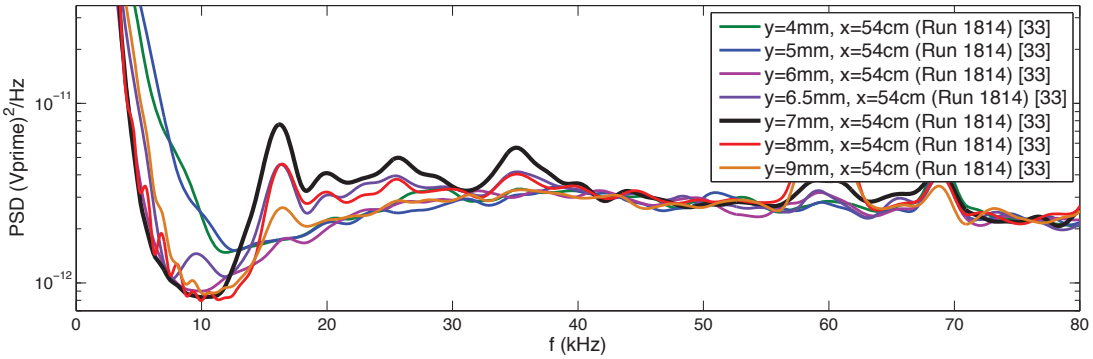

(b) Hot-wire PSD above the 33-degree model at x=0.54m, P_0=120psia.

Fig. 7.18. Power spectra from hot-wire measurements above the 33-degree cone-ogive-cylinder at two axial locations after the entropy-layer instability starts to become visually distinguishable in the power spectra.

The spectra in Figure 7.19(a) are from measurements made at 0.56 meters. They show that the disturbance magnitude is greatest 5.5 millimeters from the model surface, which is just inside the predicted edge of the boundary layer. The dark blue line shows a band of frequencies between 15 and 40 kHz that shows up at 5.5 millimeters.

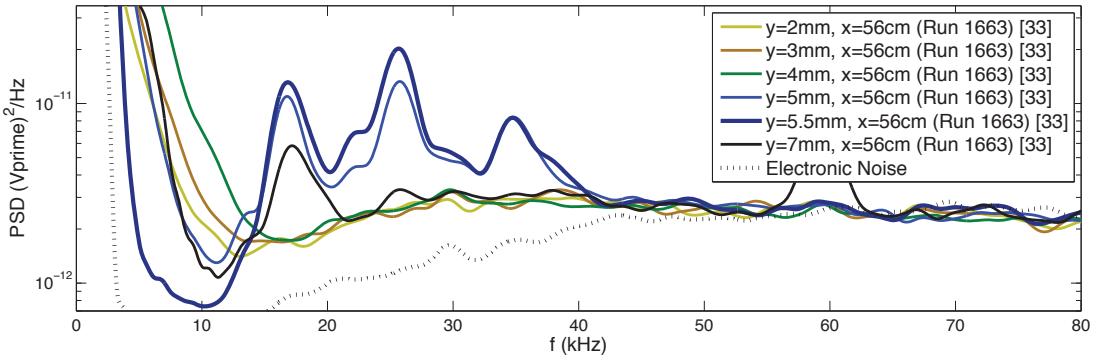

(a) Hot-wire PSD above the 33-degree model at x=0.56m, P_0=120psia.

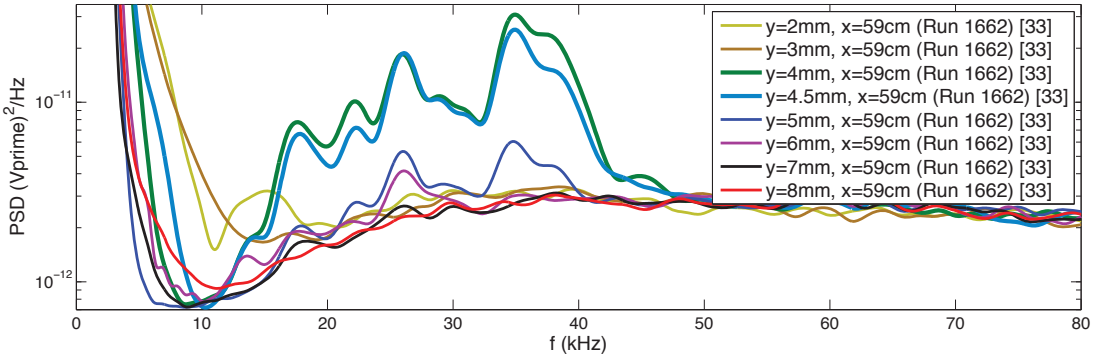

(b) Hot-wire PSD above the 33-degree model at x=0.59m, P_0=120psia.

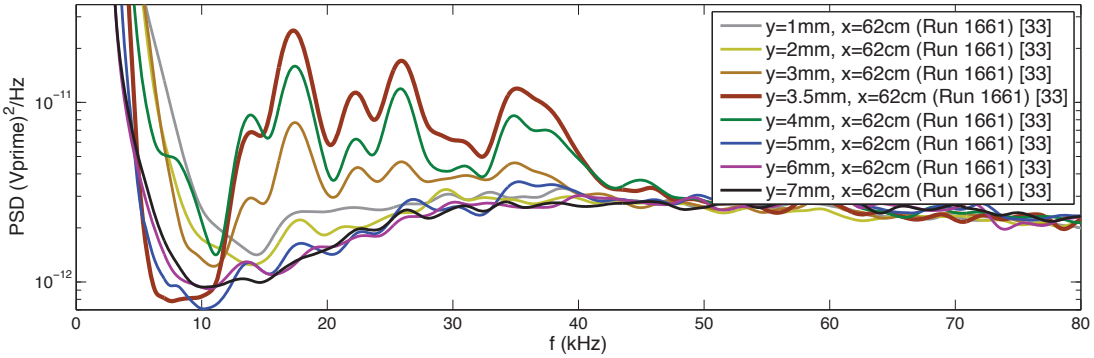

(c) Hot-wire PSD above the 33-degree model at x=0.62m, P_0=120psia.

Fig. 7.19. Power spectra from hot-wire measurements above the 33-degree cone-ogive-cylinder at several axial locations showing the instability enter the boundary layer above the model as it proceeds downstream.

The largest of these spectral peaks are at about 16, 25, and 35 kHz. There are also large peaks at those same frequencies in the spectra from measurements 5 millimeters off the surface. These are shown by the blue line. At 7 millimeters (black line), there is a peak at about 16 kHz and a very small peak at 25 kHz. None of the other measurements show any indication of the disturbance.

Spectra from measurements at 0.59 meters are shown in Figure 7.19(b). The green and light blue lines show spectra from measurements at a height of 4 and 4.5 millimeters respectively where the disturbance has the greatest magnitude. They show large peaks at the same frequencies measured at 0.56 meters. However, the relative magnitude of these peaks has changed from what was measured at 0.56 meters (Figure 7.19(a)). The 16-kHz peak has decreased slightly, the 25-kHz peak has approximately the same magnitude, and the magnitude of the 35-kHz peak has increased substantially.

Figure 7.19(c) shows spectra from measurements above the 33-degree model at 0.62 meters. The brown line shows the spectrum with the largest peaks. The hot wire was just 3.5 millimeters above the model surface for these measurements. The yellow and green lines are from measurements at 3 and 4 millimeters respectively. They both show spectral peaks that identify the disturbance. However, the measurements at 2 and 5 millimeters show few significant peaks in their spectra. While the largest spectral peaks are at about the same frequencies as those for the 0.59 meter measurements, the relative magnitude has changed again. This time the 16 kHz frequency has increased significantly and the 35-kHz peak has decreased in magnitude. The reasons for these shifts in relative magnitude are not completely understood, but they may be a result of the disturbance entering the boundary layer.

7.2.12 Summary of Measured Instability Locations using each Nosetip

The preceding two sections show disturbance measurements above the 30 and 33-degree cone-ogive-cylinders. The power spectra for each show that the disturbance

is measurable only at a certain height above the model at each axial location. They also show that the disturbance measured above the 33-degree cone-ogive-cylinder is closer to the surface than the disturbance measured above the 30-degree model.

Hot-wire measurements were also made over the other cone-ogive-cylinder configurations. Figure 7.20 summarizes the height at which the disturbance was measured above the model using each of the nosetips ranging from 30 to 35 degrees. The horizontal axis is the axial distance from the nosetip in meters and the vertical axis shows the disturbance height above the model in millimeters. The symbols mark where the disturbance was measured in relation to the model and lines were added to show the trends for each nosetip.

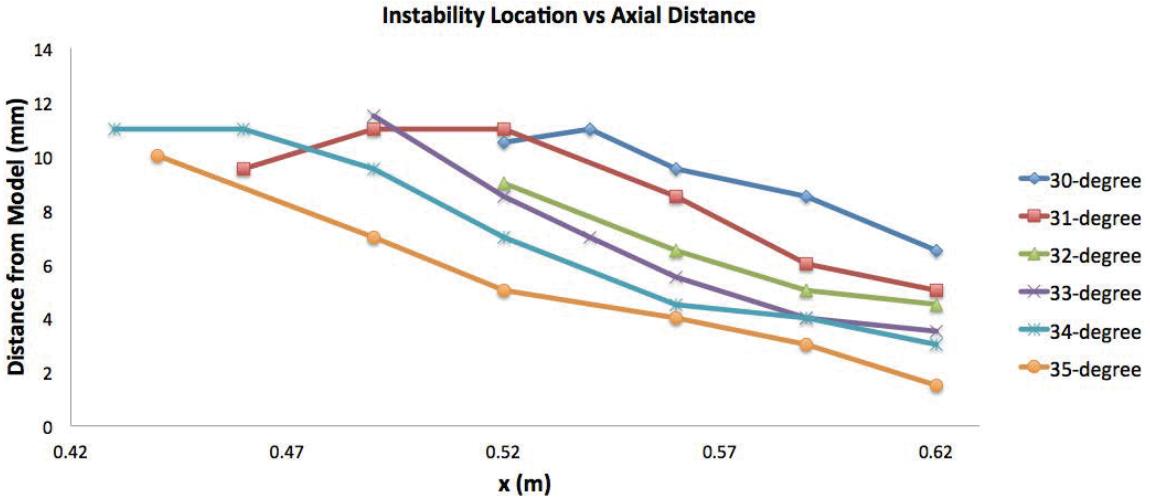

Fig. 7.20. Plot showing the locations of the maximum measured entropy-layer instability magnitude off the surface of each of the cone-ogive-cylinder configurations.

The blue diamonds show each location that the disturbance was measured over 30-degree model. Measurement were made of the disturbance at five axial locations from 0.52 to 0.62 meters. There is a small increase in the height above the model between the first two measured locations at 0.52 and 0.54 meters. However, each location after 0.54 meters shows the disturbance closer to the model than the previous. At 0.62 meters the disturbance is about 6.5 millimeters above the model.

The measured locations above the 31-degree model are shown by the red squares. The first measurement was made at 0.46 meters and showed the disturbance at a height of 9.5 millimeters. The next two measurements at 0.49 and 0.52 meters show the disturbance about 11 millimeters off the surface. All the measurements further downstream show the disturbance getting closer to the model until it is about 5 millimeters off the model surface at 0.62 meters.

The green triangles indicate the location of the measured disturbance above the 32-degree model. The disturbance was measured at four axial locations from 0.52 to 0.62 meters. The measurement at 0.52 meters shows the disturbance at a height of about 9 millimeters. At 0.62 meters the disturbance is about 4.5 millimeters above the surface.

This trend continues for each of the other nosetips. The purple and light blue symbols show the measured locations above the 33 and 34-degree models respectively. The disturbance was measured at six locations above the 33-degree model and at seven locations above the 34-degree model.

The orange circles show the disturbance height measured at six locations above the 35-degree model. The first measurement location was at 0.44 meters when the disturbance was about 10 millimeters above the surface. Each measurement downstream of that showed the disturbance getting closer to the model surface. At 0.62 meters, the locus of the disturbance was about 1.5 millimeters off the surface of the model.

The hot-wire measurements for each nosetip clearly show the disturbance approaching the model as it proceeds downstream. They also show that as the nosetip angle increases, the axial location at which the disturbance approaches the model decreases. This direct relation between the nosetip angle and the measured disturbance supports the idea that the disturbance may be a result of the entropy layer created by the nosetip.

7.2.13 Hot-Wire Instability Measurements are Repeatable

As with the surface measurements, the hot-wire measurements are also very repeatable. Most of the hot-wire measurements presented were made during four different tunnel entries. The location and relative magnitude of the disturbance measured between all of these entries were very consistent. Figure 7.21 shows spectra for hot-wire measurements above the 32-degree cone-ogive-cylinder at 0.62 meters. The solid lines show spectra from measurements taken in January 2014 and the dashed lines are from measurements made in March of the same year, both using the same calibrated hot wire. The green lines show spectra from the measurements when the hot wires were 4 millimeters above the model surface. In both cases there are spectral peaks at several frequencies between 15 and 45 kHz and the disturbance was measured most clearly at a height of 4 millimeters from the surface.

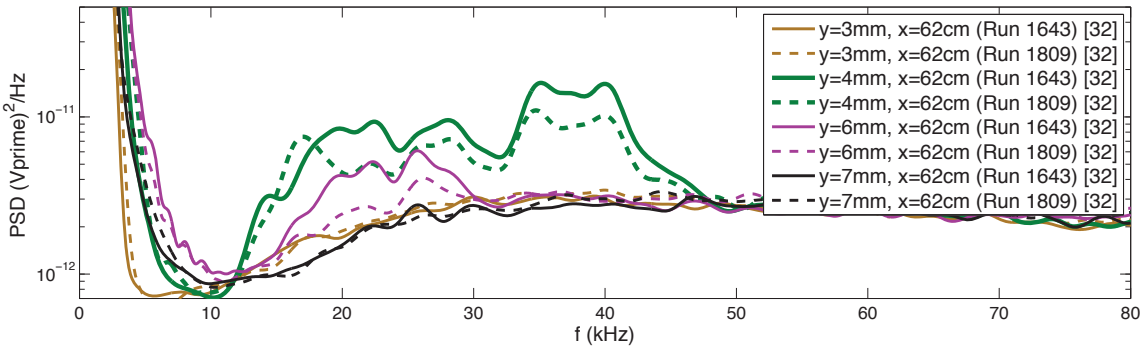

Fig. 7.21. Comparison of spectra from hot-wire measurements off the surface of the 32-degree cone-ogive-cylinder at x=62cm.

Another example of the measurement repeatability is shown in Figure 7.22. It shows spectra for hot-wire measurements above the 34-degree cone-ogive-cylinder at 0.56 meters. The solid lines are from hot-wire measurements made in March and the dashed lines are from January of 2014, using the same calibrated hot wire. The maximum disturbance was measured at 4.5 millimeters off the surface. It is very similar in both amplitude and frequency. The repeatability shown in these two examples is typical of the repeatability in all cases.

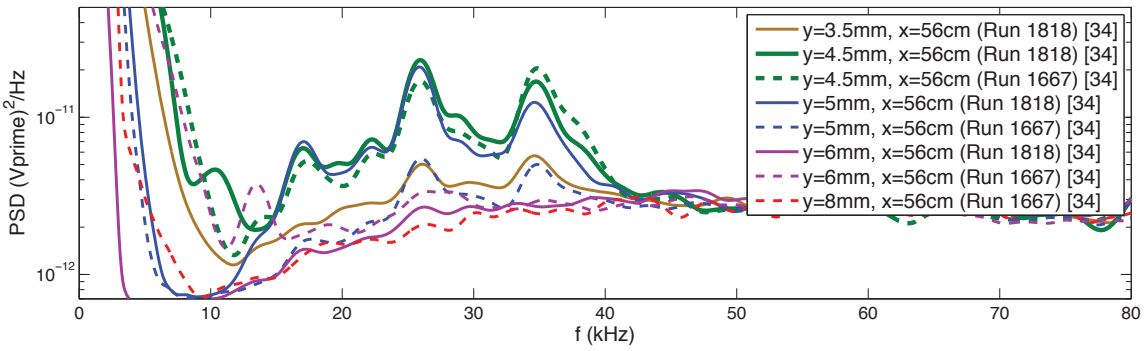

Fig. 7.22. Comparison of spectra from hot-wire measurements off the surface of the 34-degree cone-ogive-cylinder at x=56cm.

A majority of the surface and hot-wire measurements were taken before any angle of attack measurements were made. Therefore, no special care was taken to ensure that the model was at a consistent angle of attack. In spite of this, the spectra between these and other measurements compare very well and show good repeatability.

7.2.14 Cross-Correlations show that the Hot Wire and Surface Sensors are Measuring the same Instability

Cross-correlations between the signals measured by the hot wire and the surface Kulites show that the disturbance that is being measured off the model surface by the hot wire is the same one that is being measured at the model surface with the pressure sensor.

Figure 7.23(b) shows the coherence between the surface Kulite and the hot-wire measurements above the 30-degree model at 0.62 meters. The coherence is calculated for data obtained with the hot wire at several distances from the model surface, starting at 3 millimeters, and ending at 9 millimeters. The coherence peaks line up with the power spectra peaks shown in Figure 7.23(a).

At locations where the hot wire does not measure the disturbance, it shows very little coherence with the surface measurements. However, at those locations where the hot wire measures the instability, there is significant coherence between the surface and off-surface measurements. In this case, the hot wire is about 6 to 7 millimeters off the model surface when the coherence is the greatest.

Spectra from measurements above the 34-degree cone-ogive-cylinder are shown in Figure 7.24(a). The coherence between these and the surface measurements at 0.56 meters are shown in Figure 9.23(b). For the higher-frequency peaks at about 25 and 35 kHz, the coherence is greater between these measurements than that shown in Figure 7.23(b). This is likely due to the greater disturbance magnitude and closer proximity of the two sensors. However, the lower-frequency peak below 20 kHz shows

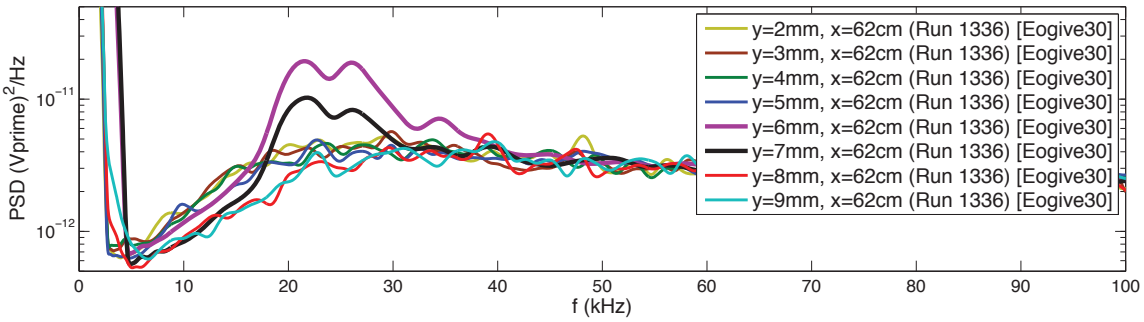

(a) Power spectra of hot-wire measurements above the 30-degree cone-ogive-cylinder at 62 cm.

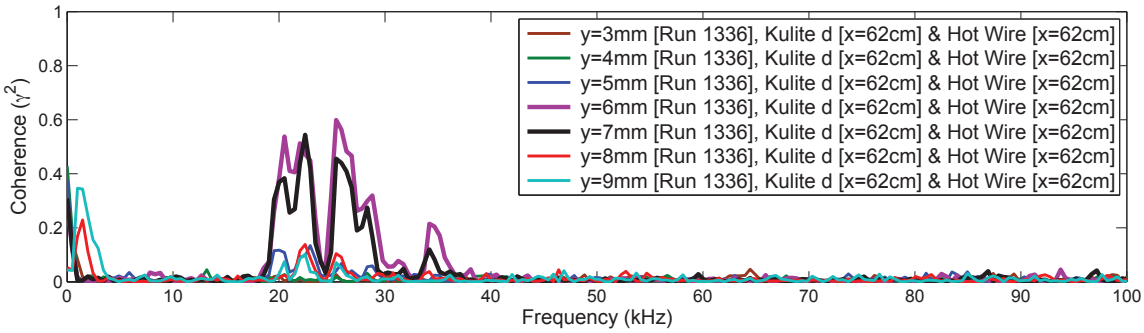

(b) Coherence between Hot-Wire and Surface Measurements (Run 1336).

Fig. 7.23. Power spectra of the hot-wire measurements and their coherence with surface measurements for Run 1336.

coherence of only 0.2. The reason for the low coherence at the lower frequency is not known.

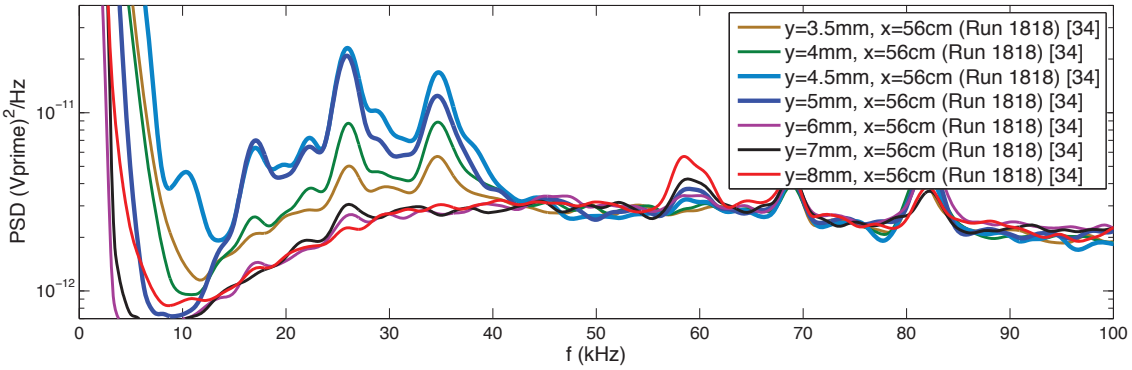

(a) Power spectra of hot-wire measurements above the 34-degree cone-ogive-cylinder at 56 cm.

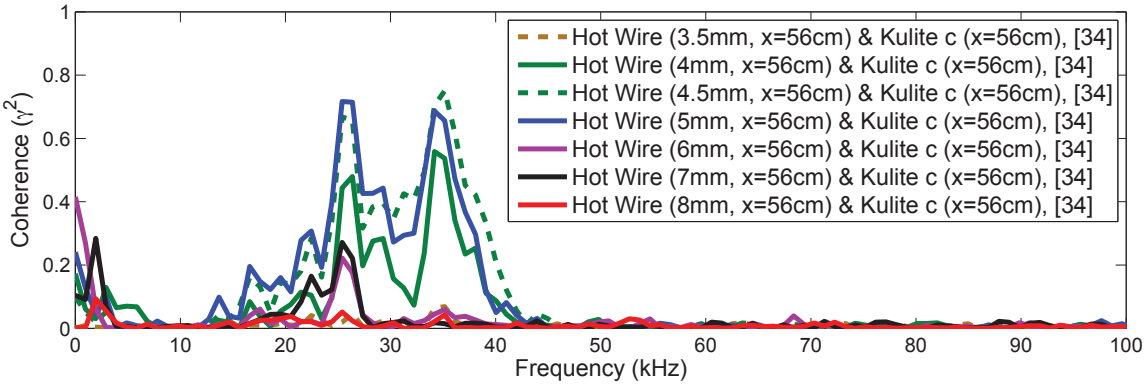

(b) Coherence between the hot-wire and surface measurements on the 34-degree cone-ogive-cylinder at 0.56m (Run 1818).

Fig. 7.24. Power spectra of the hot-wire measurements and their coherence with surface measurements for Run 1818.

7.2.15 Surface Measurements show Transition on the 35-degree Model

The power spectra from surface measurements on the 35-degree cone-ogive-cylinder from 0.52 meters to 0.62 meters are shown in Figure 7.25. The two lower Reynolds number measurements are shown by the brown and green lines. The green lines are from a measurement at a unit Reynolds number of $5.8 * 10^6$ per meter. At 0.52 meters there are small peaks in the spectra at about 25 and 35 kHz. At 0.54 meters the 25-kHz peak has decreased in magnitude and the 35-kHz peak has increased. At 0.56 meters the 25-kHz peak has disappeared and the 35-kHz peak has decreased in magnitude. At 0.62 meters, neither peak is visible in the spectra.

At higher Reynolds numbers, the boundary layer appears to transition downstream on the 35-degree model. The black lines in Figure 7.25 show the power spectra at a unit Reynolds number of $9.6 * 10^6$ per meter. The power spectra at 0.52 meters shows broadband low frequencies typical of instability breakdown leading to a transitioning boundary layer. The amplitudes of the broadband low frequencies continue to increase further downstream, indicative of a more fully transitioned boundary layer.

The blue lines ($Re/m = 7.3 * 10^6$) in Figure 7.25 show spectra for a Reynolds number that is not high enough to cause transition immediately. At 0.52 and 0.54 meters there are several peaks in the spectra between 20 and 40 kHz. The disturbance appears to undergo some stabilization between 0.54 and 0.56 meters. Stabilization also occurs at that location for the lower Reynolds-number measurements. Between 0.56 and 0.62 meters the disturbance magnitude grows significantly. This growth is especially apparent in a peak at about 22 kHz. Broadband low frequencies also start to appear below 50 kHz.

Figure 7.26 provides a closer look at the spectra on the 35-degree model between 0.52 and 0.62 meters at the two highest Reynolds numbers. Figure 7.26(a) shows spectra at a unit Reynolds number of $7.3 * 10^6$ per meter. They show the disturbance change only slightly in magnitude and frequency between 0.52 and 0.56 meters. Then at 0.62 meters, the spectra show a large peak at just over 20 kHz.

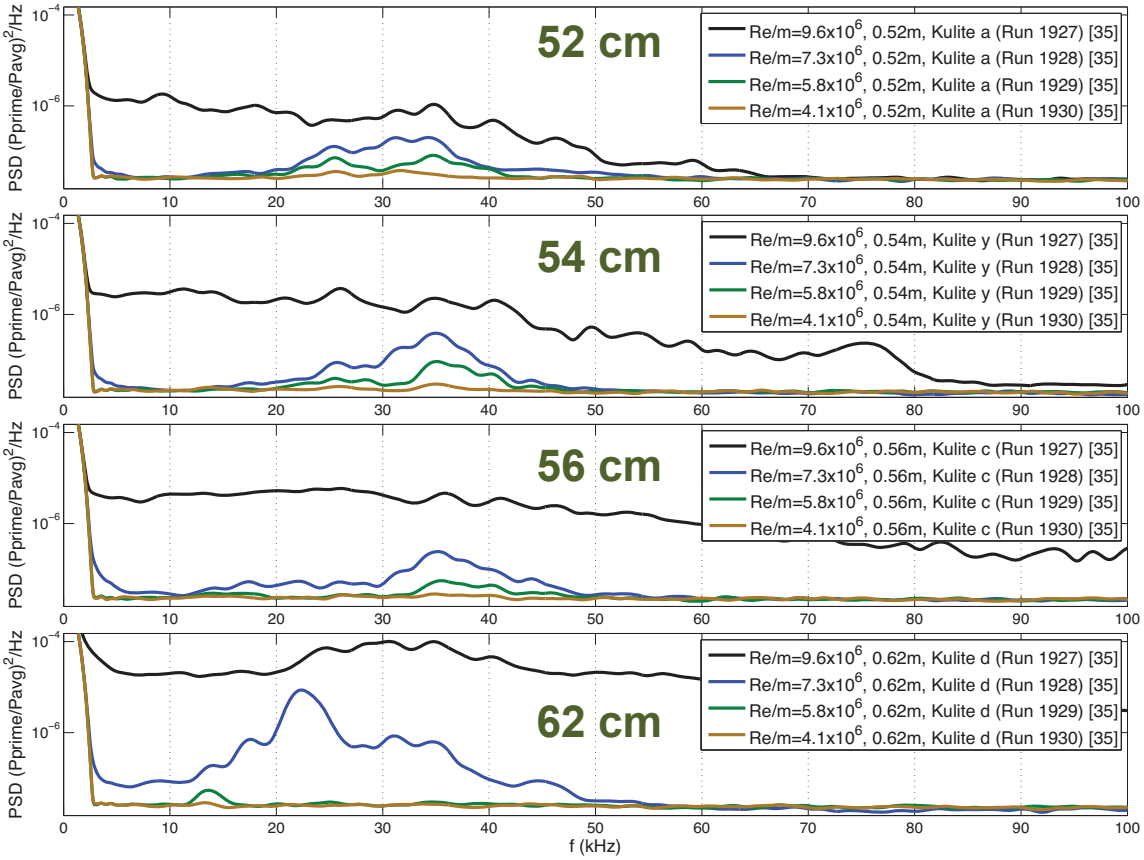

Fig. 7.25. Spectra from surface measurements 0.52 to 0.62 meters on the 35-degree cone-ogive-cylinder. These spectra show a stabilization of the disturbance at 0.62 meters for lower Re and transitional characteristics at higher Re.

Figure 7.26(b) shows spectra at a slightly higher unit Reynolds number, $Re/m = 9.6 * 10^6$. This increase in Reynolds number appears to be enough for the boundary layer to become transitional. The spectra at 0.52 meters (orange line) already show the broadband low frequencies below 60 kHz. At 0.54 (green line) and 0.56 meters (blue line), these broadband low frequencies get higher. The black line shows the spectra at 0.62 meters, showing what appears to be a transitioning boundary layer.

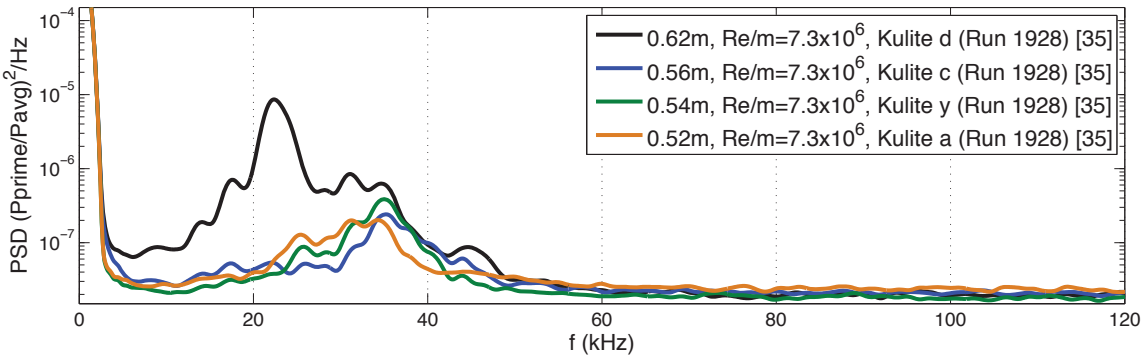

(a) Power spectra from measurements below the transitional Reynolds number.

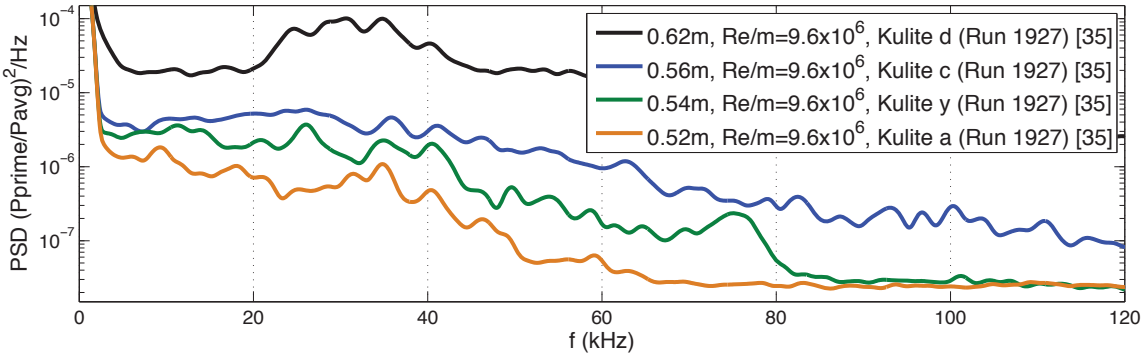

(b) Power spectra from measurements showing transitional characteristics.

Fig. 7.26. Comparison of a pre-transitional power spectra with a power spectra showing transitional characteristics (35-degree cone-ogive-cylinder).

Figure 7.27 shows what this change in Reynolds number from above to below the transitional Reynolds number looks like on the oscilloscope when making measurements. It shows an image of the oscilloscope screen with traces from three surface

Kulite sensors on the 35-degree cone-ogive-cylinder. The large fluctuations from the measurement at 0.86 meters (green trace) for the first part of the run are indicative of a turbulent or transitional boundary layer. Then at some point as the freestream Reynolds number decreases during the run from an Re/m of about $7.6 * 10^6$ to about $6.8 * 10^6$, the fluctuation magnitude decreases abruptly. This happens as the downstream boundary layer becomes laminar.

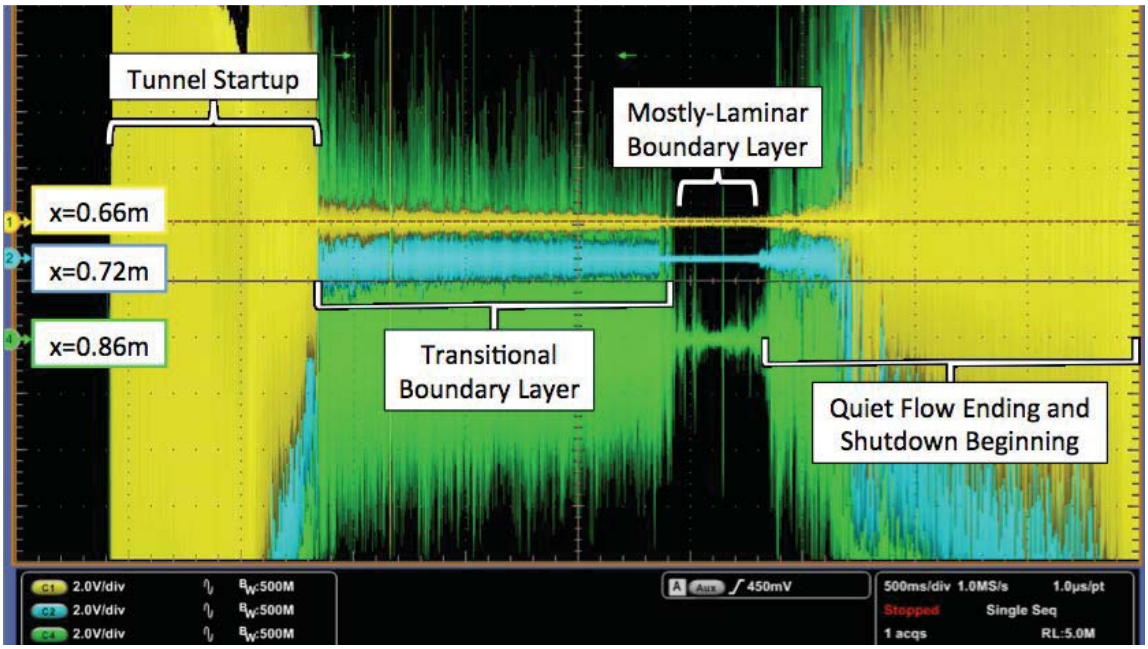

Fig. 7.27. An image taken from an oscilloscope showing the ac voltage traces from surface measurements on the 35-degree cone-ogive-cylinder at 0.66, 0.72, and 0.86 meters. They show a transitional boundary layer for the first part of the run, then a laminar boundary layer as the Re decreases (Run 1219).

The boundary layer only remains laminar for a short period. Then it becomes transitional with the increase in tunnel noise that precedes tunnel shutdown. The amplitude of these fluctuations increase through the end of the screen as tunnel shutdown begins.

This is shown quantitatively in Figure 7.28. It plots the RMS amplitudes at several axial locations on the 35-degree model against the unit Reynolds number. The RMS

values are normalized by the freestream pressure, which is just over 0.5 psia for these conditions. At 0.52 meters, the RMS amplitudes are low over the entire range of Reynolds numbers. The RMS amplitudes at 0.62 meters increase slightly as the unit Reynolds number increases from 6.8 to $7.6 * 10^6$.

At 0.66 and 0.72 meters, the RMS amplitudes increase significantly as the the unit Reynolds number increases between $6.8 * 10^6$ and $7.0 * 10^6$. They then remain somewhat constant as the Reynolds number continues to increase.

The RMS amplitude at 0.86 meters is shown by the black symbols. As the unit Reynolds number increases from $6.8 * 10^6$ to $7.0 * 10^6$ there is a very large increase in RMS from about 0.2 to over 2. At even higher Reynolds numbers the RMS continues to increase slightly. This large increase in RMS is indicative of a transitional boundary layer.

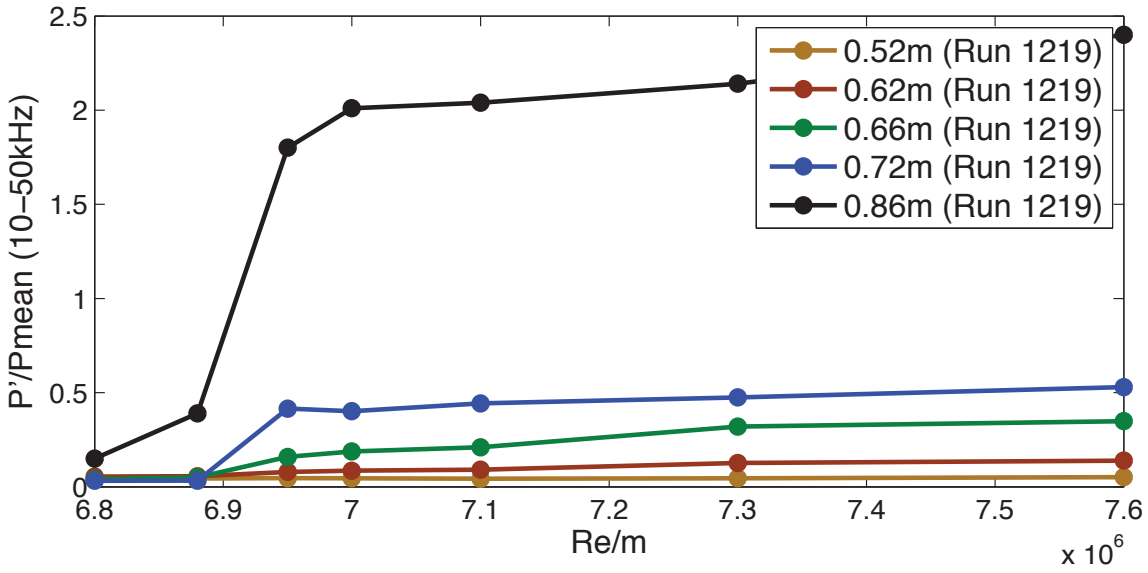

Fig. 7.28. A plot of the RMS values at several axial locations on the 35-degree model vs the unit Reynolds number (Run 1219) [35-degree model].

7.2.16 Transition on the 35-degree Model appears to be caused by the Measured Instability

The summary of the measured disturbance locations in Figure 7.20 showed that the disturbance was closer to the model with the 35-degree nosetip than with any of the other nosetips. Spectra from hot-wire measurements above the 35-degree model at four axial locations are shown in Figure 7.29. At 0.49 meters, the disturbance was measured 7 millimeters above the model surface. The spectrum for this measurement is shown by the black line.

At 0.56 meters, the disturbance is measured most clearly when the hot wire is 4 millimeters above the surface as shown by the green line in the second plot from the top in Figure 7.29. At this height, the disturbance is already well within the boundary layer. The brown and light blue lines are from measurements at 3.5 and 4.5 millimeters and both show the disturbance also. At 5 millimeters (blue line), there are only very small peaks in the spectra.

The disturbance is even closer to the model at 0.59 meters as shown by the third plot from the top in Figure 7.29. The relative magnitude of the spectral peaks also change slightly. The measurement at 4 millimeters is shown by the green line and has peaks between 10 and 40 kHz at similar frequencies to those measured at 0.56 meters. However, the spectrum with the highest peak is at 3 millimeters asd is shown by the brown line. The main peaks in it are between 10 and 30 kHz.

It should be noted that the vertical axis on these plots have a range about 2 orders of magnitude larger than used to show the spectra from the 33-degree model (Figure 7.19). So the disturbance peaks in the power spectra at 0.49, 0.56, and 0.59 meters are not necessarily smaller than those seen on the 33-degree nosetip.

The range of the vertical axis was increased to show spectra from measurements at 0.62 meters. These spectra are shown in the bottom plot of Figure 7.29. The highest peaks are shown by the dark grey line from when the hot wire was only 1.5

millimeters from the model surface. The spectra at this location is starting to show a rise in broadband low frequencies. This is an early indication of transitional behavior.

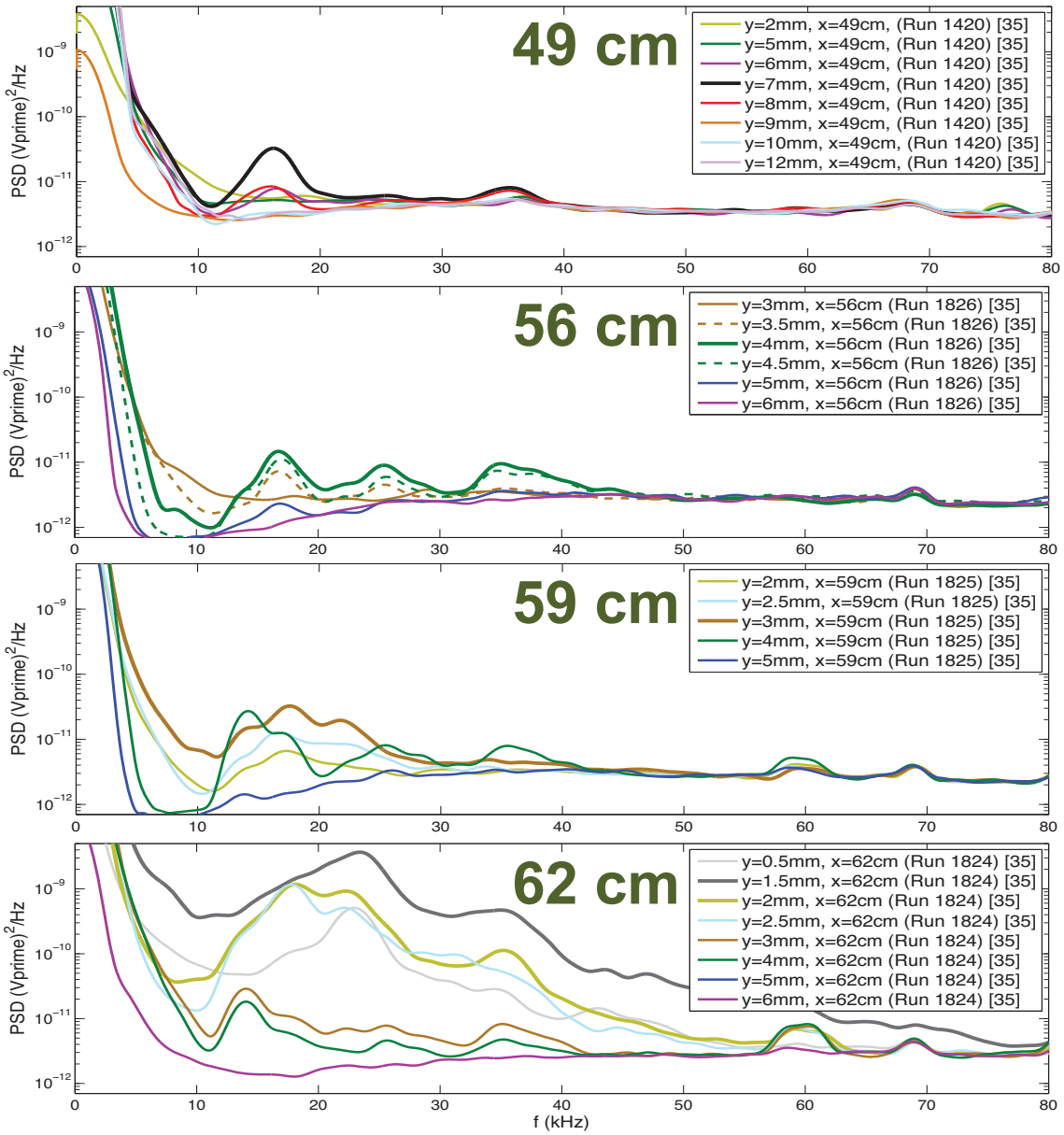

Fig. 7.29. Spectra from hot-wire measurements above the 35-degree cone-ogive-cylinder at several axial locations showing the disturbance enter the boundary layer and approach the model ($P_0 = 120$ psia).

This large increase in disturbance magnitude measured by the hot wire above the 35-degree model at 0.62 meters is also shown in Figure 7.30. It shows the RMS amplitudes for each of the cone-ogive-cylinder configurations when the spectra is integrated from 10 to 50 kHz. It shows the RMS amplitude stay below 0.06 at each location on each of the models except for the 35-degree model at 0.62 meters where it increases by nearly an order of magnitude. That data point is shown by the red diamond in the upper right-hand corner of the plot.

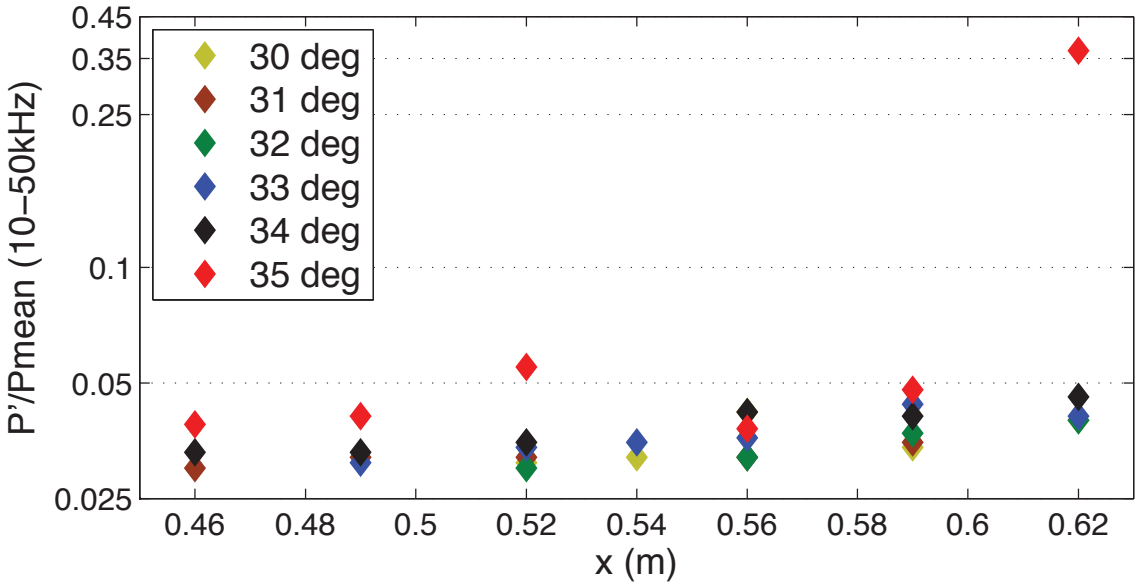

Fig. 7.30. RMS amplitude from hot-wire measurements using each of the 35-degree cone-ogive-cylinders (P_0 = 120 psia).

This large increase in RMS occurs at the same location on the 35-degree model where an increase in RMS is measured by the surface sensors as shown in Figure 7.28. Since no other instabilities have been measured during this investigation, it appears that the measured disturbance is the cause of the transition measured by the surface sensors. If that is the case, this is an example of transition being caused by an instability that originates outside of the boundary layer.

7.3 Investigation of Possible Experimental Error Sources

7.3.1 Flow Symmetry Experiments

To determine how symmetric the measured disturbance is, measurements were made using azimuthally-displaced surface sensors with the model placed at different roll angles. Figure 7.31 shows the power spectra of azimuthally-displaced surface sensors at 0.54 meters on the 34-degree model. The black line shows spectra from measurements made at the top of the model. It shows several peaks between 15 and 45 kHz. The blue and green lines show spectra from sensors azimuthally-displaced by 15 and -25 degrees respectively. Their spectra show the same peaks measured on the top of the model, but the spectra don't match up very well at frequencies less than 15 kHz.

The brown line shows spectra from measurements made at the side of the model (-90°) during a different run at a similar Reynolds number. It shows peaks in about the same 15 to 45-kHz range as measured at the top of the model. However, the peaks have a smaller amplitude and many of them do not match up exactly with those measured at the top of the model.

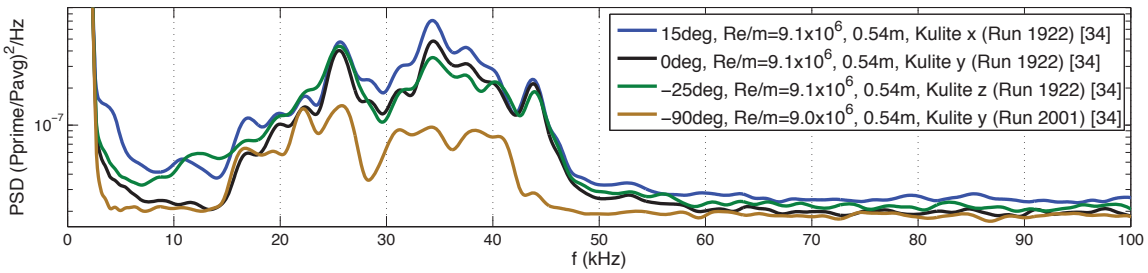

Fig. 7.31. Comparison of the power spectra from azimuthally-displaced surface sensors on the 34-degree cone-ogive-cylinder.

Spectra from surface measurements made on the sides of the 30-degree cone-ogive-cylinder at 0.54 and 0.62 meters are shown in Figure 7.32. The orange lines show spectra for the when the model was turned so the sensors were oriented at an

azimuthal angle of -90 degrees. The blue lines show the spectra from a different run with the sensors turned 180 degrees to be oriented at an azimuthal angle of 90 degrees. At 0.54 meters, both spectra show peaks between 15 and 45 kHz. They both have peaks at about 16 and 22 kHz, although the amplitudes do not match up exactly. The frequencies of the spectral peaks between 30 and 45 kHz do not match up very well, but they have about the same amplitude.

Spectra for the measurements at 0.62 meters match up well. The -90 and 90-degree measurements both have peaks at about 16, 22, 26, and 31 kHz with similar amplitudes.

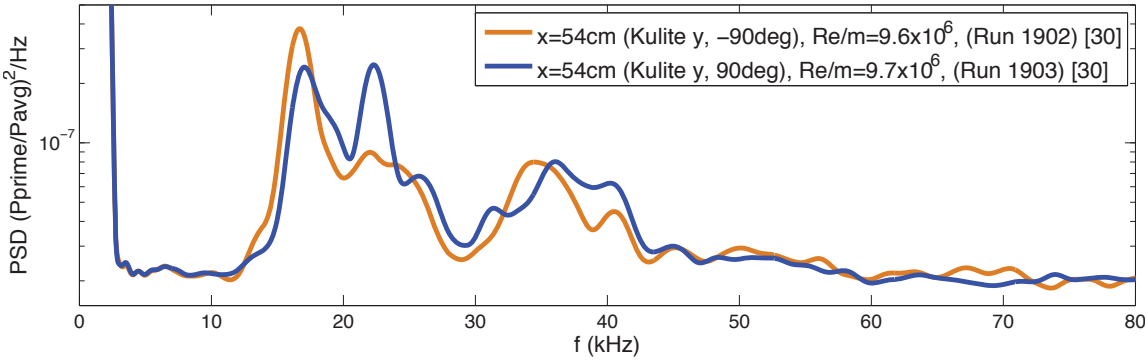

(a) Power spectra of surface measurements at 0.54 meters.

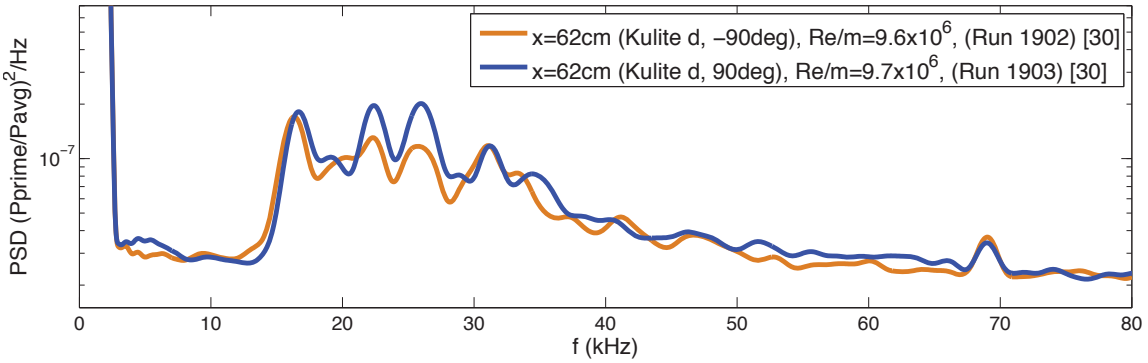

(b) Power spectra of surface measurements at 0.62 meters.

Fig. 7.32. Power spectra of surface measurements at 0.54 and 0.62 meters with the model rotated 90 and -90 degrees (30-degree cone-ogive-cylinder, P_0=160psia).

Spectra from measurements made on the top and bottom of the 30-degree cone-ogive-cylinder at 0.62 meters are shown in Figure 7.33. The red and brown lines are from measurements taken when the sensors are facing the bottom of the tunnel and the black line is from a measurement on the top. The spectra are comparable, but they do not compare as well as the power spectra from measurements on the two sides. Spectra from measurements when the sensors are facing down do not have the same magnitude of instability peaks as those taken from the top. However, they are amplified over the same frequency range.

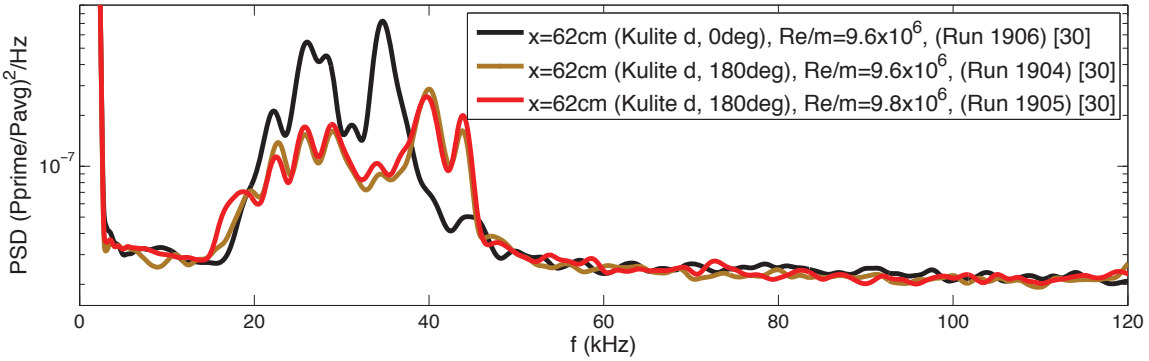

Fig. 7.33. Power spectra of surface measurements at 0.62 meters on the 30-degree cone-ogive-cylinder oriented at 0 and 180 degrees.

To get a better idea of the flow symmetry, simultaneous surface measurements were made at 0.54 meters with sensors on the top, side, and bottom of the model. The power spectra from the measurements made using the 34-degree cone-ogive-cylinder are shown in Figure 7.34. The black and grey lines are from measurements made at the top of the model. The orange and blue lines show spectra at the side and bottom respectively. These measurements complement earlier results made with the model installed at various roll angles. Spectra from all sensors show approximately the same band of frequencies amplified, but spectra from sensors at the side and bottom show smaller peak amplitudes. Spectra from the bottom measurement also show an increase in amplitude for a peak at about 16 kHz.

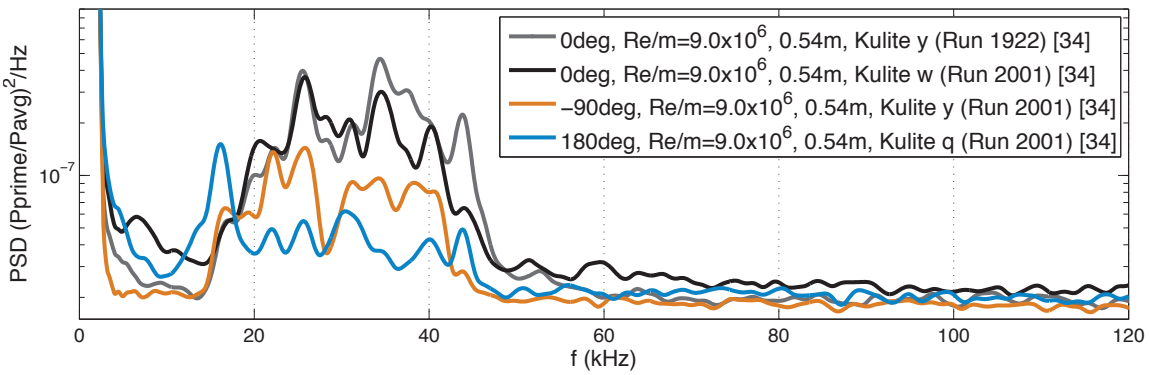

Fig. 7.34. Power spectra of surface measurements at 0.54 meters with sensors at the top, side, and bottom of the 34-degree cone-ogive-cylinder.

These measurements indicate there is an asymmetry in the flow field. There are several possible sources of the asymmetry. One possible source is the slight positive angle of attack. Measurements have shown that the cone-ogive-cylinder model can have an angle of attack of up to 0.1 degrees. Even a very small angle of attack can become significant far enough downstream. These measurements were made at an axial location of 0.54 meters.

Ideally, the angle of attack would be adjusted during each model installation to maintain a consistent angle of attack as close to zero as possible for all the measurements. However, since the existence of the possible angle of attack was discovered only after a majority of the measurements were made, no attempts were made during any of the model installations to ensure a specific angle of attack. Despite the possible angle of attack issue, and other experimental unknowns, both the surface and hot-wire measurements were very repeatable as discussed in Sections 7.2.5 and 7.2.13.

It is also possible that the different measurements made on the top and bottom of the model are due to flow asymmetries within the BAM6QT. Whatever the source of the asymmetry may be, the measurements also show that the disturbance can still be measured at every azimuthal angle.

7.3.2 Effect of Model Placement on the Surface Measurements

It was necessary to install the cone-ogive-cylinder forward in the tunnel in order to make hot-wire measurements far enough back on the model. For most measurements the model was installed on the sting with the rear of the model 0.13 meters forward of the mount. This was done to enable measurements as far back as 0.62 meters. It resulted in the model nosetip extending about 0.28 meters ahead of the nominal onset of Mach-6 uniform flow in the BAM6QT [69]. The calculated Mach number at the nosetip is still 5.97 when installed in this manner, very close to the nominal 6.00.

To determine if the axial placement of the cone-ogive-cylinder affected the disturbance, measurements were made with the cone-ogive-cylinder placed at various axial positions in relation to the BAM6QT. The power spectra for surface measurements made at 0.52 meters on the 30-degree model are shown in Figure 7.35. The orange lines show spectra when the model is installed 3 to 12 centimeters forward of its normal location. The blue lines show spectra from measurements with the model pulled back 3 and 6 centimeters.

For each model placement, the spectra show a range of peaks between 15 and 30 kHz. The two highest peaks for most of these placements are at about 22 and 26 kHz. The magnitude of the highest peak at about 22 kHz does not differ significantly between any of the measurements. The magnitude of the peak at 26 kHz fluctuates slightly but the peak is still clear in each spectra. There are also several other smaller peaks that fluctuate in magnitude between the measurements. While there is some variability, the measurements with the model installed furthest forward (solid blue line) and furthest backward (solid orange line) have peaks at the same frequencies. These peaks are also similar in magnitude. It appears from these measurements that axial placement of the model does not have a significant effect on the magnitude or frequency of the disturbances as measured on the surface.

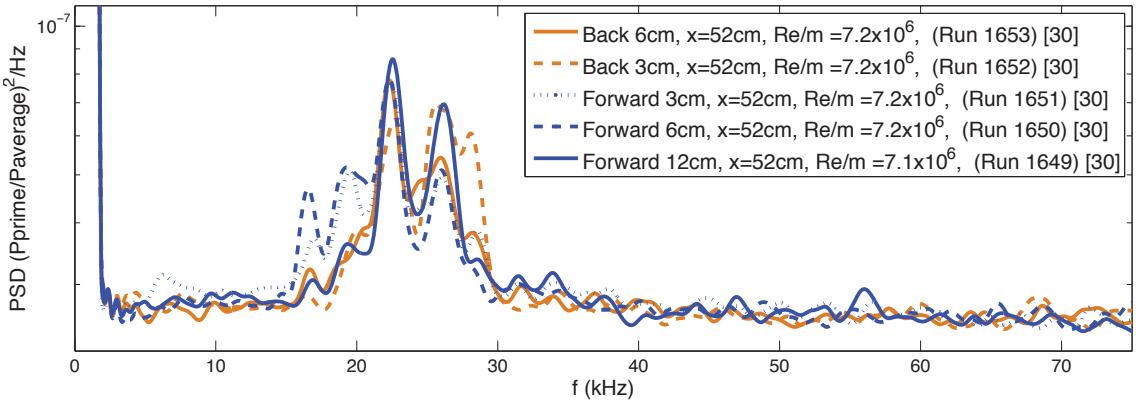

Fig. 7.35. Power spectra of surface measurements showing the effect of moving the model axially in the BAM6QT (30-degree cone-ogive-cylinder).

7.3.3 Effect of Model Placement on the Hot-Wire Measurements

Hot-wire measurements were made on the 30-degree model at 0.56 meters to determine the effect of the axial placement of the model on the disturbance. The power spectra obtained with the model installed at the original and two further-back locations are shown in Figure 7.36. The black, light blue, and orange lines show spectra from measurements above and below the disturbance and are included as a reference. The green line shows spectra from the hot-wire measurement with the model at its original location. For this placement, the maximum disturbance was measured 10 millimeters above the model surface and the spectra show several peaks between 15 and 40 kHz.

The blue line shows spectra from when the model was moved backward 3 centimeters. For this placement, the maximum disturbance was measured 9.5 millimeters above the surface. The magnitude of the disturbance is slightly smaller than for the original location, but the spectral peaks are all in the same frequency band. The purple line shows spectra from when the model was moved backward 6 centimeters. For this placement the disturbance was measured only 9 millmeters above the surface.The spectra from this measurement show a similar magnitude and frequency as

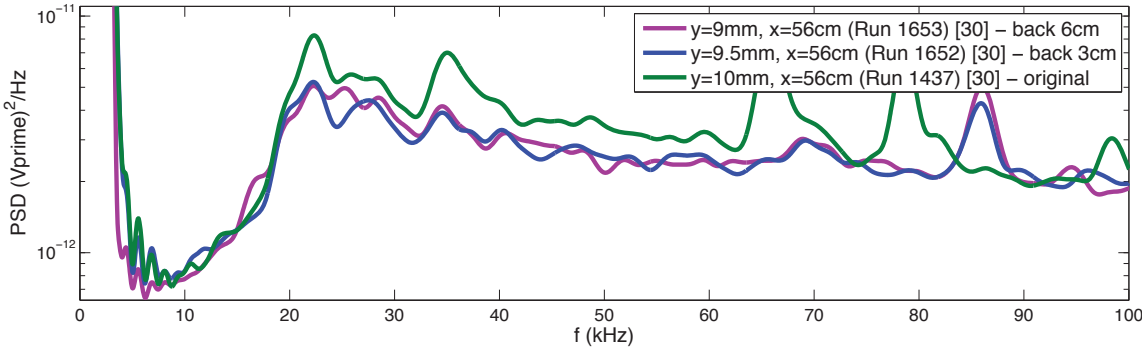

Fig. 7.36. Power spectra of hot-wire measurements showing the effect of moving the model backward in the BAM6QT (30-degree cone-ogive-cylinder).

when the model was moved back 3 centimeters. Moving the model backward appears to have little effect on the disturbance magnitude or frequency. However, a backward placement of 6 millimeters decreased the instability height above the model by about 1 millimeter. The reason for this slight downward shift is not known.

Hot-wire instability measurements were also made at 0.62 meters with the model placed further forward in the BAM6QT. The power spectra from these measurements are shown in Figure 7.37. Spectra from the original placement is shown by the black line. It has several peaks peaks between 15 and 40 kHz with the highest peak at about 20 kHz. The purple line shows the spectra from when the model is place forward 3 centimeters from the original location. It shows peaks in the same band of frequencies, but the disturbance magnitude is smaller and the highest peak is at about 16 kHz. Spectra from measurements when the model was placed forward 6 and 12 centimeters from the original location are shown by the blue and green lines respectively. They show that as the model moves further forward, the disturbance magnitude decreases. For each placement, the maximum disturbance was measured at a height between 6 and 6.5 millimeters above the surface. Forward placement does not have much effect on the measured distance between the disturbance and the model, but it does affect the magnitude of the measured disturbance.

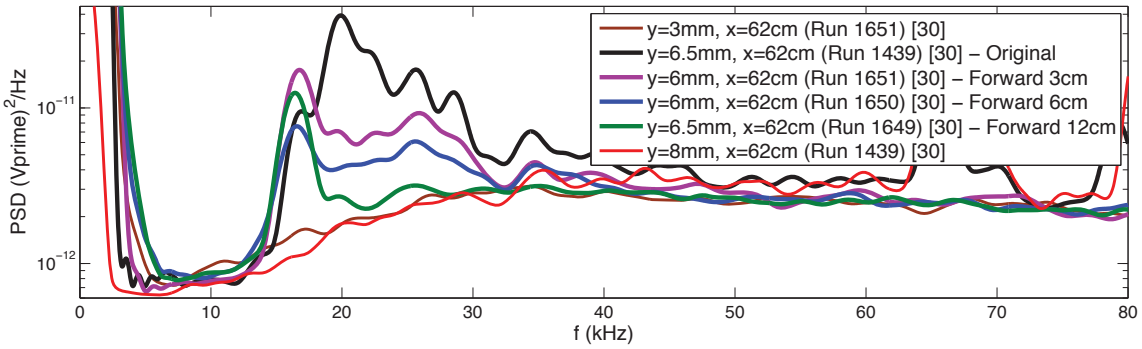

Fig. 7.37. Power spectra of hot-wire measurements showing the effect of moving the model forward in the BAM6QT (30-degree cone-ogive-cylinder).

Table 7.2 shows the RMS amplitude calculated for the band between 10 and 50 kHz for each of the spectra shown in Figure 7.37. It shows the decrease in RMS amplitude that results from the model being pushed forward in the BAM6QT. The percent decrease in RMS from the original location is also included, showing a decrease in RMS amplitude of over 15 percent when the model is pushed forward 12 centimeters.

Table 7.2
Variation in hot-wire RMS amplitude due to model placement.

Model Placement	RMS ($\frac{V'}{V_{mean}}$)	% RMS Change	Run
Original Location	0.0375		1439
Forward 3cm	0.0358	4.8	1651
Forward 6cm	0.0327	14.7	1650
Forward 12cm	0.0325	15.4	1649

7.3.4 Effect of Turning the Model on the Hot-Wire Measurements

A majority of the experimental measurements were made with the row of surface sensors within 10 degrees of straight up. Measurements were made while rolling the

model to determine if the roll angle of the model affects the measured instability. The spectra obtained from hot-wire measurements at three roll orientations from 10 to 165 degrees are shown in Figure 7.38.

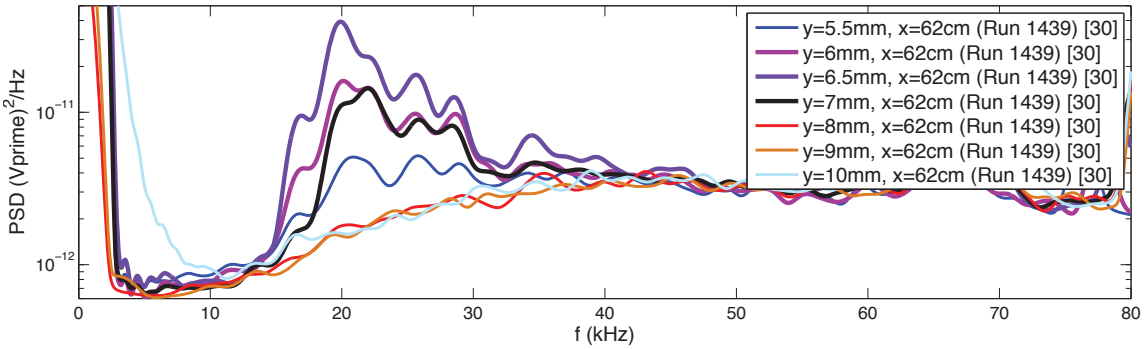

(a) Power spectra when the surface sensors are turned 10 degrees from vertical.

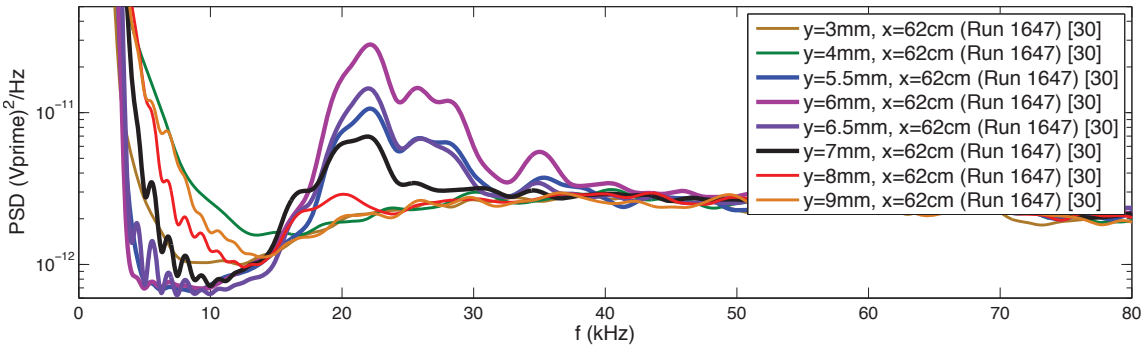

(b) Power spectra when the surface sensors are turned 90 degrees from vertical.

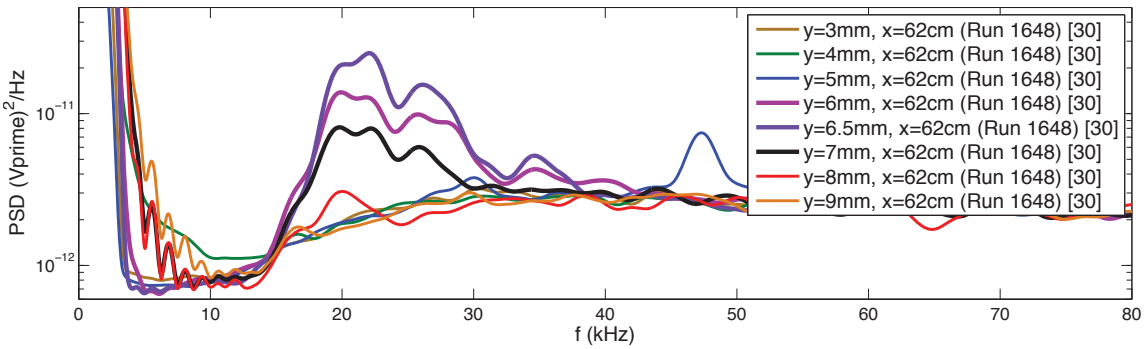

(c) Power spectra when the surface sensors are turned 165 degrees from vertical.

Fig. 7.38. Hot-wire measurements above the 30-degree cone-ogive-cylinder at 62 cm showing the effect of turning the model.

Figure 7.39 compares the spectra from the hot-wire measurement for each of these roll angles where the largest disturbance was measured. The angle of attack for the model was not measured for these experiments so if there are AoA difference they are not known. However, from these measurements, made during two different tunnel entries, it can be seen that turning the model had little effect on the location, magnitude, or frequency of the measured instability.

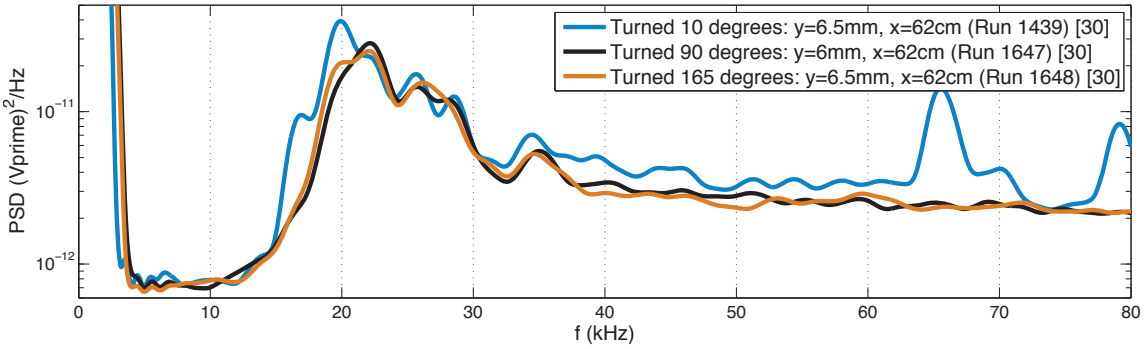

Fig. 7.39. Comparison of hot-wire spectra from measurements with the 30-degree model rolled to various degrees in the BAM6QT.

These experiments were not designed to show an axisymmetric flow field since the hot-wire measurement location does not change in relation to the tunnel. However, a significant difference in power spectra would have indicated that the model may have been causing a flow asymmetry.

8. COMPUTATIONAL EVIDENCE FOR AN ENTROPY-LAYER INSTABILITY

8.1 Mean-Flow Analysis for the Cone-Ogive-Cylinder

Mean-flow calculations are used to provide an understanding of some of the flow physics that could result in an instability. Computed flow features such as the shock curvature, boundary-layer thickness, and areas of high gradients provide a better spatial awareness. Angular momentum profiles are also analyzed for local maxima outside the boundary layer. A local maximum indicates an instability is theoretically possible.

8.1.1 Density Contours for the 30 and 35-degree Models

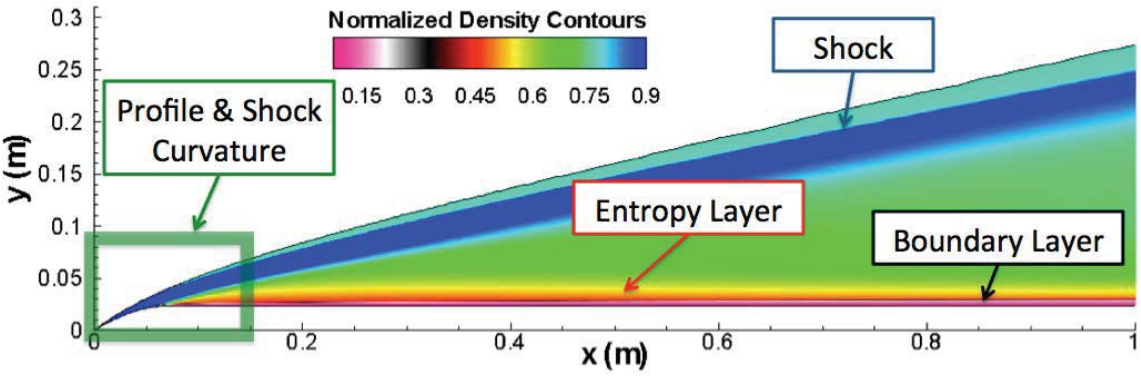

Fig. 8.1. Normalized density contours ($\frac{\rho}{\rho_0}$) above the 30-degree cone-ogive-cylinder at P_0=160psi with several flow features identified ($T0$=433K, T_w=300K).

The normalized density contours for flow around the 30-degree cone-ogive-cylinder at a stagnation pressure of 160 psia are shown in Figure 8.1. The density is normalized

by the stagnation density (ρ_0). The shock is identified in the figure as the interface between the light and dark blue areas just inside the grid border. A thin black line just above the surface shows the edge of the boundary layer. The entropy layer is identified as the area of high gradients just outside of the boundary layer. The small green box on the lower left of the picture highlights the part of the flow where the shock curvature is important. This curvature is changed slightly for each nosetip configuration, thus changing the shock profile and affecting the entropy layer.

Because most of the hot-wire instability measurements were at a stagnation pressure of 120 psi, mean-flow computations were also conducted under those conditions. The normalized density contours for 120-psia flow over the 30-degree cone-ogive-cylinder are shown in Figure 8.2(a). The density in these figures is normalized by ρ_0 so the contours look very similar to those for a stagnation pressure of 160 psia (Figure 8.1).

As the nosetip angle increases, the shock near the nose becomes stronger and the overall shock curvature increases. These effects can be seen by comparing the calculated density contours over the 30-degree model with those of the 35-degree model as shown in Figure 8.2(b). The contour scales on Figures 8.2(a) and 8.2(b) are identical to enable comparisons between the two.

One obvious difference between the contour plots of the 30 and 35-degree cone-ogive-cylinders is the thicker layer of low-density air above the boundary layer of the 35-degree model. The 35-degree model has a stronger shock near the leading edge which results in higher density behind the shock. Then there is a supersonic expansion as the air flows around the ogive. The turning angle of the expansion fan is greater for the 35-degree model. So, although the 35-degree model has greater density right after the shock, the air also undergoes a much greater expansion. This results in the 35-degree model having a lower density just outside of the boundary layer.

This area of lower-density flow outside the boundary layer is also shown in Figure 8.3. It shows calculated density profiles at 0.4, 0.6, and 0.8 meters. The solid lines show the profiles for the 30-degree cone-ogive-cylinder and the dashed lines are

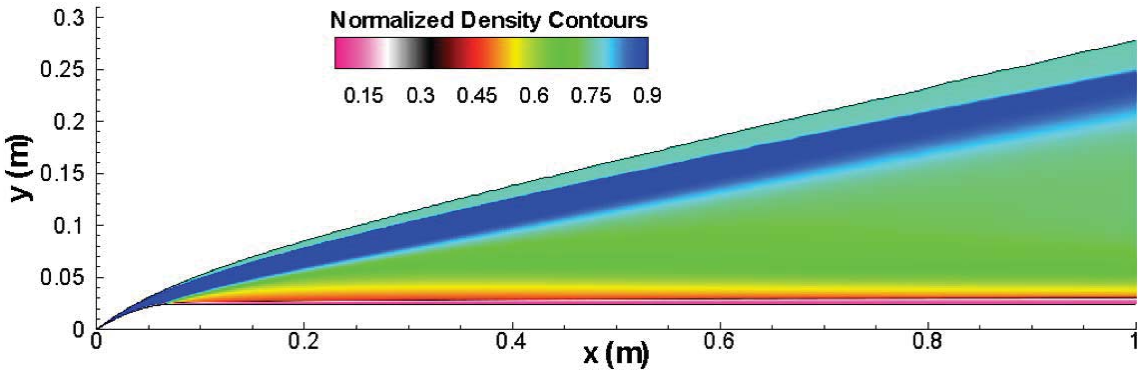

(a) Calculated contours of $\frac{\rho}{\rho_0}$ above the 30-degree cone-ogive-cylinder at P_0=120psi.

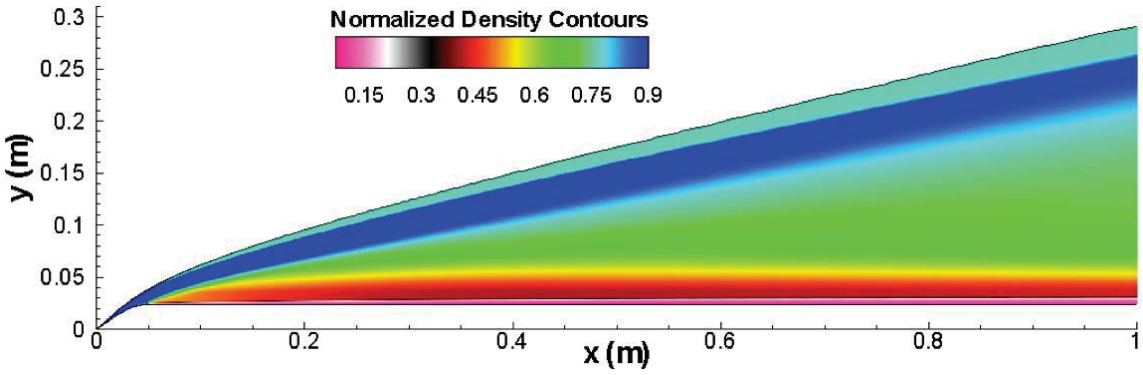

(b) Calculated contours of $\frac{\rho}{\rho_0}$ above the 35-degree cone-ogive-cylinder at P_0=120psi.

Fig. 8.2. Normalized density contour plots for the 30 and 35-degree cone-ogive-cylinders.

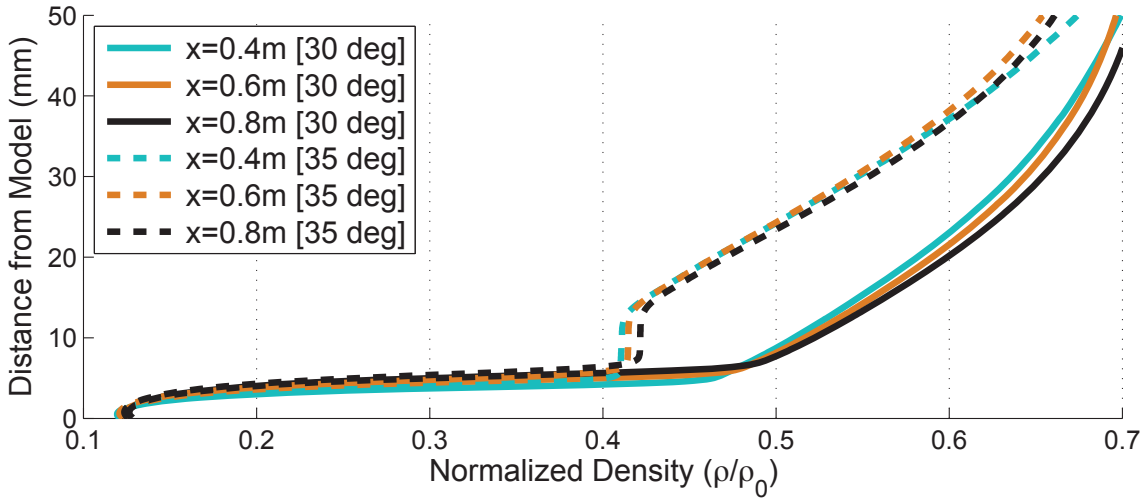

Fig. 8.3. Calculated $\frac{\rho}{\rho_0}$ profiles for the 30 and 35-degree cone-ogive-cylinders.

for the 35-degree model. The density profiles through the boundary layer are similar for each model. However, outside of the boundary layer, the 35-degree model has a significantly lower density than the 30-degree model.

8.1.2 Comparison of Hot-Wire Measurements with Mass Flux Calculations

Figure 8.4 compares the calculated mass flux profile above the 30-degree model at 0.52 meters with the mass flux measured by the hot wire. The hot-wire measurements are shown by the red stars and have been scaled in order to put the experimentally-computed values at a magnitude similar to that of the computed values. This was done even for calibrated measurements because it allows for better comparison of the distance above the model where the computed and measured mass flux has the highest gradients.

At just over 10 millimeters there is a large increase in the voltage measured by the hot wire. This is the same location where the disturbance is measured by the hot wire as shown in Figure 7.16. Below 10 millimeters, there is a gradual increase in

the measured values. The mass flux calculated using STABL is shown by the green line. Up until just over 5 millimeters, it shows a rapid increase in mass flux. Above 5 mm the mass flux continues to increase but at a lower rate. The computations do not show the rapid rise in mass flux at just over 10 millimeters that is shown by the measurements.

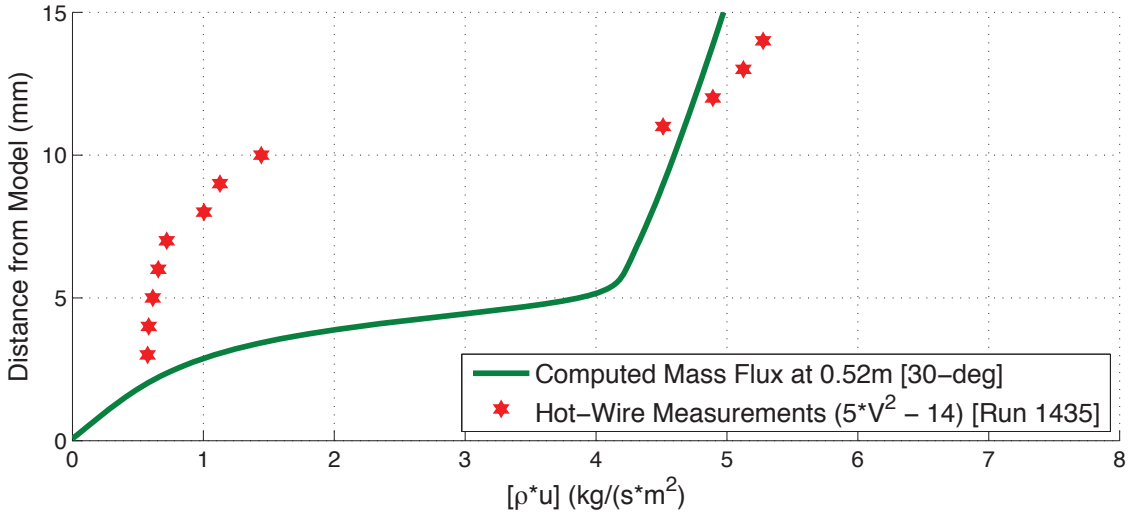

Fig. 8.4. Comparison of the calculated mass flux with that measured by the hot wire above the 30-degree model at x=0.52m (Run1435, P_0=120psia).

Figure 8.5 compares the calculated mass flux profile above the 30-degree model at 0.62 meters with the mass flux measured by the hot wire during two different runs. The calculated mass flux is shown by the green line. It has a similar profile to the mass flux profile at 0.52 meters (Figure 8.4). There is a rapid increase in mass flux through about 6 millimeters as it goes through the boundary layer. Above 6 millimeters there is a gradual increase in mass flux.

The hot-wire measurements are shown by the red and blue symbols. As in the previous figure, the measured values have been scaled for better comparison with the computations. Both of the hot-wire measurements show a large increase in voltage at a height of about 7 millimeters. This is the location where the disturbance is measured using the hot wire as shown by the peaks in the spectra in the bottom plot

shown in Figure 7.29. Below 7 millimeters, the measured values increase, showing a similar curvature to the computations.

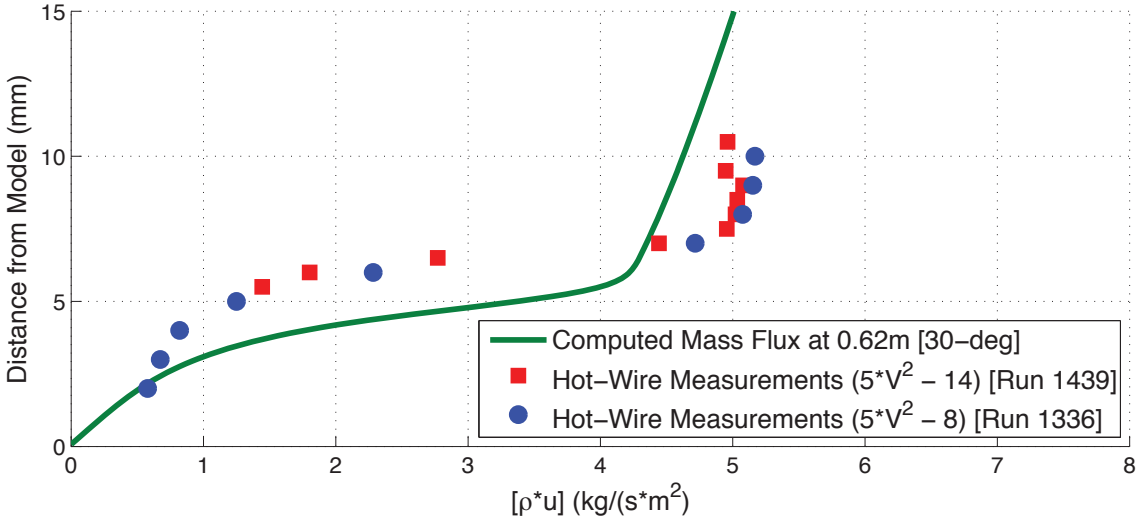

Fig. 8.5. Comparison of the calculated mass flux with that measured by the hot wire above the 30-degree model at x=0.62m (Runs 1336/1439, P_0=120psia).

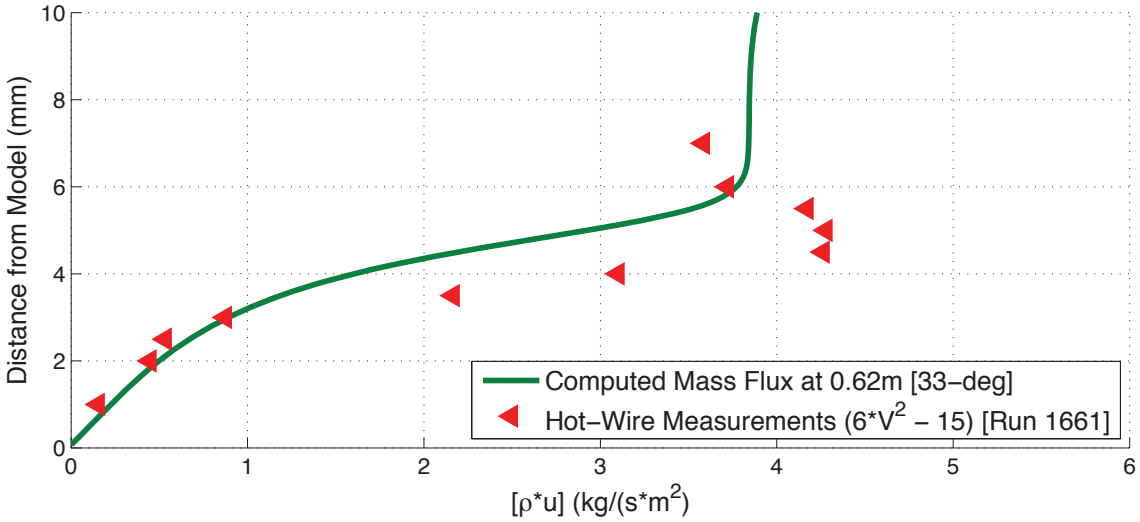

Fig. 8.6. Comparison of the calculated mass flux with that measured by the hot wire above the 33-degree model at x=0.62m (Run 1661, P_0=120psia).

These comparisons show a discrepancy between the measured and computed mass flux values. The computations are showing a rapid increase in mass flux through the boundary layer. Above the edge of the boundary layer, the mass flux increases at a nearly linear rate. The hot-wire measurements do not necessarily show a large increase in mass flux through the boundary layer. However, they do show a rapid rise in mass flux at the height at which the disturbance is measured.

The hot-wire measurements show a rapid rise in mass flux at the height of the disturbance even when the measured disturbance is inside the boundary layer. Figure 8.6 compares the calculated mass flux above the 33-degree model at 0.62 meters with the mass flux measured by the hot wire. The green line shows the calculated mass flux. It shows the typical rapid increase of mass flux through the boundary layer which has a thickness of about 6 millimeters. The red triangles show the hot-wire measurements, scaled to compare more easily with the computations. They show the rapid increase in mass flux starting at a distance of around 3.5 millimeters. This is the height at which the disturbance is measured with the hot wire and is inside the boundary layer. The reason for this computational/experimental difference is not known.

8.1.3 Angular-Momentum Profiles indicate that an Entropy-Layer Instability is Theoretically Possible

Angular-momentum profiles are significant in instability calculations because of the generalized inflection criterion identified by Lees and Lin. This criterion states that where there is a local maximum in an angular-momentum profile, there is the possibility of an instability [19, 55]. This makes the inflection point one important indicator of the stability of the entropy layer.

Computations of the mean flow yielded the angular-momentum profiles shown in Figure 8.7. The profiles for the 30-degree model at four different axial locations are shown by the solid lines. The dotted and dashed lines show the profiles for the 32 and

34-degree models respectively. The profiles for each of the models extend to the right beyond the shown angular-momentum values. This provides an approximation of the edge of the boundary layer since the rapid increase in angular momentum occurs as the rate of change of velocity increases inside the edge of the boundary layer.

All of the cone-ogive-cylinder configurations have generalized inflection points above the boundary layer. These inflection points are shown by local maxima in the profile curves. The inflection points for the plotted profiles range from about 6 to 13 millimeters off the surface.

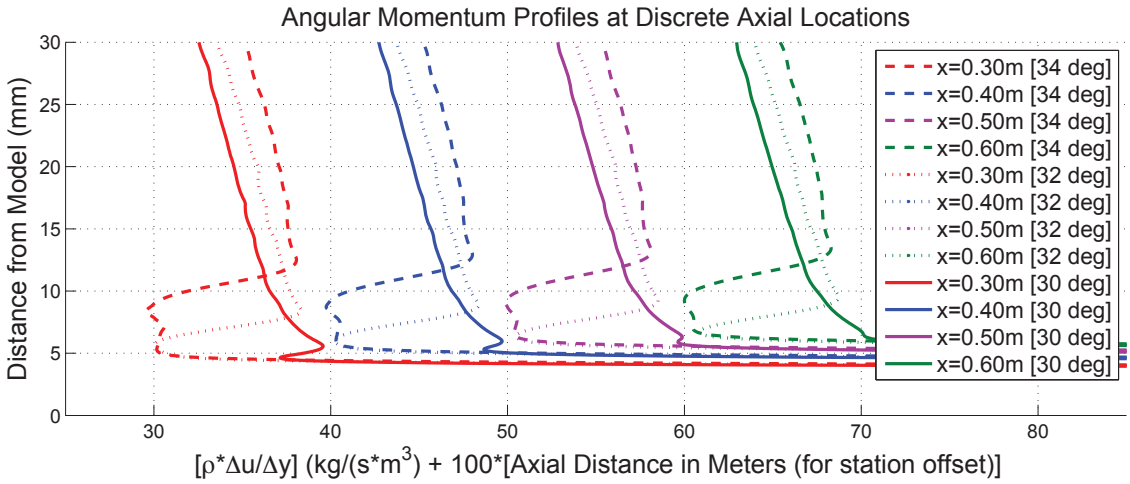

Fig. 8.7. Calculated angular-momentum profiles for the 30, 32, and 34-degree cone-ogive-cylinder configurations.

Profiles at 0.3 and 0.4 meters on the 30-degree configuration have distinct inflection points shown by the red and blue lines. These inflection points are between 5 and 6 millimeters off the model surface. At 0.5 and 0.6 meters the inflection point appears to merge into the growing boundary layer. The inflection point at 0.6 meters is no longer clearly visible.

There is a clear inflection point visible at each plotted location in the angular-momentum profiles for the 32-degree model. The inflection points for the plotted profiles are between 8 and 10 millimeters off the model surface. This is well outside the edge of the boundary layer. The profiles calculated for the 34-degree model show

clear inflection points even further from the model. The locations of these local maxima range from about 12 to 13 millimeters off the model surface.

The angular-momentum profiles for each of the cone-ogive-cylinder configurations at axial locations of 0.5 and 0.6 meters downstream are shown in Figure 8.8. The two profiles look very similar since there is little change in the flow conditions between the two locations. The figure shows that the trends for the 31, 33, and 35-degree configurations are the same as those shown by the previous three configurations. As the nosetip angle increases, the distance of the most distinct angular-momentum inflection point from the surface increases. As was the case with Figure 8.7, there is no visible data near the bottom of the chart inside the boundary layer because of the extremely large velocity gradients.

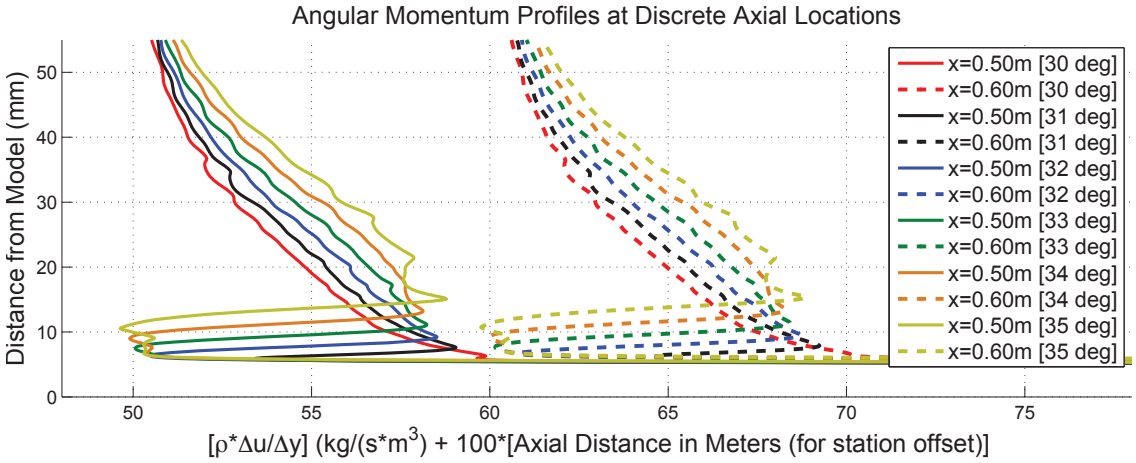

Fig. 8.8. Calculated angular-momentum profiles for each of the cone-ogive-cylinder configurations at 0.5 and 0.6 meters.

The existence of a generalized inflection point shows that an instability is theoretically possible. However, the location of the calculated inflection point does not correspond well with the measured instability location. This apparent discrepancy between the computational and experimental results is shown in Figure 8.9. The dotted lines follow the local maximum in the angular momentum from the calculations. They show that as the nosetip angle increases, the distance between the generalized

inflection point and the model surface increases. The locations where the instabilities were measured are shown by the symbols. They show that as the nosetip angle increases, the distance between the instability and the model surface decreases. The reason for this discrepancy is unknown.

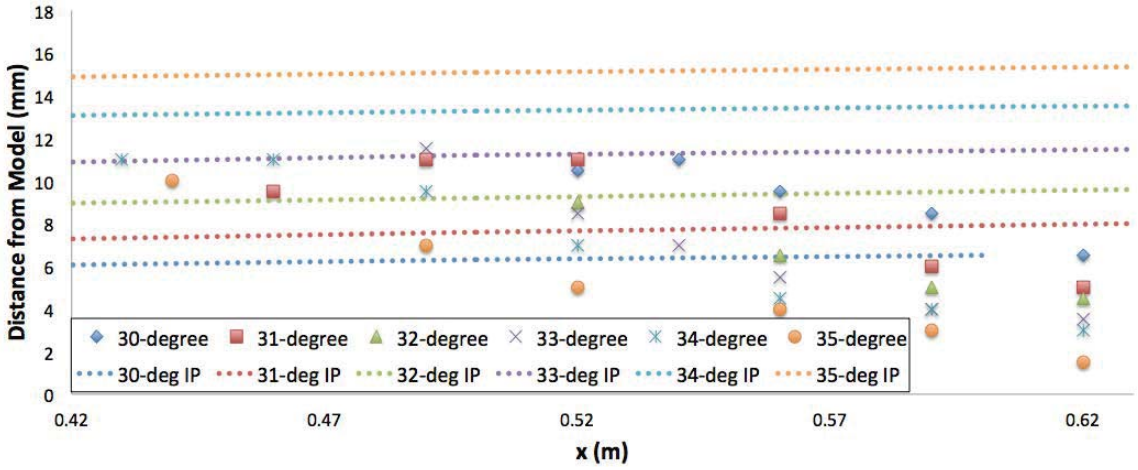

Fig. 8.9. Comparison of the locations of the calculated generalized inflection points (IP) with the measured instability locations for each of the cone-ogive-cylinders.

8.1.4 Rate of Change of the Local Mach Number

Another indicator of a possible entropy-layer instability is a local maximum in the rate of change of the local Mach number ($\frac{\delta M}{\delta y}$). Stetson made hot-wire measurements of the entropy-layer instability above a blunt cone at Mach 8. In these experiments, he found that profiles of $\frac{\delta M}{\delta y}$ gave a clearly-defined maximum. The location of this maximum coincided with the experimentally-measured unstable region outside of the boundary layer. Therefore, Stetson compared his experimental data to the $\frac{\delta M}{\delta y}$ profile instead of the angular-momentum profile [49].

The $\frac{\delta M}{\delta y}$ profiles were calculated for each of the cone-ogive-cylinder configurations. Calculations were done in Matlab using the STABL mean-flow results. The profiles for the 30, 32, and 34-degree cone-ogive-cylinder configurations at axial locations of

0.3, 0.5, and 0.7 meters are shown in Figures 8.10 and Figure 8.11. The dotted lines show the $\frac{\delta M}{\delta y}$ profiles for the 30-degree model. The dashed and solid lines correspond to profiles for the 32 and 34-degree models respectively.

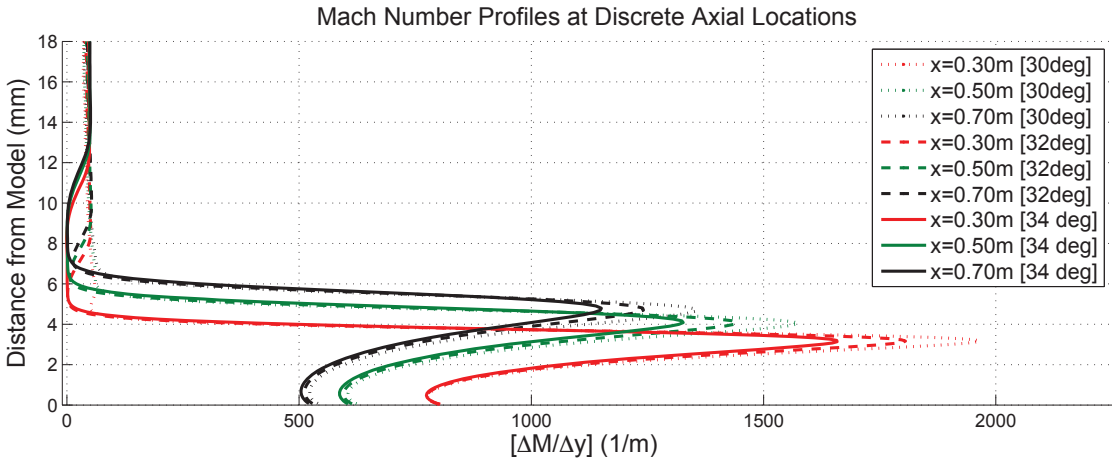

Fig. 8.10. Calculated $\frac{\Delta M}{\Delta y}$ profiles over the 30, 32, and 34-degree cone-ogive-cylinder configurations.

Figure 8.10 shows the calculated $\frac{\delta M}{\delta y}$ profiles at several axial locations from the model surface to 18 millimeters off the surface. The profiles show very clear local maxima between 3 and 5 millimeters. These maxima show $\frac{\delta M}{\delta y}$ inflection points inside the boundary layer. The magnitude of these inflection points decrease as the nosetip angle increases.

There are also local maxima outside of the boundary layer that are much smaller. Stetson compared his experimental results to inflection points outside of the boundary layer. Figure 8.11 shows the same $\frac{\delta M}{\delta y}$ profiles as Figure 8.10, with the axes changed to better identify the local maxima outside of the boundary layer. It shows that as the nosetip angle increases, the inflection point outside of the boundary layer increases in magnitude and moves further from the surface of the model. The locations of these local maxima are approximately the same as for the generalized inflection points.

As is the case with the angular-momentum profiles shown in Figure 8.7, the $\frac{\delta M}{\delta y}$ profiles for the 30-degree configuration show that the inflection point disappears fur-

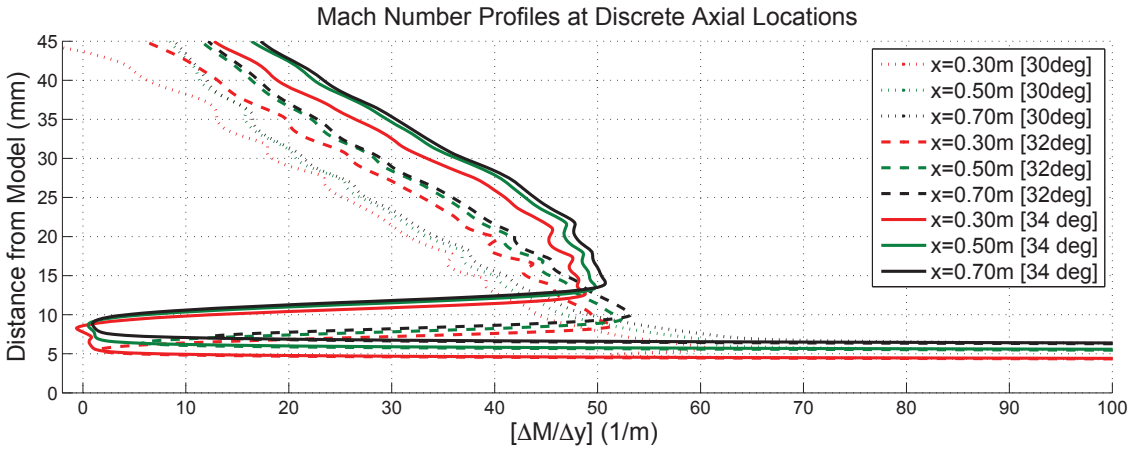

Fig. 8.11. Calculated $\frac{\Delta M}{\Delta y}$ profiles - showing local maxima outside of the boundary layer for the 30, 32, and 34-degree models.

ther downstream as the boundary layer gets thicker. The location of this disappearance appears to be the axial location where the entropy layer is being swallowed by the boundary layer.

As was discussed in Section 8.1.3, the assumption that entropy-layer instabilities enter the boundary layer as the entropy layer is being swallowed shows a discrepancy between the experiments and computations that is not resolved in this thesis. For both the angular momentum and the $\frac{\delta M}{\delta y}$ profiles, the distance of the computed inflection point above the boundary layer increases as the nosetip angle increases. However, the experimental measurements clearly show that as the nosetip angle increases, the instability enters the boundary layer further upstream. It appears from this experimental/computational comparison there may be some other flow characteristic not yet understood that can bring the instability close to the model surface.

8.2 Stability Analysis completed at Texas A&M shows Entropy-Layer Modes that are Marginally Unstable for Higher Nosetip Angles

While the measured disturbance appears to be a real entropy-layer instability, it has not yet been confirmed by stability computations. Purdue does not yet have the

capability to perform stability calculations outside of the boundary layer. Therefore, the results of mean-flow calculations were sent to Texas A&M for computations. The axisymmetric mean-flow results completed at Purdue for the 30 to 35-degree cone-ogive-cylinders at a stagnation pressure of 120 psia were used as the starting point of the stability computations. The stability calculations and analyses were performed by Pedro Paredes, Travis Kocian, Nick Oliviero, and Helen Reed at Texas A&M [37,111,112]. They performed a spatial local analysis for each model, analyzing the entropy and boundary layers for perturbation growth for frequencies up to 50 kHz.

Their PSE results for the 30-degree model showed no evidence of instability growth for the boundary or entropy layer modes. Their analysis of the 31-degree model also showed that the entropy-layer modes were always locally stable.

The lowest-angle cone-ogive-cylinder with positive growth rates was the 32-degree model. PSE results showed that the entropy-layer mode for the 32-degree model becomes marginally unstable, but with N factors remaining less than 0.2. The growth rates calculated for the 31 and 32-degree models are shown in Figure 8.12.

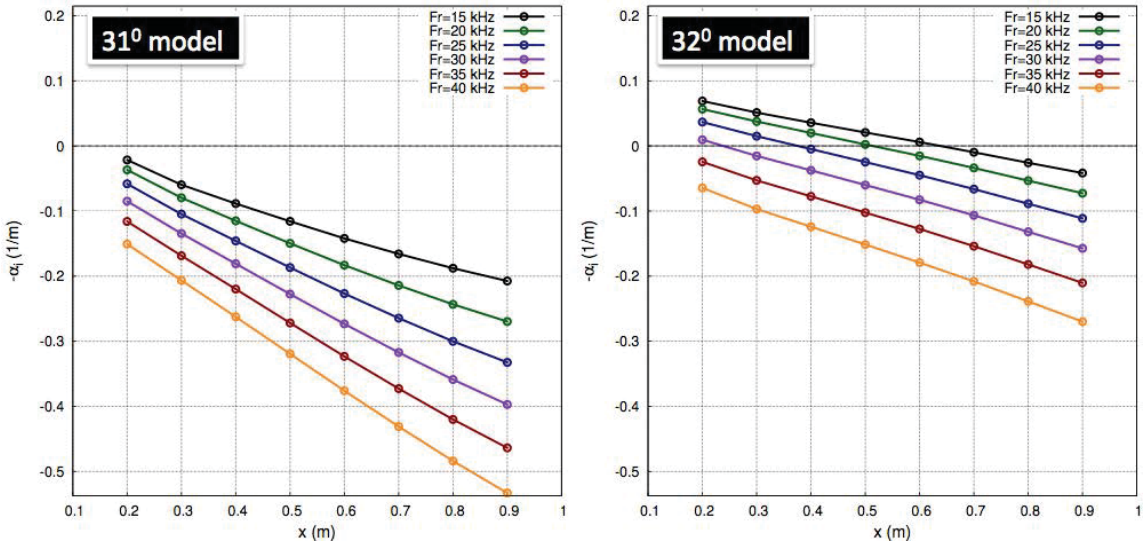

Fig. 8.12. Growth rates for entropy-layer modes for the 31 and 32-degree models (PSE calculations and figures by Texas A&M).

As the nosetip angle increased, the entropy-layer modes were shown to become more unstable. However, the growth rates and resulting N factors are still small. The growth rates calculated for the 33 and 35-degree models are shown in Figure 8.13.

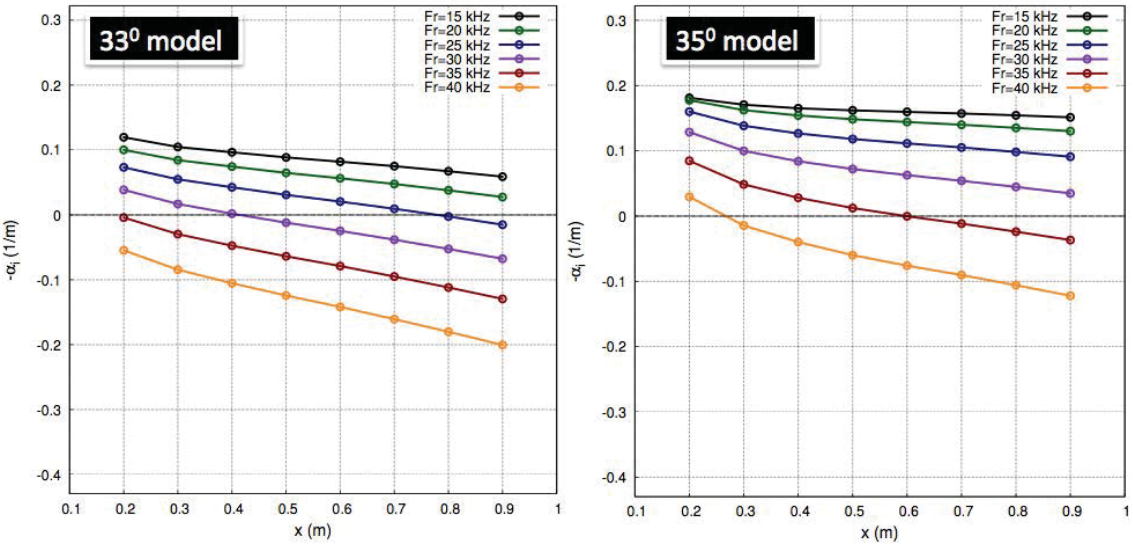

Fig. 8.13. Growth rates for entropy-layer modes for the 33 and 35-degree models (PSE calculations and figures by Texas A&M).

There are several possible reasons for the differences between the experiments and computations. One of these is that the mean-flow computations assume axisymmetric flow. However, the experiments have shown that there are asymmetries in the flow. It was also shown that there can be an angle of attack of up to 0.1 degrees. Even that small of an AoA can be significant on a model as long as the cone-ogive-cylinder.

One goal of these measurements is to provide experimental measurements that can be used to improve computational methods. This can best be done when direct comparisons can be made between the experiments and the computations. It is hoped that future computations can provide this comparison.

9. ADDITIONAL MEASUREMENTS AND CHARACTERIZATION OF THE APPARENT INSTABILITY

9.1 Surface Measurements for 25-degree Cone-Ogive-Cylinder

Power spectra from surface measurements at several axial locations on the 25-degree model are shown in Figure 9.1. No disturbance is identifiable in the spectra from measurements at 0.52 meters. At 0.56 meters there are peaks in the spectra between 15 and 50 kHz that increase in magnitude as the Reynolds number increases. At 0.72 meters, the disturbance magnitude has increased significantly for stagnation pressures greater than 100 psia as shown by the larger peaks in the green, blue, and black spectral traces. At 0.86 meters, the magnitude of the disturbance peaks appears to have decreased slightly.

The RMS amplitudes for surface measurements at 175 psia are shown in Table 9.1. They show that the magnitude of the disturbance increases from 0.52 to 0.62 meters. The RMS amplitude is approximately the same at 0.62 and 0.72 meters. However, at 0.86 meters RMS has decreased significantly. This decrease in disturbance magnitude is similar to that seen on the 30 to 35-degree models and shown in Section 7.2.7.

Table 9.1
Variation in RMS along the surface of the 25-degree cone-ogive-cylinder.

x (m)	0.52	0.56	0.62	0.72	0.86
RMS ($\frac{P'}{P_{mean}}$)	0.034	0.043	0.065	0.064	0.053

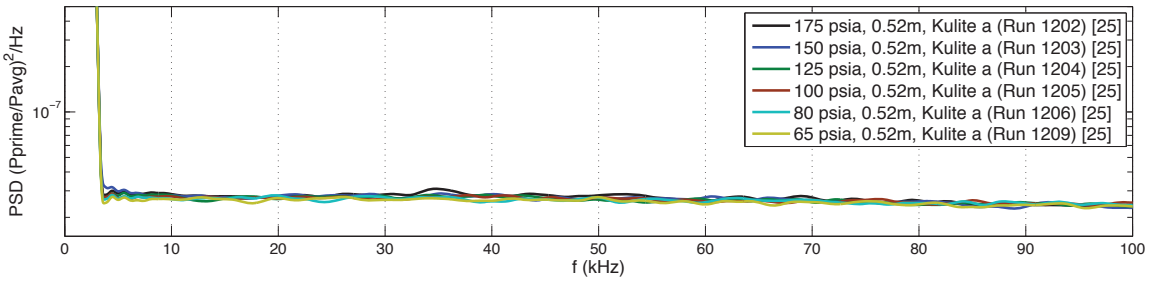

(a) Surface measurements at x=52cm.

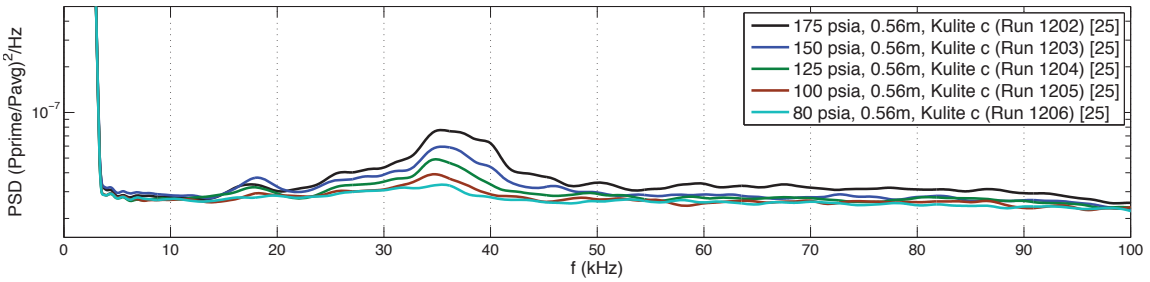

(b) Surface measurements at x=56cm.

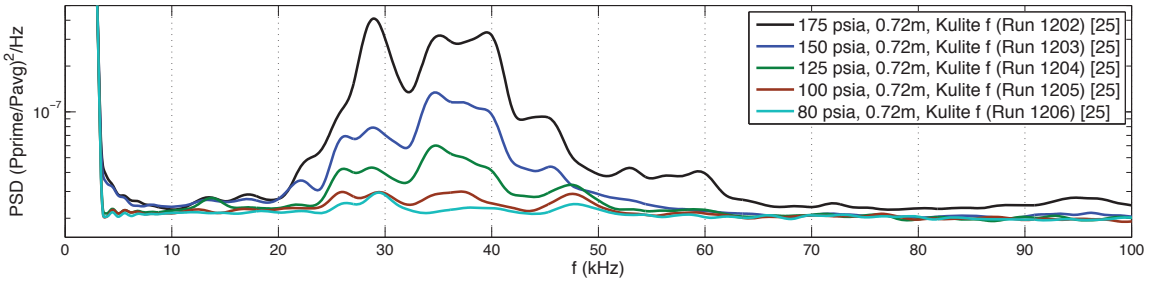

(c) Surface measurements at x=72cm.

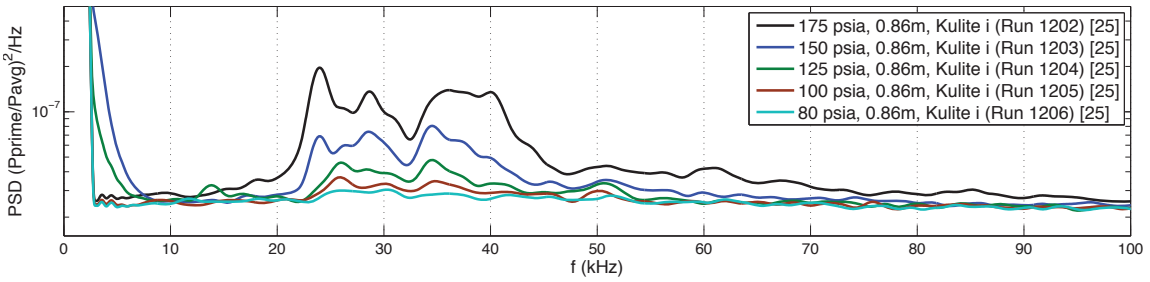

(d) Surface measurements at x=86cm.

Fig. 9.1. Power spectra of surface measurements at increasing axial locations on the 25-degree cone-ogive-cylinder.

9.2 Surface Measurements for the 30 to 35-degree Cone-Ogive-Cylinders

Figure 9.2 shows spectra from measurements at 0.56 meters. Spectra for each of the nosetip configurations are shown at four different Reynolds numbers. The green labels on each plot indicate the nosetip angle used to obtain that set of spectra. The blue and red labels under the legend for each plot indicate the height above the model that the maximum amplitude of the disturbance was measured with the hot wire. A summary of the heights where the disturbance is measured above each model is shown in Section 7.2.12. The labels are colored red where the measured disturbance is inside the predicted boundary layer ($\delta_{99.5}$) at 120 psia. When the disturbance height label is colored blue, that shows that the disturbance was measured above the predicted boundary layer.

Spectra for the 30 to 31-degree models in Figure 9.2 have distinct peaks between 15 and 50 kHz that decrease in frequency as the nosetip angle is increased. The 32-degree nosetip has similar spectra except for the peaks between 20 and 30-kHz for an $Re/m = 9.6 * 10^6$. The decrease in frequency with increasing nosetip angle shown in these spectra is similar to the characteristics seen in the spectra at 0.52 meters (Figure 7.14).

Spectra for measurements on the 33 and 34-degree nosetips start to show an increase in the magnitude of the higher-frequency peaks. Since the hot-wire measurements show that the disturbance is about 5.5 millimeters off the surface of the 33-degree model at this location, the disturbance should be just inside the edge of the boundary layer. For the 34-degree model, the disturbance at this location is approximately 4.5 millimeters above the surface.

Spectra for the 35-degree nosetip show a peak at about 35 kHz for the green and blue lines which are from measurements made at a unit Reynolds numbers of $4.1 * 10^6$ and $5.8 * 10^6$ per meter. The black line is from an $Re/m = 9.6 * 10^6$ and shows broadband low frequencies indicating that the boundary layer may be starting to become transitional (see Section 7.2.15).

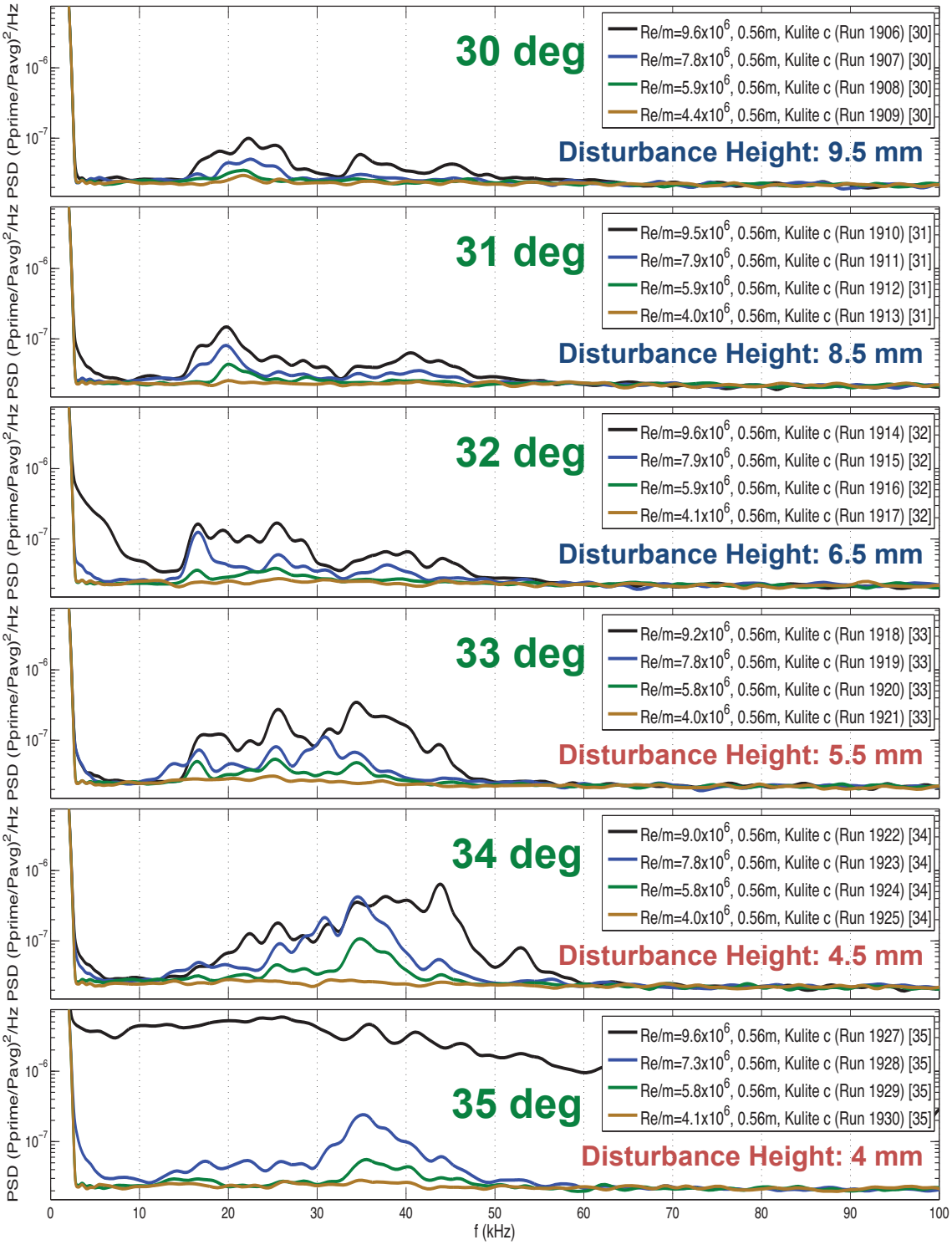

Fig. 9.2. Power spectra of surface measurements at 0.56 meters for the 30 to 35-degree cone-ogive-cylinder configurations.

The increase in magnitude for the higher-frequency peaks for the bigger nosetip angles in Figure 9.2 may be a result of the disturbance entering the boundary layer. A similar increase in the higher-frequency peaks was seen in the hot-wire spectra for measurements above the 33-degree model at 0.59 meters (see Figure 7.19(b)). Those measurements were made at 4.5 millimeters above the surface, just after the disturbance had entered the predicted boundary layer.

Figure 9.3 shows spectra from measurements at 0.62 meters. Spectra for the 30 to 32-degree nosetip configurations are shown at four different Reynolds numbers. The green labels on each plot indicate the nosetip angle used to obtain that set of spectra. The blue and red labels under the legend for each plot indicate the height above the model that the disturbance was measured with the hot wire. The label for the 30-degree plot is blue because the disturbance height was measured outside of the predicted boundary layer. The disturbance was measured inside the boundary layer for the 31 and 32-degree models so their labels are colored red.

Spectra for the 30-degree model in Figure 9.3 have distinct peaks between 20 and 45 kHz. Spectra for the 31-degree model show the higher-frequency peaks increase in magnitude. This is the same axial location where the disturbance starts to enter the boundary layer on the 31-degree model. This trend continues for the 32-degree model which has higher-frequency peaks of an even greater magnitude. These measurements also support the idea that as the disturbance enters the boundary layer, there is an increase of higher-frequency peaks in the spectra.

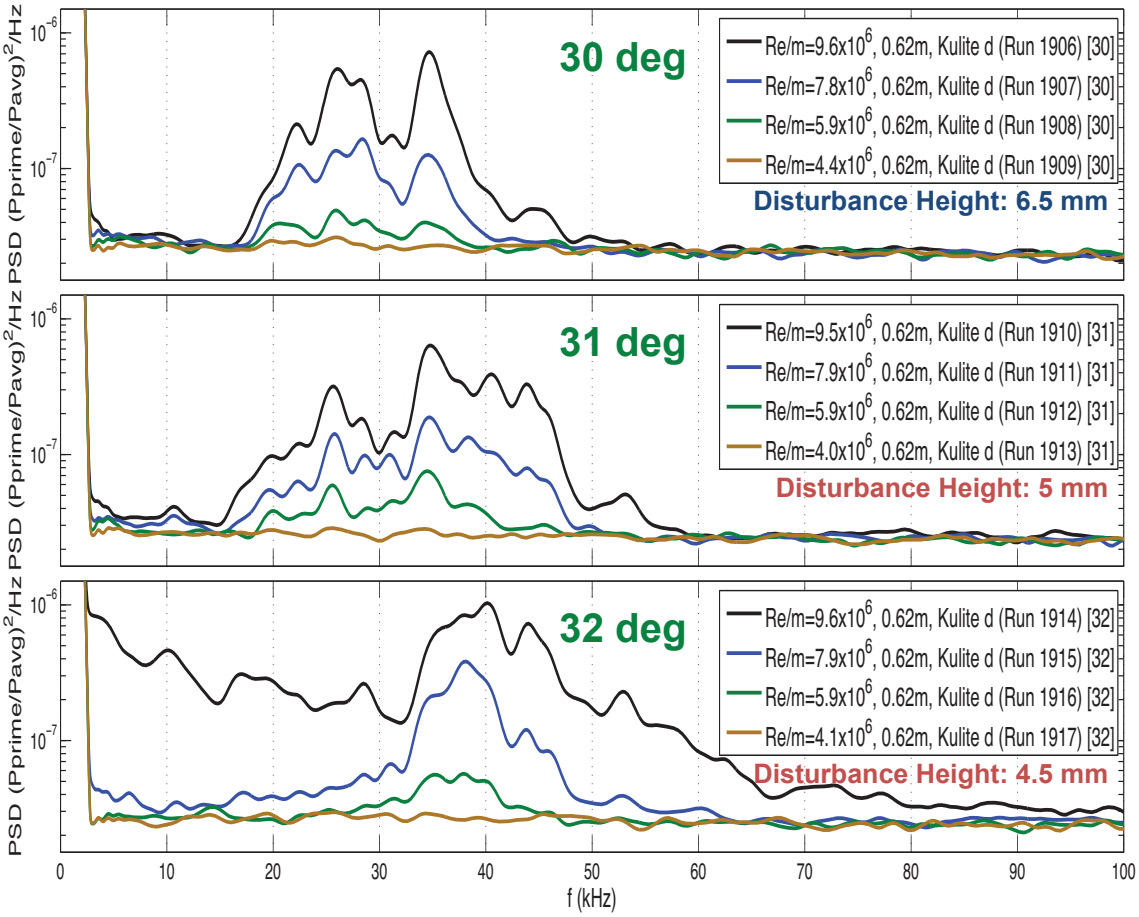

Fig. 9.3. Power spectra of surface measurements at 0.62 meters for the 30 to 35-degree cone-ogive-cylinder configurations.

9.3 Pitot Kulite Measurements for the Original Cone-Ogive-Cylinder

Pitot Kulite probe measurements were made at axial locations of 0.58 and 0.62 meters on the original cone-ogive-cylinder with the 28 and 30-degree nosetips. Measurements were made at discrete radial locations ranging from 2 to 26 millimeters above the model surface. Spectra for these pitot measurements showed no discernible disturbance inside the predicted boundary-layer thickness of approximately 5 millimeters. However, the power spectra for the measurements made outside of the boundary layer showed disturbances in the same frequency range as the disturbances measured by the surface sensors.

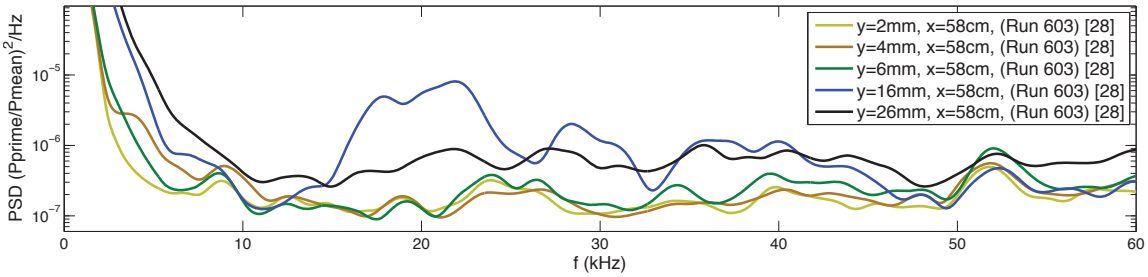

Fig. 9.4. Power spectra from Kulite pitot measurements above the original cone-ogive-cylinder at 0.58m (28-degree nosetip, P_0=165psia)

The power spectra from the measurements above the original cone-ogive-cylinder at 0.58 meters with the 28-degree nosetip installed are shown in Figure 9.4. The measurements were made at a few radial locations inside and outside the predicted boundary layer. No disturbance is measured inside the boundary layer. Spectra from the measurement at 16 millimeters from the model surface are shown by the blue line. They show peaks around 20 and 30 kHz with the biggest amplification around 22 kHz.

Figure 9.5 shows the spectra from measurements at 0.62 meters. The green line shows the spectra from measurements when the pitot probe is 6 millimeters off the surface. It shows peaks between 15 and 40 kHz. As with the measurements at 0.58 meters, the biggest amplification is near 22 kHz. It was not readily apparent from

these experiments why the 22 kHz disturbance was measured much closer to the model at 0.62 meters than 0.58 meters.

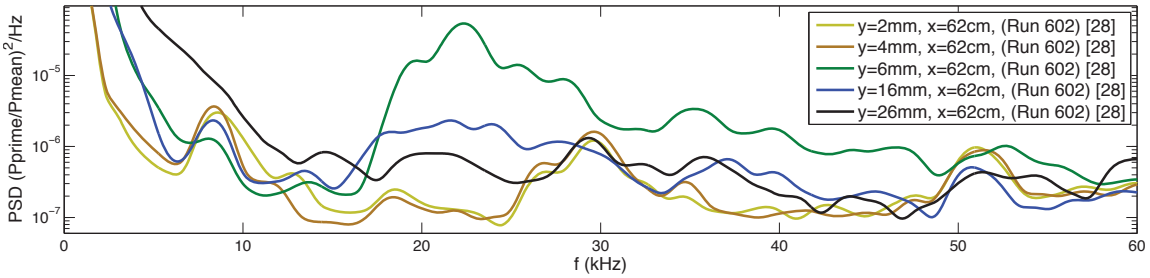

Fig. 9.5. Power spectra from Kulite pitot measurements above the original cone-ogive-cylinder at 0.62m (28-degree nosetip, P_0=165psia)

The results are similar with the 30-degree nosetip installed. The power spectra from the measurements at 0.62 meters are shown in Figure 9.6. As with measurements using the 28-degree nosetip, no disturbances were identified inside the predicted boundary-layer thickness and the most amplified disturbance is measured at 6 millimeters off the surface.

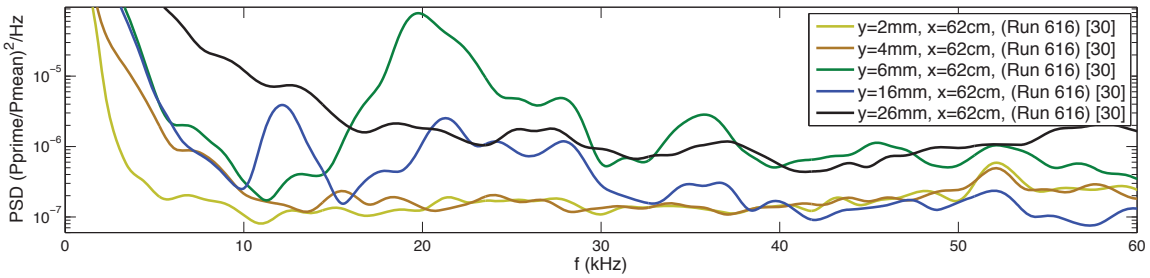

Fig. 9.6. Power spectra from Kulite pitot measurements above the original cone-ogive-cylinder at 0.62m (30-degree nosetip)

The pitot Kulite measurements were not very clear. However, the spectra from measurements did show peaks in the same frequency range as the surface measurements. These spectral peaks were also found only in measurements outside of the boundary layer. These observations provided justification to continue the experimental investigation with hot wires.

9.4 Hot-Wire Measurements

9.4.1 Hot-wire Spectra

Even with proper tuning, each hot wire has characteristic spectra that are more or less "clean". Some of the hot wires, no matter how well they are tuned, produce measurements with large spectral peaks that are independent of the flow. An example of the power spectra derived from one of these hot-wire measurements is shown in Figure 9.7(a). The spectra show large peaks between 50 and 80 kHz which are not flow instabilities. They may be due to vibrational characteristics or strain gauging problems of the hot wire. An example of a much cleaner power spectra from another hot wire is shown in Figure 9.7(b). These measurements were taken over the same model, at the same location, and under the same flow conditions. The power spectra from both hot-wire measurements show the same instability peaks between 15 and 40 kHz. However, the cleaner spectra is much easier to analyze.

Post-processing can cometimes remove these hot-wire specific peaks, however, analysis of measurements made with hot wires with cleaner spectra is much easier and faster. Analysis is particularly difficult when the hot-wire specific peaks are close to the flow instability peaks. For this reason, an analysis of the characteristic spectra of each hot wire used should be conducted early on.

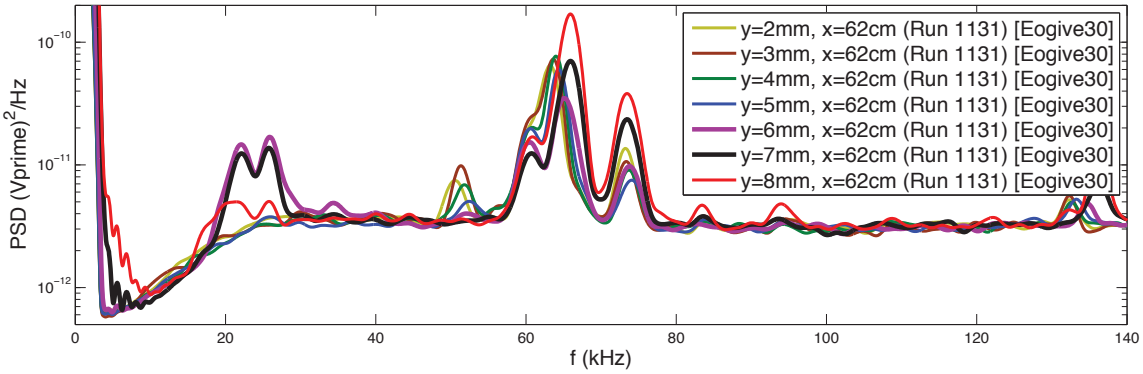

(a) Example of a power spectra with peaks that are hot-wire specific, in this case there are large frequency peaks between 60 and 80 kHz that are not a result of any flow instability

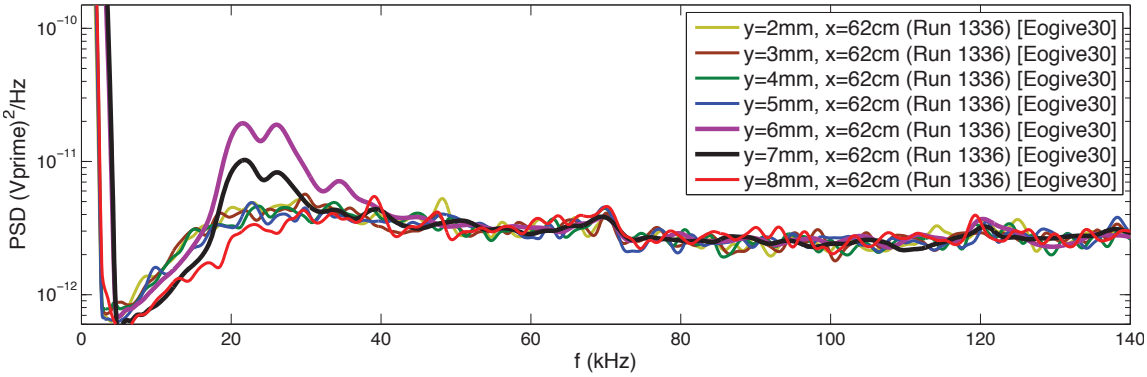

(b) Example of a clean power spectra.

Fig. 9.7. Comparison of two power spectra from different hot wires at x=0.62m and at various distances above the 30-degree cone-ogive-cylinder. The peaks between 20 and 30 kHz for the purple and black traces (6 and 7mm) are due to the measured instability and are common between the two spectra.

9.4.2 Hot-wire Measurements above the 31-degree Cone-Ogive-Cylinder

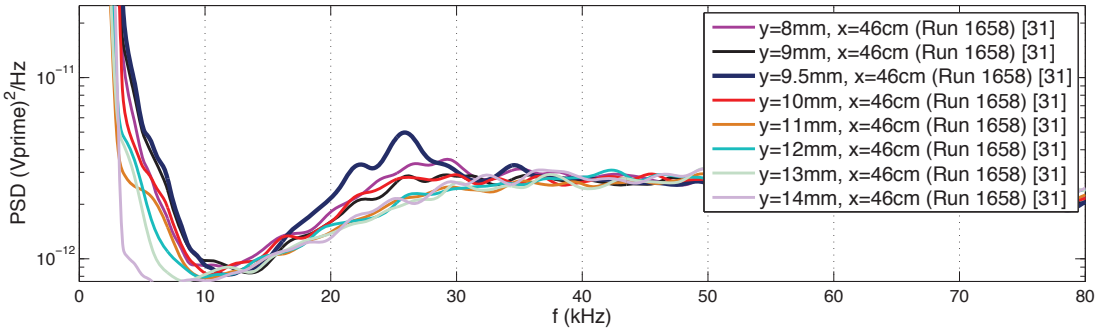

(a) Hot-wire PSD above the 31-degree model at x=0.46m, P_0=120psia.

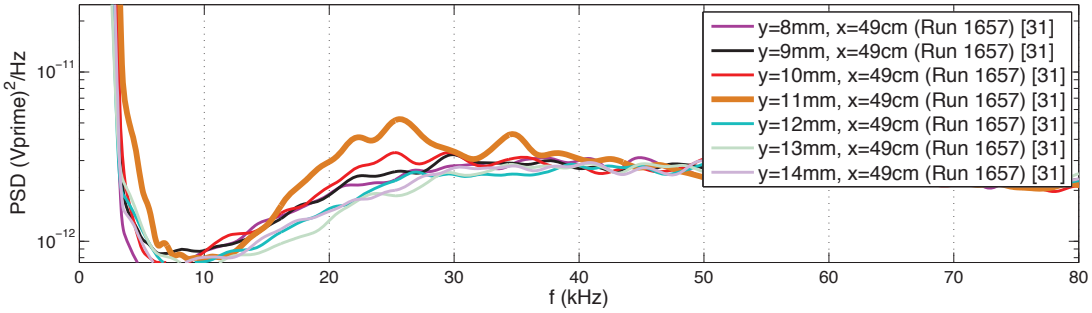

(b) Hot-wire PSD above the 31-degree model at x=0.49m, P_0=120psia.

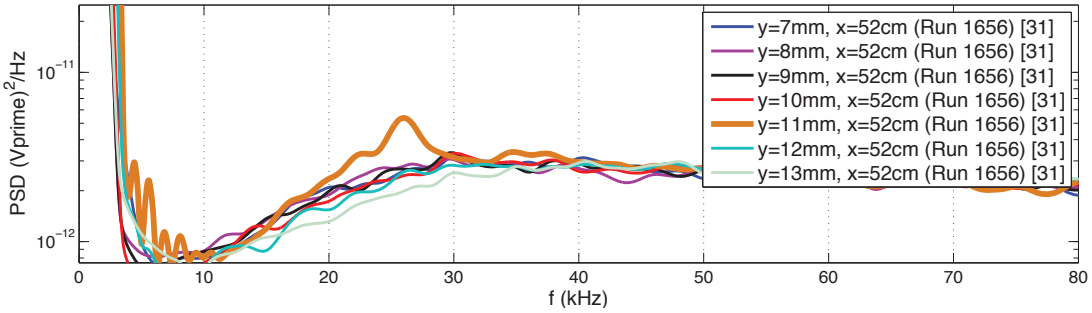

(c) Hot-wire PSD above the 31-degree model at x=0.52m, P_0=120psia.

Fig. 9.8. Power spectra from hot-wire measurements above the 31-degree cone-ogive-cylinder at several axial locations after the instability starts to become visually distinguishable in the power spectra.

Spectra from hot-wire measurements above the surface of the 31-degree model at six axial locations from 0.46 to 0.62 meters are shown in Figures 9.8 and 9.9. The

measured disturbance increases in magnitude and approaches the model as it proceeds downstream.

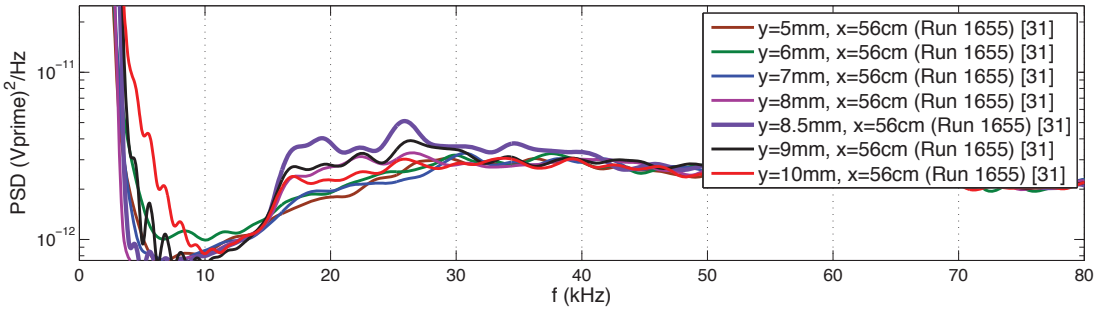

(a) Hot-wire PSD above the 31-degree model at x=0.56m, P_0=120psia.

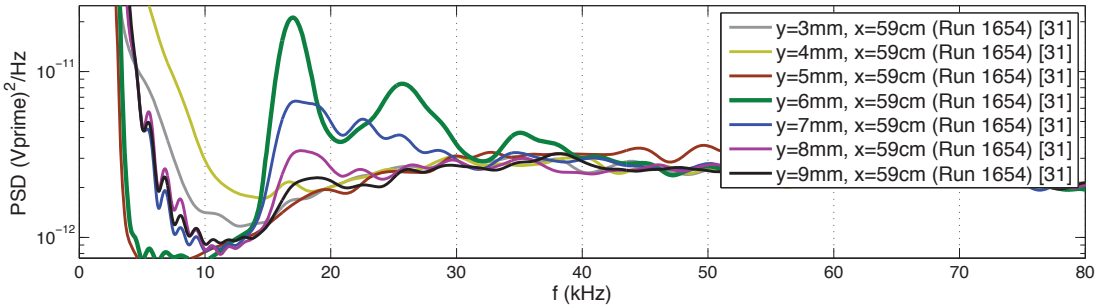

(b) Hot-wire PSD above the 31-degree model at x=0.59m, P_0=120psia.

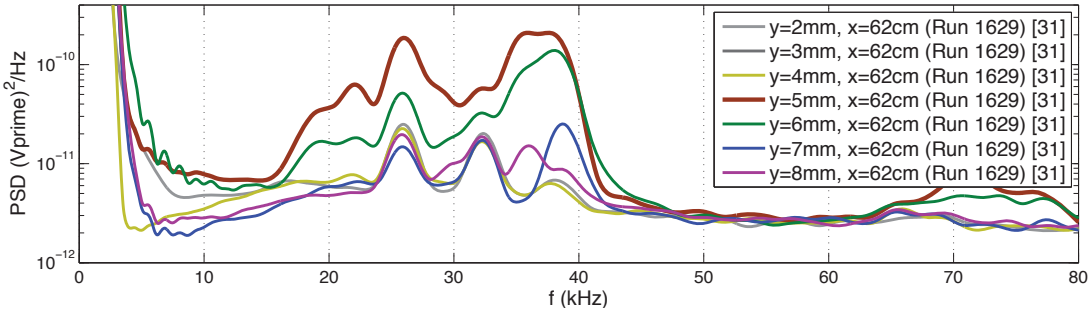

(c) Hot-wire PSD above the 31-degree model at x=0.62m, P_0=120psia.

Fig. 9.9. Power spectra from hot-wire measurements above the 31-degree cone-ogive-cylinder at several axial locations showing the instability approach the model as it proceeds downstream.

The same hot wire was used at each of these axial locations to measure the disturbance, except for that shown in Figure 9.9(c). The measurement from which that

power spectra was calculated used a 0.0003" hot wire that broke during the shutdown of that particular run. A closer inspection of this power spectra shows some peaks between 20 and 40 kHz that are independent of the flow condition.

9.4.3 Hot-wire Measurements above the 32-degree Cone-Ogive-Cylinder

Spectra from three locations on the 32-degree model are shown in Figure 9.10. They show the disturbance approach the model and enter the predicted boundary layer as it proceeds downstream. Spectra from the last measured location of 0.62 meters (Figure 9.10(c)) show the disturbance about 4-4.5 millimeters off the model surface. Spectra at that location show an increase in the magnitude of the higher-frequency peaks. This is similar to what is seen in the surface spectra in Section 9.2 as the disturbance enters the boundary layer.

9.4.4 Hot-wire Measurements above the 34-degree Cone-Ogive-Cylinder

Figure 9.11 shows spectra from measurements at three axial locations from 0.49 to 0.59 meters on the 34-degree cone-ogive-cylinder configuration. As was shown with each of the configurations, the disturbance is first measured outside of the boundary layer and then approaches the model and enters the boundary layer as it proceeds downstream. At 0.56 meters (Figure 9.11(b)), the instability has a locus of about 4.5 millimeters off the model surface.

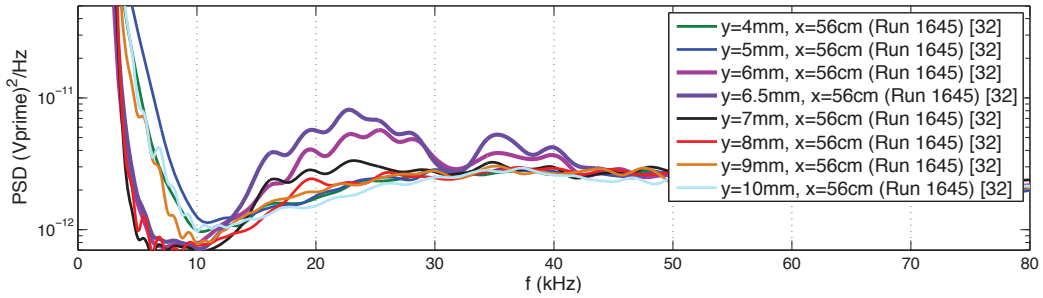

(a) Hot-wire PSD above the 32-degree model at x=0.56m, P_0=120psia.

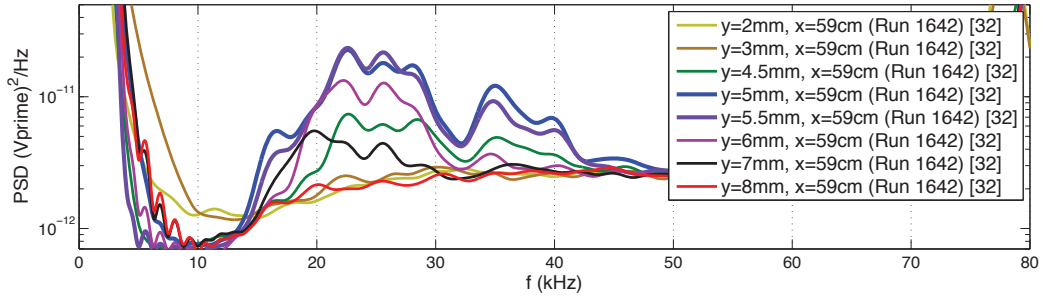

(b) Hot-wire PSD above the 32-degree model at x=0.59m, P_0=120psia.

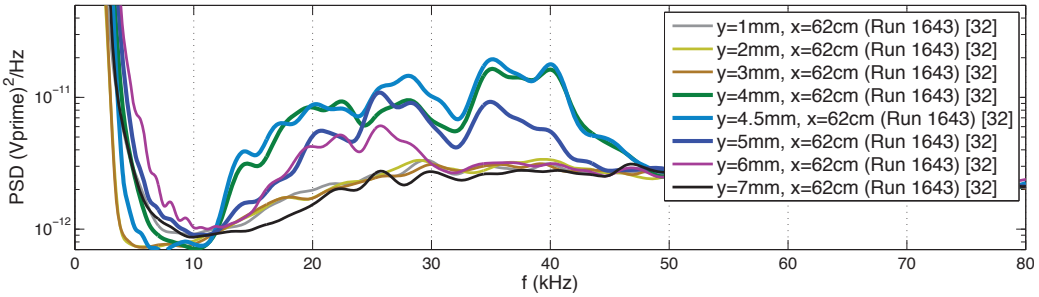

(c) Hot-wire PSD above the 32-degree model at x=0.62m, P_0=120psia.

Fig. 9.10. Power spectra from hot-wire measurements above the 32-degree cone-ogive-cylinder at several axial locations showing the instability grow in magnitude and approach the model as it proceeds downstream.

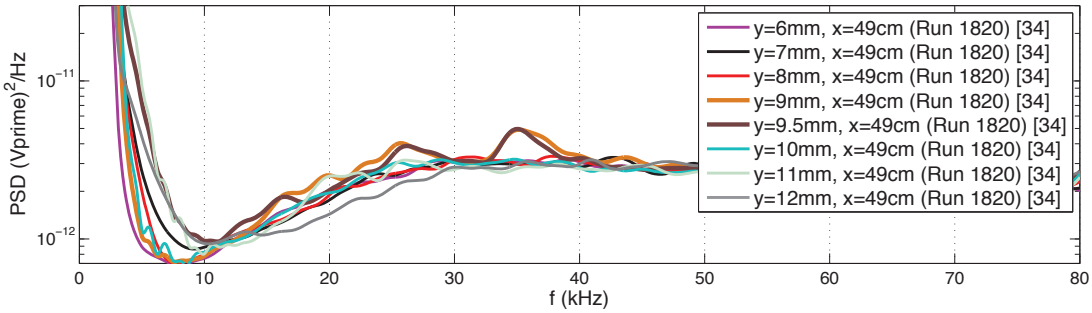

(a) Hot-wire PSD above the 34-degree model at x=0.49m, P_0=120psia.

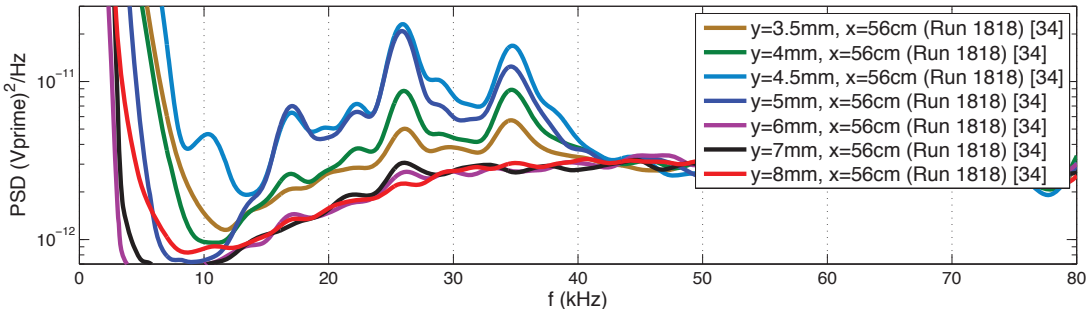

(b) Hot-wire PSD above the 34-degree model at x=0.56m, P_0=120psia.

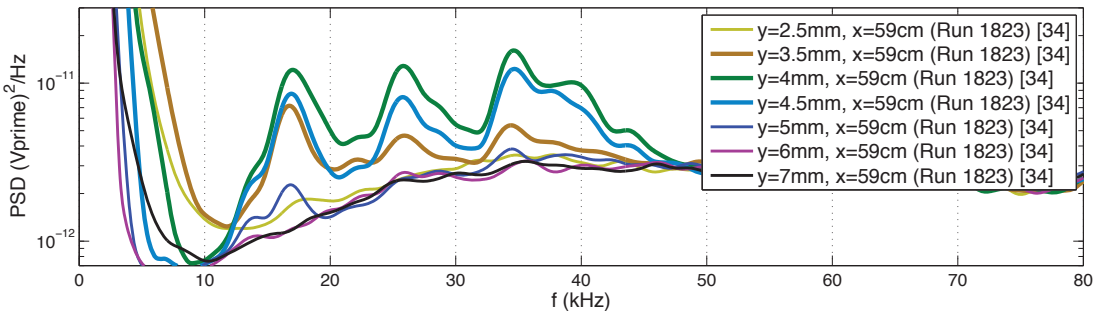

(c) Hot-wire PSD above the 34-degree model at x=0.59m, P_0=120psia.

Fig. 9.11. Power spectra from hot-wire measurements above the 34-degree cone-ogive-cylinder at three axial locations showing the disturbance approach the model as it proceeds downstream.

9.4.5 Hot-Wire Measurements using the Ball Valve to Operate the BAM6QT

Figure 9.12 shows an image of the digital oscilloscope screen after five seconds of hot-wire measurements when using the ball valve to operate the tunnel. Large fluctuations in the hot-wire voltage traces show up for a longer period of time at the beginning and end of the measurements when using the ball valve for tunnel operation than when using a diaphragm. The longer period of high fluctuations occurs because of the time required to open the ball valve fully. The screen traces shown in the Figure 7.15 were from a diaphragm run.

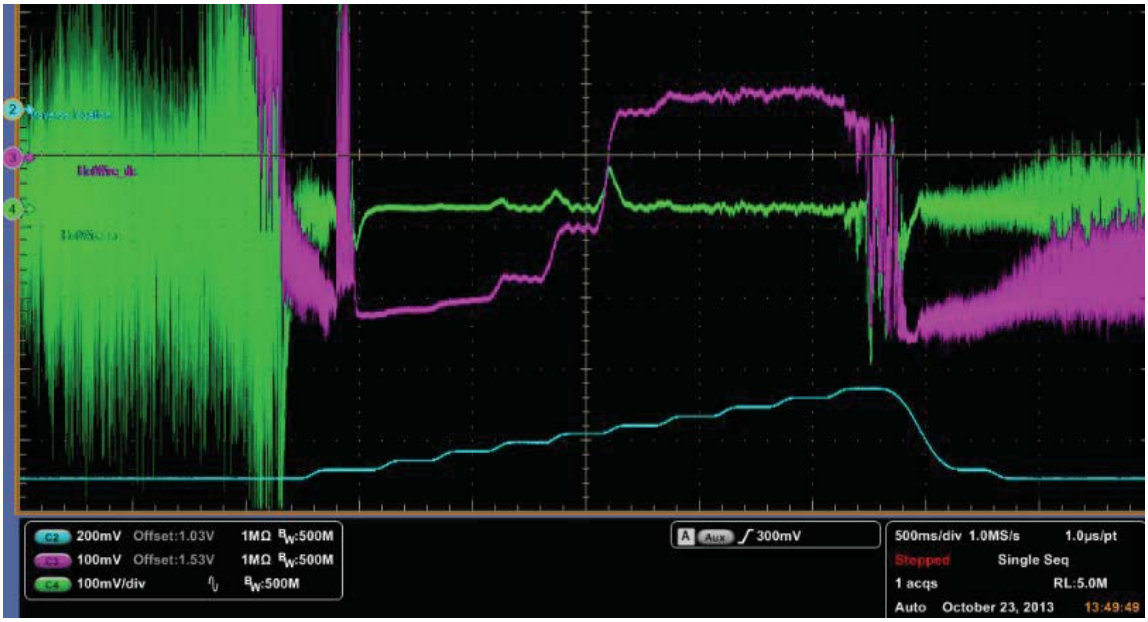

Fig. 9.12. Image of hot-wire voltage traces during measurements over the 30-degree cone-ogive-cylinder at x=0.62 meters (Run 1336, P_0=120psia).

Because of this, using the ball valve to start the BAM6QT decreases the amount of time available to make measurements. At 120 psia, a run using the ball valve typically gets between 2 and 2.5 seconds of quiet flow. Quiet run times of about 3.5 seconds are typical for runs at the same pressure using a diaphragm. Other than the duration of quiet flow, there seems to be little difference between hot-wire measurements made

using the ball valve instead of a diaphragm. Figure 9.13 shows the power spectra from two consecutive runs above the 32-degree model. The solid lines show the spectra from measurements made during the run that used a diaphragm. The dashed lines show the spectra from measurements made during a run using the ball valve. The spectra shows little difference in the magnitude or frequency of the measured disturbances. However, the diaphragm run had 3.55 seconds of quiet flow while the ball valve run had only 2.4 seconds.

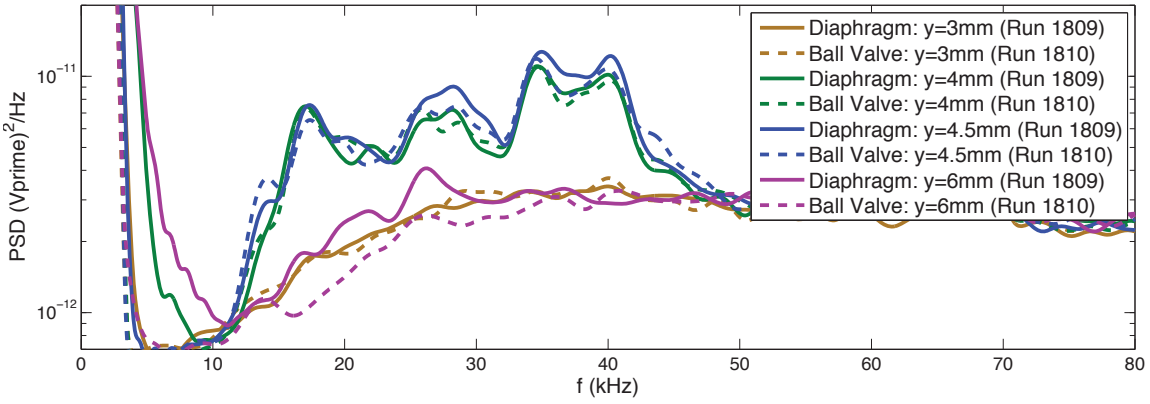

Fig. 9.13. Comparison of the power spectra from runs using a diaphragm (Run 1809) and a ball valve (Run 1810). Both runs were over the 32-degree cone-ogive-cylinder at 0.62 meters (P_0=120psia).

9.5 Effect of Reynolds Number on the Measured Instability

Entropy-layer instabilities are an inviscid phenomenon and are expected to be weakly sensitive to Reynolds number [113]. In order to show the effect of the Reynolds number on the measured disturbance, spectra from measurements at three different stagnation pressures are shown in Figure 9.14. These measurements were made at 0.62 meters using the 30-degree model. In each plot, the purple line shows spectra from when the hot wire was 6 millimeters off the model surface. That was the location at each stagnation pressure that the largest disturbance signal was measured. Each plot has two main peaks at about 20 and 25 kHz. The disturbance is barely visible

in the spectra when measured at a tunnel stagnation pressure of 90 psia. As the stagnation pressure is increased, the peaks in the spectra showing the disturbance become much larger.

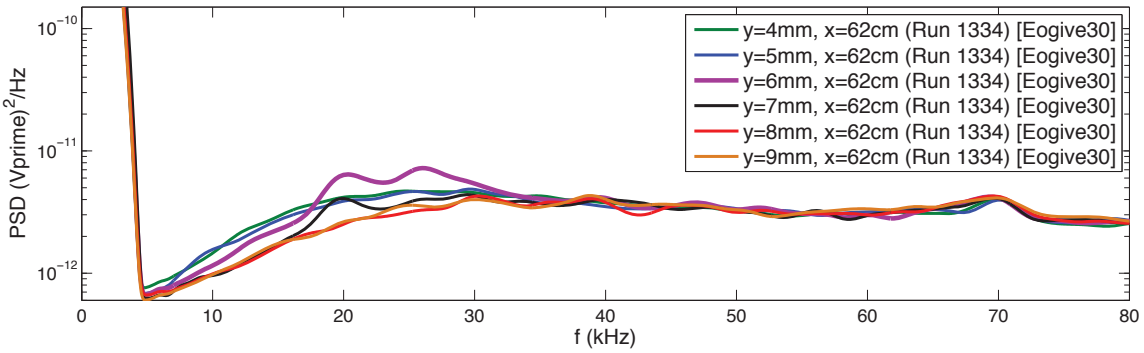

(a) Power spectra showing the measured instability for P_0=90psia ($Re/m = 5.1 * 10^6$).

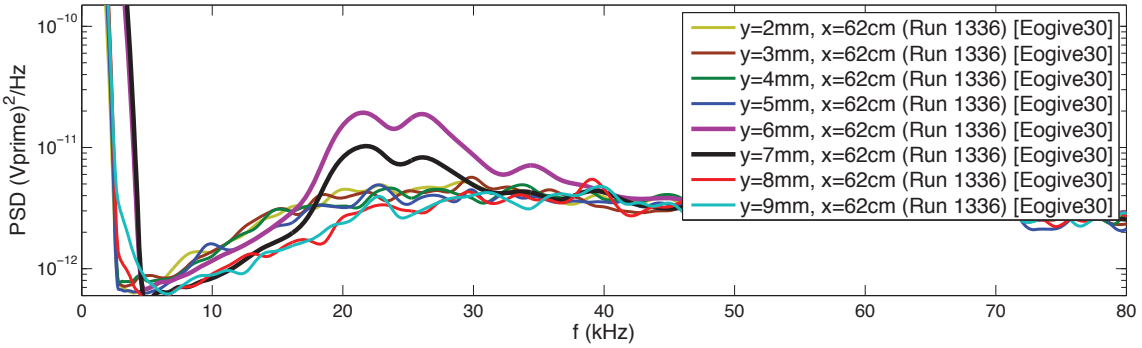

(b) Power spectra showing the measured instability for P_0=120psia ($Re/m = 6.8 * 10^6$).

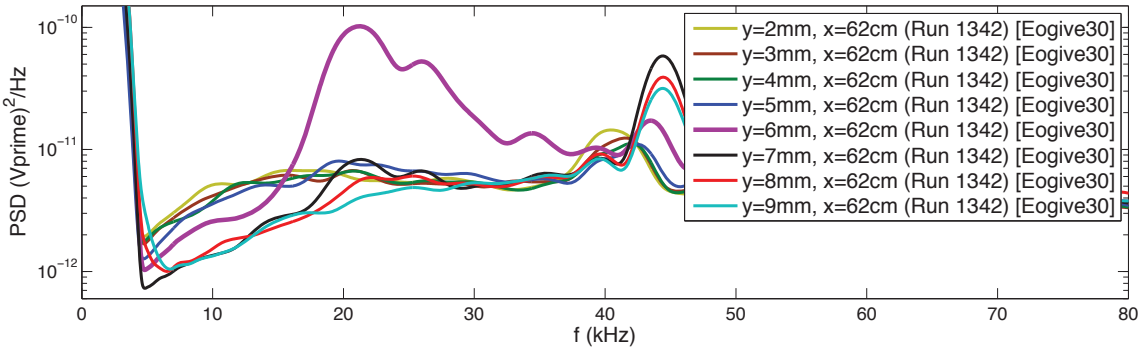

(c) Power spectra showing the measured instability for P_0=135psia ($Re/m = 9.3 * 10^6$).

Fig. 9.14. Hot-wire measurements above the 30-degree cone-ogive-cylinder at 62 cm under various Reynolds number flow conditions.

As the stagnation pressure is increased, the location and frequency of the measured disturbance remain constant. However, the disturbance magnitude increases with the Reynolds number. Two peaks between 40 and 50 kHz appear on the power spectra for the 135 psia measurement (Figure 9.14(c)). They do not appear to be part of the measured instability. It is unknown whether they come from a flow instability or are a result of an unclean spectra for that particular hot wire.

The RMS values for each of the measurements at 6 millimeters above the 30-degree cone-ogive-cylinder are shown in Table 9.2. It compares the unit Reynolds number in the BAM6QT to the RMS calculated from the hot-wire measurement over the frequency range of 10 to 50 kHz. The Reynolds number increases as the stagnation pressure is increased from 90 to 135 psia. This increase in Reynolds number results in the RMS nearly doubling in magnitude.

Table 9.2
Effect of Reynolds number on instability RMS measured with the hot wire above the 30-degree cone-ogive-cylinder.

Re/m	$5.1 * 10^6$	$6.8 * 10^6$	$7.7 * 10^6$
RMS ($\frac{V'}{V_{mean}}$)	0.036	0.046	0.070

9.6 Wave-Angle Calculations using Azimuthally-Displaced Surface Measurements

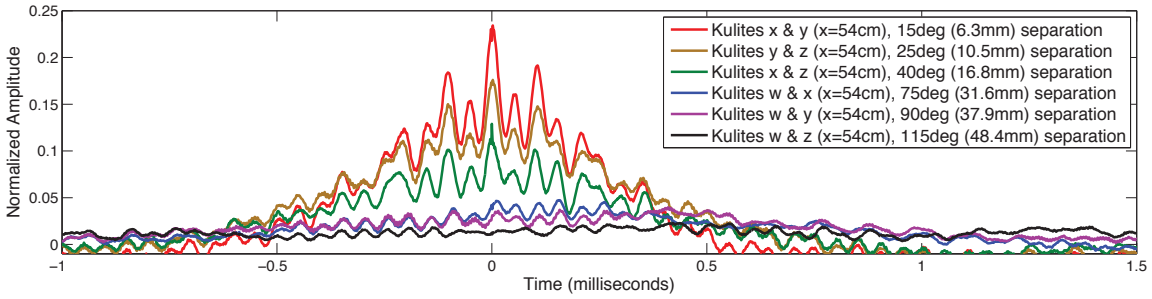

Fig. 9.15. Cross-correlation of the azimuthally-displaced surface Kulites (Run 1707, P_0=170psia).

The normalized correlation values for pairs of measurements from the azimuthally-displaced sensors on the 32-degree model are shown in Figure 9.15. For each correlation, the peak with the highest magnitude is at a time lag of zero. The smaller peaks for positive and negative time delays appear when the repeating frequencies of the two signals become more in phase. Measurements with the three sensors with the closest proximity all have normalized correlation values greater than 0.1. This correlation peak decreases as the distance between the sensors increases.

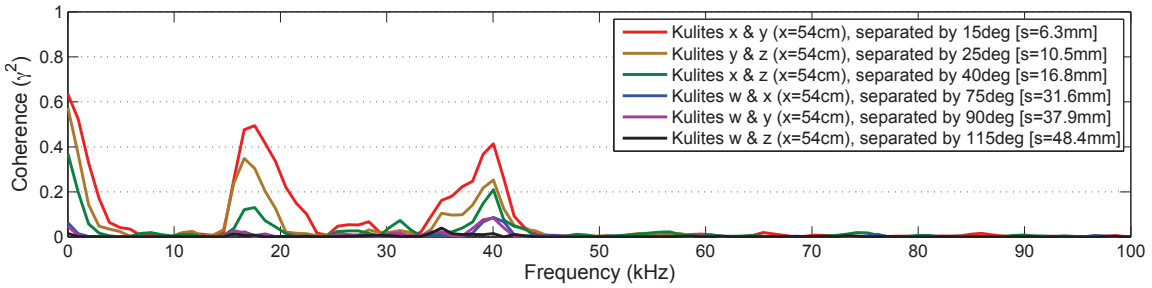

Fig. 9.16. Coherence between azimuthally-displaced surface Kulites at x=54cm (Run 1707, 32-degree cone-ogive-cylinder).

The coherence between measurements on the same 32-degree model is shown in Figure 9.16. The coherence decreases as the distance between the sensors increases.

There is no significant coherence between the sensors that are azimuthally-displaced by more than 75 degrees (30 mm).

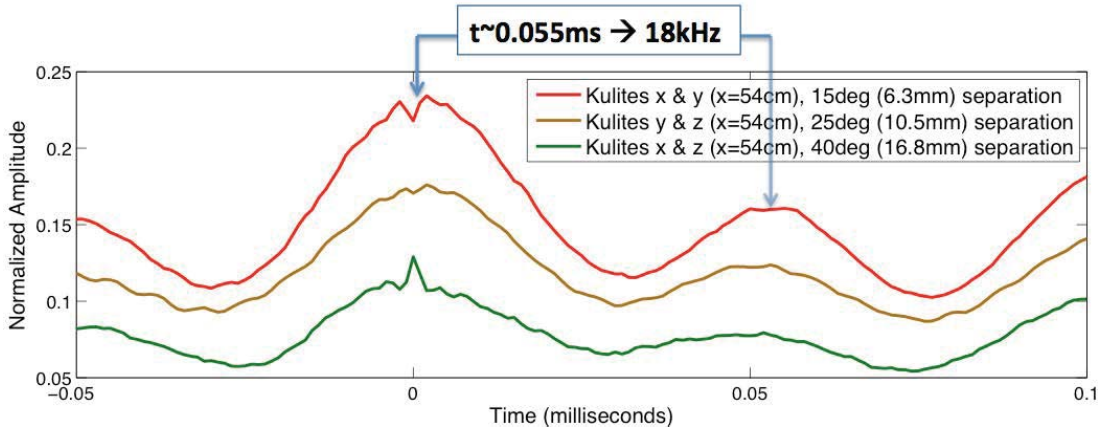

Fig. 9.17. Close-up look at the cross-correlation of the azimuthally-displaced surface Kulites (Run 1707, 32-degree cone-ogive-cylinder).

A closer look at the correlation traces is shown in Figure 9.17. It shows the normalized correlation values between the three closest pairs of sensors. All three pairs show a maximum at time zero, indicating a two-dimensional instability. The time between the peak at zero and the next peak is also noted. This time corresponds to a frequency of about 18 kHz. This is the same frequency found in the power spectra and the coherence (Figure 9.16).

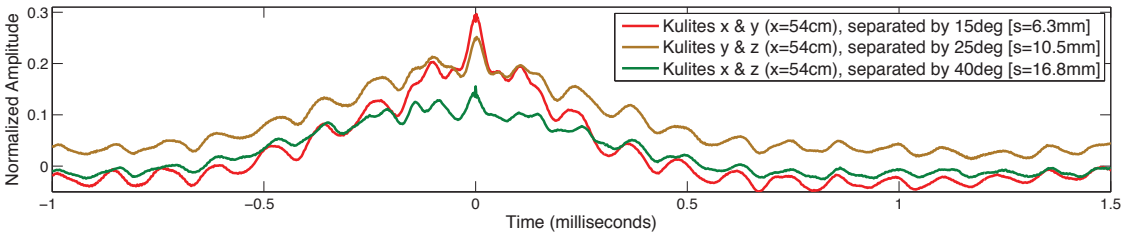

Fig. 9.18. Cross-correlations between azimuthally-displaced surface Kulites on the 33-degree cone-ogive-cylinder at x=54cm (Run 1710, P_0=170psia)

Cross-correlations between azimuthally-displaced sensors using the 33-degree model are shown in Figure 9.18. As with the 32-degree model, cross-correlations between pairs of the closest sensors have a maximum correlation at time zero indicating an axisymmetric instability.

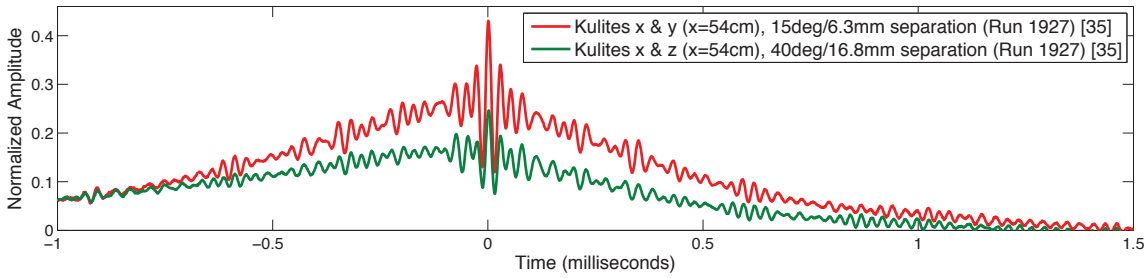

Fig. 9.19. Cross-correlations between azimuthally-displaced surface Kulites on the 35-degree cone-ogive-cylinder at x=54cm (Run 1927, P_0=160psia).

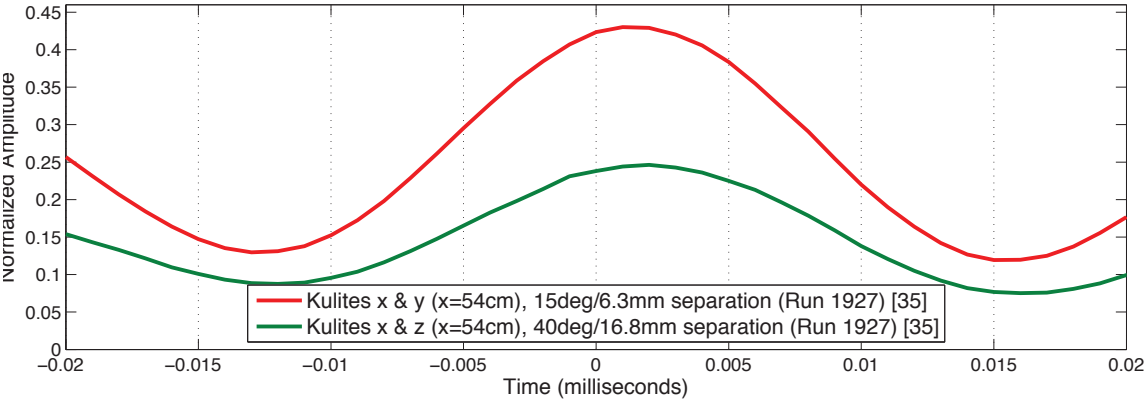

Fig. 9.20. Close-up view of cross-correlations between azimuthally-displaced surface Kulites on the 35-degree cone-ogive-cylinder at x=54cm (Run 1927, P_0=160psia).

Cross-correlations between azimuthally-displaced sensors using the 35-degree model are shown in Figure 9.19. As with the 32 and 33-degree models, the cross-correlations appear to show a maximum correlation near time zero indicating an axisymmetric instability. However, when the horizontal axis range is reduced as shown in Figure 9.20,

it can be seen that the maximum correlation is slightly different than zero. The time lag for each of these sets of sensors and the corresponding calculated wave angles are shown in Table 9.3. Additional measurements are necessary to determine if the instability above the 35-degree model has a consistently oblique wave front or if this is within the experimental variability.

Table 9.3
Time lag measured between azimuthally-displaced sensors on the 35-degree cone-ogive-cylinder at 0.54m (Run 1927, P_0=160psia).

Separation (mm)	Time Lag (milliseconds)	Wave Angle (degrees)
6.32	0.0012	8.6
16.85	0.002	5.4

9.7 Convection-Velocity Calculations using Axially-Displaced Surface Measurements

Cross-correlations between axially-displaced surface sensors were used to calculate the approximate convection velocity of the disturbance. Figure 9.21 shows the cross-correlations between measurements at four axial locations on the 34-degree model. The blue and black lines correspond to sensors that are separated by 2 centimeters. The orange line shows the correlation between measurements a distance of 6 centimeters apart.

The velocity is calculated by dividing the distance between the two sensors by the time of highest correlation. Figure 9.22 shows a close-up view of the correlations between the first three sensors. It is marked to show the time of greatest correlation between each set of sensors. They also indicate the velocity to which this time difference corresponds.

The instability appears to have a convection velocity about equal to the flow velocity. Computations show a flow velocity of about 837 meters per second just outside

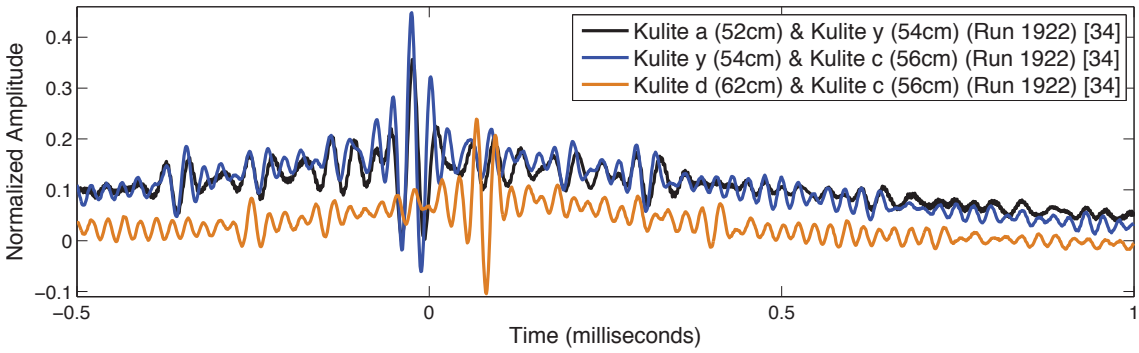

Fig. 9.21. Cross-correlation of axially-displaced surface sensors on the 34-degree cone-ogive-cylinder (P_0=160psia).

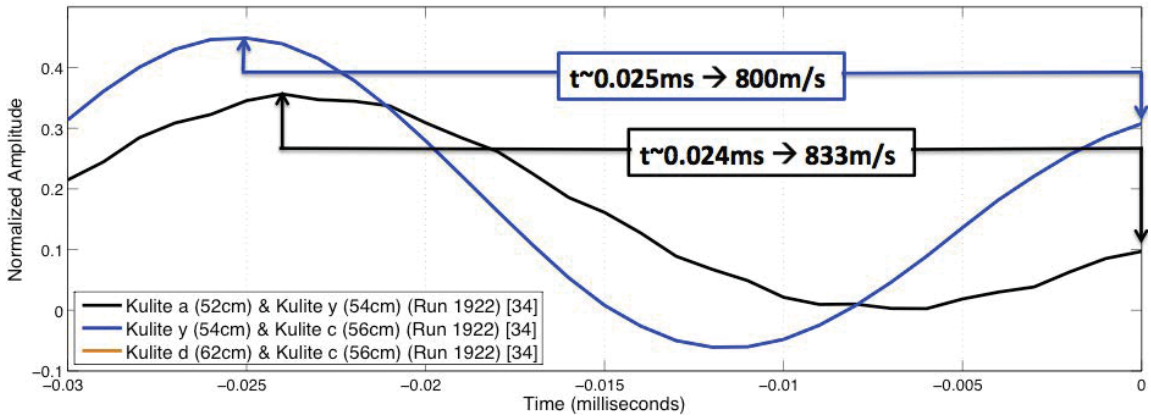

Fig. 9.22. Cross-correlation of axially-displaced surface sensors on the 34-degree cone-ogive-cylinder zoomed in and annotated to show the time lapse between the highest correlation and time zero.

of the boundary layer on the 34-degree model. The velocity calculated between 0.52 and 0.54 meters is 833 meters per second. The calculated velocity between the 0.54 and 0.56 meters is 800 meters per second, slightly slower than the computationally-predicted flow velocity.

9.8 Cross-Correlations of Surface and Hot-Wire Measurements

An example of the coherence when the disturbance was measured further from the model is shown in Figure 9.23. The hot wire for this measurement is 11 millimeters off the surface. At this height, there are still coherence peaks of almost 0.6.

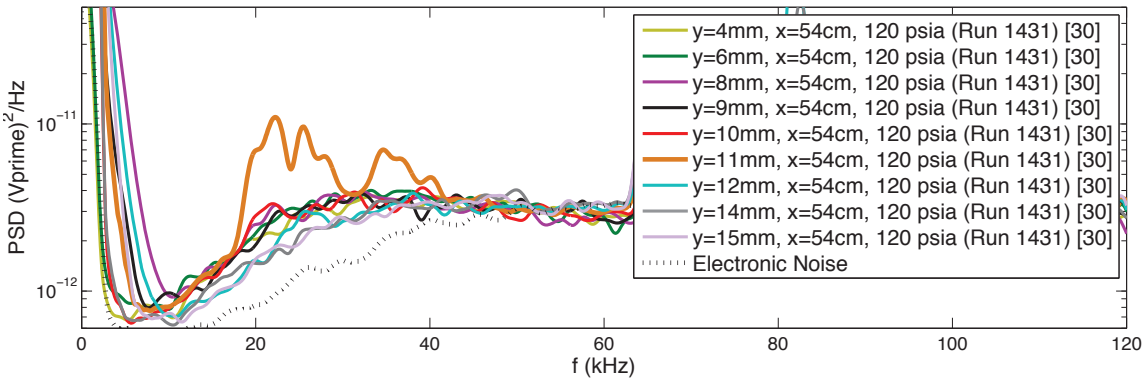

(a) Power spectra of hot-wire measurements above the 30-degree cone-ogive-cylinder at 52 cm.

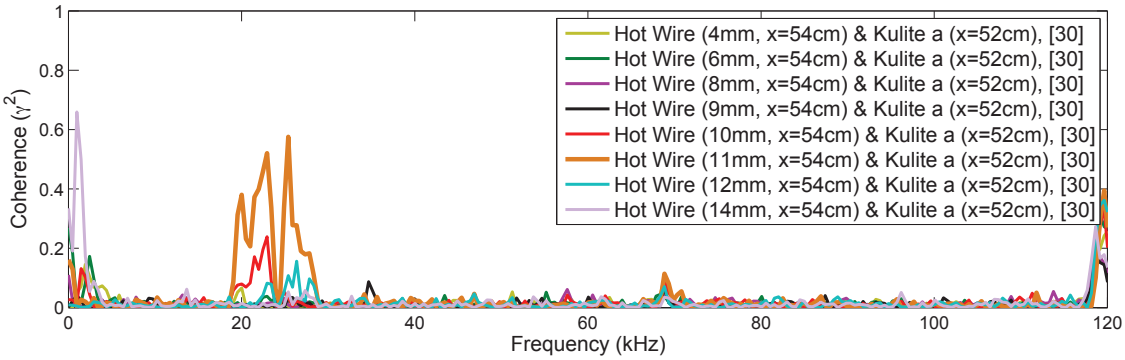

(b) Coherence between the hot-wire measurement at 0.54m and the surface measurement at 0.52m on the 30-degree cone-ogive-cylinder (Run 1431).

Fig. 9.23. Power spectra of the hot-wire measurements and their coherence with surface measurements for Run 1431 ($P_0 = 120$psia).

9.9 Cross-Correlations between Axially and Radially-Separated Sensors.

The coherence is also affected by axial displacement. Figure 9.24(b) shows the coherence between the hot-wire and surface sensors over the 33-degree cone-ogive-cylinder. Spectra from the hot-wire measurements are shown in Figure 9.24(a). The vertical distance between the hot wire and the surface sensor varied between 1 and 7 millimeters for these measurement. In addition, the hot wire was 0.1 meters downstream of the surface sensor. With this amount of separation, the highest coherence peak is about 0.5 when the hot wire is 4 millimeters from the surface.

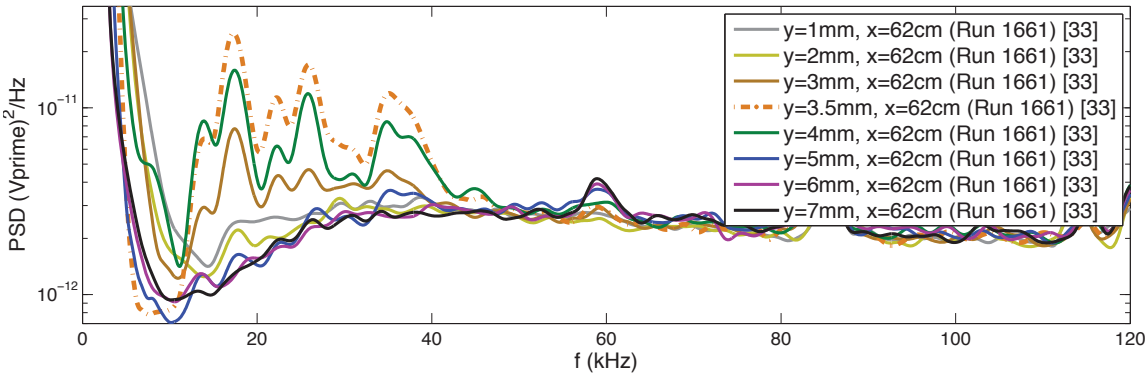

(a) PSD of hot-wire measurements above the 33-degree cone-ogive-cylinder at 62 cm.

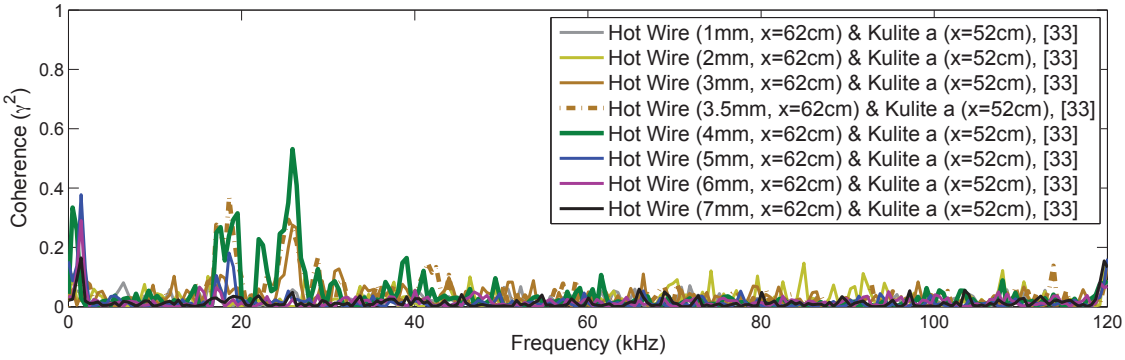

(b) Coherence between Hot-Wire and Surface Measurements (Run 1661).

Fig. 9.24. Power spectra of hot-wire measurements and their coherence with surface measurements at 62 cm using the 33-degree model (Run 1661).

Figure 9.25(a) shows the schematic of an experiment measuring the effect of axial distance on the coherence when the hot wire is 4 millimeters above the surface. The coherence values of measurements between the hot wire and surface sensors are shown in Figure 9.25(c). There is high coherence between the signals from each of the surface sensors in front of the hot wire and the hot-wire measurement. However, as expected, the coherence decreases slightly as the distance increases. The surface sensor behind the hot wire is shown by the black line and has no appreciable coherence. This is likely because of the flow interference caused by the hot wire inserted above the model.

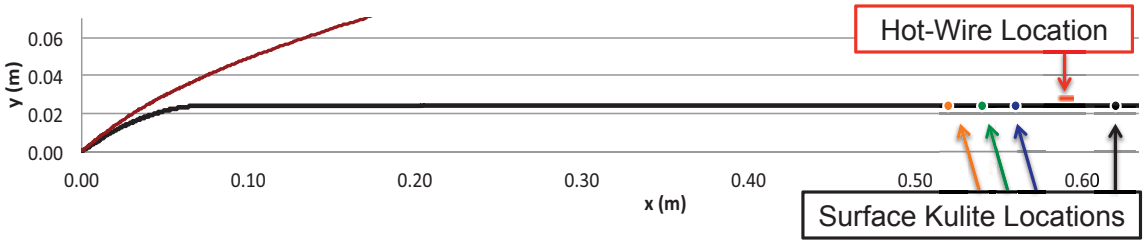

(a) Schematic showing the location of the hot-wire and surface sensor measurements.

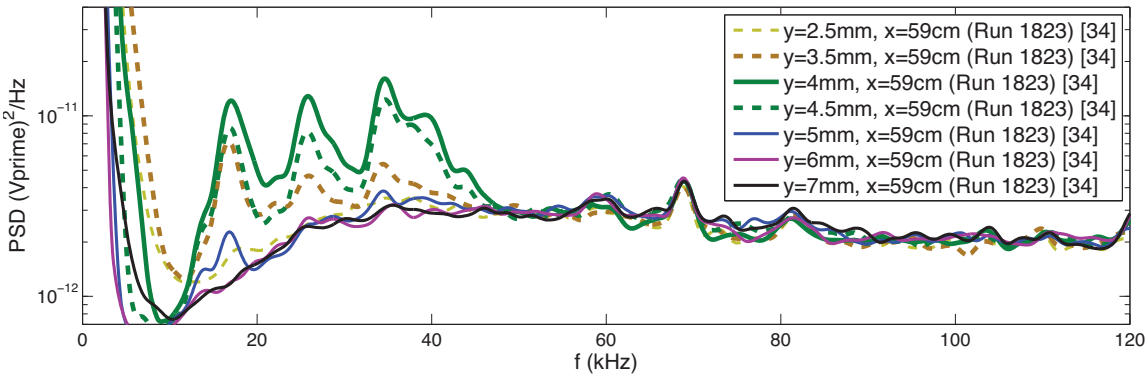

(b) PSD of hot-wire measurements above the 34-degree cone-ogive-cylinder at 59 cm.

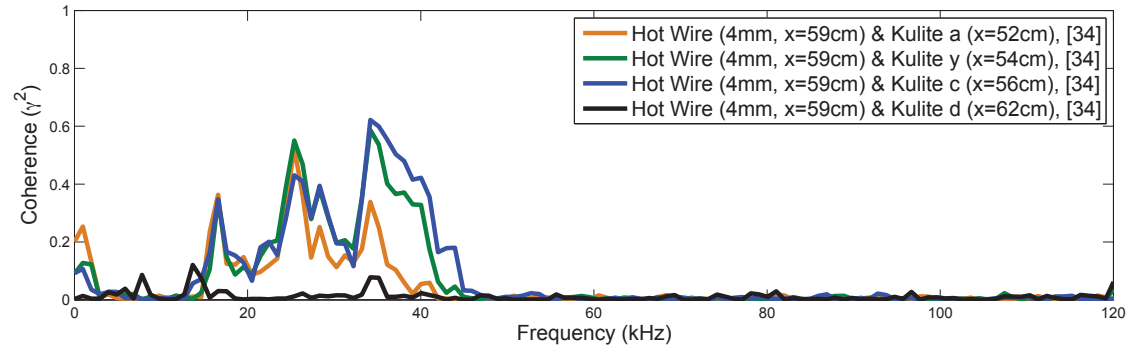

(c) Coherence between Hot-Wire measurements at 59 cm, and Surface Measurements at 52, 54, 56, and 62 cm (Run 1823).

Fig. 9.25. Power spectra of hot-wire measurements and their coherence with surface measurements at 59 cm using the 34-degree model.

10. SUMMARY AND CONCLUSIONS

Numerical computations of increasing complexity were used to design an axisymmetric model with which to conduct instability experiments in the BAM6QT. A low-fidelity method of characteristics code was used to determine an approximate model design, then higher-fidelity mean-flow computations combined with a linear stability analysis were used to refine the design. These computations predicted that by changing important model parameters, first-mode instabilities can have higher N factors than second-mode instabilities under BAM6QT flow conditions.

Computational stability results indicated that two major design features that affect the magnitude of first-mode instabilities on an axisymmetric cone-ogive-cylinder are the leading-edge cone angle and the flare. The leading-edge cone angle was shown to decrease the edge Mach number to the point that the first-mode instability became larger than the second mode. However, the predicted N factor for model lengths of less than 1 meter were lower than desired. Computations for the various cone-ogive-cylinder models predict a maximum N factor of about 3 at an axial distance of 0.5 meters. The addition of flare to the cone-ogive-cylinder increased the magnitude of both first and second-mode instabilities, but with a significantly greater increase of the second mode, which then dominates.

Surface measurements were made on various cone-ogive-cylinder configurations in an attempt to measure first-mode instability waves. These measurements were made in both quiet and noisy flow. Some low-frequency disturbances were measured under quiet flow conditions. However, these disturbances did not behave as predicted for first-mode instabilities. It now appears that the measurements were of an entropy-layer instability, and no first-mode instabilities were measured.

A computational optimization conducted by Lindsey Kirk resulted in a flared cone that was numerically optimized to maximize the first-mode instability. The resulting

design was predicted to have high first-mode instabilities with N factors of about 5 at 0.5 meters. However, the predicted N factors for second-mode instabilities at 0.5 meters was about 8.5. Surface measurements were made on the flared cone in the BAM6QT in an attempt to measure both first and second-mode instabilities. The spectral results from the surface Kulite measurements show second-mode instabilities of up to 190 kHz. However, they were unable to show the first-mode instability.

Measurements on the surface of a 30-degree cone-ogive-cylinder model provided evidence of an different kind of instability. These surface measurements show an instability magnitude that increases, then decreases, and eventually increases rapidly with downstream distance.

Off-surface measurements confirmed the existence of an instability outside of the predicted boundary layer and hot wires were used to measure the location and relative magnitude of the instability. These measurements were made above the surface of a long cone-ogive-cylinder model with interchangeable nosetips in the BAM6QT, always under quiet flow. Interchangeable nosetips of 25, 30 to 35 (in one-degree increments), and 40 degrees were attached to the long model during experiments, each providing a distinct shock shape from the other nosetips, and thereby changing the entropy-layer characteristics.

Hot-wire measurements show an instability that originates outside of the boundary layer. It grows in magnitude with downstream distance and becomes measurable about halfway down the 94-centimeter model. Measurements above each of the 30 to 35-degree models show the instability approach the model. As the nosetip angle is increased, the instability approaches the model further upstream. Measurements above the higher-angle nosetips also show the instability enter the boundary layer. In the case of the 35-degree model, it appears that the measured instability is what causes the boundary-layer to transition further downstream.

Surface measurements also show a change in the measured instability as the nosetip angle is changed. They show that as the nosetip angle increases, the instability frequency decreases.

Cross-correlations between sensors were used to confirm that the surface and off-surface sensors were measuring the same instability. Cross-correlations between azimuthally-displaced surface sensors indicate that the measured instability is most likely a two-dimensional disturbance. Correlations between axially-displaced sensors show that the convection speed for the instability is approximately the boundary-layer edge velocity.

Mean-flow computations were used to compare with experimental measurements. They show that for the 30-degree models and above, there is a generalized inflection point in the angular momentum outside of the boundary layer. This inflection point is a requirement for an entropy layer to be theoretically possible. However, stability calculations have not yet confirmed the existence of the measured instability. Pedro Paredes at Texas A&M performed stability calculations and found that the entropy-layer modes were always locally stable on the 30-degree model at 120 psia conditions. Stability calculations for the higher nosetip angles found that they were "marginally unstable".

11. RECOMMENDATIONS

As our understanding of entropy-layer and boundary-layer instabilities increases, our capacity to predict boundary-layer transition will also increase. The author recommends that the following work be completed to aid in our understanding of first-mode and entropy-layer instabilities.

11.1 Additional Surface Measurements of the Entropy-Layer Instability

11.1.1 Axisymmetry Measurements

Surface sensors installed at various azimuthal locations were used in initial tests to determine if the measured instabilities were axisymmetric. Entropy-layer instabilities were measured at each azimuthal location. However, the magnitude of the measured instability was dependent on the azimuthal location, indicating an asymmetry in the flow. Since this was discovered only near the end of this research, only a few measurements were made. Additional measurements made simultaneously at various azimuthal locations could be made at several axial locations. These measurements could then be analyzed to give a better understanding of the asymmetric nature of the instability around the cone-ogive-cylinder.

11.1.2 Change of Instability Magnitude with Axial Location

Surface measurements on each of the cone-ogive-cylinder configurations show a reduction in magnitude of the measured instability after an initial growth. The location of that stabilization appears to change with the nosetip angle, but there are not enough surface measurements to show where that stabilization begins for each configuration. Additional surface measurements at small axial increments from 0.6

meters to about 0.72 meters would more closely identify the axial location where the stabilization begins. A comparison can then be made between this location and the location where the instability enters the boundary layer.

It appears that the measured instability is an entropy-layer instability. It also appears that the entropy-layer swallowing process has an initial stabilizing effect on the instability. An understanding of the effects of entropy-layer swallowing is an important piece of our overall understanding of transition. However, the data set obtained by these experiments is insufficient to explain this phenomenon.

11.2 Additional Surface Measurements to Determine Angle of Attack and other Asymmetric Effects

The effects of the slight variation in angle of attack of the cone-ogive-cylinder when installed in the BAM6QT need to be better understood. Measurements have shown that the angle of attack varies by less than 0.1 degree from the horizontal plane and the surface and hot-wire measurements showed good repeatability. However, additional measurements with the model installed at measured attack angles should be made. These measurements could then be compared with one another to determine the effect, if any, of the slight angle of attack on the measured instabilities.

11.3 Additional Hot-Wire Measurements of the Entropy-Layer Instability

Additional hot-wire measurements of the entropy-layer instability would also be beneficial. Measurements at very small vertical increments could map out the entropy layer and supply a wealth of knowledge regarding its structure. This would also not be very difficult- as long as the hot wire doesn't break.

Hot-wire measurements could also be made using different nosetips. The entropy-layer instability from the 35-degree nosetip appears to initiate transition at higher Reynolds numbers and it would be interesting to see the effect of a slightly larger

nosetip angle of 36 or 37 degrees. Smaller-angle nosetips could also be used to see where the entropy layer is no longer measureable.

Hot-wire measurements further downstream on each of the models would be very insightful. There are two ways to do this with the current setup. The first way is to build a different hot-wire sting that is set back a little further in the model. That might be rather complex and only gain a couple of inches at most. The other option is to push the model further forward in the tunnel. Hot-wire measurements with the model pushed forward showed a decreased instability magnitude, but the same frequency band was magnified. The effects of pushing the model forward even further would have to be discussed, but it may provide a lot of new insight.

11.4 Surface Measurements on the Flared Cone with a Different Sensor

Kulite sensor measurements on the flared cone show what appears to be second-mode instabilities. However, measurements using different sensors, such as PCBs, could be used to verify the existence of the second-mode instability on that model.

11.5 Additional First-Mode Instability Investigations

Future attempts should be made to measure first-mode instabilities. However, the path to do so is not well defined. The author recommends that future efforts start back with the computations. An optimization code such as that used by Lindsay Kirk could be used in the design process. However, the stipulation should be included that the second-mode N factors must be less than or equal to those of the first-mode instability.

Another effort could be made to excite first-mode instabilities using the glow perturber. There was a limited amount of time and resources available to make the glow perturber experiments a success. A dedicated focus on managing the electronic noise may allow for first-mode waves to be excited and measured. Another focus

should be on how the glow perturber is operated to best excite those instability waves.

APPENDICES

A. CONE-OGIVE-CYLINDER GEOMETRY

A.1 Body Coordinates for the Original Cone-Ogive-Cylinder

Table A.1
Coordinates for the Body of the Original Cone-Ogive-Cylinder (nosetip has a length of 0.9544 inches*)

Body Coordinates, (1 of 6)		Body Coordinates, (2 of 6)	
Diameter (in)	x (in)	Diameter (in)	x (in)
1.0163	0.9544*	1.2454	1.2341
1.0307	0.9708	1.2578	1.2505
1.0450	0.9873	1.2701	1.2670
1.0592	1.0037	1.2823	1.2834
1.0733	1.0202	1.2943	1.2999
1.0872	1.0366	1.3063	1.3164
1.1011	1.0531	1.3181	1.3328
1.1148	1.0695	1.3298	1.3493
1.1284	1.0860	1.3413	1.3657
1.1418	1.1025	1.3528	1.3822
1.1552	1.1189	1.3641	1.3986
1.1684	1.1354	1.3754	1.4151
1.1816	1.1518	1.3865	1.4315
1.1946	1.1683	1.3975	1.4480
1.2075	1.1847	1.4083	1.4644
1.2202	1.2012	1.4191	1.4809
1.2329	1.2176	1.4297	1.4974

Table A.2
Coordinates for the Body of the Original Cone-Ogive-Cylinder, continued

Body Coordinates, (3 of 6)		Body Coordinates, (4 of 6)	
Diameter (in)	x (in)	Diameter (in)	x (in)
1.4402	1.5138	1.6491	1.8923
1.4506	1.5303	1.6568	1.9087
1.4609	1.5467	1.6643	1.9252
1.4710	1.5632	1.6718	1.9416
1.4811	1.5796	1.6791	1.9581
1.4910	1.5961	1.6863	1.9745
1.5008	1.6125	1.6933	1.9910
1.5104	1.6290	1.7003	2.0074
1.5200	1.6454	1.7071	2.0239
1.5294	1.6619	1.7138	2.0404
1.5388	1.6784	1.7204	2.0568
1.5480	1.6948	1.7269	2.0733
1.5571	1.7113	1.7332	2.0897
1.5660	1.7277	1.7395	2.1062
1.5749	1.7442	1.7456	2.1226
1.5836	1.7606	1.7516	2.1391
1.5922	1.7771	1.7574	2.1555
1.6007	1.7935	1.7632	2.1720
1.6091	1.8100	1.7688	2.1884
1.6173	1.8264	1.7744	2.2049
1.6255	1.8429	1.7798	2.2214
1.6335	1.8594	1.7851	2.2378
1.6414	1.8758	1.7902	2.2543

Table A.3
Coordinates for the Body of the Original Cone-Ogive-Cylinder, continued

Body Coordinates, (5 of 6)		Body Coordinates, (6 of 6)	
Diameter (in)	x (in)	Diameter (in)	x (in)
1.7953	2.2707	1.8763	2.6327
1.8002	2.2872	1.8786	2.6492
1.8050	2.3036	1.8808	2.6656
1.8097	2.3201	1.8828	2.6821
1.8143	2.3365	1.8848	2.6985
1.8187	2.3530	1.8866	2.7150
1.8231	2.3694	1.8884	2.7314
1.8273	2.3859	1.8900	2.7479
1.8314	2.4024	1.8915	2.7644
1.8353	2.4188	1.8928	2.7808
1.8392	2.4353	1.8941	2.7973
1.8429	2.4517	1.8952	2.8137
1.8466	2.4682	1.8962	2.8302
1.8501	2.4846	1.8971	2.8466
1.8535	2.5011	1.8979	2.8631
1.8567	2.5175	1.8985	2.8795
1.8599	2.5340	1.8991	2.8960
1.8629	2.5504	1.8995	2.9124
1.8658	2.5669	1.8998	2.9289
1.8686	2.5834	1.8999	2.9454
1.8713	2.5998	1.9000	2.9618
1.8738	2.6163	1.9000	40.000

A.2 Nosetip Coordinates for the Original Cone-Ogive-Cylinder

Table A.4
Coordinates for the 30-degree Nosetip for the Original Cone-Ogive-Cylinder

Nosetip Coord, (1 of 3)		Nosetip Coord, (2 of 3)		Nosetip Coord, (3 of 3)	
Diam (in)	x (in)	Diam (in)	x (in)	Diam (in)	x (in)
0.0000	0.0000	0.3989	0.3455	0.7693	0.6911
0.0190	0.0165	0.4178	0.3620	0.7856	0.7075
0.0380	0.0329	0.4365	0.3785	0.8018	0.7240
0.0570	0.0494	0.4551	0.3949	0.8179	0.7405
0.0760	0.0658	0.4735	0.4114	0.8339	0.7569
0.0950	0.0823	0.4919	0.4278	0.8497	0.7734
0.1140	0.0987	0.5101	0.4443	0.8655	0.7898
0.1330	0.1152	0.5282	0.4607	0.8811	0.8063
0.1520	0.1316	0.5462	0.4772	0.8966	0.8227
0.1710	0.1481	0.5641	0.4936	0.9119	0.8392
0.1900	0.1645	0.5818	0.5101	0.9272	0.8556
0.2090	0.1810	0.5995	0.5265	0.9423	0.8721
0.2280	0.1975	0.6170	0.5430	0.9574	0.8885
0.2470	0.2139	0.6344	0.5595	0.9723	0.9050
0.2660	0.2304	0.6516	0.5759	0.9871	0.9215
0.2850	0.2468	0.6688	0.5924	1.0017	0.9379
0.3040	0.2633	0.6858	0.6088	1.0163	0.9544
0.3230	0.2797	0.7028	0.6253		
0.3420	0.2962	0.7196	0.6417		
0.3610	0.3126	0.7363	0.6582		
0.3800	0.3291	0.7528	0.6746		

Table A.5
Selected Coordinates for the 28 and 33-degree Nosetips that attach to the body of the Original Cone-Ogive-Cylinder

28-Degree Nosetip		33-Degree Nosetip	
Diam (in)	x (in)	Diam (in)	x (in)
0.0000	0.0000	0.0000	0.0000
0.1203	0.1132	0.1140	0.0878
0.2106	0.1980	0.2090	0.1609
0.3008	0.2829	0.3040	0.2341
0.4211	0.3960	0.4178	0.3218
0.5114	0.4809	0.5101	0.3950
0.6016	0.5658	0.6170	0.4870
0.7128	0.6726	0.7028	0.5737
0.8040	0.7642	0.8018	0.6727
0.9059	0.8710	0.9119	0.7878
1.0029	0.9778	1.0017	0.8866
1.0163	0.9931	1.0163	0.9030

A.3 Coordinates for the Cone-Ogive-Cylinder with Interchangeable Nosetips

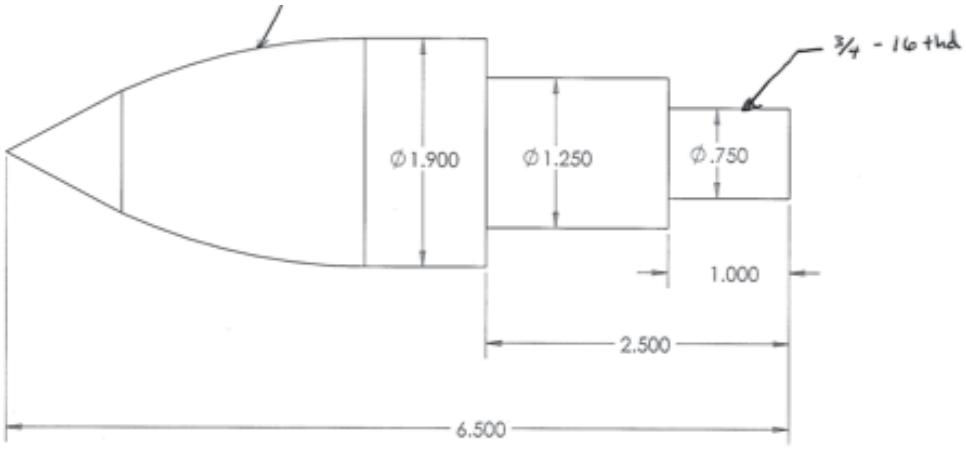

Fig. A.1. Diagram of interchangeable cone-ogive-cylinder nosetip design. Coordinates of the cone-ogive portion varied for each nosetip. All dimensions are in inches.

Table A.6
Values of ζ used in Equation 3.1 to Calculate the Nosetip Geometries.

Nosetip Angle	25	30	31	32	33	34	35	40
zeta	0.1	0.2	0.26	0.32	0.38	0.44	0.5	0.7

Table A.7
25-Degree Nosetip Coordinates

Nosetip Coord, (1 of 3)		Nosetip Coord, (2 of 3)		Nosetip Coord, (3 of 3)	
Diam (in)	x (in)	Diam (in)	x (in)	Diam (in)	x (in)
0.0000	0.0000	0.9856	1.1893	1.7052	2.6332
0.0285	0.0306	1.0319	1.2580	1.7263	2.7019
0.0570	0.0611	1.0770	1.3268	1.7461	2.7707
0.0855	0.0917	1.1209	1.3955	1.7647	2.8395
0.1140	0.1222	1.1636	1.4643	1.7822	2.9082
0.1425	0.1528	1.2050	1.5331	1.7984	2.9770
0.1710	0.1834	1.2453	1.6018	1.8134	3.0457
0.2113	0.2266	1.2844	1.6706	1.8273	3.1145
0.2744	0.2954	1.3223	1.7393	1.8399	3.1833
0.3364	0.3642	1.3589	1.8081	1.8513	3.2520
0.3971	0.4329	1.3944	1.8768	1.8615	3.3208
0.4566	0.5017	1.4287	1.9456	1.8705	3.3895
0.5149	0.5704	1.4617	2.0144	1.8784	3.4583
0.5720	0.6392	1.4936	2.0831	1.8850	3.5270
0.6279	0.7080	1.5243	2.1519	1.8904	3.5958
0.6826	0.7767	1.5537	2.2206	1.8946	3.6646
0.7361	0.8455	1.5820	2.2894	1.8976	3.7333
0.7884	0.9142	1.6090	2.3582	1.8994	3.8021
0.8395	0.9830	1.6349	2.4269	1.9000	3.8708
0.8894	1.0517	1.6595	2.4957	1.9000	4.0000
0.9381	1.1205	1.6830	2.5644		

Table A.8
Selected Coordinates for the 30 to 32-Degree Nosetips

30-Degree		31-Degree		32-Degree	
Diam (in)	x (in)	Diam (in)	x (in)	Diam (in)	x (in)
0.0000	0.0000	0.0000	0.0000	0.0000	0.0000
0.1140	0.0950	0.1235	0.1028	0.1216	0.0973
0.2090	0.1810	0.2223	0.1850	0.2128	0.1703
0.3040	0.2633	0.3211	0.2672	0.3040	0.2433
0.4178	0.3620	0.4199	0.3494	0.4256	0.3406
0.5101	0.4443	0.5115	0.4257	0.5168	0.4135
0.6170	0.5430	0.6143	0.5135	0.6080	0.4865
0.7028	0.6253	0.7132	0.6012	0.7031	0.5640
0.8018	0.7240	0.8081	0.6889	0.8094	0.6545
0.9119	0.8392	0.9138	0.7913	0.9108	0.7450
1.0017	0.9379	1.0002	0.8791	1.0073	0.8354
1.1011	1.0531	1.1091	0.9961	1.1114	0.9388
1.2075	1.1847	1.2111	1.1131	1.2091	1.0422
1.3063	1.3164	1.3060	1.2301	1.3004	1.1456
1.4083	1.4644	1.4043	1.3617	1.4054	1.2748
1.5008	1.6125	1.5032	1.5079	1.5002	1.4040
1.6007	1.7935	1.6073	1.6834	1.6008	1.5591
1.7003	2.0074	1.7023	1.8736	1.7060	1.7529
1.8002	2.2872	1.8031	2.1368	1.8023	1.9855
1.9000	2.9618	1.9000	2.7511	1.9000	2.5541
1.9000	4.0000	1.9000	4.0000	1.9000	4.0000

Table A.9
Selected Coordinates for the 33 to 35-Degree Nosetips

33-Degree		34-Degree		35-Degree	
Diam (in)	x (in)	Diam (in)	x (in)	Diam (in)	x (in)
0.0000	0.0000	0.0000	0.0000	0.0000	0.0000
0.1083	0.0834	0.1254	0.0930	0.1425	0.1018
0.2166	0.1668	0.2090	0.1549	0.2375	0.1696
0.3249	0.2502	0.3344	0.2479	0.3325	0.2374
0.4332	0.3335	0.4180	0.3099	0.4275	0.3053
0.5054	0.3891	0.5016	0.3718	0.5225	0.3731
0.6137	0.4725	0.6270	0.4648	0.6175	0.4409
0.7220	0.5559	0.7106	0.5268	0.7125	0.5088
0.8087	0.6239	0.8360	0.6197	0.8075	0.5766
0.9056	0.7033	0.9015	0.6690	0.9025	0.6445
1.0109	0.7940	1.0019	0.7497	1.0084	0.7208
1.1103	0.8847	1.1085	0.8366	1.1090	0.7971
1.2038	0.9754	1.2084	0.9253	1.2035	0.8734
1.3020	1.0774	1.3015	1.0141	1.3015	0.9582
1.4023	1.1908	1.4062	1.1225	1.4007	1.0515
1.5020	1.3155	1.5008	1.2310	1.5063	1.1617
1.6055	1.4629	1.6067	1.3690	1.6061	1.2804
1.7056	1.6329	1.7021	1.5169	1.7022	1.4161
1.8026	1.8370	1.8002	1.7141	1.8035	1.6026
1.9000	2.3585	1.9000	2.1873	1.9000	2.0266
1.9000	4.0000	1.9000	4.0000	1.9000	4.0000

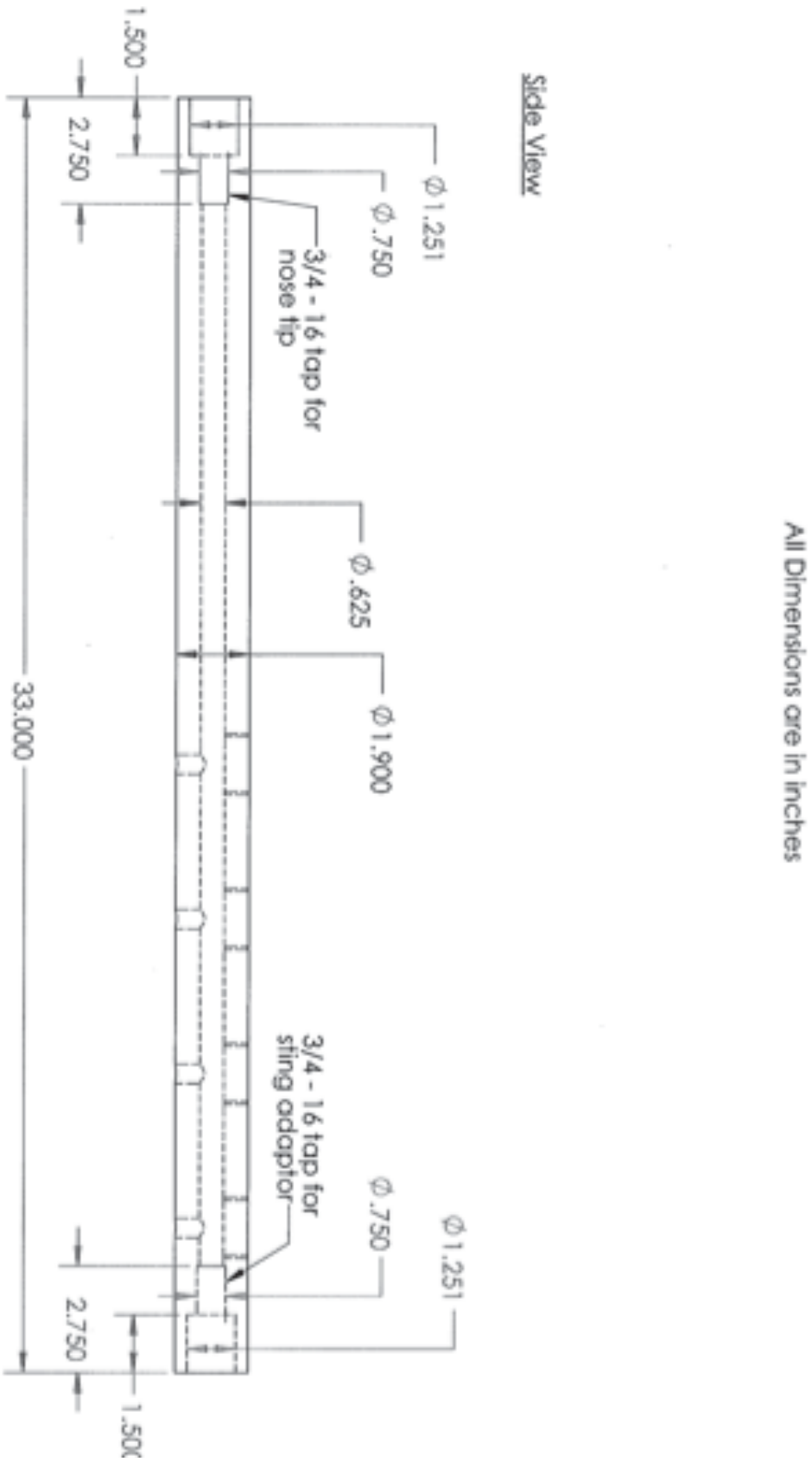

Fig. A.2. Diagram of cone-ogive-cylinder body

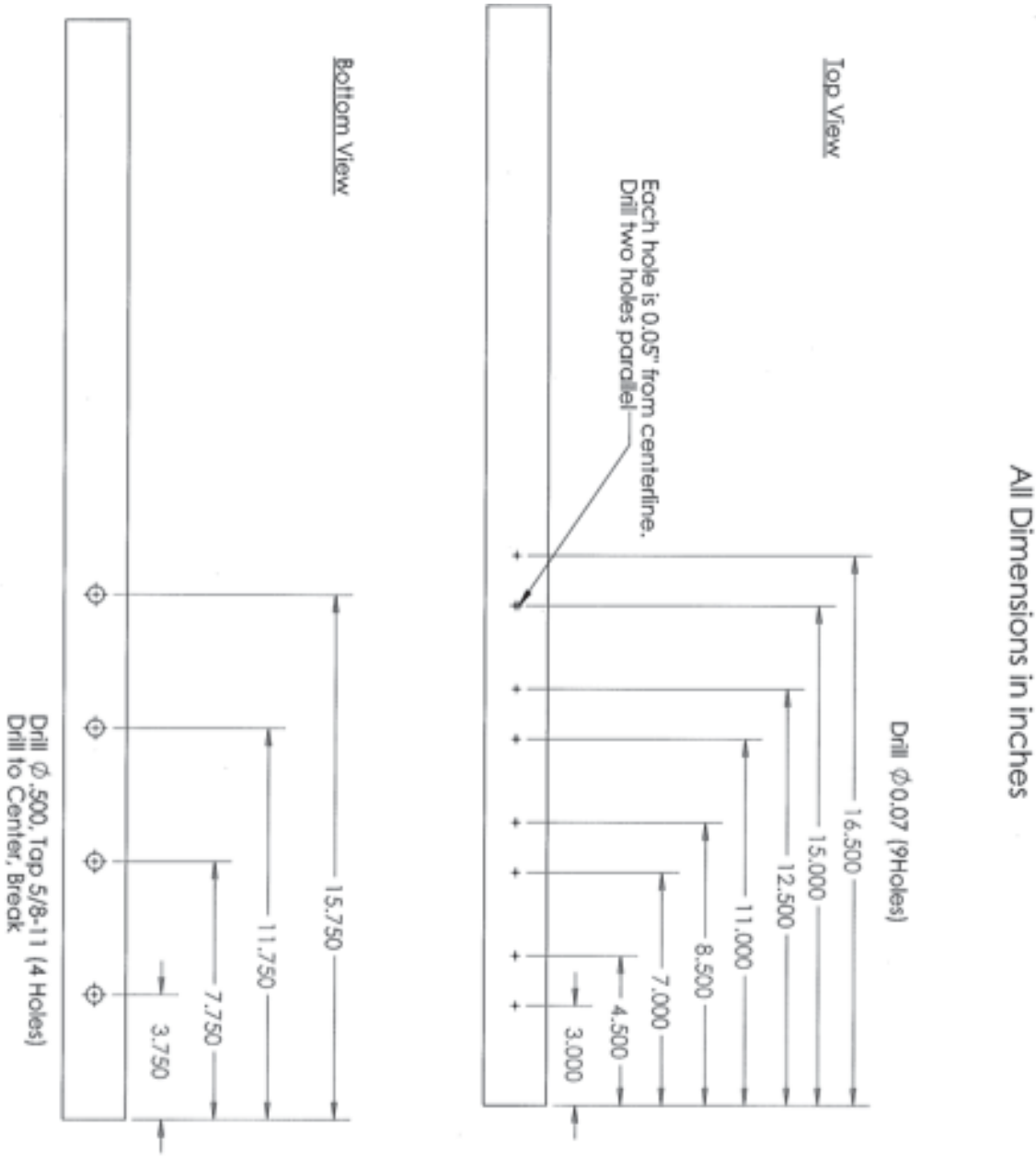

Fig. A.3. Diagram of sensor and access ports for cone-ogive-cylinder body

B. SUMMARY OF TUNNEL RUN CONDITIONS

Table B.1
BAM6QT Conditions at Tunnel Start for Referenced Runs

Run #	Date	P_0 (psia)	T_0 ($^\circ C$)	Flow	Model
412	10/2/2012	149.5	159	quiet	30-deg cone-ogive-cylinder
417	10/3/2012	34.2	161	quiet	30-deg cone-ogive-cylinder
418	10/3/2012	150.2	159	noisy	30-deg cone-ogive-cylinder
451	11/27/2012	81.5	168	quiet	30-deg cone-ogive-cylinder
452	11/28/2012	100.1	168	quiet	30-deg cone-ogive-cylinder
453	11/28/2012	126.5	167	quiet	30-deg cone-ogive-cylinder
454	11/28/2012	147.1	164	quiet	30-deg cone-ogive-cylinder
455	11/29/2012	171.2	165	quiet	30-deg cone-ogive-cylinder
458	11/30/2012	161.7	164	quiet	30-deg cone-ogive-cylinder
459	12/3/2012	160.4	170	quiet	30-deg cone-ogive-cylinder
461	12/3/2012	161.2	165	quiet	30-deg cone-ogive-cylinder
462	12/10/2012	165.3	171	quiet	30-deg cone-ogive-cylinder
463	12/11/2012	162.7	168	quiet	30-deg cone-ogive-cylinder
602	2/12/2013	170.0	167	quiet	28-deg cone-ogive-cylinder
603	2/12/2013	170.7	168	quiet	28-deg cone-ogive-cylinder
616	2/13/2013	170.0	172	quiet	30-deg cone-ogive-cylinder
619	2/14/2013	170.8	166	quiet	30-deg cone-ogive-cylinder
802	5/16/2013	82.7	164	quiet	30-deg cone-ogive-cylinder
807	5/17/2013	128.4	163	quiet	30-deg cone-ogive-cylinder
809	5/17/2013	149.5	159	quiet	30-deg cone-ogive-cylinder

Table B.2
BAM6QT Conditions at Tunnel Start for Referenced Runs, continued

Run #	Date	P_0 (psia)	T_0 ($^\circ C$)	Flow	Model
810	5/17/2013	146.7	158	quiet	30-deg cone-ogive-cylinder
813	5/20/2013	170.8	163	quiet	30-deg cone-ogive-cylinder
822	5/22/2013	136.5	159	quiet	30-deg cone-ogive-cylinder
823	5/22/2013	159.5	158	quiet	30-deg cone-ogive-cylinder
1001	8/2/2013	80.0	162	quiet	flared cone
1002	8/2/2013	61.3	160	quiet	flared cone
1003	8/2/2013	100.4	159	quiet	flared cone
1004	8/2/2013	122.5	157	quiet	flared cone
1005	8/2/2013	142.1	156	quiet	flared cone
1006	8/3/2013	158.2	170	quiet	flared cone
1007	8/3/2013	174.7	165	quiet	flared cone
1008	8/3/2013	177.9	162	quiet	flared cone
1119	9/3/2013	117.7	163	quiet	30-deg cone-ogive-cylinder
1131	9/5/2013	116.5	166	quiet	30-deg cone-ogive-cylinder
1202	10/16/2013	173	164	quiet	25-deg cone-ogive-cylinder
1203	10/16/2013	151.1	166	quiet	25-deg cone-ogive-cylinder
1204	10/16/2013	124.4	165	quiet	25-deg cone-ogive-cylinder
1205	10/16/2013	100.5	166	quiet	25-deg cone-ogive-cylinder
1206	10/16/2013	78.8	166	quiet	25-deg cone-ogive-cylinder
1209	10/17/2013	66.5	168	quiet	25-deg cone-ogive-cylinder
1210	10/17/2013	64.3	169	quiet	30-deg cone-ogive-cylinder
1211	10/17/2013	79.8	168	quiet	30-deg cone-ogive-cylinder
1212	10/17/2013	100.5	167	quiet	30-deg cone-ogive-cylinder
1213	10/17/2013	124.9	166	quiet	30-deg cone-ogive-cylinder
1214	10/17/2013	150.5	165	quiet	30-deg cone-ogive-cylinder

Table B.3
BAM6QT Conditions at Tunnel Start for Referenced Runs, continued

Run #	Date	P_0 (psia)	T_0 ($^\circ C$)	Flow	Model
1215	10/17/2013	173.0	164	quiet	30-deg cone-ogive-cylinder
1217	10/18/2013	173.5	169	quiet	35-deg cone-ogive-cylinder
1218	10/18/2013	150.3	169	quiet	35-deg cone-ogive-cylinder
1219	10/18/2013	124.5	168	quiet	35-deg cone-ogive-cylinder
1220	10/18/2013	100.0	168	quiet	35-deg cone-ogive-cylinder
1221	10/18/2013	76.6	168	quiet	35-deg cone-ogive-cylinder
1222	10/18/2013	49.9	168	quiet	35-deg cone-ogive-cylinder
1319	10/22/2013	135.0	160	quiet	35-deg cone-ogive-cylinder
1327	10/23/2013	90.0	165	quiet	30-deg cone-ogive-cylinder
1334	10/23/2013	89.0	162	quiet	30-deg cone-ogive-cylinder
1335	10/23/2013	89.2	161	quiet	30-deg cone-ogive-cylinder
1336	10/23/2013	119.0	161	quiet	30-deg cone-ogive-cylinder
1342	10/23/2013	134.8	161	quiet	30-deg cone-ogive-cylinder
1415	12/5/2013	120.8	170	quiet	30-deg cone-ogive-cylinder
1416	12/6/2013	120.4	169	quiet	30-deg cone-ogive-cylinder
1417	12/6/2013	120.7	166	quiet	30-deg cone-ogive-cylinder
1418	12/6/2013	120.6	169	quiet	35-deg cone-ogive-cylinder
1420	12/9/2013	120.7	164	quiet	35-deg cone-ogive-cylinder
1424	12/11/2013	135.5	164	quiet	35-deg cone-ogive-cylinder
1431	12/13/2013	121.3	164	quiet	30-deg cone-ogive-cylinder
1435	12/13/2013	121.2	160	quiet	30-deg cone-ogive-cylinder
1437	12/14/2013	120.7	166	quiet	30-deg cone-ogive-cylinder
1438	12/14/2013	121.3	165	quiet	30-deg cone-ogive-cylinder
1439	12/14/2013	119.9	163	quiet	30-deg cone-ogive-cylinder
1501	1/14/2014	168.2	167	quiet	34-deg cone-ogive-cylinder

Table B.4
BAM6QT Conditions at Tunnel Start for Referenced Runs, continued

Run #	Date	P_0 (psia)	T_0 ($^\circ C$)	Flow	Model
1502	1/14/2014	148.6	166	quiet	34-deg cone-ogive-cylinder
1503	1/14/2014	125.6	167	quiet	34-deg cone-ogive-cylinder
1504	1/14/2014	99.9	166	quiet	34-deg cone-ogive-cylinder
1505	1/14/2014	75.2	169	quiet	34-deg cone-ogive-cylinder
1506	1/14/2014	75.6	170	quiet	34-deg cone-ogive-cylinder
1507	1/14/2014	50.0	169	quiet	34-deg cone-ogive-cylinder
1508	1/15/2014	173.4	169	quiet	33-deg cone-ogive-cylinder
1509	1/15/2014	149.9	168	quiet	33-deg cone-ogive-cylinder
1510	1/15/2014	124.1	166	quiet	33-deg cone-ogive-cylinder
1511	1/15/2014	98.9	167	quiet	33-deg cone-ogive-cylinder
1512	1/15/2014	75.2	168	quiet	33-deg cone-ogive-cylinder
1513	1/15/2014	51.3	171	quiet	33-deg cone-ogive-cylinder
1515	1/15/2014	150.6	165	quiet	32-deg cone-ogive-cylinder
1516	1/15/2014	124.3	165	quiet	32-deg cone-ogive-cylinder
1517	1/15/2014	100.3	170	quiet	32-deg cone-ogive-cylinder
1518	1/15/2014	75.7	171	quiet	32-deg cone-ogive-cylinder
1519	1/15/2014	50.3	172	quiet	32-deg cone-ogive-cylinder
1520	1/16/2014	171.2	169	quiet	31-deg cone-ogive-cylinder
1521	1/16/2014	151.9	167	quiet	31-deg cone-ogive-cylinder
1522	1/16/2014	126.8	166	quiet	31-deg cone-ogive-cylinder
1523	1/16/2014	97.0	168	quiet	31-deg cone-ogive-cylinder
1524	1/16/2014	75.7	169	quiet	31-deg cone-ogive-cylinder
1525	1/16/2014	57.5	168	quiet	31-deg cone-ogive-cylinder
1605	1/17/2014	121.1	161	quiet	32-deg cone-ogive-cylinder
1610	1/17/2014	120.5	160	quiet	32-deg cone-ogive-cylinder

Table B.5
BAM6QT Conditions at Tunnel Start for Referenced Runs, continued

Run #	Date	P_0 (psia)	T_0 ($^\circ C$)	Flow	Model
1627	1/20/2014	122.0	165	quiet	32-deg cone-ogive-cylinder
1628	1/20/2014	122.2	164	quiet	32-deg cone-ogive-cylinder
1629	1/20/2014	121.3	159	quiet	31-deg cone-ogive-cylinder
1630	1/20/2014	122.8	164	quiet	31-deg cone-ogive-cylinder
1639	1/22/2014	121.7	164	quiet	34-deg cone-ogive-cylinder
1640	1/22/2014	121.5	161	quiet	34-deg cone-ogive-cylinder
1641	1/22/2014	121.7	161	quiet	34-deg cone-ogive-cylinder
1642	1/23/2014	121.6	163	quiet	32-deg cone-ogive-cylinder
1643	1/23/2014	122.5	163	quiet	32-deg cone-ogive-cylinder
1645	1/24/2014	121.3	164	quiet	32-deg cone-ogive-cylinder
1646	1/24/2014	122.1	164	quiet	32-deg cone-ogive-cylinder
1647	1/24/2014	122.1	165	quiet	30-deg cone-ogive-cylinder
1648	1/24/2014	122.1	163	quiet	30-deg cone-ogive-cylinder
1649	1/24/2014	121.0	161	quiet	30-deg cone-ogive-cylinder
1650	1/24/2014	122.0	161	quiet	30-deg cone-ogive-cylinder
1651	1/24/2014	122.2	161	quiet	30-deg cone-ogive-cylinder
1652	1/25/2014	121.7	166	quiet	30-deg cone-ogive-cylinder
1653	1/25/2014	122.5	163	quiet	30-deg cone-ogive-cylinder
1654	1/25/2014	122.4	162	quiet	31-deg cone-ogive-cylinder
1655	1/25/2014	122.5	162	quiet	31-deg cone-ogive-cylinder
1656	1/25/2014	122.5	161	quiet	31-deg cone-ogive-cylinder
1657	1/25/2014	122.4	161	quiet	31-deg cone-ogive-cylinder
1658	1/25/2014	121.7	160	quiet	31-deg cone-ogive-cylinder
1661	1/25/2014	121.4	160	quiet	33-deg cone-ogive-cylinder
1662	1/25/2014	121.7	160	quiet	33-deg cone-ogive-cylinder

Table B.6
BAM6QT Conditions at Tunnel Start for Referenced Runs, continued

Run #	Date	P_0 (psia)	T_0 ($^\circ C$)	Flow	Model
1663	1/25/2014	121.4	160	quiet	33-deg cone-ogive-cylinder
1664	1/25/2014	121.9	160	quiet	33-deg cone-ogive-cylinder
1665	1/25/2014	120.8	159	quiet	33-deg cone-ogive-cylinder
1666	1/25/2014	122.2	160	quiet	34-deg cone-ogive-cylinder
1667	1/25/2014	121.4	159	quiet	34-deg cone-ogive-cylinder
1668	1/25/2014	121.9	160	quiet	34-deg cone-ogive-cylinder
1704	3/11/2014	152.1	166	quiet	30-deg cone-ogive-cylinder
1705	3/11/2014	151.1	166	quiet	31-deg cone-ogive-cylinder
1707	3/12/2014	171.7	170	quiet	32-deg cone-ogive-cylinder
1708	3/12/2014	149.8	170	quiet	32-deg cone-ogive-cylinder
1710	3/12/2014	170.5	169	quiet	33-deg cone-ogive-cylinder
1711	3/12/2014	150.6	168	quiet	33-deg cone-ogive-cylinder
1714	3/12/2014	150.6	167	quiet	34-deg cone-ogive-cylinder
1717	3/12/2014	154.9	166	quiet	35-deg cone-ogive-cylinder
1720	3/13/2014	154.3	168	quiet	25-deg cone-ogive-cylinder
1809	3/18/2014	120.0	162	quiet	32-deg cone-ogive-cylinder
1810	3/18/2014	120.2	166	quiet	32-deg cone-ogive-cylinder
1811	3/19/2014	122.0	168	quiet	32-deg cone-ogive-cylinder
1812	3/19/2014	121.3	165	quiet	32-deg cone-ogive-cylinder
1813	3/19/2014	122.3	164	quiet	33-deg cone-ogive-cylinder
1814	3/19/2014	121.0	162	quiet	33-deg cone-ogive-cylinder
1815	3/19/2014	121.7	163	quiet	33-deg cone-ogive-cylinder
1816	3/19/2014	121.9	162	quiet	33-deg cone-ogive-cylinder
1817	3/19/2014	122.2	163	quiet	34-deg cone-ogive-cylinder
1818	3/19/2014	122.5	161	quiet	34-deg cone-ogive-cylinder

Table B.7
BAM6QT Conditions at Tunnel Start for Referenced Runs, continued

Run #	Date	P_0 (psia)	T_0 ($^\circ C$)	Flow	Model
1819	3/19/2014	122.5	160	quiet	34-deg cone-ogive-cylinder
1820	3/19/2014	122.1	165	quiet	34-deg cone-ogive-cylinder
1821	3/20/2014	122.5	167	quiet	34-deg cone-ogive-cylinder
1822	3/20/2014	122.3	163	quiet	34-deg cone-ogive-cylinder
1823	3/20/2014	122.4	162	quiet	34-deg cone-ogive-cylinder
1824	3/20/2014	121.1	162	quiet	35-deg cone-ogive-cylinder
1825	3/21/2014	121.9	167	quiet	35-deg cone-ogive-cylinder
1826	3/21/2014	122.0	166	quiet	35-deg cone-ogive-cylinder
1901	5/22/2014	160.1	163	quiet	30-deg cone-ogive-cylinder
1902	5/22/2014	159.3	161	quiet	30-deg cone-ogive-cylinder
1903	5/22/2014	159.0	160	quiet	30-deg cone-ogive-cylinder
1904	5/23/2014	159.9	166	quiet	30-deg cone-ogive-cylinder
1905	5/23/2014	162.2	165	quiet	30-deg cone-ogive-cylinder
1906	5/23/2014	160.2	164	quiet	30-deg cone-ogive-cylinder
1907	5/23/2014	1629.9	164	quiet	30-deg cone-ogive-cylinder
1908	5/23/2014	99.6	163	quiet	30-deg cone-ogive-cylinder
1909	5/23/2014	74.8	163	quiet	30-deg cone-ogive-cylinder
1910	5/23/2014	159.3	160	quiet	31-deg cone-ogive-cylinder
1911	5/23/2014	130.9	161	quiet	31-deg cone-ogive-cylinder
1912	5/23/2014	100.3	161	quiet	31-deg cone-ogive-cylinder
1913	5/23/2014	69.3	162	quiet	31-deg cone-ogive-cylinder
1914	5/23/2014	160.3	159	quiet	32-deg cone-ogive-cylinder
1915	5/23/2014	133.2	160	quiet	32-deg cone-ogive-cylinder
1916	5/23/2014	100.6	160	quiet	32-deg cone-ogive-cylinder
1917	5/23/2014	70.5	160	quiet	32-deg cone-ogive-cylinder

Table B.8
BAM6QT Conditions at Tunnel Start for Referenced Runs, continued

Run #	Date	P_0 (psia)	T_0 ($^\circ C$)	Flow	Model
1918	5/23/2014	159.8	158	quiet	33-deg cone-ogive-cylinder
1919	5/23/2014	131.3	158	quiet	33-deg cone-ogive-cylinder
1920	5/23/2014	100.1	159	quiet	33-deg cone-ogive-cylinder
1921	5/23/2014	70.5	160	quiet	33-deg cone-ogive-cylinder
1922	5/23/2014	159.6	158	quiet	34-deg cone-ogive-cylinder
1923	5/23/2014	132.0	159	quiet	34-deg cone-ogive-cylinder
1924	5/23/2014	99.8	159	quiet	34-deg cone-ogive-cylinder
1925	5/23/2014	70.4	160	quiet	34-deg cone-ogive-cylinder
1926	5/23/2014	159.9	159	quiet	35-deg cone-ogive-cylinder
1927	5/24/2014	160.4	167	quiet	35-deg cone-ogive-cylinder
1928	5/24/2014	130.7	165	quiet	35-deg cone-ogive-cylinder
1929	5/24/2014	100.1	164	quiet	35-deg cone-ogive-cylinder
1930	5/24/2014	70.3	164	quiet	35-deg cone-ogive-cylinder
1931	5/24/2014	159.8	161	quiet	25-deg cone-ogive-cylinder
2001	5/31/2014	161.9	166	quiet	34-deg cone-ogive-cylinder
2002	5/31/2014	129.4	166	quiet	34-deg cone-ogive-cylinder
2003	6/1/2014	157.7	160	quiet	34-deg cone-ogive-cylinder
2004	6/1/2014	154.3	160	quiet	34-deg cone-ogive-cylinder

C. RUN NUMBERS ASSOCIATED WITH ENTROPY-LAYER INSTABILITY LOCATION MEASUREMENTS

Table C.1
Referenced Off-Surface Instability Location Measurement Runs.

Nosetip	0.43m	0.46m	0.49m	0.52m	0.54m	0.56m	0.59m	0.62m
30 deg				1435	1431	1416	1438	1336, 1439
31 deg		1658	1657	1656		1655	1654	1629
32 deg				1646		1645	1642	1643
33 deg			1665	1813	1814	1663	1662	1661
34 deg	1822	1821	1820	1819		1818	1823	1817
35 deg	1424		1420	1418		1826	1825	1824

D. INPUT FILE FOR STABL MEAN-FLOW CALCULATIONS

```
! CFD solver input file.  Format last modified: 11/19/08
! Revised on 21 May 2012 by Roger Greenwood
! Grid filename,
 'Eogive35_grid2.dat'
!
! chemistry input filename,
 'air_5sp_90.chem'
!
! wall temperature filename,
 'notused.inp'
!
!    itvd     iorder    iextst      kmax      ivis      iwall    jorder
       -1,          3,       -1,         4,        1,          2,         3
!
!   istop      iplot     iconr      iaxi      inor        isn       kbl
    50000,          1,       -1,         1,        1,          0,       200
!
!   nplot      igrid       ilt       i2n     igeom        irm       iej
      250,          0,       -1,         5,        3,          1,        -1
!
!   ichem       ivib       itv       itl       irk       iset   icfljmp
        1,          1,         1,       -1,         1,          1       100
!
!  machin    density       Tin      Tvin     Twall        vin       rvr
   6.00d0,  3.446d-2, 0.5300d2, 0.5300d2,   3.00d2,   8.756d2,    1.3d0
!
! cflmode       epsi      epsj      epsk      pmul      alpha       yaw
```

```
        1,       0.3,      0.3,      0.3,      0.5,     0.0d0,    0.0d0
!
!   stime      rconv   rfreeze    raccel    vaccel      emisw     radrx
     20.0    1.0d-12      -1.0    1.0d+5    1.0d+5      0.8d0     0.5d0
!
!   iblow     brelax     binit    ibdiff
        0      1.0d0         1         1
! ---------------------------------------------------------------------
!  Mass fractions.  Must have one line for each species defined in the
!  chemistry input file.  See chemistry input file for species order.
!  For air, species order: N2,O2,NO,N,O
!   cs
 0.767000
 0.233000
 0.000000
 0.000000
 0.000000
!
! List of additional CFL numbers, one per line, that you want to use.
! If you wish to repeat a CFL a number of times, put a comma and an
! integer number of times to repeat the CFL. At the end of the list, put -1.
!
0.00001
0.001
0.01
0.02,2
0.05,5
1.,15
2.,10
3.,5
4.,5
5.,5
10.,15
20.,15
50.,15
```

```
100.,15
200.,5
300.,5
400.,5
500.,15
1000.,5
-1
!
itvd   --->         not used
iorder --->     (1) First order  SW i-fluxes
                (2) Second order SW i-fluxes
                (3) Primitive variable MUSCL
iextst --->     (1) Explicit first order Euler [Else: implicit DPLR]
kmax   --->     (n) number of implicit relaxation steps
ivis   --->     (1) viscous simulation
iwall  --->     (1) adiabatic wall
                (2) isothermal wall
                (3) varying-temperature wall, values read from file
                (4) radiative equilibrium
                (5) user-specified wall temperature via user subroutine
jorder --->     (1) First order  SW j-fluxes
                (2) Second order SW j-fluxes
                (3) Primitive variable MUSCL
istop  --->     (n) number of iterations before stop
iplot  --->     (1) write restart files
iconr  --->     (1) restart from saved solution for this block
iaxi   --->     (1) axisymmetric
inor   --->     (1) correction term to Steger-Warming wall flux
isn    --->         not used
kbl    --->     (n) body normal epsilon set to zero for k<kbl
nplot  --->     (n) write restart file every n iterations
igrid  --->     (0) take grid format from suffix
                (other) read grid in specified format.  See grid module
ilt    --->     (1) local timestepping
i2n    --->         not used
```

```
igeom  --->     (1) blunt body
                (2) flat plate
                (3) wedge
                (4) channel/nozzle
irm    --->     (1) read input Mach number [Else: read input velocity]
iej    --->     (1) turn on body normal eigenvalue limiter only in shock
ichem  --->     (1) chemistry is on
ivib   --->     (1) vibrational relaxation is on
                (2) simulated vibrational equilibrium (check to make sure)
                (0) vibrational energy neglected for perfect gas
itv    --->     (n) how many iterations should elapse between Tv update
itl    --->     (1) implicit thin layer approximation
irk    --->         not used
iset   --->     (1) 5 species air
                (2) 8 species CO2-N2
                (3) 9 species CO2-H2O
icfljmp -->     How many iterations to perform before moving to next CFL number
vin    --->     If irm !=1, then this sets the freestream velocity [m/s].
                Otherwise the Mach number is used to set the velocity.
machin --->     If irm =1, then this is the Mach number used to set the freesteam.
cflmode--->     Tells how CFL numbers will be advanced.  Currently unused.
epsi   --->     i-direction eigenvalue limiter
epsj   --->     j-direction eigenvalue limiter
epsk   --->     k-direction eigenvalue limiter
pmul   --->     pressure weight in SW flux
alpha  --->     not used
yaw    --->     not used
stime   ---> Minimum time in seconds between solver status checks
rconv   ---> Consider solution to be converged if it reaches this normalized
             RMS residual relative to the maximum value for a given solution.
rfreeze ---> If set to a positive number, freeze the solution from
             updating starting at the i location that reaches this
             surface distance.
raccel  ---> Reaction acceleration factor for trying to simulate chemical
             equilibrium. Currently unimplemented.
```

```
vaccel  --->  To simulate thermal (vibrational-translational) equilibrium,
              then set ivib=2 and use this parameter to accelerate the vibrational-
              translational relaxation.  A typical value might be 1.0d+5.
emisw   --->  Surface emissivity if you choose the radiative equilibrium option
              for the wall temperature.
radrx   --->  Relaxation factor for updating the wall temperature if you choose
              the radiative equilibrium option for the wall temperature.
iblow   --->  Whether to model surface blowing or suction
              (0) Blowing or suction off
              (1) Blowing/suction with specified mass flux rate (mdot) (kg/m^2-s)
              (2) Blowing/suction with specified wall velocity (vsp) (m/s)
brelax  --->  Relaxation parameter for Newton-Raphson blowing solution updates.
              Generally this should be left at 1.0 although smaller values may
       help in cases where convergence of wall solution is troublesome
binit   --->  Method for setting the initial wall blowing mixture for
      N-R iterations.
              (1) Take the near-wall mass fractions
              (2) Take the blowing mass fractions
              (3) Mix the near-wall and blowing mass fractions
ibdiff  --->  Whether to include diffusion in the calculation of blowing
      species at the wall. Typically this would be on, but in same cases, to
      start problems it might need to be off.
              (0) Diffusion off.  Blowing species mass fractions are specified
              (1) Diffusion on.  This is the default value.
```

E. MATLAB CODES

E.1 Main TSP Program

```
%  call Iratio function
% save IratioMatrix to file
clear all
close all
clc
tic

%%%%%%%%%%% INPUTS %%%%%%%%%%%%%%

entry               =   4;          % Entry Number
run                 =   412;        % Run Number
drive               =   'D';        % drive for hard drive
Tref                =   297;
B                   =   363;
fsize               =   2;          % size of averaging filter
fnumber             =   2;          % #of times to run through filter
a                   =   [-1 2];     % scale of dT colourbar
filtering           =   1;          % 0 = no filtering, 1 = filtering
minframe            =   1;          % min frame for tiff files (usually=1)
skip                =   1;          % if you want to skip frames
frameoff            =   15;         % number of frames in off image
framedark           =   10;         % number of frames in dark image
NoiseLevel          =   5000;
exposure            =   5/1000;     % not always
loop                =   0;          % 1 = loop through all images, 0 = DDC
```

```
%%%%%%%%%%%%%%%%%%%%%%%%

% gathering necessary info for TSP images

string1 = char(strcat('b',num2str(run+1-400)));
string2 = char(strcat('k',num2str(run+1-400)));
TSP_Image_Details = xlsread(char(strcat(drive,':\Tunnel Data_Roger\Entry'...
    ,num2str(entry),'\Entry',num2str(entry),...
    'a_TSP\Entry4_TSP_Image_Details.xlsx')),strcat(string1,':',string2));

x_offset = TSP_Image_Details(1);        % offset in x-axis of image
y_offset = TSP_Image_Details(2);        % offset in y-axis of image
pix_per_m = TSP_Image_Details(3);       % number of pixels per metre in images
pixelcompx = TSP_Image_Details(4);
% pixel value of left x-coordinate where comparison to tsp will be made
pixelcompy = TSP_Image_Details(5);
% pixel value of top y-coordinate where comparison to tsp will be centered
max_time = TSP_Image_Details(6);
% max time to be used in TSP ht reduction, seconds
desired_time = TSP_Image_Details(7);
% desired time to examine more closely, seconds
min_frame = TSP_Image_Details(8);
% min frame to be used in TSP ht reduction
freq = TSP_Image_Details(9);           % frequency of camera pictures
mid_y = TSP_Image_Details(10);
% the pixel that approximately lines up with middle of model in y-direction

maxframe = max_time*freq+minframe;

desired_frame = desired_time*freq;

imagefile = char(strcat(drive,':\Tunnel Data_Roger\Entry',num2str
(entry),'\Entry4a_TSP\run',num2str(run),'.tif'));
offimage = char(strcat(drive,':\Tunnel Data_Roger\Entry',num2str
(entry),'\Entry4a_TSP\run',num2str(run),'off.tif'));
```

```
darkimage = char(strcat(drive,':\Tunnel Data_Roger\Entry',num2str
(entry),'\Entry4a_TSP\dark.tif'));

ts =                .16;
B =                 363;

timeframe   = freq * skip;  %seconds per frame

[ IratioMatrix shiftX shiftY] = Iratio(offimage,imagefile,darkimage,minframe...
,maxframe,skip,framedark,frameoff,NoiseLevel, filtering);

toc
max_x = length(IratioMatrix(1,:,1));    % maximum x-pixel in TSP image
max_y = length(IratioMatrix(:,1,1));    % maximum y-pixel in TSP image
%save (strcat('e',entrynum,'r',runnum,'_IratioFile.mat'), 'IratioMatrix')
save (strcat(drive,':\Tunnel_Data_Roger\Entry4\Entry4a_TSP\Results\Run...
',num2str(run),'\IratioFile.mat'), 'IratioMatrix')
toc

fontsize = 16;
load TSPcolormap;

xpixel = 1:max_x;
ypixel = 1:max_y;
xaxis = x_offset + xpixel/pix_per_m;
yaxis = y_offset - ypixel/pix_per_m;

% figure(1)
% DeltaT = (Tref-B) .* IratioMatrix(:,:,desired_frame) + B - Tref;
% imagesc(xaxis,yaxis,DeltaT,a)
% colormap(TSPcolormap);
% colorbar;
% xlabel('Distance from nosetip (m)','FontSize',16);
% ylabel('Spanwise reference (m)','FontSize',16);
% t = colorbar('peer',gca);
```

```
% set(get(t,'YLabel'),'String','Temperature Change \DeltaT, ^\circC')
% set(get(t,'YLabel'),'FontSize',16)
% set(get(t,'YLabel'),'FontWeight','bold')
% set(t,'FontSize',16)
% set(t,'FontWeight','bold')
% axis image
%
% figure(2)
% DeltaT = (Tref-B) .* IratioMatrix(:,:,desired_frame) + B - Tref;
% imagesc(xpixel,ypixel,DeltaT,a)
% colormap(TSPcolormap);
% colorbar;
% xlabel('Distance from nosetip (m)','FontSize',16);
% ylabel('Spanwise reference (m)','FontSize',16);
% t = colorbar('peer',gca);
% set(get(t,'YLabel'),'String','Temperature Change \DeltaT, ^\circC')
% set(get(t,'YLabel'),'FontSize',16)
% set(get(t,'YLabel'),'FontWeight','bold')
% set(t,'FontSize',16)
% set(t,'FontWeight','bold')
% axis image

shiftX = 1000*shiftX/pix_per_m;
shiftY = 1000*shiftY/pix_per_m;

maxtime=(1/timeframe)*(maxframe-1);
mintime=(1/timeframe)*(minframe-1);
t_tsp = (mintime:1/timeframe:maxtime)';
figure (3)
plot(t_tsp,(-shiftX)/(2.25),'g')
% change sign for "on" model motion not ref motion
hold on
plot(t_tsp,(-shiftY)/(2.25)+.0125,'r')
grid
xlabel('t (s)','FontSize', fontsize);
```

```
ylabel('Displacement (mm)','FontSize', fontsize);
legend('Xshift', 'Yshift');
hold off

%leave this in if you want to loop through all the images
if loop == 1
    for j = 1:maxframe
        figure(j+2)
        DeltaT = (Tref-B) .* IratioMatrix(:,:,j) + B - Tref;
        imagesc(xpix,ypix,DeltaT,a)
        colormap(TSPcolormap);
        colorbar;
        xlabel('Distance from nosetip (m)','FontSize',16);
        ylabel('Spanwise reference (m)','FontSize',16);
        t = colorbar('peer',gca);
        set(get(t,'YLabel'),'String','Temperature Change \DeltaT, ^\circC')
        set(get(t,'YLabel'),'FontSize',16)
        set(get(t,'YLabel'),'FontWeight','bold')
        set(t,'FontSize',16)
        set(t,'FontWeight','bold')
        axis image
    end
end
```

E.2 Analysis of Temperature Sensitive Paint Data

```
function [ IratioMatrix shiftX shiftY ] = Iratio( Off_file,On_file...
,Dark_file,minframe,maxframe,skip,framedark,frameoff,NoiseLevel, filtering)
% Returns IratioMatrix with image registration and cleanup outside the model

% setup filter parameters
fsize   = 4;
h       = fspecial('average',fsize);

%get dark image
j = 0;
darksum = zeros(size(double(imread(Dark_file,1))));
for i=1:framedark
    darksum=  darksum + double(imread(Dark_file,i));
end
dark=  darksum ./ framedark;

%get off image
offsum = zeros(size(double(imread(Off_file,1))));
for i=1:frameoff
    offsum=  offsum + double(imread(Off_file,i));
end
off=  offsum ./ frameoff;

if filtering==1
    dark    = filter2(dark,h,'full');
    off     = filter2(off,h,'full');
end

% Get on images
 [m n ]=size(off);
 IratioMatrix=single(zeros(m,n,(maxframe-minframe+1)/skip));
```

```
for i=1:skip:maxframe-minframe+1
    on = double(imread(On_file,i+minframe-1));

    if filtering==1
        on      = filter2(on,h,'full');
    end

    % image registration
    [output off1] = dftregistration(fft2(on),fft2(off),100);
    shiftX(i)=output(4);
    shiftY(i)=output(3);
    offShift=abs(ifft2(off1));

    % remove noise outside of model
    IndexNoise=on<NoiseLevel;
    on(IndexNoise)=0;

    Iratio = (on-dark) ./ (offShift-dark);
    Iratio=single(Iratio);
    if filtering==0
        Iratio      =fliplr(Iratio);
    elseif filtering==1
        Iratio      = flipud(Iratio);
    end
    IratioMatrix(:,:,i)= Iratio;
 end
% j = 0;
% if skip>1
%     for i=1:skip:maxframe-minframe
%         j = j+1;
%         IratioMatrix2(:,:,j)=IratioMatrix(:,:,i);
%     end
% IratioMatrix = IratioMatrix2;
end
```

E.3 Function to Align TSP Images

```
function [output Greg] = dftregistration(buf1ft,buf2ft,usfac)
% function [output Greg] = dftregistration(buf1ft,buf2ft,usfac);
% Efficient subpixel image registration by crosscorrelation. This code
% gives the same precision as the FFT upsampled cross correlation in a
% small fraction of the computation time and with reduced memory
% requirements. It obtains an initial estimate of the crosscorrelation peak
% by an FFT and then refines the shift estimation by upsampling the DFT
% only in a small neighborhood of that estimate by means of a
% matrix-multiply DFT. With this procedure all the image points are used to
% compute the upsampled crosscorrelation.
% Manuel Guizar - Dec 13, 2007

% Portions of this code were taken from code written by Ann M. Kowalczyk
% and James R. Fienup.
% J.R. Fienup and A.M. Kowalczyk, "Phase retrieval for a complex-valued
% object by using a low-resolution image," J. Opt. Soc. Am. A 7, 450-458
% (1990).

% Citation for this algorithm:
% Manuel Guizar-Sicairos, Samuel T. Thurman, and James R. Fienup,
% "Efficient subpixel image registration algorithms," Opt. Lett. 33,
% 156-158 (2008).

% Inputs
% buf1ft    Fourier transform of reference image,
%           DC in (1,1)   [DO NOT FFTSHIFT]
% buf2ft    Fourier transform of image to register,
%           DC in (1,1) [DO NOT FFTSHIFT]
% usfac     Upsampling factor (integer). Images will be registered to
%           within 1/usfac of a pixel. For example usfac = 20 means the
```

```
%           images will be registered within 1/20 of a pixel. (default = 1)

% Outputs
% output =  [error,diffphase,net_row_shift,net_col_shift]
% error     Translation invariant normalized RMS error between f and g
% diffphase     Global phase difference between the two images (should be
%               zero if images are non-negative).
% net_row_shift net_col_shift   Pixel shifts between images
% Greg      (Optional) Fourier transform of registered version of buf2ft,
%           the global phase difference is compensated for.

% Default usfac to 1
if exist('usfac')~=1, usfac=1; end

% Compute error for no pixel shift
if usfac == 0,
    CCmax = sum(sum(buf1ft.*conj(buf2ft)));
    rfzero = sum(abs(buf1ft(:)).^2);
    rgzero = sum(abs(buf2ft(:)).^2);
    error = 1.0 - CCmax.*conj(CCmax)/(rgzero*rfzero);
    error = sqrt(abs(error));
    diffphase=atan2(imag(CCmax),real(CCmax));
    output=[error,diffphase];

% Whole-pixel shift - Compute crosscorrelation by an IFFT and locate the
% peak
elseif usfac == 1,
    [m,n]=size(buf1ft);
    CC = ifft2(buf1ft.*conj(buf2ft));
    [max1,loc1] = max(CC);
    [max2,loc2] = max(max1);
    rloc=loc1(loc2);
    cloc=loc2;
    CCmax=CC(rloc,cloc);
    rfzero = sum(abs(buf1ft(:)).^2)/(m*n);
```

```
    rgzero = sum(abs(buf2ft(:)).^2)/(m*n);
    error = 1.0 - CCmax.*conj(CCmax)/(rgzero(1,1)*rfzero(1,1));
    error = sqrt(abs(error));
    diffphase=atan2(imag(CCmax),real(CCmax));
    md2 = fix(m/2);
    nd2 = fix(n/2);
    if rloc > md2
        row_shift = rloc - m - 1;
    else
        row_shift = rloc - 1;
    end

    if cloc > nd2
        col_shift = cloc - n - 1;
    else
        col_shift = cloc - 1;
    end
    output=[error,diffphase,row_shift,col_shift];

% Partial-pixel shift
else

    % First upsample by a factor of 2 to obtain initial estimate
    % Embed Fourier data in a 2x larger array
    [m,n]=size(buf1ft);
    mlarge=m*2;
    nlarge=n*2;
    CC=zeros(mlarge,nlarge);
    CC(m+1-fix(m/2):m+1+fix((m-1)/2),n+1-fix(n/2):n+1+fix((n-1)/2)) = ...
        fftshift(buf1ft).*conj(fftshift(buf2ft));

    % Compute crosscorrelation and locate the peak
    CC = ifft2(ifftshift(CC)); % Calculate cross-correlation
    [max1,loc1] = max(CC);
    [max2,loc2] = max(max1);
```

```
rloc=loc1(loc2);cloc=loc2;
CCmax=CC(rloc,cloc);

% Obtain shift in original pixel grid from the position of the
% crosscorrelation peak
[m,n] = size(CC); md2 = fix(m/2); nd2 = fix(n/2);
if rloc > md2
    row_shift = rloc - m - 1;
else
    row_shift = rloc - 1;
end
if cloc > nd2
    col_shift = cloc - n - 1;
else
    col_shift = cloc - 1;
end
row_shift=row_shift/2;
col_shift=col_shift/2;

% If upsampling > 2, then refine estimate with matrix multiply DFT
if usfac > 2,
    %%% DFT computation %%%
    % Initial shift estimate in upsampled grid
    row_shift = round(row_shift*usfac)/usfac;
    col_shift = round(col_shift*usfac)/usfac;
    dftshift = fix(ceil(usfac*1.5)/2); %Center of output array at dftshift+1
    % Matrix multiply DFT around the current shift estimate
    CC = conj(dftups(buf2ft.*conj(buf1ft),ceil(usfac*1.5)...
   ,ceil(usfac*1.5),usfac,dftshift-row_shift*usfac...
   ,dftshift-col_shift*usfac))/(md2*nd2*usfac^2);
    % Locate maximum and map back to original pixel grid
    [max1,loc1] = max(CC);
    [max2,loc2] = max(max1);
    rloc = loc1(loc2); cloc = loc2;
    CCmax = CC(rloc,cloc);
```

```
        rg00 = dftups(buf1ft.*conj(buf1ft),1,1,usfac)/(md2*nd2*usfac^2);
        rf00 = dftups(buf2ft.*conj(buf2ft),1,1,usfac)/(md2*nd2*usfac^2);
        rloc = rloc - dftshift - 1;
        cloc = cloc - dftshift - 1;
        row_shift = row_shift + rloc/usfac;
        col_shift = col_shift + cloc/usfac;

    % If upsampling = 2, no additional pixel shift refinement
    else
        rg00 = sum(sum( buf1ft.*conj(buf1ft) ))/m/n;
        rf00 = sum(sum( buf2ft.*conj(buf2ft) ))/m/n;
    end
    error = 1.0 - CCmax.*conj(CCmax)/(rg00*rf00);
    error = sqrt(abs(error));
    diffphase=atan2(imag(CCmax),real(CCmax));
    % If its only one row or column the shift along that dimension has no
    % effect. We set to zero.
    if md2 == 1,
        row_shift = 0;
    end
    if nd2 == 1,
        col_shift = 0;
    end
    output=[error,diffphase,row_shift,col_shift];
end

% Compute registered version of buf2ft
if (nargout > 1)&&(usfac > 0),
    [nr,nc]=size(buf2ft);
    Nr = ifftshift([-fix(nr/2):ceil(nr/2)-1]);
    Nc = ifftshift([-fix(nc/2):ceil(nc/2)-1]);
    [Nc,Nr] = meshgrid(Nc,Nr);
    Greg = buf2ft.*exp(i*2*pi*(-row_shift*Nr/nr-col_shift*Nc/nc));
    Greg = Greg*exp(i*diffphase);
elseif (nargout > 1)&&(usfac == 0)
```

```
    Greg = buf2ft*exp(i*diffphase);
end
return

function out=dftups(in,nor,noc,usfac,roff,coff)
% function out=dftups(in,nor,noc,usfac,roff,coff);
% Upsampled DFT by matrix multiplies, can compute an upsampled DFT in just
% a small region.
% usfac         Upsampling factor (default usfac = 1)
% [nor,noc]     Number of pixels in the output upsampled DFT, in
%               units of upsampled pixels (default = size(in))
% roff, coff    Row and column offsets, allow to shift the output array to
%               a region of interest on the DFT (default = 0)
% Recieves DC in upper left corner, image center must be in (1,1)
% Manuel Guizar - Dec 13, 2007
% Modified from dftus, by J.R. Fienup 7/31/06

% This code is intended to provide the same result as if the following
% operations were performed
%   - Embed the array "in" in an array that is usfac times larger in each
%     dimension. ifftshift to bring the center of the image to (1,1).
%   - Take the FFT of the larger array
%   - Extract an [nor, noc] region of the result. Starting with the
%     [roff+1 coff+1] element.

% It achieves this result by computing the DFT in the output array without
% the need to zeropad. Much faster and memory efficient than the
% zero-padded FFT approach if [nor noc] are much smaller than [nr*usfac nc*usfac]

[nr,nc]=size(in);
% Set defaults
if exist('roff')~=1, roff=0; end
if exist('coff')~=1, coff=0; end
if exist('usfac')~=1, usfac=1; end
if exist('noc')~=1, noc=nc; end
```

```
if exist('nor')~=1, nor=nr; end
% Compute kernels and obtain DFT by matrix products
kernc=exp((-i*2*pi/(nc*usfac))*( ifftshift([0:nc-1]).' - floor(nc/2) )...
*( [0:noc-1] - coff ));
kernr=exp((-i*2*pi/(nr*usfac))*( [0:nor-1].' - roff )...
*( ifftshift([0:nr-1]) - floor(nr/2)  ));
out=kernr*in*kernc;
return
```

F. DIAGRAM OF GLOW PERTURBER DESIGN

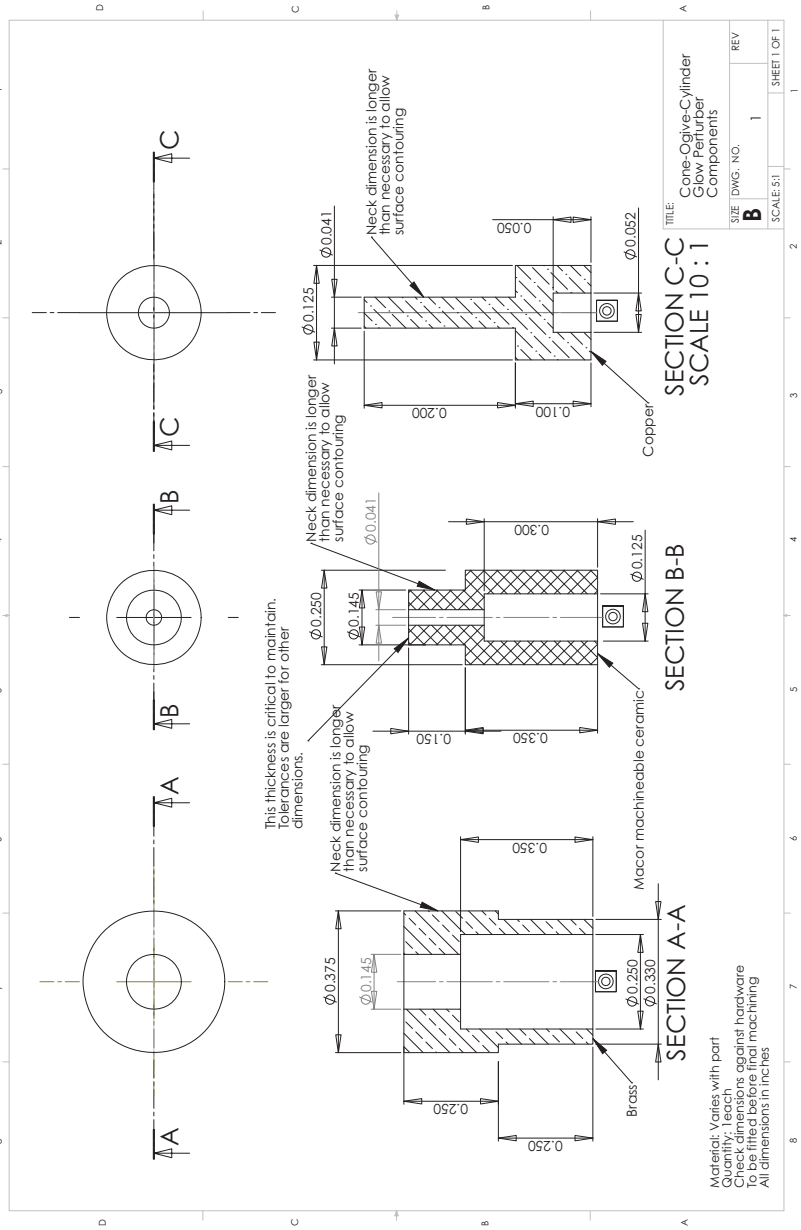

Fig. F.1. Drawing of glow perturber components for the cone-ogive-cylinder.

G. HOT-WIRE SURVIVAL SPREADSHEET

Table G.1
Hot-Wire Survival Spreadsheet, page 1.

Probe Body	Runs	Diameter (in)	Oven	Supersonic Jet	Pressures (psia)	Break Comments
2	2	.0002	No	No	20 - 80	startup
3	1	.0002	No	No	80	startup
4	1	.0002	No	No	80	startup
F	6	.0002	No	No	20 - 120	startup
8	2	.0002	No	No	20 - 40	shutdown
Y	19	.0002	No	No	30 - 145	startup
X	2	.0002	No	No	20 - 40	shutdown
A	7	.0002	No	No	20 - 120	during run
Y	13	.0002	No	No	20 - 135	shutdown
F	1	.0002	No	No	30	startup
E	7	.0002	No	No	20 - 90	startup
4	8	.0002	No	No	20 - 120	shutdown
1	7	.0002	No	No	20 - 135	shutdown
3	1	.0002	No	No	30	startup
2	5	.0002	No	No	20 - 135	shutdown
2	3	.0002	No	No	20 - 45	shutdown

Table G.2
Hot-Wire Survival Spreadsheet, page 2.

Probe Body	Runs	Diameter (in)	Oven	Supersonic Jet	Pressures (psia)	Break Comments
3	6	.0002	No	No	20 - 90	during run
4	3	.0002	No	No	25 - 90	shutdown
V	0	.0002	Yes	No	n/a	supersonic jet
V	0	.0002	Yes	No	n/a	supersonic jet
2	0	.0002	Yes	No	n/a	supersonic jet
3	0	.0002	Yes	No	n/a	oven
X	0	.0002	Yes	No	n/a	oven
E	0	.0002	Yes	No	n/a	oven
8	0	.0002	Yes	No	n/a	supersonic jet
4	0	.0002	Yes	No	n/a	oven
E	0	.0002	Yes	No	n/a	supersonic jet
F	0	.0002	Yes	No	n/a	oven
Y	0	.0002	Yes	No	n/a	supersonic jet
1	16	.0002	Yes	Yes	120 - 135	during run
W	11	.0002	Yes	Yes	120	before run
X	0	.0003	Yes	No	n/a	supersonic jet
4	0	.0003	Yes	No	n/a	supersonic jet

Table G.3
Hot-Wire Survival Spreadsheet, page 3.

Probe Body	Runs	Diameter (in)	Oven	Supersonic Jet	Pressures (psia)	Break Comments
B	0	.0003	Yes	No	n/a	oven
V	0	.0003	Yes	No	n/a	supersonic jet
F	11	.0003	Yes	No	20 - 120	poor spectra
1	5	.0003	No	No	20 - 120	shutdown
3	4	.0002	No	No	20 - 90	shutdown
2	5	.0003	No	No	20 - 120	still working
5	8	.0002	No	No	20 - 120	shutdown
6	1	.0002	No	No	20	startup
5	1	.0002	No	No	120	shutdown
D	1	.0002	No	No	120	during removal
X	2	.0002	No	No	120	shutdown
4	1	.0002	No	No	120	shutdown
V	1	.0002	No	No	120	shutdown
Y	0	.0002	No	No	n/a	installation
W	53	.0002	No	No	20 - 120	shutdown
Y	4	.0002	No	No	20 - 90	still working

LIST OF REFERENCES

LIST OF REFERENCES

[1] S. P. Schneider, "Paper 1 - Introduction and Goals," in *NATO RTO-MP-AVT-200 - Hypersonic Laminar-Turbulent Transition*, (San Diego, CA), April 2012.

[2] S. P. Schneider, "Hypersonic laminar-turbulent transition on circular cones and scramjet forebodies," *Progress in Aerospace Sciences*, vol. 40, pp. 1–50, 2004.

[3] E. Reshotko, "Is $\mathrm{Re}_\theta/\mathrm{M}_e$ a Meaningful Transition Criterion?," *AIAA Journal*, vol. 45, no. 7, pp. 1441–1443, 2007.

[4] E. Reshotko, "Hypersonic Stability and Transition," in *Hypersonic Flows for Reentry Problems* (J.-A. Desideri, R. Glowinski, and J. Periaux, eds.), pp. 18–34, Springer-Verlag, Berlin, Germany, 1991.

[5] K. F. Stetson, "Comments on Hypersonic Boundary-Layer Transition," Tech. Rep. High Speed Aero Performance Branch Final Report, WRDC-TR-90-3057, 1990.

[6] L. Mack, "Stability of Axisymmetric Boundary layers on Sharp Cones at Hypersonic Mach Numbers." AIAA 87-1413, June 1987.

[7] C. R. Alba, K. M. Casper, S. J. Beresh, and S. P. Schneider, "Comparison of Experimentally Measured and Computed Second-Mode Disturbances in Hypersonic Boundary-Layers." AIAA 2010-897, January 2010.

[8] M. Estorf, R. Radespiel, S. P. Schneider, H. B. Johnson, and S. Hein, "Surface-Pressure Measurements of Second-Mode Instability in Quiet Hypersonic Flow." AIAA 2008-1153, January 2008.

[9] G. Dietz, S. Mahlmann, and S. Hein, "Entropy-Layer Instabilities in Plane Supersonic Flow," in *New Results in Numerical and Experimental Fluid Mechanics II* (W. Nitsche, H.-J. Heinemann, and R. Hilbig, eds.), pp. 108–114, Springer Fachmedien Wiesbaden, 1999.

[10] A. V. Fedorov, "Instability of the Entropy Layer on a Blunt Plate in Supersonic Gas Flow," *Journal of Applied Mechanics and Technical Physics, Translated from Zhurnal Prikladnoi Mekhaniki i Tekhnicheskoi Fiziki*, vol. 31, no. 5, pp. 722–728, 1990.

[11] V. I. Lysenko, "Influence of the Entropy Layer on the Stability of a Supersonic Shock Layer and Transition of the Laminar Boundary Layer to Turbulence," *Journal of Applied Mechanics and Technical Physics, Translated from Zhurnal Prikladnoi Mekhaniki i Tekhnicheskoi Fiziki*, vol. 31, no. 6, pp. 868–873, 1990.

[12] L. M. Mack, "Boundary Layer Stability Theory," *in AGARD (Advisory Group for Aerospace Research and Development) Special Course on Stability and Transition of Laminar Flow*, no. 709, pp. 1–81, 1984.

[13] F. M. White, *Viscous Fluid Flow*. McGraw-Hill Inc., St. Louis, Missouri.

[14] G. B. Schubauer and H. K. Skramstad, "Laminar Boundary-Layer Oscillations and Stability of Laminar Flow," *Journal of Aeronautical Sciences*, vol. 14, no. 2, pp. 69–78, 1947.

[15] A. Fedorov, "Transition and Stability of High-Speed Boundary Layers," *Annual review of Fluid Mechanics*, vol. 43, pp. 79–95, 2011.

[16] L. M. Mack, "Linear Stability Theory and the Problem of Supersonic Boundary-Layer Transition," *AIAA Journal*, vol. 13, no. 3, pp. 278–289, 1974.

[17] K. F. Stetson and R. L. Kimmel, "On Hypersonic Boundary-Layer Stability." AIAA 92-0737, January 1992.

[18] S. P. Schneider. Class Notes for AAE 624: Laminar-Turbulent Transition, 2012.

[19] E. Reshotko, "Boundary Layer Instability, Transition and Control." AIAA 94-0001, January 1994.

[20] X. Zhong and X. Wang, "Direct Numerical Simulation on the Receptivity, Instability, and Transition of Hypersonic Boundary Layers," *Annual Review of Fluid Mechanics*, vol. 44, pp. 527–561, 2012.

[21] J. M. Kendall, "Wind Tunnel Experiments Relating to Supersonic and Hypersonic Boundary-Layer Transition," *AIAA Journal*, vol. 13, no. 3, pp. 290–299, 1974.

[22] J. Laufer and T. Vrebalovich, "Stability and transition of a supersonic laminar boundary layer on an insulated flat plate," *Journal of Fluid Mechanics*, vol. 9, no. 2, pp. 257–299, 1960.

[23] K. Fujii, "Experiment of Two-Dimensional Roughness Effect on Hypersonic Boundary-Layer Transition," *Journal of Spacecraft and Rockets*, vol. 43, no. 4, pp. 731–738, 2006.

[24] S. P. Schneider, "Summary of Hypersonic Transition Research Coordinated through NATO RTO AVT-136." AIAA 2010-1466, January 2010.

[25] S. P. Schneider, "Laminar-Turbulent Transition on Reentry Capsules and Planetary Probes," *Journal of Spacecraft and Rockets*, vol. 43, no. 6, pp. 1153–1173, 2006.

[26] C.-L. Chang, M. M. Choudhari, B. R. Hollis, and F. Li, "Transition Analysis for the Mars Science Laboratory Entry Vehicle." AIAA 2009-4076, June 2009.

[27] E. Reshotko, "Transition Issues at Hypersonic Speeds." AIAA 2006-707, January 2006.

[28] A. Demetriades, "Hypersonic Viscous Flow over a Slender Cone, Part III: Laminar Instability and Transition." AIAA 74-535, June 1974.

[29] A. Demetriades, "Growth of disturbances in a laminar boundary layer at Mach 3," *Phys. Fluids A*, vol. 1, no. 2, pp. 312–317, 1989.

[30] K. F. Stetson, R. L. Kimmel, E. R. Thompson, J. C. Donaldson, and L. G. Siler, "A Comparison of Planar and Conical Boundary Layer Stability and Transition at a Mach Number of 8." AIAA 91-1639, June 1991.

[31] V. Wendt, H. Kreplin, G. Hohler, F. Grosch, P. Krogmann, and M. Simen, "Planar and Conical Boundary Layer Stability Experiments at Mach 5." AIAA 93-5112, November 1993.

[32] D. A. Bountin, A. A. Sidorenko, and A. N. Shiplyuk, "Development of Natural Disturbances in a Hypersonic Boundary Layer on a Sharp Cone," *Journal of Applied Mechanics and Technical Physics*, vol. 42, no. 1, pp. 57–62, 2001.

[33] J. N. S. Dougherty and D. F. Fisher, "Boundary Layer Transition on a 10-Degree Cone: Wind Tunnel/Flight Data Correlation." AIAA 80-0154, January 1980.

[34] J. N. Sam Dougherty and D. F. Fisher, "Boundary-Layer Transition Correlation on a Slender Cone in Wind Tunnels and Flight for Indications of Flow Quality," Tech. Rep. AEDC-TR-81-26, February 1982.

[35] K. F. Stetson, E. R. Thompson, J. C. Donaldson, and L. G. Siler, "Laminar Boundary Layer Stability Experiments on a Cone at Mach 8, Part 1: Sharp Cone." AIAA 83-1761, July 1983.

[36] F. Munoz, D. Heitmann, and R. Radespiel, "Instability Modes in Boundary Layers of an Inclined Cone at Mach 6." AIAA 2012-2823, June 2012.

[37] E. Perez, H. L. Reed, and J. J. Kuehl, "Instabilities on a Hypersonic Yawed Straight Cone." AIAA 2013-2879, June 2013.

[38] C. S. J. Mayer, D. A. V. Terzi, and H. F. Fasel, "Direct numerical simulation of complete transition to turbulence via oblique breakdown at Mach 3," *Journal of Fluid Mechanics*, vol. 674, pp. 5–42, 2011.

[39] M. R. Malik, "Oblique route to turbulence," *Journal of Fluid Mechanics*, vol. 674, pp. 1–4, 2011.

[40] S. Cai-hong and Z. Heng, "Stability analysis and transition prediction of hypersonic boundary layer over a blunt cone with small nose bluntness at zero angle of attack," *Applied Mathematics and Mechanics (English Edition)*, vol. 28, no. 5, pp. 563–572, 2007.

[41] L. C. Kirk and G. V. Candler, "Geometric Effects on the Amplification of First Mode Instability Waves." AIAA 2013-0261, January 2013.

[42] J. D. Anderson, *Modern Compressible Flow with Historical Perspective*, vol. 1. The McGraw-Hill Companies, Inc., New York, New York, 3 ed., 2003.

[43] J. W. Cleary, "Effects of Angle of Attack and Nose Bluntness on the Hypersonic Flow over Cones." AIAA 66-414, June 1966.

[44] J. D. Anderson, *Hypersonic and High-Temperature Gas Dynamics*, vol. 1. American Institute of Aeronautics and Astronautics, Inc., Reston, Virginia, 1 ed., 1989.

[45] Z. Popinski, "Compressible Laminar Boundary Layers on Sharp Cone at Incidence with Entropy Swallowing," *AIAA Journal*, vol. 13, no. 9, pp. 1135–1134, 1975.

[46] P. A. Sullivan and W. W. Koziak, "Entropy Layer Effects in Constant Pressure Hypersonic Boundary Layers," *AIAA Journal*, vol. 11, no. 5, pp. 730–731, 1973.

[47] P. C. Stainback, "Some Effects of Roughness and Variable Entropy on Transition at a Mach Number of 8." AIAA 67-132, January 1967.

[48] N. R. Rotta and V. Zakkay, "Effects of Nose Bluntness on the Boundary Layer Characteristics of Conical Bodies at Hypersonic Speeds," *Astronautics Aeta*, vol. 13, no. 5/6, pp. 507–516, 1968.

[49] K. F. Stetson, E. R. Thompson, J. C. Donaldson, and L. G. Siler, "Laminar Boundary Layer Stability Experiments on a Cone at Mach 8, Part 2: Blunt Cone." AIAA 84-0006, January 1984.

[50] S. Hein, "Nonlinear Nonlocal Transition Analysis," Tech. Rep. ISRN DLR-FB–2005-10, 2005.

[51] K. F. Stetson and G. H. Rushton, "Shock Tunnel Investigation of Boundary-Layer Transition at M = 5.5," *AIAA Journal*, vol. 5, no. 5, pp. 899–906, 1967.

[52] E. J. Softley, B. C. Graber, and R. E. Zempel, "Experimental Observation of Transition of the Hypersonic Boundary Layer," *AIAA Journal*, vol. 7, no. 2, pp. 257–263, 1969.

[53] E. J. Softley, "Boundary Layer Transition on Hypersonic Blunt, Slender Cones." AIAA 69-705, June 1969.

[54] K. F. Stetson, "Nosetip Bluntness Effects on Cone Frustum Boundary Layer Transition in Hypersonic Flow." AIAA 83-1763, July 1983.

[55] L. Lees and C. C. Lin, "Investigation of the Stability of the Laminar Boundary Layer in a Compressible Fluid," Tech. Rep. Technical Note No. 1115, NACA, 1946.

[56] E. Reshotko and M. M. S. Khan, "Stability of the Laminar Boundary Layer on a Blunted Plate in Supersonic Flow," *Laminar-Turbulent Transition, IUTAM Symposium*, pp. 186–200, September 1980.

[57] E. Kufner, U. Dallmann, and J. Stilla, "Instability of Hypersonic Flow Past Blunt Cones - Effects of Mean Flow Variations." AIAA 93-2983, June 1993.

[58] S. Hein, "Numerical Investigation of Hypersonic Wall-Bounded Shear Flows - Part 2: Entropy-Layer Instability in Blunt Cone Flows," *ERCOFTAC Bulletin*, vol. 74, pp. 57–60, 2007.

[59] J. Lei and X. Zhong, "Linear Stability Analysis of Nose Bluntness Effects on Hypersonic Boundary Layer Transition," *Journal of Spacecraft and Rockets*, vol. 49, no. 1, pp. 24–37, 2012.

[60] S. C. Chang, X. Y. Wang, and C. Chow, "The Method of Space-Time Conservation Element and Solution Element: A New High-Resolution and Genuinely Multidimensional Paradigm for Solving Conservation Laws," *Journal of Computational Physics*, vol. 156, no. 1, pp. 89–136, 1999.

[61] A. Fedorov and A. Tumin, "Evolution of Disturbances in Entropy Layer on a Blunted Plate in Supersonic Flow." AIAA 2002-2847, June 2002.

[62] A. Fedorov and A. Tumin, "Evolution of Disturbances in Entropy Layer on Blunted Plate in Supersonic Flow," *AIAA Journal*, vol. 42, no. 1, pp. 89–94, 2004.

[63] C. H. Young, D. C. Reda, and A. M. Roberge, "Hypersonic Transitional and Turbulent Flow Studies on a Lifting Entry Vehicle," *Journal of Spacecraft and Rockets*, vol. 9, pp. 883–888, 1972.

[64] M. Malik, R. E. Spall, and C.-L. Chang, "Effect of Nose Bluntness on Boundary Layer Stability and Transition." AIAA 90-0112, January 1990.

[65] G. Dietz and A. Meijering, "Numerical investigation of boundary-layer instabilities over a blunt flat plate at angle of attack in supersonic flow," in *New Results in Numerical and Experimental Fluid Mechanics* (H. Korner and R. Hilbig, eds.), pp. 103–110, Friedr. Vieweg and Sohn Verlagsgesellschaft mbH, Braunschweig/Wiesbaden.

[66] P. C. Stainback, "Hypersonic Boundary-Layer Transition in the Presence of Wind-Tunnel Noise," *AIAA Journal*, vol. 9, no. 12, pp. 2475–2476, 1971.

[67] E. Reshotko, "A Program for Transition Research," *AIAA Journal*, vol. 13, no. 3, pp. 261–265, 1975.

[68] I. E. Beckwith, "Development of a High Reynolds Number Quiet Tunnel for Transition Research," *AIAA Journal*, vol. 13, no. 3, pp. 300–306, 1975.

[69] S. P. Schneider, "Design of a Mach-6 Quiet-flow Wind-Tunnel Nozzle Using the e**N Method for Transition Estimation." AIAA 98-0547, 1998.

[70] F. J. Chen, M. R. Malik, and I. E. Beckwith, "Boundary-Layer Transition on a Cone and Flat Plate at Mach 3.5," *AIAA Journal*, vol. 27, no. 6, pp. 687–693, 1989.

[71] S. R. Pate and C. J. Schueler, "Radiated Aerodynamic Noise Effects on Boundary-Layer Transition in Supersonic and Hypersonic Wind Tunnels," *AIAA Journal*, vol. 7, no. 3, pp. 450–457, 1969.

[72] S. R. Pate, "Measurements and Correlations of Transition Reynolds Numbers on Sharp Slender Cones at High Speeds," *AIAA Journal*, vol. 9, no. 5, pp. 1082–1090, 1971.

[73] S. R. Pate, "Supersonic Boundary-Layer Transition: Effects of Roughness and Freestream Disturbances," *AIAA Journal*, vol. 9, no. 5, pp. 797–803, 1971.

[74] S. R. Pate, "Effects of Wind Tunnel Disturbances on Boundary-Layer Transition with Emphasis on Radiated Noise: A Review." AIAA 80-0431, March 1980.

[75] R. A. King, "Three-dimensional boundary-layer transition on a cone at Mach 3.5," *Experiments in Fluids*, vol. 13, pp. 305–314, 1992.

[76] S. P. Schneider, "Effects of High-Speed Tunnel Noise on Laminar-Turbulent Transition," *Journal of Spacecraft and Rockets*, vol. 38, no. 3, pp. 323–333, 2001.

[77] L. M. Mack, "Early History of Compressible Linear Stability Theory," in *IUTAM Symposium on Laminar-Turbulent Transition* (H. F. Fasel and W. S. Saric, eds.), pp. 9–34, Springer-Verlag, Berlin, Germany, September.

[78] T. Herbert, "Parabolized Stability Equations," *Annual Review of Fluid Mechanics*, vol. 29, pp. 245–283, 1997.

[79] M. R. Malik, "Hypersonic Flight Transition Data Analysis Using Parabolized Stability Equations with Chemistry Effects," *Journal of Spacecraft and Rockets*, vol. 40, no. 3, pp. 332–344, 2003.

[80] H. B. Johnson and G. V. Candler, "Hypersonic Boundary Layer Stability Analysis Using PSE-Chem." AIAA 2005-5023, June 2005.

[81] C. R. Alba, H. B. Johnson, and G. V. Candler, "Oblique Wave Disturbance Analysis of Supersonic Flow Past Axisymmetric and 2D Bodies at Angles of Attack." AIAA 2008-4396, June 2008.

[82] S. P. Schneider, "Development of Hypersonic Quiet Tunnels," *Journal of Spacecraft and Rockets*, vol. 45, no. 4, pp. 641–663, 2008.

[83] M. M. Choudhari. Email to Steven Schneider, 2011.

[84] C. A. C. Ward, B. M. Wheaton, A. Chou, D. C. Berridge, L. E. Letterman, R. P. K. Luersen, and S. P. Schneider, "Hypersonic Boundary-Layer Transition Experiments in the Boeing/AFOSR Mach-6 Quiet Tunnel." AIAA 2012-0282, January 2012.

[85] M. J. Zucrow and J. D. Hoffman, *Gas Dynamics, Multidimensional Flow*, vol. 2. Robert E. Krieger Publishing Company, Malabar, Florida, 2 ed., 1985.

[86] A. Abney, C. Ward, D. Berridge, R. Greenwood, and S. P. Schneider, "Hypersonic Boundary-Layer Transition Experiments in the Boeing/AFOSR Mach-6 Quiet Tunnel." AIAA 2013-0375, January 2013.

[87] D. R. Lord and E. F. Ulmann, "Pressure Measurements on an Ogive-Cylinder Body at Mach 4.04," Tech. Rep. L51L20, NACA, February 1952.

[88] A. E. Blanchard, J. T. Lachowicz, and S. P. Wilkinson, "NASA Langley Mach 6 Quiet Wind-Tunnel Performance," *AIAA Journal*, vol. 35, no. 1, pp. 23–28, 1997.

[89] S. P. Schneider, T. J. Juliano, and M. P. Borg, "High-Reynolds-Number Laminar Flow in the Mach-6 Quiet-Flow Ludwieg Tube." AIAA 2006-3056, June 2006.

[90] S. P. Schneider, "Measurements of the Mechanisms of Laminar-Turbulent Transition in the Mach-6 Quiet Tunnel," Tech. Rep. AFRL-OSR-VA-TR-2012-0386, February 2012.

[91] C.-H. Zhang, Q. Tang, and C.-B. Lee, "Hypersonic boundary-layer transition on a flared cone," *Acta Mechanica Sinica*, vol. 29, pp. 48–53, 2013.

[92] T. Juliano, S. Schneider, S. Aragag, and D. Knight, "Quiet-Flow Ludwieg Tube for Hypersonic Transition Research," *AIAA Journal*, vol. 46, no. 7, pp. 1757–1763, 2008.

[93] L. E. Steen, "Characterization and Development of Nozzles For A Hypersonic Quiet Wind Tunnel," Master's thesis, Department of Aeronautics and Astronautics, Purdue University, West Lafayette, IN, November 2010.

[94] P. L. Gilbert, "Effect of Tunnel Noise on Laminar Stagnation-Point Heating at Mach 6," Master's thesis, Department of Aeronautics and Astronautics, Purdue University, West Lafayette, IN, December 2010.

[95] L. E. Letterman, "Instability and Transition on a Von Karman Ogive in a Mach-6 Quiet Tunnel," Master's thesis, Department of Aeronautics and Astronautics, Purdue University, West Lafayette, IN, August 2012.

[96] C. A. C. Ward, R. T. Greenwood, A. D. Abney, and S. P. Schneider, "Boundary-Layer Transition Experiments in a Hypersonic Quiet Wind Tunnel." AIAA 2013-2738, June 2013.

[97] R. P. K. Luersen, "Techniques for Application of Roughness for Manipulation of Second-Mode Waves on a Flared Cone at Mach 6," Master's thesis, Department of Aeronautics and Astronautics, Purdue University, West Lafayette, IN, December 2012.

[98] C. A. Ward, "Hypersonic Crossflow Instability and Transition on a Circular Cone at Angle of Attack," Master's thesis, Department of Aeronautics and Astronautics, Purdue University, West Lafayette, IN, December 2010.

[99] J. J. Dussling, "Development of an Improved Temperature Sensitive Paint System for the Boeing/AFOSR Mach-6 Quiet Tunnel," Master's thesis, Department of Aeronautics and Astronautics, Purdue University, West Lafayette, IN, December 2011.

[100] K. M. Casper, "Hypersonic Wind-Tunnel Measurements of Boundary-Layer Pressure Fluctuations," Master's thesis, Department of Aeronautics and Astronautics, Purdue University, West Lafayette, IN, August 2009.

[101] B. M. Wheaton, "Roughness-Induced Instability in a Laminar Boundary Layer at Mach-6," Master's thesis, Department of Aeronautics and Astronautics, Purdue University, West Lafayette, IN, December 2009.

[102] S. J. Rufer, *Hot-Wire Measurements of Instability Waves on Sharp and Blunt Cones at Mach 6*. PhD thesis, Department of Aeronautics and Astronautics, Purdue University, West Lafayette, IN, December 2005.

[103] S. J. Rufer, "Development of Burst-Diaphragm and Hot-Wire Apparatus for use in the Mach-6 Purdue Quiet-Flow Ludwieg Tube," Master's thesis, Department of Aeronautics and Astronautics, Purdue University, West Lafayette, IN, December 2000.

[104] M. V. Morkovin, "Fluctuations and Hot-Wire Anemometry in Compressible Flows," in *AGARDograph 24*, (Palais de Chaillot, Paris), North Atlantic Treaty Organization Advisory Group for Aeronautical Research and Development, November 1956.

[105] B. M. Wheaton and S. P. Schneider, "Roughness-Induced Instability in a Hypersonic Laminar Boundary Layer," *AIAA Journal*, vol. 50, no. 6, pp. 1245–1256, 2012.

[106] D. W. Ladoon, *Wave Packets Generated by a Surface Glow Discharge on a Cone at Mach 4*. PhD thesis, Department of Aeronautics and Astronautics, Purdue University, West Lafayette, IN, December 1998.

[107] C. Dupuy and X. Savalle, "First-mode instabilities emphasis generated by glow discharges at Mach-6." Final report for Summer 2013 internship of French Air Force Academy students in the BAM6QT, May 2013.

[108] K. M. Casper, *Pressure Fluctuations Beneath Instability Wave Packets and Turbulent Spots in a Hypersonic Boundary Layer*. PhD thesis, Department of Aeronautics and Astronautics, Purdue University, West Lafayette, IN, August 2012.

[109] D. C. Berridge, K. M. Casper, S. J. Rufer, C. R. Alba, D. R. Lewis, S. J. Beresh, and S. P. Schneider, "Measurements and Computations of Second-Mode Instability Waves in Three Hypersonic Wind Tunnels." AIAA 2010-5002, June 2010.

[110] J. A. Masad, "Relationship Between Transition and Modes of Instability in High-Speed Boundary Layers," *AIAA Journal*, vol. 33, no. 4, pp. 774–776, 1993.

[111] N. D. Tullio, P. Paredes, N. D. Sandham, and V. Theofilis, "Laminar-turbulent transition induced by a discrete roughness element in a supersonic boundary layer," *Journal of Fluid Mechanics*, vol. 735, pp. 613–646, 2013.

[112] P. Paredes. Personal Communication, May 2014.

[113] A. Fedorov. Personal Email, August 2013.

VITA

VITA

Roger Greenwood was born in a small farming community in southeast Idaho. He was raised on a dairy farm and attended North Gem Schools before moving to Utah when he was 17. In 1994 he graduated from American Fork High School and was accepted to study at Brigham Young University in Provo, UT. He studied for one year, then took a two year leave of absence to serve as a missionary for The Church of Jesus Christ of Latter-Day Saints in Rio de Janeiro, Brazil. He returned to finish up his bachelor of science degree in Mechanical Engineering.

While attending BYU, Roger met and married his sweetheart, Marci Forsberg, and they had their first child just before they both graduated in December 2000. Upon graduation, Roger was commissioned an officer in the United States Air Force and they went to Hanscom AFB, near Boston, MA for their first assignment. The Air Force then took them to Wright-Patterson AFB in Ohio for where Roger received his master of science degree in Aeronautical Engineering from the Air Force Institute of Technology. He stayed at Wright-Patterson AFB for several years serving as a developmental engineer and a program manager.

From Ohio the Air Force sent Roger to the Air Force Academy in Colorado Springs where he taught in the Aeronautical Engineering department. After three years of teaching, the Academy sponsored Roger to pursue his PhD at Purdue University as part of the Academy's faculty pipeline program. This program has the goal of bringing officers back to teach in the department after earning their PhD and serving another Air Force Assignment.

For his next assignment Roger has been assigned to serve in the Space and Missiles Center at Los Angeles AFB in California. He will move there in August 2014 with his wife, Marci, and their five children.